



**HAL**  
open science

# Modeling and control of hybrid PV thermal panels

Zain Ul Abdin

► **To cite this version:**

Zain Ul Abdin. Modeling and control of hybrid PV thermal panels. Modeling and Simulation. Université de Picardie Jules Verne, 2022. English. NNT : 2022AMIE0057 . tel-04079629

**HAL Id: tel-04079629**

**<https://theses.hal.science/tel-04079629>**

Submitted on 24 Apr 2023

**HAL** is a multi-disciplinary open access archive for the deposit and dissemination of scientific research documents, whether they are published or not. The documents may come from teaching and research institutions in France or abroad, or from public or private research centers.

L'archive ouverte pluridisciplinaire **HAL**, est destinée au dépôt et à la diffusion de documents scientifiques de niveau recherche, publiés ou non, émanant des établissements d'enseignement et de recherche français ou étrangers, des laboratoires publics ou privés.



# Thèse de Doctorat

*Mention : Science pour l'Ingénieur  
Spécialité : Automatique*

présentée à l'*Ecole Doctorale en Sciences Technologie et Santé (ED 585)*

**de l'Université de Picardie Jules Verne**

par

**Zain UL ABDIN**

pour obtenir le grade de Docteur de l'Université de Picardie Jules Verne

***Modélisation et Contrôle des panneaux photovoltaïques  
hybrides***

Soutenue le 28 Septembre 2022, après avis des rapporteurs, devant le jury d'examen :

<b>M. Jean-Paul GAUBERT, Professeur, Université de Poitiers</b>	<b>Président</b>
<b>M. Hamid GUALOUS, Professeur, Université de Caen Normandie</b>	<b>Rapporteur</b>
<b>M. Vladan KONCAR, Professeur, Université de Lille</b>	<b>Rapporteur</b>
<b>M. Victor BECERRA, Professeur, University of Portsmouth - UK</b>	<b>Examineur</b>
<b>M. Ahmed RACHID, Professeur, Université de Picardie Jules Verne</b>	<b>Directeur de thèse</b>



## Declaration of Authorship

I, Zain UL ABDIN, declare that this thesis titled, "Modeling and control of hybrid PV thermal panels" and the work presented in it are my own. I confirm that:

- This work was done wholly or mainly while in candidature for a research degree at this University.
- Where any part of this thesis has previously been submitted for a degree or any other qualification at this University or any other institution, this has been clearly stated.
- Where I have consulted the published work of others, this is always clearly attributed.
- Where I have quoted from the work of others, the source is always given. With the exception of such quotations, this thesis is entirely my own work.
- I have acknowledged all main sources of help.
- Where the thesis is based on work done by myself jointly with others, I have made clear exactly what was done by others and what I have contributed myself.

Signed:

---

Date:

---



*“You are a falcon, flight is your vocation,  
You have other skies stretching out before you.”*

**Allama Muhammad Iqbal - Poet of the East.**



## *Acknowledgements*

The present thesis was carried out in the Laboratoire des technologies innovantes (LTI), at the Université de Picardie Jules Verne, Amiens, under the direction of Professor Ahmed Rachid. This work was carried out as part of the SOLARISE project of the Interreg 2 Seas 2014-2020 programme co-financed by the European Regional Development Fund sub-grant contract No. 2S04-004 and I'm grateful for their confidence in funding this thesis.

Most of all, I would like to thank my thesis director Professor Ahmed RACHID for his unconditional support, major contribution to the direction of my research work, and for his academic support to achieve this work. His advice and necessary instructions have enriched this thesis and made it original. I gained to be autonomous under his supervision. May he find here the expression of my deep respect and sincere gratitude.

Professor Jean-Paul Gaubert from Université de Poitiers, honored me by accepting the presidency of the jury of this thesis. I want to thank and express my gratitude to him. I am thankful to the members of the jury, Professors Vladan Koncar, Hamid Gualous and Victor Becerra for accepting to be part of my PhD Thesis Committee. I would like to thank them for spending their valuable time in evaluating this work.

My warm and sincere thanks also goes to all my LTI colleagues for their encouragement and the working atmosphere they have created. All of them were important in this process more than they realize. My friends in France and Pakistan also played a vital role in my motivation process. I would also like to thank my friend and MISCIT class fellow Samuro LIU for the valuable discussions that we shared during the beginning of my PhD. For all the people whom maybe I unintentionally forgot, thank you.

A thought to my entire family, for being the source of my strength throughout my PhD process and my life in general. Special thanks to my beloved mother and father for their faith in me and for providing me with great love and support. My parents may not be able to read this paragraph but I owe my parents what I am today and this accomplishment would have not been possible without them. Every sacrifice you have done, has finally paid off.

Finally, I say: praise to God who gave me the courage and faith necessary to carry out this work.



# Contents

<b>Declaration of Authorship</b>	<b>iii</b>
<b>Acknowledgements</b>	<b>vii</b>
<b>0 General Introduction</b>	<b>1</b>
<b>1 Hybrid Solar PV-T Panels</b>	<b>5</b>
1.1 Classification of photovoltaic cells . . . . .	6
1.2 Types of medium used for heat extraction . . . . .	9
1.2.1 Water based PV-T systems . . . . .	9
1.2.2 Nano-fluid based PV-T systems . . . . .	10
1.2.3 PCM based PV-T systems . . . . .	11
1.2.4 Air based PV-T systems . . . . .	12
1.2.5 Bi-fluid based PV-T systems . . . . .	12
1.3 Mode of operation . . . . .	14
1.4 Type of solar collector . . . . .	14
1.4.1 Non-concentrated . . . . .	15
1.4.2 Concentrated . . . . .	15
1.5 Glazing . . . . .	16
1.6 Applications . . . . .	17
1.6.1 PV-Ts versus PV+ST . . . . .	18
1.6.2 Building . . . . .	18
1.6.3 Cooling (air conditioning) . . . . .	20
1.6.4 Greenhouse drying . . . . .	25
1.6.5 Desalination . . . . .	26
1.6.6 District heating/cooling . . . . .	28
1.6.7 Trigeneration . . . . .	29
1.6.8 Refrigeration . . . . .	30
1.6.9 Heat Pump integrated with a PV-T collector . . . . .	31
1.7 Software tools . . . . .	32
1.8 Hybrid PV-T products and market . . . . .	33
1.9 Future developments . . . . .	39
<b>2 Modeling of a PV-T collector</b>	<b>41</b>
2.1 Air-based PV-T model-I . . . . .	45
2.1.1 Bond graph modeling . . . . .	45
2.1.2 Identification . . . . .	47
2.2 Air-based PV-T model-II . . . . .	48
2.2.1 Bond graph modeling . . . . .	48
2.2.2 Linearization and state-space representation . . . . .	50
2.3 Water-based PV-T model . . . . .	51
2.3.1 Bond graph modeling . . . . .	52
2.3.2 State-space representation . . . . .	54

2.3.3	Multiple model construction	54
2.4	Drying using air-based PV-T collector	56
2.5	Modeling using artificial intelligence	58
2.5.1	Decision tree algorithm	59
2.5.2	Artificial neural network	60
2.6	Results and Discussion	61
2.6.1	Air-based model-I	61
2.6.2	Air-based model-II	64
2.6.3	Validation of Air-based model-II	65
2.6.4	Drying	66
2.6.5	Water-based model	68
2.6.6	Validation of Water-based PV-T model	71
2.6.7	Decision tree algorithm and neural network	72
2.7	Conclusion	74
<b>3</b>	<b>Design and Optimization</b>	<b>75</b>
3.1	System description	76
3.2	Electrical model	77
3.3	Thermal model	80
3.3.1	Addition of electrical resistance	83
3.3.2	Influence of internal geometrical parameters	85
3.4	Computational fluid dynamics study	86
3.5	Optimization	89
3.5.1	Genetic algorithm	89
3.6	Results and discussion	92
3.6.1	PV-T collector with embedded tank	92
3.6.2	Optimization	98
3.7	Conclusion	100
<b>4</b>	<b>Observation and Control</b>	<b>101</b>
4.1	Air-based model	102
4.1.1	PI-controller design	102
4.1.2	H-infinity using feedback control approach	103
4.1.3	H-infinity control using mixed sensitivity approach	105
4.2	Water-based model	107
4.2.1	Sliding mode control	107
4.2.2	Neural network control	108
4.2.3	Observer design with known input	111
4.2.4	Observer design with unknown input	113
4.3	Results and Discussion	117
4.3.1	Air-based Model	117
4.3.2	Water-based model	119
4.4	Conclusion	125
<b>5</b>	<b>Conclusion and Perspective</b>	<b>127</b>
<b>A</b>	<b>Additional Parameters</b>	<b>131</b>
A.1	Parameters used for multiple-model construction	131

<b>B Additional results</b>	<b>133</b>
B.1 Air-based PV-T model-I . . . . .	133
B.2 Air-based PV-T model-II . . . . .	133
B.3 PV-T collector with embedded tank . . . . .	134
B.3.1 Physical results . . . . .	134
B.3.2 CFD results . . . . .	135
B.3.3 Influence of internal geometrical parameters . . . . .	135
<b>Bibliography</b>	<b>137</b>
<b>Résumé long en Français</b>	<b>146</b>
<b>Abstract</b>	<b>156</b>



# List of Figures

1.1	Basic working principle of the PV-T collector. . . . .	5
1.2	Overall view of the solar PV-T collector. . . . .	6
1.3	Spectral range of crystalline silicon solar PV cells. . . . .	7
1.4	Classification of photovoltaic-thermal collector. . . . .	8
1.5	Sectional view of water based PV-T collector. . . . .	9
1.6	Different flow passages in a liquid-based PV-T collector. . . . .	10
1.7	A schematic diagram of a PV-T collector with nano-fluid as heat transfer fluid and spectral filter with double-pass channel. . . . .	11
1.8	Sectional view of PCM based PV-T collector. . . . .	12
1.9	Different configuration of air-based PV-T collectors. . . . .	13
1.10	Sectional view of bi-fluid based PV-T collector. . . . .	13
1.11	Schematic of forced circulation PV-T system. . . . .	14
1.12	Non-concentrated solar collector. . . . .	15
1.13	Non-concentrated solar collector. . . . .	15
1.14	Single-cell concentrator. . . . .	16
1.15	PV-T roof-top array supplying heating and electricity to a building. . . . .	17
1.16	Two main types of BIPV-T collectors: (a) roof-integrated BIPV-T collector (opaque). (b) semi-transparent BIPV-T collector. . . . .	19
1.17	Schematic diagram of solar adsorption cooling. . . . .	21
1.18	Schematic diagram of desiccant cooling. . . . .	22
1.19	(a) Schematic diagram: (a) adsorption chiller. (b) absorption chiller. . . . .	23
1.20	Schematic diagram of solar hot-air drying system. . . . .	26
1.21	Schematic diagram of hybrid solar desalination. . . . .	27
1.22	Schematic diagram of PV-T district heating. . . . .	28
1.23	Structure of Community Energy Internet (CEI) with PV-T and heat pump (PVT-HP) prosumers. . . . .	29
1.24	Schematic diagram of PV-T tri-generation system setup. . . . .	30
1.25	Schematic diagram of the proposed PV-T heat pump system on refrigeration mode. . . . .	31
1.26	Solar driven direct-expansion heat pump system employing the novel PV/minichannels-evaporator modules. . . . .	32
1.27	Global solar thermal installed capacity and energy yield. . . . .	33
2.1	Cross-sectional view of an air-based PV-T collector with fluid flowing below PV module. . . . .	45
2.2	Bond graph model-I of air-based PV-T collector. . . . .	46
2.3	Cross-sectional view of an air-based PV-T collector with fluid flowing above PV module. . . . .	48
2.4	Bond graph model-II of air-based PV-T collector. . . . .	49
2.5	(a) Metallic tube and bond. (b) PV-T collector flow dynamics. . . . .	51
2.6	Bond graph model of water-based PV-T collector. . . . .	52
2.7	Bloc-diagram of the solar dryer. . . . .	56

2.8	The solar dryer with air recirculation. . . . .	57
2.9	Applications and subsets of artificial intelligence. . . . .	59
2.10	Schematic representation. . . . .	59
2.11	Basic model of the neural network. . . . .	60
2.12	Hourly variation of solar radiation and ambient temperature. . . . .	61
2.13	Temperature evolution of PV-T components for air-based model-I without an absorber component. . . . .	62
2.14	Daily hourly variation of electrical and thermal efficiencies for air-based model-I without glazing. . . . .	62
2.15	Variation of outlet air temperature with the increase in mass flow rate at $T_{am} = T_{f,i} = 30\text{ }^{\circ}\text{C}$ and $I_{sun} = 500\text{ Wm}^{-2}$ . . . . .	63
2.16	Daily hourly variation of electrical and thermal efficiencies for air-based model-I with glazing. . . . .	63
2.17	Temperature evolution of PV-T components for air-based model-I with an absorber component. . . . .	63
2.18	Temperature evolution of a PV-T components for air-based model-II. . . . .	64
2.19	Daily hourly variation of electrical and thermal efficiencies for air-based model-II. . . . .	64
2.20	Temperature evolution of a PV-T components for air-based model-II (CFD study). . . . .	65
2.21	Temperature distributions of the air-based PV-T collector components; (a) Glass cover. (b) PV cell layer. (c) Fluid (air channel). (d) Insulator. . . . .	65
2.22	Temperature evolution of cell layer, tedlar layer, fluid and insulator at $T_{am} = 30^{\circ}\text{C}$ and $I_{sun} = 400\text{ Wm}^{-2}$ (for mass flow = 0.0025, 0.0075 and $0.02\text{ kgs}^{-1}$ ). . . . .	66
2.23	Temperature evolution of cell layer, tedlar layer, fluid and insulator at $T_{am} = 34^{\circ}\text{C}$ and $I_{sun} = 700\text{ Wm}^{-2}$ (for mass flow = 0.0025, 0.0075 and $0.02\text{ kgs}^{-1}$ ). . . . .	66
2.24	Mass flow required to achieve a desire output temperature ( $47.50$ , $52.50$ and $57.50^{\circ}\text{C}$ ). . . . .	67
2.25	With and without recycling profile for air outlet temperature and solar radiation. . . . .	67
2.26	Daily temperature evolution of water-based PV-T components. . . . .	68
2.27	Hourly variation of PV efficiency and thermal efficiency. . . . .	69
2.28	Fluid temperature with a step change in solar radiation. . . . .	69
2.29	Influence of insulator thickness on the output temperature. . . . .	70
2.30	Influence of wind speed on thermal efficiency. . . . .	70
2.31	Influence of mass flow rate on the output temperature. . . . .	70
2.32	(a) Hourly evolution of solar radiation and ambient temperature experimentally. (b) Hourly evolution of temperatures ( $T_c$ and $T_{wo}$ ) both experimentally (experimental studies) and theoretically (this study). . . . .	72
2.33	Comparison of actual and predicted outputs using decision tree algorithm. . . . .	73
2.34	Mean squared error using neural network. . . . .	73
2.35	Comparison of actual and predicted outputs using neural network. . . . .	74
3.1	(a) Storage tank placed separately from the collector. (b) Storage tank placed on-top of the collector. . . . .	75
3.2	Cross-sectional view of hybrid photovoltaic-thermal system integrating a storage tank. . . . .	76

3.3	Current–voltage (I-V) and power-voltage (P-V) characteristics curve-STC conditions. . . . .	79
3.4	Schematic diagram of a closed-loop system. . . . .	82
3.5	Cross-sectional view of hybrid photovoltaic-thermal system equipped with heating element. . . . .	84
3.6	(a) Copper and aluminium as materials. (b) Thickness of the materials. (c) Used engine oil as an absorber material. (d) Glycol, Water and Paraffin wax as serpentine fluids. . . . .	85
3.7	A schematic diagram of the boundary conditions. . . . .	86
3.8	(a) Mesh independency. (b) Mesh quality distribution of the hybrid PV-T system. . . . .	88
3.9	Genetic algorithm flowchart. . . . .	90
3.10	Average temperature evolution of each component of the collector for case-I with an air-gap between the glass cover and PV cell layer. . . . .	93
3.11	Average temperature evolution of each component of the collector for case-I without an air-gap between the glass cover and PV cell layer. . . . .	94
3.12	Average temperature evolution of each component of the collector for case-II without an air-gap between the glass cover and PV cell layer. . . . .	94
3.13	Variation of PV efficiency and solar radiation. . . . .	95
3.14	Temperature distributions for the three different cases (a) PV cell layer. (b) Serpentine tube fluid. (c) Storage tank fluid. . . . .	96
3.15	Temperature distributions of the storage tank fluid incorporating an electric heater. . . . .	98
3.16	(a) Best thickness variables. (b) Best mass flow. . . . .	99
3.17	PV cell, outlet water temperature and PV efficiency evolution with high mass flow and low mass flow. . . . .	99
3.18	PV cell, outlet water temperature and PV efficiency with optimized thickness and mass flow. . . . .	100
4.1	Simple feedback control loop. . . . .	103
4.2	Control scheme for hybrid PV-T thermal model. . . . .	104
4.3	Generalized feedback system. . . . .	105
4.4	Complete control scheme. . . . .	106
4.5	Sensitivity functions of the robust control system: (a) Sensitivity function. (b) Controller*Sensitivity. . . . .	107
4.6	Scheme for a simple controller implementation. . . . .	109
4.7	Structure of model predictive control process. . . . .	109
4.8	Structure of NARMA-L2 controller. . . . .	110
4.9	Response of PI-controller with constant solar radiation. . . . .	117
4.10	Tracking of desired temperature and disturbance rejection. . . . .	118
4.11	External inputs imposed on the system. . . . .	118
4.12	Tracking of reference setpoints by the state variables. . . . .	119
4.13	Evolution of the control input exerted on the system. . . . .	119
4.14	Evolution of the outlet temperature. . . . .	119
4.15	Convergence of output $T_{wo}$ to the desired point $y_{ref}$ . . . . .	120
4.16	Control input with a change in solar radiation. . . . .	120
4.17	Control input with a change in ambient temperature. . . . .	120
4.18	External inputs imposed on the system. . . . .	121
4.19	Evolution of the PV efficiency and control input. . . . .	121
4.20	Evolution of the outlet temperature and disturbance rejection. . . . .	122
4.21	Evolution of state temperatures. . . . .	122

4.22	Response using basic controller, predictive controller and NARMA-L2 controller. . . . .	122
4.23	Real states of the system. . . . .	123
4.24	Estimation of states. . . . .	123
4.25	Estimation error. . . . .	124
4.26	State estimation errors: $e_1$ through $e_7$ . . . . .	124
4.27	True states and their estimations without unknown input. . . . .	124
4.28	True states and their estimations with sinusoidal input $T_{wi}$ . . . . .	125
B.1	Temperature evolution of a PV-T components for air-based model-I with glazing. . . . .	133
B.2	Mesh structure of air-based model-II. . . . .	133
B.3	Temperature distribution of PV-T collector (air-based model-II). . . . .	134
B.4	Temperature distributions of Case-I; (a) Glass cover. (b) Tedlar layer. (c) Absorber plate. . . . .	135

# List of Tables

1.1	PV-T products available in the market and their specifications. . . . .	34
2.1	Thermal parameters of the air-based and water-based collectors. . . . .	44
2.2	Summary of results for the current work and other studies in literature.	71
2.3	Lower and upper bounds of input variables. . . . .	72
3.1	Electrical parameters of the PV module at standard test conditions. . .	78
3.2	Thermal parameters of the collector. . . . .	81
3.3	Lower and upper bounds of the design parameters. . . . .	89
3.4	Genetic algorithm optimization parameters. . . . .	91
3.5	Ambient conditions considered for three different cases . . . . .	93
3.6	Temperature of the PV-T collector components for physical and CFD analysis. . . . .	96
3.7	Influence of heat extraction fluid running within the serpentine tube. .	97
3.8	Summary of temperatures and efficiency considering upper and lower bounds. . . . .	99
B.1	Temperature of the PV-T components for physical analysis (with $0.01\text{kg s}^{-1}$ mass flow). . . . .	134
B.2	Error for all the PV-T components. . . . .	134
B.3	Pure glycol, water mixed with glycol and paraffin wax (PCM) as a serpentine fluid. . . . .	135
B.4	Used engine oil as an absorber material. . . . .	135



# List of Abbreviations

<b>AI</b>	<b>Artificial Intelligence</b>
<b>ANN</b>	<b>Artificial Neural Network</b>
<b>BIPV-T</b>	<b>Building Integrated Photovoltaic-thermal</b>
<b>CFC</b>	<b>Chlorofluorocarbons</b>
<b>COP</b>	<b>Coefficient of Performance</b>
<b>CPV-T</b>	<b>Concentrating Photovoltaic-thermal</b>
<b>GA</b>	<b>Genetic Algorithm</b>
<b>HVAC</b>	<b>Heating, Ventillation, and Air-conditioning</b>
<b>IEA</b>	<b>International Energy Agency</b>
<b>LMI</b>	<b>Linear Matrix Inequality</b>
<b>MPPT</b>	<b>Maximum Power Point Tracking</b>
<b>MSE</b>	<b>Mean Squared Error</b>
<b>PID</b>	<b>Proportional-Integral-Derivative</b>
<b>PV</b>	<b>Photovoltaic</b>
<b>PV-T</b>	<b>Photovoltaic-thermal</b>
<b>PCM</b>	<b>Phase Change Material</b>
<b>RANS</b>	<b>Reynolds averaged Navier Stokes</b>
<b>RMSE</b>	<b>Root Mean Square Error</b>
<b>SMC</b>	<b>Sliding Mode Control</b>
<b>SHC</b>	<b>Solar Heating and Cooling</b>
<b>ST</b>	<b>Solar-thermal</b>



# List of Symbols

## <sup>1</sup> Variables

$A_{mod}$	module area of a PV panel
$A_{hz}$	air channel area
$a$	modified ideality factor
$C$	heat capacity
$d_{hy}$	hydraulic diameter
$d_i$	inner diameter of the tube
$d_o$	outer diameter of the tube
$E_p$	electric power
$G$	radiation energy absorbed
$G_r$	Grashof number
$h_r$	radiative heat transfer coefficient between two components
$h_c$	conductive heat transfer coefficient between two components
$h_v$	convective heat transfer coefficient between two components
$I$	current
$I_{sun}$	solar radiation
$K_B$	Boltzmann constant
$l$	thickness
$M$	mass
$\dot{m}$	mass flow rate
$N_u$	Nusselt number
$P$	power
$P_r$	Prandtl number
$q$	Elementary charge
$\dot{Q}$	thermal heat flow
$R_a$	Raleigh number
$R_e$	Reynold number
$T$	temperature
$V$	voltage
$V_t$	thermal voltage
$V_w$	wind speed
$W$	width of air channel
$x$	length of the panel
$y$	width of the panel

## Greek symbols

$\alpha$	absorptivity
$\beta$	packing factor
$\beta_p$	temperature coefficient

---

<sup>1</sup>Unless it is specified, all variables are in SI Metric Units.

$\delta$	solar radiation coefficient
$\eta_{ele}$	photovoltaic efficiency
$\eta_{ra}$	air recycling efficiency
$\eta_{th}$	thermal efficiency
$\eta_{ov}$	total efficiency
$\epsilon$	emissivity
$\epsilon_H$	heat exchange effectiveness
$\gamma$	diode ideality factor
$\kappa$	thermal diffusivity
$\lambda$	thermal conductivity
$\mu$	dynamic viscosity
$\rho$	density
$\sigma$	Stefan Boltzmann constant
$\tau$	transmissivity
$\theta$	angle
$\nu$	kinematic viscosity
$\zeta$	ratio of channel area to PV module area

### Subscripts

<i>am</i>	ambient
<i>c</i>	PV cell
<i>f</i>	fluid (air)
<i>g</i>	glass cover
<i>he</i>	heating element or resistance heater
<i>i</i>	thermal insulator
<i>m</i>	metallic tube
<i>mp</i>	maximum power
<i>r</i>	absorber
<i>ref</i>	reference
<i>s</i>	sky
<i>t</i>	tedlar
<i>ta</i>	tank
<i>tg</i>	additional top glass cover
<i>w</i>	water

*To my Parents, symbol of sacrifice and dedication,  
To all my family...*



## Chapter 0

# General Introduction

This research project concerns the modeling, design, optimization and control of a hybrid photovoltaic-thermal (PV-T) system. Energy plays a vital role in the economic stability and quality of life of a nation. High consumption of conventional energy sources has caused a rise in global temperature. The average global temperature has been on increase at the rate of  $1.7^{\circ}\text{C}$  per century since 1970 (Marcott et al., 2013). Threatened by this menace, and warned by many scientists and researchers, almost all countries are going for renewable energy technology. With the significant rise in the standard of living as compared to the standard of living a century ago, global energy demand has increased. A lot of research is going on in the renewable energy field which includes solar, wind and thermal energy and its utilization is rapidly increasing day by day. These sustainable energy sources i.e. solar energy can be found abundantly throughout the year. Solar energy as the main component is becoming more popular and widely adopted, due to many factors; rise in fuel prices, low carbon technology, drop in prices of solar photovoltaic, delivering savings on energy bills, environment-friendly, climate change, and worldwide availability of solar energy. Therefore, the development of solar power plants is faster than other renewable power plants around the world (Luo et al., 2020). It is estimated to have 16% of solar photovoltaic energy generation globally till 2050 (Sathe and Dhoble, 2017).

Today, the installed capacity of solar PV is approximately 350 GW, the installation rate will increase and by 2040 the installed capacity will reach the 700 GW mark (Diwania et al., 2020). Approximately, 60-70% of solar radiation absorbed by the photovoltaic (PV) module is converted into heat. The priority of the PV-T systems is to generate electricity whereas the produced heat gets wasted to the environment by radiative and convective heat losses if not utilized for heating purposes i.e. space heating, domestic hot water, etc. PV-T systems are a good solution, they not only offer low carbon electricity but also extract the waste heat energy simultaneously via a heat extraction medium by combining photovoltaic and solar-thermal (ST) modules into one integrated unit. This heat extraction medium also enhances the PV efficiency by reducing the PV cell temperature. PV-T collector has several applications such as building integrated photovoltaic thermal (BiPV-T) system, tri-generation, desalination, air conditioning, district heating/cooling, drying, heat storage, solar greenhouse, refrigeration, and industrial applications.

A general background concerning PV-T systems is provided where it points out the motivation behind this revealing explicitly the need of developing such systems. The context, desired objectives, encountered challenges, developed approach and the performed applications are presented sequentially in this manuscript.

The main contributions of the work are summarized as follows;

**Chapter 1** presents the background of hybrid PV-T systems, their classification and major applications to highlight their feasibility and usefulness and to raise awareness for adoption in the industry and buildings sector. It also points out the simulation tools, future developments, market, available products. This should be considered as a reference form of PV-Ts to extract key points for future research and development.

**Chapter 2** illustrates the detailed modeling of PV-T systems and the modeling requires a thorough study of heat transfer between the collector's components. The aim is to develop nonlinear dynamic models for air and water-based collectors which give a realistic and reasonable performance of the system. A steady state model is not suitable for predicting temperature. The fundamental equations for the thermal part are determined using a bond graph approach which is a generic and general tool to represent thermal transfers. It also addresses PV-T system application, a solar dryer based on hybrid solar panels and waste heat recovery together with air recycling. Simulations are a good way to analyze the thermal performances of the collectors. Lastly, the collector was modeled using an artificial neural network (ANN) and a decision tree algorithm. The results and discussions of this study are explained and finally, the chapter ends with conclusive remarks.

**Chapter 3** presents a new design of a PV-T system that incorporates a storage tank at the back of the thermal module to store heat as well as an electrical resistance to increase thermal production when necessary. The modeling proves to be useful in analyzing the influence of internal geometrical parameters such as the thickness of a component, material used and type of fluid. An electric resistance heater is added to compensate the temperature reduction. Computational fluid dynamics (CFD) was employed to simulate and validate the temperature of various components of the collector. The consistency of the physical and CFD model was validated and the results are explained. To the best of our knowledge, this type of design is not addressed yet in the literature. In addition, an attempt was made to optimize thickness parameters and the control parameter of the collector in order to reduce the cost and maximize the thermal output. A genetic algorithm (GA) is best suited for such a case.

**Chapter 4** deals with a controller design and observer construction. Designing a controller for a nonlinear model is a challenging problem and here, the temperature range of the collector fluid should be controlled and used for various applications. The output temperature of the collector is controlled using a simple PI controller, an H-infinity controller, a sliding mode controller and using ANN. In automatic control, designing an observer is very important, especially for control, monitoring and fault detection purposes. An observer is designed for estimating the states of the multiple model developed using a water-based model. Moreover, instead of knowing the input, an observer is constructed subjected to an unknown input.

**Chapter 5** summarizes the main findings, achieved contributions and limitations of the presented work. Also, some future work and interesting expanding ideas are exposed.

This work led to the publication of three peer-reviewed international journal papers and articles in the proceedings of international peer-reviewed conferences.

### *Journal papers*

1. **Ul Abdin, Z**, Rachid, A, & Korkut, T.B. (2022). Design and analysis of an innovative photovoltaic-thermal collector with embedded tank. *Solar Energy*, 245, 290-298.
2. **Ul Abdin, Z**, & Rachid, A. (2021). Bond graph modeling of a water-based photovoltaic thermal (PV/T) collector. *Solar Energy*, 220, 571-577.
3. **Ul Abdin, Z**, & Rachid, A. (2021). A survey on applications of hybrid PV/T panels. *Energies*, 14(4), 1205.

### *Conference papers*

1. **Ul Abdin, Z** & Rachid, A. (2022, October). State observer for water-based hybrid PV/T system with unknown input. In *IECON 2022-48th Annual Conference of the Industrial Electronics Society*. IEEE. (**Accepted for presentation**)
2. Rachid, A. & **Ul Abdin, Z**. (2022, August). Multiple model and observer design for a water-based PV/T collector. In *2022 IEEE Conference on Control Technology and Applications (CCTA)*. IEEE.
3. **Ul Abdin, Z**, & Rachid, A. (2020, August). Modeling, Identification and Control of Photovoltaic/Thermal Solar Panel. In *2020 IEEE Conference on Control Technology and Applications (CCTA)* (pp. 1-6). IEEE.
4. Rachid, A. & **Ul Abdin, Z**. (2022, June). Solar hybrid PV/T panels for drying. In *2022 International Drying Symposium (IDS)*.



## Chapter 1

# Hybrid Solar PV-T Panels

A good deal of attention is being given by researchers and academicians all over the world to photovoltaic-thermal (PV-T) technology due to its benefits as compared to the solar thermal (ST) or photovoltaic (PV) systems alone. These systems provide heat and low carbon electricity at the same time from the same renewable energy source, combining photovoltaic and solar thermal modules into one integrated module by minimizing space and cost. Photovoltaic converts ultraviolet and visible rays to solar spectrum whereas solar thermal uses and utilizes infrared rays of the spectrum. The basic working principle is shown in Figure 1.1, where electrical energy is produced by solar cells and the waste heat is extracted using the thermal collector. A cold fluid is injected from one end and warm fluid is collected from another end along with the electrical gain as illustrated in Figure 1.2. Even with a lot of atten-

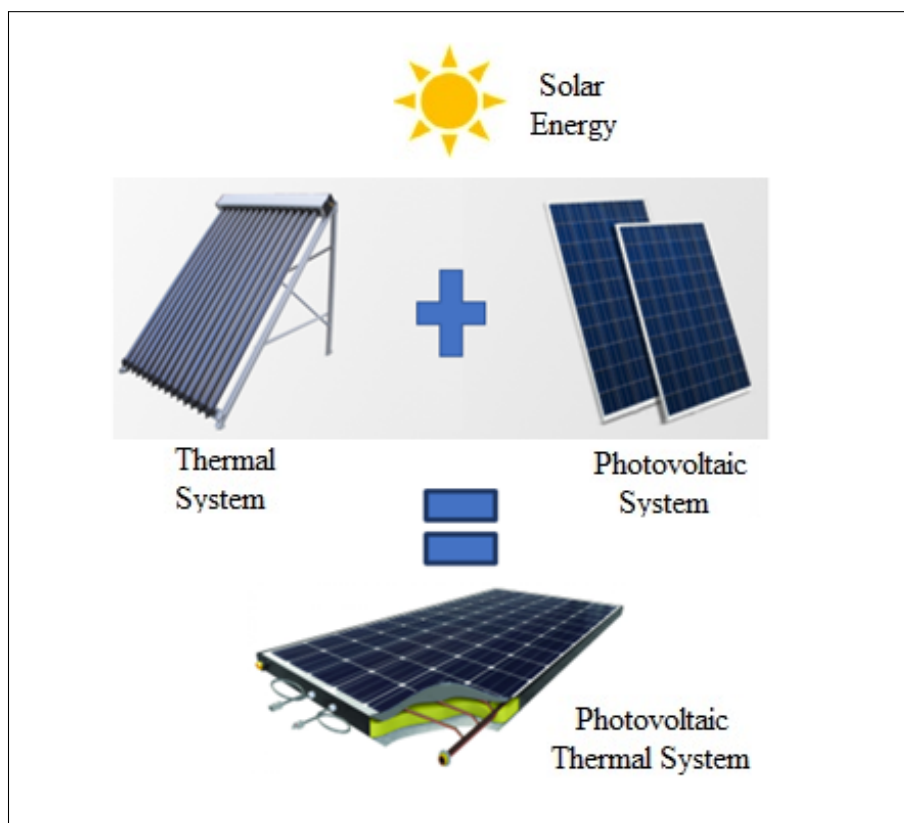


FIGURE 1.1: Basic working principle of the PV-T collector.

tion given to this technology and research activities, the number of PV-T systems commercially available is very limited. These systems are the solution to improve the efficiency of a photovoltaic collector and can be utilized for various purposes

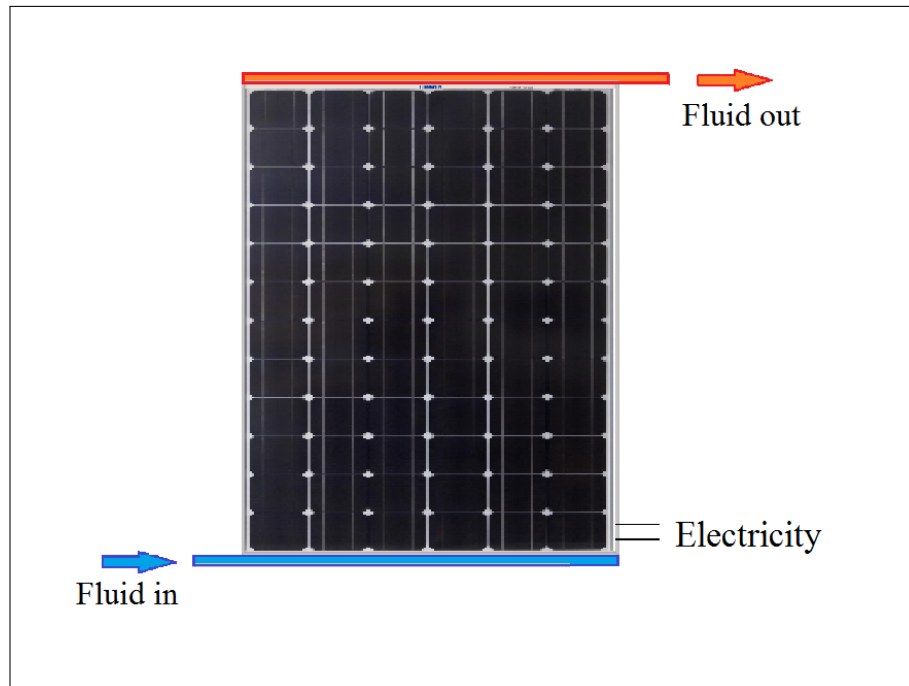


FIGURE 1.2: Overall view of the solar PV-T collector.

like heating and cooling. The factors that are pausing using up this technology are; complex system designs for extra storage capacity, insufficient knowledge of the technology, and longer reimbursement as compared to PV technology. Common components to capture and convert solar energy are on the one hand solar photovoltaic panels to produce electricity with an efficiency of about 10-22%. Generally, this PV part includes a glass cover, PV cells layer, and a tedlar. On the other hand, solar thermal panels produce heat with efficiency up to 50% (Ramos et al., 2017) and consist of an absorber, tubes/duct, insulator, and a working fluid that flows mostly under the PV module either in an air duct or within the tubes.

## 1.1 Classification of photovoltaic cells

A photovoltaic cell is an electrical device, when exposed to light, converts light energy to electricity through a process called the photovoltaic effect. These PV cells are basically semiconductor diodes, either connected in parallel or in series to make a PV module and process energy is transferred from photons to electrons. These solar cells are divided into two main categories, silicon, and non-silicon based solar cells. Silicon-based solar cells are widely adapted for photovoltaic applications because of their high performance, market domination, and lower cost. Based on n-type multi-crystalline silicon, a solar cell can have a record efficiency of 22% (Schindler et al., 2017b). These semiconductors are manufactured using various techniques and are divided into various types depending on the efficiency.

- Mono-crystalline PV cells have the highest efficiency between 15 to 22%. These types of PV cells are high-priced and are deposited at high temperatures.
- Polycrystalline silicon PV cells are economical, reasonable, and have low efficiency. The efficiency range is between 11 to 15%. The good thing about these cells is that they can be manufactured using leftover electronics.

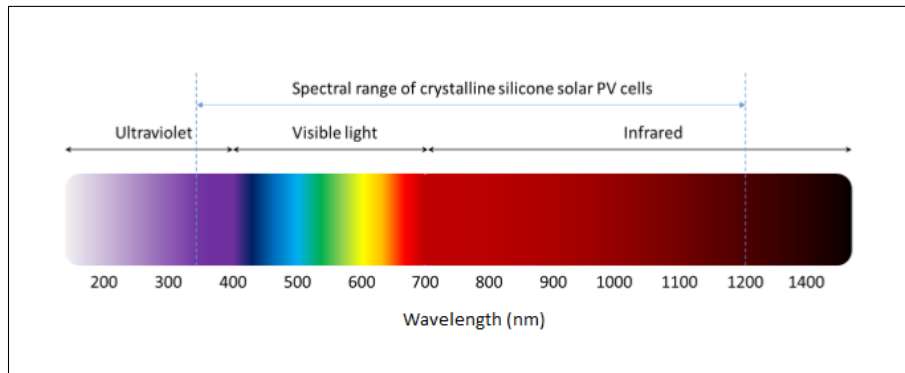


FIGURE 1.3: Spectral range of crystalline silicon solar PV cells (Energy and Strategy, 2016).

- Amorphous silicon PV cells or so-called second-generation cells are low-cost, have a shorter life, and less efficient among all the cells, and have an efficiency range between 6 to 8%. Today, this technology is adopted commercially for PV applications because cell efficiency highly depends on cell temperature. Using such types of cells, efficiency remains almost the same even with the change in cell temperature.

Work on new technologies and enhancement in their efficiency is also going on, especially organic solar cells or plastic solar cells which are relatively inexpensive, lightweight, third-generation solar cells with an efficiency of around 9%. Such kind of cells uses carbon-based materials and organic electronics to harvest energy from the sun.

When the solar radiation reaches the solar cells almost 90% of it is absorbed by the solar cells whereas the rest is reflected and under ideal conditions, 13% - 15% of radiation is converted to useful electricity (Santbergen and Zolingen, 2008). These solar radiations consist of 48% visible, 43% infrared, and 9% ultraviolet rays. They are in a wavelength of 0.25 - 2.5 micrometer. The PV cells operate between a wavelength of 0.35 – 1.2 micrometers as shown in Figure 1.3 and solar radiations outside this range are collected in the form of heat. To produce electricity, not everything is put in use but only the radiations related to the response range of a solar cell are used and the remains dissipate their energy as heat. This dissipation causes thermal losses due to which the performance of a system is reduced.

There are various approaches used to extract the heat from solar collectors by passing air or liquid across the back of the panel which is discussed in detail in the later sections. The extracted heat is transferred either directly for space heating or consequentially to a storage tank. There must be a temperature difference between the panel and the storage tank, for a PV-T system to operate. The priority of the PV-T systems is to generate electricity (Ramos et al., 2017) and the photovoltaic efficiency highly depends on the cell temperature. Mostly, optimization techniques are used for electrical generation in PV-T systems. One of the major benefits of such systems over PV only systems is that they come up with cooling which ultimately reduces cell temperature. Thereby enabling it to produce better photovoltaic efficiency and high overall efficiency of the system (Ji, Chow, and He, 2003). An increase of every 2°C temperature can degrade the PV efficiency by 1% (Thong et al., 2016). Another advantage of the PV-T system is that the temperature control increases the life of the panel. In order to increase the performance and efficiency of PV panels, the following actions have been considered;

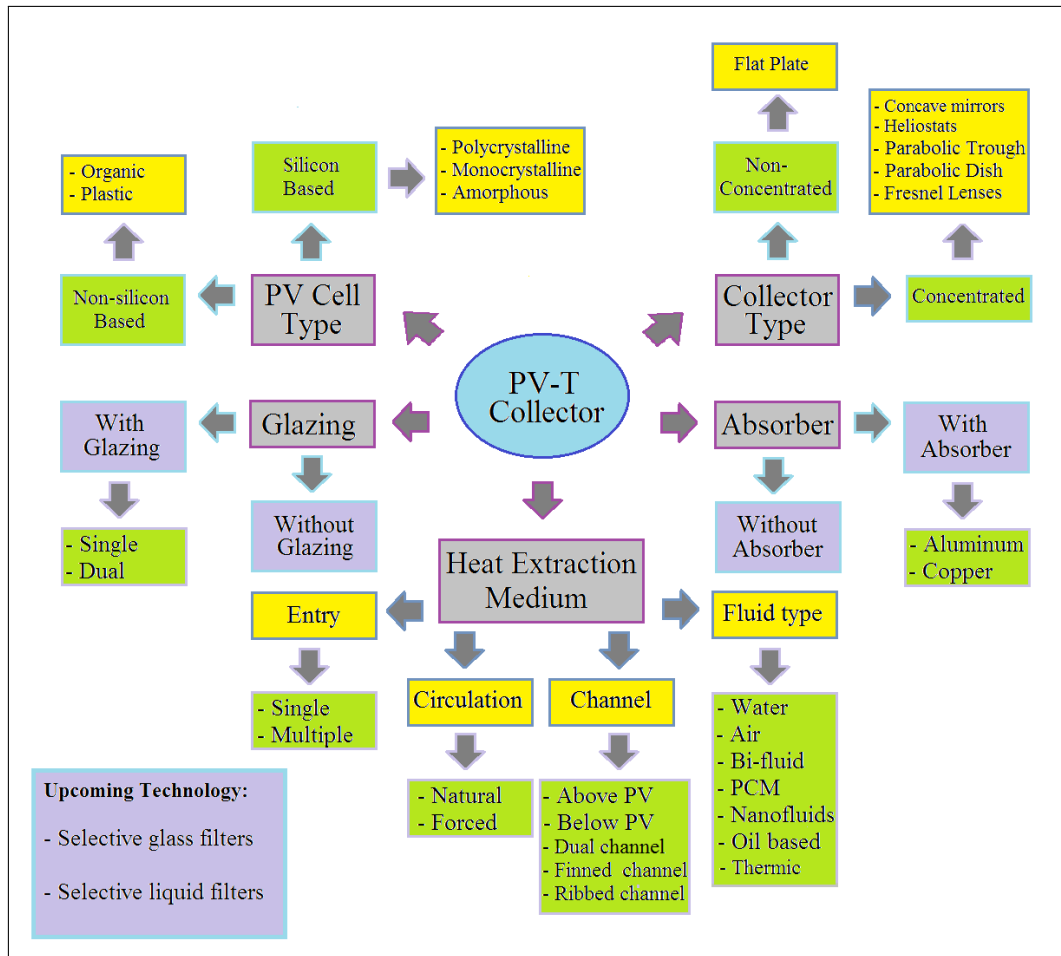


FIGURE 1.4: Classification of photovoltaic-thermal collector.

- keep the operating temperature at the desired value otherwise, the cell's output reduces as well as their efficiency (Garg and Adhikari, 1998).
- recover the waste heat for use in appropriate applications, otherwise, heat gets wasted.

The other parameters can include; the type of PV lamination and the type of insulation which includes covered and uncovered. Lastly, how a PV module is attached to the absorber.

The design and material of the PV-T hybrid collector play a crucial role in acquiring high energy conversion efficiency which is discussed with the results in Chapter 3. The design of a system depends on the load requirements and incorporation of the system. Today, you can find different types of PV-T collectors;

- PV-T collectors with vacuum tubes
- PV-T liquid collectors
- PV-T air collectors

The most common is the unglazed PV-T panel with thermal insulation and water as a heat transfer medium. PV-T panel interpretation and detail vary from manufacturer to manufacturer which makes it challenging for designers and customers to assess and compare products. Figure 1.4 presents a complete classification of hybrid PV-T systems that includes heat extraction mediums, collector type, cell type, etc.

## 1.2 Types of medium used for heat extraction

Sunlight absorbed by the panel is directly converted to heat and is transferred to the fluid. A heat transfer medium plays a significant role by extracting the unused heat from the PV module through circulation within the installation or else the temperature can reach up to 80°C. There are two common types of mediums used to extract heat from PV-T systems, air and water. PV-T with air has few advantages over liquid-based collectors; there is no freezing, no boiling, and leakage will not harm the panel. A liquid-based PV-T collector can produce up to 40% more energy than individual PV and ST collectors installed over the same area. The one major drawback with air type collectors is low heat transfer which is because of low heat capacity and low thermal conductivity. The heat transfer mediums help in improving photovoltaic efficiency by lowering the cell temperature. Liquid-based PV-T collectors are subdivided into various categories which include water-based, refrigerant-based, and PCM-based PV-T collectors. Apart from this, there is a bi-fluid PV-T collector which uses air and liquid at the same time to raise thermal performance.

### 1.2.1 Water based PV-T systems

A water-based PV-T collector is a domestically used panel to produce heat using water as a medium exhibiting thermodynamic properties. These are further subdivided into many categories (Jia, Alva, and Fang, 2019). In the first category, the PV-T collector consists of a tube that is fitted at the back of the collector, it may be four-sided/square or circular in shape. The layered diagram of the water-based tube PV-T collector is shown in Figure 1.5. The latter has a channel that is installed either

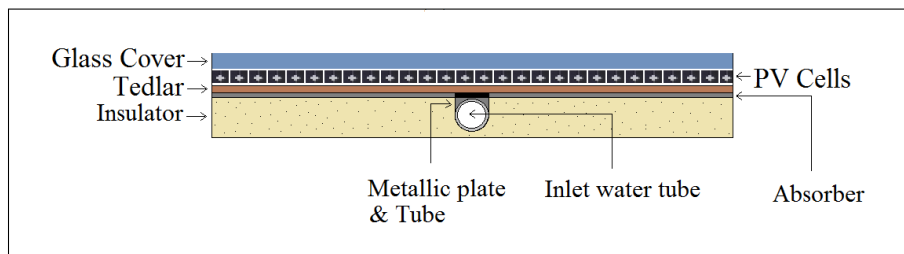


FIGURE 1.5: Sectional view of water based PV-T collector.

under or on top of the PV module. The third type of water-based PV-T collector makes use of dual absorbers. PV lamination serves as a primary absorber and a black-colored layer on metal performs the function of a secondary absorber. Mostly, black chrome over a nickel base or a titanium-nitride oxide layer is used on metals and it is more productive (Alghoul et al., 2005). These collectors have greater thermal efficiency when compared with others. In a tube PV-T collector, there can be multiple water tubes parallel to each other in which water is inserted from a single point and is distributed equally to all the tubes and heated water is collected from the other end of the panel or it can be a single tube in a moving snake-like shape (serpentine flow). The design of tube paths can also be in the shape of (Brahim and Jemni, 2017);

- web flow
- oscillatory flow
- spiral flow

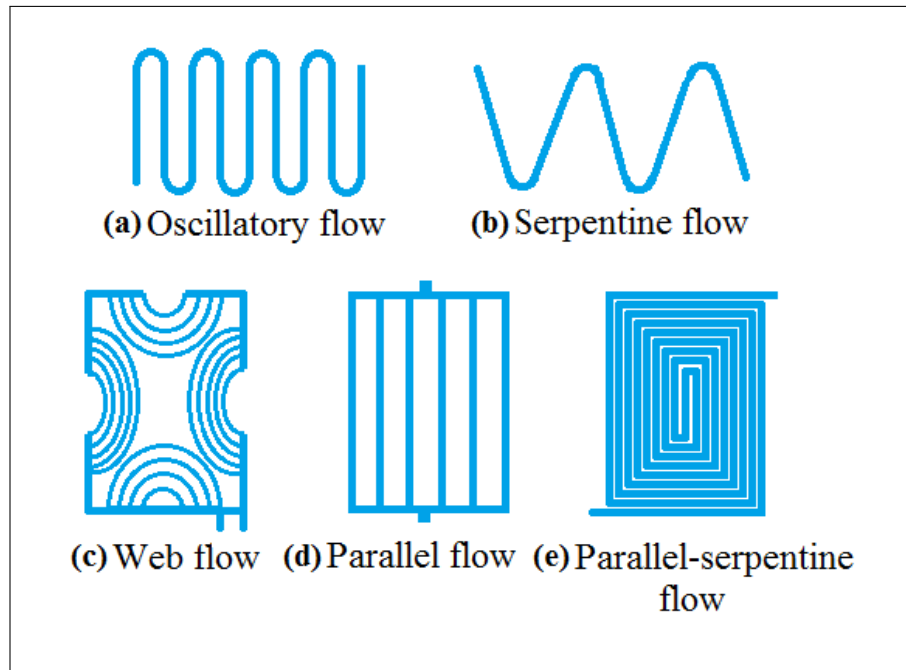


FIGURE 1.6: Different flow passages in a liquid-based PV-T collector.

Classification of water-based PV-T collector based on paths for the flow pattern is shown in Figure 1.6. Another type of water-based PV-T collector is a Roll bond in which absorbing plates are metallic-based e.g. aluminium, steel, copper, etc. These water-based panels are not appropriate for the regions where there is a risk of freezing.

The advantages of using water as a heat transfer fluid are; nontoxic, low-cost, and readily available. The major drawback of using water as a heat transfer fluid is freezing, additionally, these collectors are costly and complicated. In order to overcome the freezing issue, glycol is mixed with water which protects metal from rusting and aging. Space heating, water heating, and water distillation are the common applications of water-based PV-T systems.

### 1.2.2 Nano-fluid based PV-T systems

These systems use nano-fluids, circulating as working material with a slight change in the design as represented in Figure 1.7, respectively. The nano-fluid can act as a coolant, as a spectral filter, coolant and spectral filter with a double-pass channel and coolant and spectral filter with separate channels. The fluids are composed of solid metallic nano-sized particles which are dispersed in base fluids uniformly. Nano-sized must disperse and represent high stability and chemical compatibility with the base fluid so that nano-fluid materials may be prepared. A single-step and two-step method are two different processes to prepare a nano-fluid (Sachit et al., 2018). In order to prepare nano-fluids, a two-step method is comparatively easy, straightforward, and commonly used but with low stability and small dispersion (Murshed and De Castro, 2014).

The main reason why these collectors demonstrate better performance is because the thermal conductivity of solid metallic materials is higher than that of base fluids. There are also some disadvantages of using these collectors that include instability

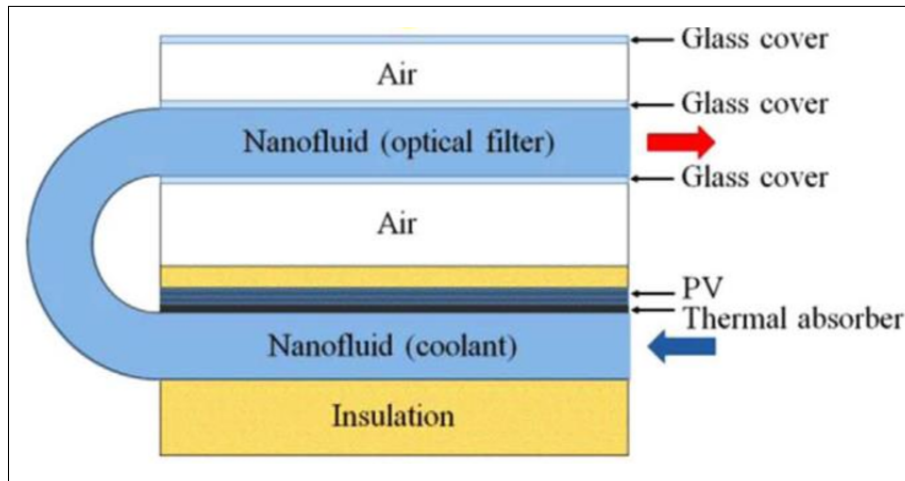


FIGURE 1.7: A schematic diagram of a PV-T collector with nano-fluid as heat transfer fluid and spectral filter with double-pass channel (De-Jarnette et al., 2014).

of fluid, the cost of the nano-particles, and enhancement in the fluid viscosity, increased pumping power requirements (Sachit et al., 2018). Experimental investigations have been carried out in (He et al., 2007; Yousefi et al., 2012; Esmailzadeh et al., 2013; Heyhat et al., 2013) on thermal conductivity and heat transfer of  $\text{Al}_2\text{O}_3$  nano-particles when water is used as a base fluid. Gangadevi, Vinayagam, and Senthilraja (2017) and Moradgholi, Nowee, and Farzaneh (2018) investigated the thermal and electrical performance of the PV-T collector experimentally using  $\text{Al}_2\text{O}_3$  with water. Gangadevi, Vinayagam, and Senthilraja (2017) concluded that electrical efficiency is increased from 10% to 13% whereas thermal efficiency is increased from 30% to 40% using 2 wt% of  $\text{Al}_2\text{O}_3$ /water nano-fluid when compared with water-based PV-T collector. The results in (Moradgholi, Nowee, and Farzaneh, 2018), indicate an improvement in electrical and thermal efficiency using  $\text{Al}_2\text{O}_3$ /water nano-fluids. Sardarabadi et al. (2017) considered metal-oxides/water as working fluids in order to check the performance of the PV-T collector. The experiments proved that there is much improvement in efficiency when ZnO and  $\text{TiO}_2$  are used. Glycol can also be used as a base fluid with oxides such as MgO,  $\text{TiO}_2$ , ZnO,  $\text{Al}_2\text{O}_3$ , and  $\text{SiO}_2$  in order to prepare nano-fluids, besides water (Xie, Yu, and Chen, 2010).

### 1.2.3 PCM based PV-T systems

These collectors are in the early stage of development and are like water-based collectors. The only difference is that it makes use of phase change material (PCM) within the PCM unit placed at the back of the PV module instead of water as a working fluid. The layered diagram of the PCM-based PV-T collector is presented in Figure 1.8 integrated with the PCM unit which absorbs and stores an ample amount of heat within the material from the PV module. PCM materials possess high energy storage density, chemical stability, and high thermal conductivity. During the day, the PCM melts by absorbing heat from the sun. At night, the PCM freezes and releases its latent heat, so that the heat stored in the PCM can be used for thermal applications. The selection and quantity of these materials are very important factors as materials with low thermal conductivity transfer heat slowly and do not provide the required thermal energy.

PCM materials used in PV-T collectors have two types: organic and inorganic.

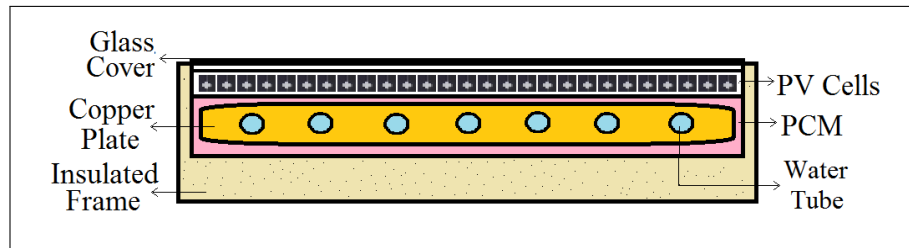


FIGURE 1.8: Sectional view of PCM based PV-T collector.

- Organic PCM materials are extracted from animals, plants, or petroleum products. These materials have low thermal conductivity but are safe to use and can be reprocessed.
- Inorganic PCM materials have low prices, are easily available and have better thermal conductivity (Mofijur et al., 2019).

The best PCM materials for heating water are myristic acid, stearic acid and palmitic acid which keep a lot of heat for a long time (Hasan, 1994a; Hasan, 1994b; Hasan and Sayigh, 1994). The most common and largely used PCM material is paraffin wax which is cheaper and easily available as compared to other materials (Abbas et al., 2018).

#### 1.2.4 Air based PV-T systems

Air-based PV-T collectors use air as heat transfer fluid so that heat may be extracted from the PV module. Warm air is collected from the output end by injecting cold air from the inlet side of the duct. In air-based PV-T systems, mass flow is another element that plays a vital role in decreasing the cell temperature. These systems are again divided into many subsystems on the basis of airflow pattern (Rukman et al., 2019): conventional air-based or back-pass air-based PV-T collector shown in Figure 1.9a is the simplest airflow pattern in which air flows below the PV module in a single air channel. In the second type which is a double-pass collector, the air is injected above the PV module and collected from the second channel that is below the PV module. In such a manner, heat transfer fluid stays for a long time owing to using two channels as shown in Figure 1.9b. A single-pass parallel PV-T collector is also a dual air channel configuration in which air runs simultaneously in both channels as depicted in Figure 1.9c. In a single-pass, the air duct lies over the PV module as depicted in Figure 1.9d. Figure 1.9e shows another dual-pass collector that is opposite to a dual-pass channel with an inlet air channel above the PV module and an outlet air channel below the PV module. In this case, the cold air is injected below the PV module and warm air is collected from the upper air channel. Aluminium fins are attached to the air channel as shown in Figure 1.9f to enhance the heat transfer rate from the PV module to the air channel. In a dual-pass configuration, these fins are arranged in the lower channel of the collector (Tonui and Tripanagnostopoulos, 2008).

#### 1.2.5 Bi-fluid based PV-T systems

Bi-fluid based PV-T collector uses both air and water simultaneously, enables PV cell cooling, and increases heat transfer. Cold air is inserted from one side of the collector and warm air is collected from the other end of the collector. Mostly water

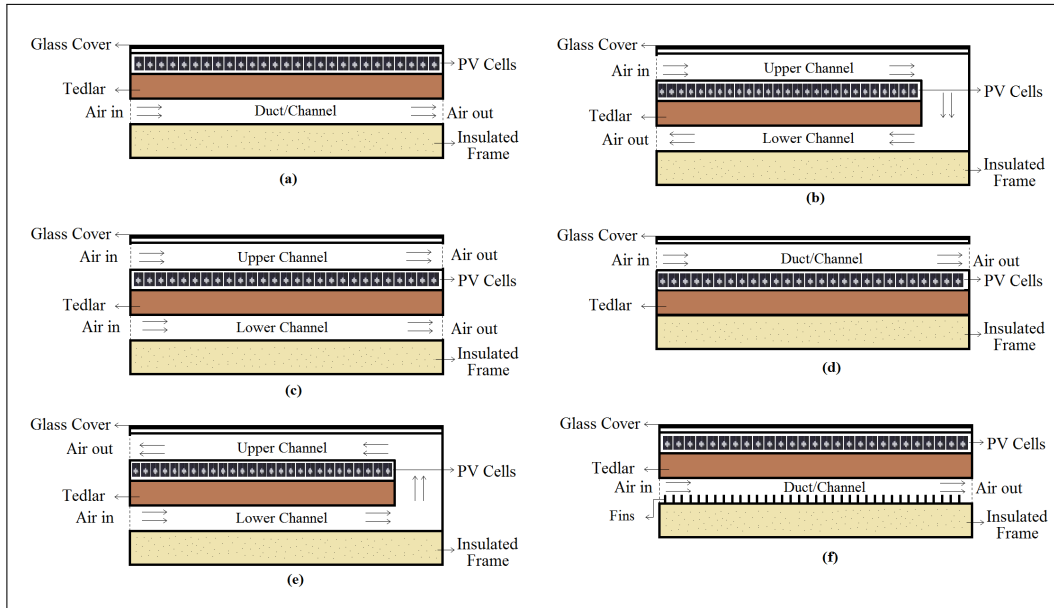


FIGURE 1.9: Different configuration of air-based PV-T collectors.

mixed with glycol is used that runs simultaneously perpendicular to the air channel. These collectors accommodate and draw out more heat. In comparison with single working fluid-based collectors, bi-fluid based collectors provide better performance. These types of collectors can be subdivided into further four categories (Rukman et al., 2018);

- single-pass with glass cover
- single-pass without glass cover
- double-pass without thermal storage
- double-pass with thermal storage.

A schematic diagram of a bi-fluid based PV-T collector is illustrated in Figure 1.10 where both air and water are simultaneously used as heat transfer fluids. It is impor-

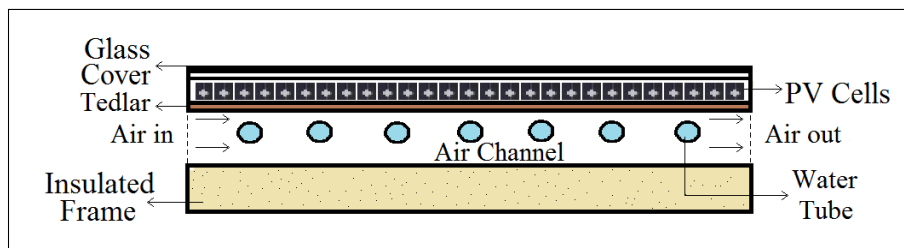


FIGURE 1.10: Sectional view of bi-fluid based PV-T collector.

tant to have some form of thermal storage which can accommodate and store all the heat extracted from the collector in order to get the maximum benefit from the PV-T collector. These systems are usually installed for domestic use to preheat thermal storage for warm water or space heating. They are more efficient for higher electrical and thermal performance, provide warm air and hot water simultaneously. The major drawbacks of these PV-T collectors are complicated design and high-cost (Jia, Alva, and Fang, 2019).

### 1.3 Mode of operation

There are two different types of heat extraction, forced circulation, and natural circulation.

- In forced circulation, a pump is used to circulate the fluid inside a collector and this fluid circulates in a closed system as illustrated in Figure 1.11. The pump requires an external energy source, a safety valve, and the maintenance cost of the system. Thermal efficiency could be up to 80% higher than natural circulation due to the high collector flow rate (Khalifa, 1998). Additionally, a control unit is needed to control the pump when the temperature exceeds the desired value.
- In a natural circulation, fluid circulates due to the action of buoyancy force, the design of these systems is not complicated and they are less expensive. Despite the fact that natural circulation collectors have low efficiencies, they are widely used in domestic applications. In a natural circulation, the flow rate can be increased by increasing the difference in height between the collector and storage tank but comparative results presented by Zerrouki, Boumediene, and Bouhadef (2002) show that there is a minor difference in the efficiencies.

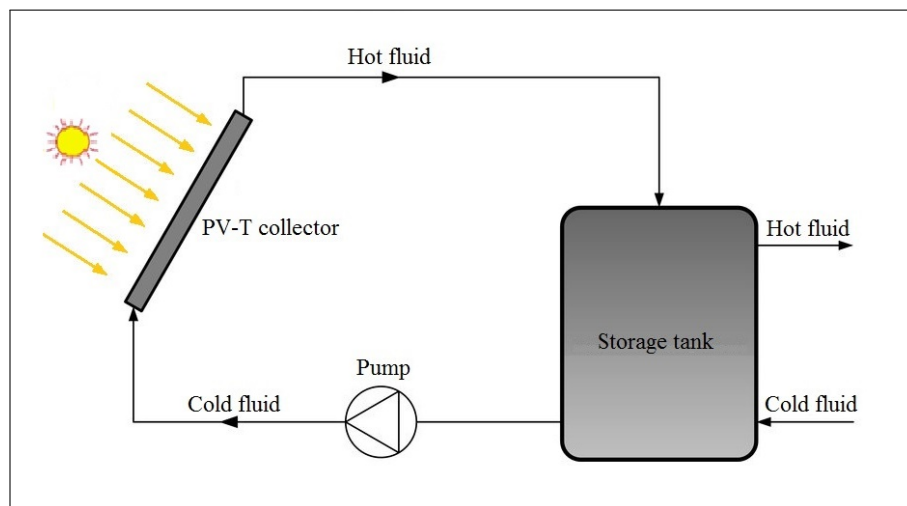


FIGURE 1.11: Schematic of forced circulation PV-T system.

An experimental investigation has been presented by Jadhao et al. (2017) and it is concluded that low pump capacity and thermal losses degrade the efficiency of forced circulation collectors than natural circulation collectors.

### 1.4 Type of solar collector

In a PV-T system, solar radiation is collected and transferred to the fluid flowing in it. One of the major drawbacks of solar collectors is that it works well when the sunlight is direct, otherwise some part of the sunlight is taken away if a tracking system is not implemented. There are two types of solar collectors; non-concentrating and concentrating.

### 1.4.1 Non-concentrated

Non-concentrated is the simplest type in which solar radiation is absorbed without any concentrating arrangements as illustrated in Figure 1.12. The collector area which intercepts the solar radiation is the same as the absorber area. The output of the collector is adversely proportional to the PV cell temperature. In a non-concentrated type solar collector, high temperature cannot be achieved because of no optical concentration. The two common types of non-concentrated solar collectors are;

- flat plate collector
- evacuated tube collector.

Hot water demand especially in Northern regions has a big impact on bills so flat plate collectors are recommended for such regions. It is also possible to use hot water collected from the collector for commercial applications such as car wash and laundry facilities.

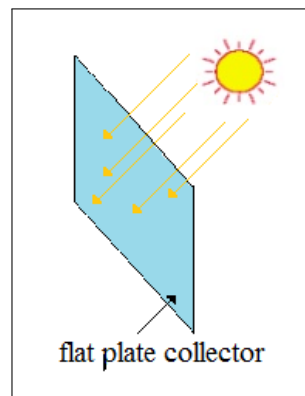


FIGURE 1.12: Non-concentrated solar collector.

### 1.4.2 Concentrated

Solar concentrators are used to concentrate the solar radiation onto PV cells which reduces the cost, increases cell efficiency, and annual energy production. To achieve maximum output, mirrors and lenses are used as solar concentrators to focus the solar radiation on the PV cell. This allows replacing costly semiconductor materials

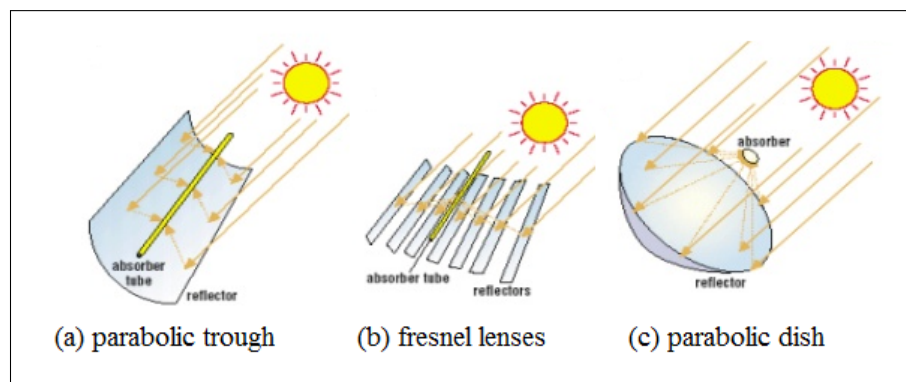


FIGURE 1.13: Non-concentrated solar collector.

of the solar cell with low-price optical elements. PV-T concentrators with densely packed modules are further sub-divided into various categories;

- spectral beam splitting
- concave mirrors
- parabola-shaped reflectors to concentrate sunlight as shown in Figure 1.13a
- Fresnel lenses as presented in Figure 1.13b
- parabolic trough (see Figure 1.13c).

Mostly, concentrated solar collectors are used for commercial applications because they are designed for larger heating loads. Beam split is another promising method where solar radiations are broken into two parts to get better efficiency. It is useful to only allow and filter the desirable part of the incoming solar radiation to fall on the solar cell of the solar spectrum. Because of this photovoltaic efficiency increases, as the operating temperature drops down. Apart from concentrating the solar radiation on the whole PV panel, single-cell concentrators can also be used for each of the solar cells where the focus of the light is on each of the solar cells individually as shown in Figure 1.14.

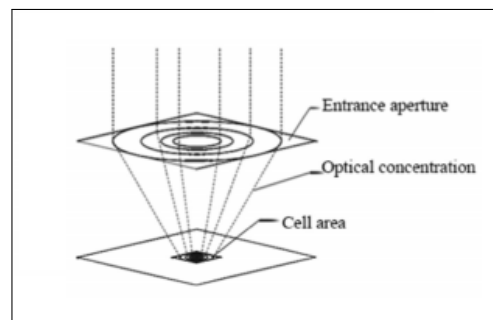


FIGURE 1.14: Single-cell concentrator (Royne, Dey, and Mills, 2005).

## 1.5 Glazing

The addition of an extra layer which can be a glass or the possible addition of an extra channel on top of the PV-T collector is called glazing. This additional transparent sheet plays an important part in designing a PV-T panel to trap more heat energy, reduce convective and radiative heat losses, and in most cases, it acts as a protection and protects the sensitive PV panel from several environmental impacts. Since glazed systems absorb more heat energy and halt thermal losses, which results in a better thermal energy output of the PV-T collector but at the same time, it degrades the photovoltaic output of the PV module (Diwania et al., 2020). This degradation of photovoltaic efficiency depends on the transmissivity of the glazing layer. Glazing increases the cost of the collector and affects the performance of the PV module by increasing the cell temperature and generating optical losses (Dupeyrat et al., 2011). A comparative study conducted by Tripanagnostopoulos et al. (2002) where the results presented show that there is a rise of 30% in thermal efficiency but simultaneously there is a drop of 16% in PV efficiency using glazed systems compared with the unglazed systems. Glazed systems are further divided into two areas;

- In the first approach glazed PV cells are placed on the absorber layer and there is an air gap between the PV cells and glass cover.
- In the second approach glazed PV cells are placed under a transparent glass cover and the cells are bound to the glass cover.

Most glass covers are not fully transparent and because of it, all the solar radiations cannot reach the absorber surface and PV cells encounter less temperature. Unglazed systems are also sub-divided into various approaches; unglazed with thermal insulation approach where a thermal insulation layer is attached at the back of the collector. One of the drawbacks of thermal insulation is when the heat limit is surpassed, PV efficiency starts decreasing. The latter approach is without thermal insulation systems which are comparatively simple in design, construction, and can be integrated into a roof easily. The major drawback is heat loss, which decreases thermal efficiency but favors electrical efficiency. Covered PV-T collectors provide higher temperature heat as compared to traditional uncovered collectors. Therefore, uncovered PV-T collectors are mostly used for pool heating. The life cycle of a PV module is approximately between 20 to 25 years. More than 95% of the aluminium and glass are recycled whereas about 80% of the PV cell layer can be recycled.

## 1.6 Applications

PV-T system has a number of applications like a solar greenhouse, tri-generation, air conditioning, desalination, district heating/cooling, drying, heat storage, refrigeration, and industrial applications as presented in Figure 1.15. The applications can be divided according to their temperatures as mentioned in the IEA SHC programme report (Lammle, Herrando, and Ryan, 2020).

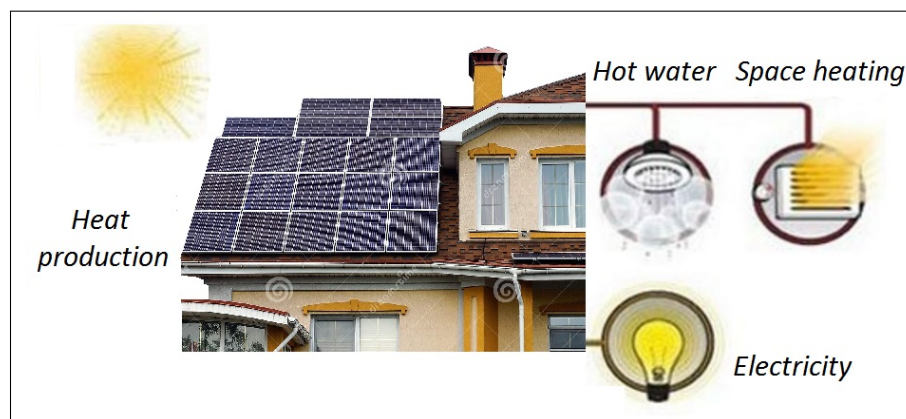


FIGURE 1.15: PV-T roof-top array supplying heating and electricity to a building.

- High temperature applications that require a temperature above 80°C are used for some industrial processes e.g desalination and agro-industrial processes.
- Medium-temperature applications are used in buildings for domestic hot water and space heating where the temperature up to 80°C is required. Moreover, PV-T integrated with a heat pump can be used for desiccant heating where 50 to 60°C temperature is required.
- Low-temperature applications take in heat pump systems and heating swimming pools or spas up to 50°C.

### 1.6.1 PV-Ts versus PV+ST

Here, hybrid PV-Ts are compared with separate use of ST+PV panels in a given space area.

Let us consider a surface  $S$  in  $\text{m}^2$  with  $x\%$  PV panels and  $(1 - x)\%$  ST panels.

We denote  $C_{PV}$ ,  $P_{PV}$  (resp.  $C_{ST}$ ,  $P_{ST}$ ) the cost and the power per  $\text{m}^2$  of the PV (resp. ST) panels. Similarly, we denote  $C_{PVT}$ ,  $P_{PVT}$  the cost and the power per  $\text{m}^2$  of the PV-Ts.

Then at the surface  $S$ , the cumulative power (heat+electricity) at  $S$  is:

- for PV + ST:

$$S[xP_{PV} + (1 - x)P_{ST}] \quad (1.1)$$

- for PV-T:

$$SP_{PVT} \quad (1.2)$$

It is assumed that  $P_{ST} > P_{PVT}$  and  $P_{ST} > P_{PV}$  (which is generally the case). Therefore, PV-Ts provide more power if the following condition is satisfied:

$$x > \frac{P_{ST} - P_{PVT}}{P_{ST} - P_{PV}}. \quad (1.3)$$

In terms of annual energy production  $E$ , if  $D$  denotes the number of radiation hours per year, then we have  $E = P * D$ . Therefore, (1.3) expressed in terms of produced annual energy remains the same because  $D$  simplifies so (1.3) is independent of  $D$ .

For numerical illustration, we consider standard conditions with radiation  $I_{sun} = 1000 \text{ Wm}^{-2}$ ,  $T_c = 25^\circ\text{C}$ , angle of inclination =  $30^\circ$ , orientation South, and we assume PV (resp. ST) panels with 15% (resp. 80%) efficiency. Therefore, we have  $P_{PV} = 150 \text{ Wp/m}^2$  and  $P_{ST} = 800 \text{ W}_{th}/\text{m}^2$ . For the PV-T, we consider 2 typical ones available in the market with the following features:

- Dualsun (DUALSUN, 2021): Unit area =  $1.66 \text{ m}^2$ ,  $P_{elec} = 280 \text{ Wp}$ ,  $P_{ther} = 570 \text{ W}_{th}$ . Therefore  $P_{PVT} = (280 + 570)/1.66 = 511 \text{ Wm}^{-2}$ . In this case, the above condition can be written  $x > 44.5\%$ .
- Solimpeks (SOLIMPEKS, 2020): Unit area =  $1.37 \text{ m}^2$ ,  $P_{elec} = 190 \text{ Wp}$ ,  $P_{ther} = 460 \text{ W}_{th}$ . Therefore  $P_{PVT} = (190 + 460)/1.37 = 474.5 \text{ Wm}^{-2}$ . The above condition writes  $x > 50\%$ .

In both cases, it can be seen that PV-Ts are better than the combination solar thermal and photovoltaic due to the fact that photovoltaics generally cover wider areas than solar thermal and their heat is not recovered. As an example in France, to meet energy transition requirements, new homes must use  $2 \text{ m}^2$  solar thermal panels or  $5 \text{ kWp}$  of photovoltaics, but there is no regulation for the PV-T system.

### 1.6.2 Building

Nowadays, one of the most common PV-T systems is building integrated photovoltaic-thermal (BiPV-T) systems which are mounted on the walls, are more efficient and occupies less space. There are two main categories of BIPV-T collectors, illustrated in Figure 1.16;

- roof-integrated BIPV-T collector

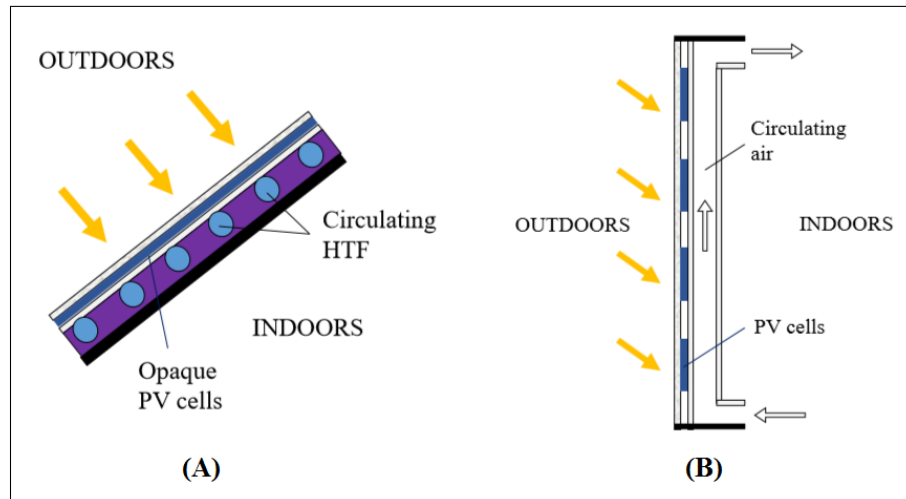


FIGURE 1.16: Two main types of BIPV-T collectors: (a) roof-integrated BIPV-T collector (opaque). (b) semi-transparent BIPV-T collector (Herrando and Ramos, 2022).

- semi-transparent BIPV-T collector

Globally, the building sector accounts for one-third of the total energy demand. In that case, the use of PV-T systems in buildings is very important (Good et al., 2015). Not only do these systems generate electricity but also provide a comfortable temperature for domestic heating purposes and lower the heating load by 27% (Baljit, Chan, and Sopian, 2016). Moreover, building integration of air-based PV-T systems is more accepted than that of water-based systems. These air-based can be divided into two categories (Bloem et al., 2012):

- In naturally driven systems, flow rate varies over time and it is difficult to forecast the performance
- In mechanically driven systems, the flow rate is kept constant and it is easy to estimate the performance.

Yang and Athienitis (2012) conducted a comparative study experimentally where single and multiple inlet PV-T designs were used for buildings. The simulation results demonstrate that using a two-inlet design, the thermal efficiency is increased by 5.7% with a minute improvement in photovoltaic efficiency. Moreover, it is observed that with an increase in mass flow rate, the fan power consumption increases which leads to a reduction in photovoltaic efficiency. Experiments were conducted to investigate the annual performance of PV-T collectors for residential application by Nualboonrueng et al. (2012) during the randomly selected day in March in Pathumthani province for medium-sized household Thai families using two PV-T collectors (amorphous and multi-crystalline silicon). It was found that the annual thermal production from the PV-T system was 1140 kWh per m<sup>2</sup> and electrical production was 72 kWh per m<sup>2</sup> with maximum energy output in March. The results indicate that the thermal efficiency varies between 35% and 64% with the maximum efficiency achieved in January and the lowest in June. It was also found that an amorphous silicon PV-T collector has better thermal efficiency but less electricity production than a multi-crystalline silicon PV-T collector. The results of this study indicate that the PV-T system is convenient and beneficial for providing thermal and electrical energy for domestic applications in tropical regions.

Kim, Park, and Kim (2014) designed an air-based PV-T collector with a monocrystalline PV module for the building. The experimental results presented in this study show that the average thermal and electrical efficiencies are 22% and 15% respectively with airflow at a rate of  $240 \text{ m}^3\text{h}^{-1}$ . The performance of PV-T collector with PCM as a part of the ceiling insulation was analyzed by Lin et al. (2014); the results showed that the presented design can increase the indoor air temperature up to  $23.1^\circ\text{C}$  during the wintertime. This design can produce an average outlet air temperature from the PCM of about  $22.55^\circ\text{C}$  during the wintertime without many fluctuations. At night-time, owing to sky radiative cooling in summer, the ambient temperature drops with a mean temperature of  $2.4^\circ\text{C}$ . Owing to the weak radiative cooling effect, the temperature change is small. Ji et al. (2006) has studied a water-based wall-mounted PV-T system that consists of a PV-T collector for an array (6 nos), a water storage tank, connecting pipes, and a circulation pump. Not only does the proposed system provide thermal and electrical energy for domestic use but also increases the thermal insulation of the building. Chow, He, and Ji (2007) proposed a similar kind of design in which collectors are mounted on vertical facades. The thermal efficiency during the late summer of Hongkong was 38.9% at zero reduced temperature and electrical efficiency of 8.56%. Moreover, it was found that the space cooling load was reduced by 50% in the peak summer time as compared with the bare wall situation.

Adnan et al. (2009) conducted an experimental investigation. Two PV-T panels having two different designs were used to obtain thermal and electrical power for building integrated applications. The first design uses water as a working fluid in a spiral flow configuration and produces a combined efficiency of 64% with 11% percent electrical efficiency with a mass flow at the rate of  $0.011 \text{ kgs}^{-1}$ . The second collector uses air as a heat transfer fluid and produces a combined efficiency of 55% with 10% electrical efficiency. Zhou, Liang, and Zhang (2017) conducted a numerical study in which an analytical expression for connection of PV-T collector array was derived for a PV-T co-generation system based on building energy demand. Moreover, an experimental setup comprised of 36 PV-T collectors was established to validate the thermal model. It was found that the total heat gain was 320 MJ with a thermal and electrical efficiency of 10% and 23% respectively. Pantic, Candanedo, and Athienitis (2010) conducted another experimental study; three different configurations of air-based BIPV-T systems which use recovered heat for house heating are proposed.

- In configuration 1, the preheated air is utilized for the HVAC system preheating.
- In configuration 2, a great amount of heat which is stored in a rock bed heat storage is used during the wintertime with an increased thermal efficiency of 26.7% and with a drop in a heating load of 48.5%.
- In configuration 3, the heat that is recovered is 75% more than the first two configurations with a thermal efficiency of 12.2% during the wintertime.

### 1.6.3 Cooling (air conditioning)

It is becoming very important to utilize solar cooling using a PV-T system because most of the heat by the PV-T collector is wasted during the summer and it is useful to apply this heat for solar cooling purposes in order to drive the cooling cycle although it is in the early stages. It should be noted that for cooling, a high temperature is

required that must be taken into consideration while for opting the system. This purpose can be achieved by using different methods such as:

- absorption cycles
- desiccant cycles
- electric compression refrigeration
- adsorption cycle
- solar mechanical processes.

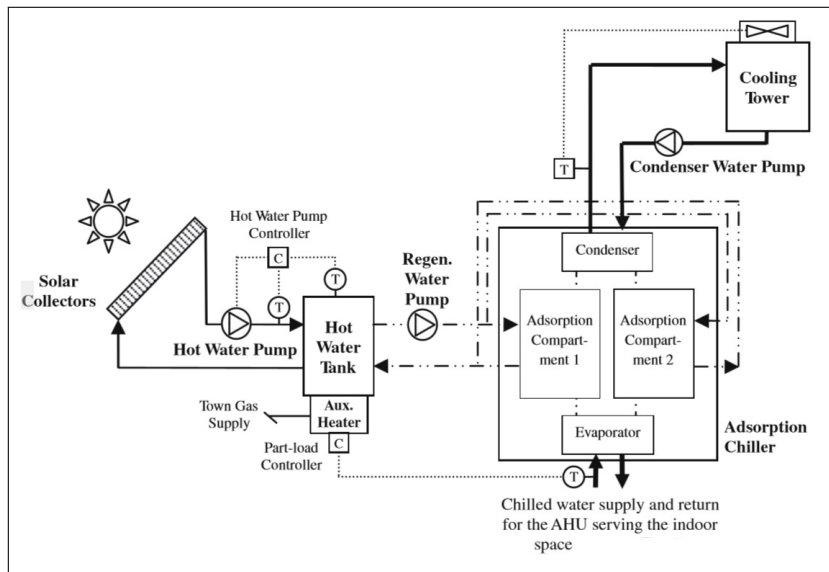


FIGURE 1.17: Schematic diagram of solar adsorption cooling (Fong et al., 2010).

These PV-T systems can also be combined with solar heating to acquire heat during the winter season, but integration is not that straightforward. An illustration of the solar adsorption cooling system is depicted in Figure 1.17. A PV-T cooling system typically comprises;

- photovoltaic solar panel
- storage tank
- control unit
- cooling unit (chiller) that operates thermally.

Chillers are the essence of the cooling process and remove heat from the fluid flowing below the PV module. They provide cooling by utilizing the excess heat coming from the collector. Absorption cycles are of two kinds;

- single-effect chillers that make use of hot water and operate at a temperature of 70-100°C.
- double-effect chillers that use steam and operate at a high temperature.

A desiccant cooling system is referred to as an open system, uses water as a refrigerant and is in direct contact with the air. The closed systems are thermally driven chillers that supply chilled water. Most of the chillers are equipped with absorption technology and some use adsorption technology.

### Desiccant technology

A rotating desiccant wheel technology is used which is equipped with absorbent material. In a desiccant wheel technology, water is used as a working fluid and the rotor wheel requires maintenance. Water runs through the solar panel and warm water is obtained. This warm water is stored in a storage tank, a solar air-conditioning unit is attached to it and the warm water is transferred from the tank to this unit. The air-conditioning unit is divided into two sections as presented in Figure 1.18.

- heat exchanger
- cooler.

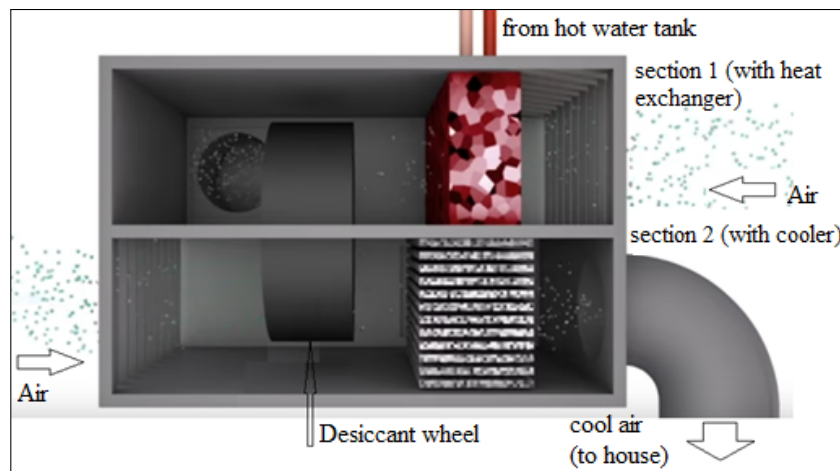


FIGURE 1.18: Schematic diagram of desiccant cooling.

A desiccant wheel runs slowly inside the air-conditioning unit and warm water enters the heat exchanger in the first section of the air-conditioning unit. Similar to a car radiator, a heat exchanger uses warm water to heat outside air which has been drawn in the first section. At the same time outside air is also being drawn into the second section into a desiccant wheel. This wheel is used to dry up the air before it goes into the house and slowly turning desiccant material in a wheel continuously absorbs moisture in the second section. The absorbent material dries out in the first section and desiccant material is dried out using the hot dried air generated by a heat exchanger. This air is then exhausted outside the house and the dried air from the desiccant wheel flows through the cooler and creates a stream of cool dry air. This cool dry air is drawn into the house and during the winter season, warm air is directly drawn into the house.

### How adsorption chiller works?

Adsorption chillers utilize silica gel as an absorption material and water as a refrigerant. They are eco-friendly and can be disposed of easily. The adsorption chiller comprises of an evaporator (low pressure) and a condenser (high pressure). Adsorption cooling is based on the evaporation and condensation of a refrigerant combined with adsorption. Silica gel adsorbs the water vapors which are produced in the evaporation unit. Hot water from the PV-T collector heats the silica gel and this heated silica gel makes the refrigerant evaporate. The water vapors which are directed to the condenser make vapors become water in the condensation unit and this water

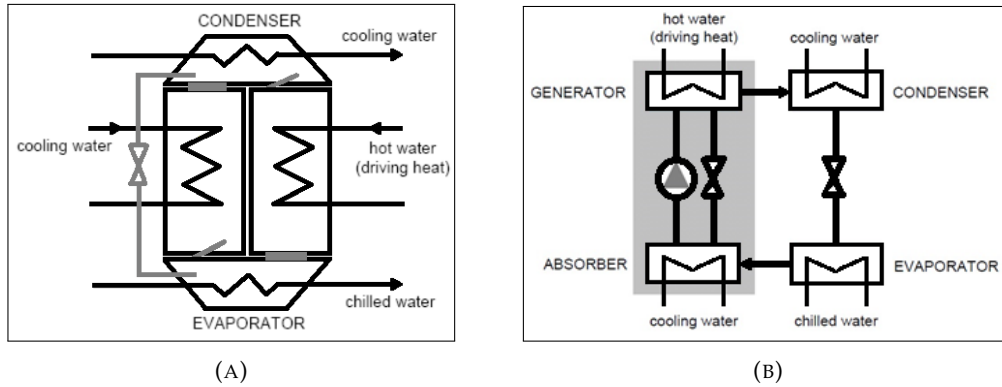


FIGURE 1.19: (a) Schematic diagram: (a) adsorption chiller. (b) absorption chiller.

is transferred to the evaporator where the condensed water is collected as shown in Figure 1.19a.

### How absorption chiller works?

Absorption chillers use water as a refrigerant and lithium bromide as an absorbent. Lithium bromide is a salt that is attracted to water moisture. The absorption chiller consists of two chambers; one chamber has a condenser and a generator whereas another chamber has an evaporator and absorber. A liquid (60% lithium bromide and 40% water) is pumped from the absorber through a heat exchanger to the generator tank. Ammonia can also be used as an absorbent with water as a refrigerant. The excess heat produced by the PV-T collector is then supplied to the generator chamber and this heat separates lithium bromide and water. Separated water particles become vapors and fill up the condenser with steam. Heavy particles of lithium bromide sink to the bottom. Once the concentrated lithium bromide solution cools down it makes its way back to the absorber where it is mixed with water. The vaporized steam goes through a cooling tower and is reinserted in the evaporator which has a very low air pressure. This sudden change in the pressure drops the temperature of the water and transforms it into chilled water as shown in Figure 1.19b. The chilled water output from adsorption is normally between 5-10°C and from the absorption chiller is 9°C or more.

The efficiency of thermally driven chillers is the thermal coefficient of performance (COP), the ratio of cooling output to the required driving heat input.

$$\text{COP} = \frac{\text{cooling output}}{\text{driving heat input}}. \quad (1.4)$$

Absorption chillers are complicated with a low thermal coefficient of performance and cannot achieve low evaporating temperatures. Adsorption chillers are heavy and have a low thermal conductivity of the absorbent.

Eicker and Dalibard (2011) proposed modeling of PV-T collectors for night radiative cooling of buildings and the simulation model was validated through experimental studies conducted in Stuttgart using two prototype PV-Twin modules. For the estimation of the sky temperature, the sky is considered as a black body. Water-based open systems function better because of high heat capacity and gain high cooling output owing to high water emissivity. The water consumption through evaporation is not negligible. The results indicate that it can be 3.5 kg per night and

because of it, the closed system with PV-T collectors was chosen in this study. When measured, the cooling power varies between 100 and 120 W per  $\text{m}^2$  with the mean mass flow rate of  $23 \text{ kgm}^{-2}\text{h}^{-1}$  during the first night and  $28 \text{ kgm}^{-2}\text{h}^{-1}$  in the second night. Moreover, another experimental study using 12 PV-T modules was also conducted during the daytime for the Madrid climatic conditions with  $35^\circ\text{C}$  ambient temperature. When measured, the average cooling power was between 43.1 and  $65.6 \text{ W per m}^2$  with an electrical coefficient of performance between 17.2 and 29.3. Fang, Hu, and Liu (2010) investigated and examined the performance parameters of hybrid PV-T solar heat pump under climatic conditions (i.e., ambient temperature  $24.5^\circ\text{C}$ , solar radiation:  $610 \text{ Wm}^{-2}$ , and wind speed:  $0.05 \text{ ms}^{-1}$ ) through experimental studies on water-heating mode. In the beginning, the presented system operates steadily with changes in condensation and evaporation pressure. During the initial 10-minute period, COP rises to 3.35. It experienced a slight drop of 0.21 in the next 10-minute period owing to a drop in evaporation pressure and then it remained between (2.75 - 2.85) for the remaining time. The temperature of the conventional PV panel goes up to  $62^\circ\text{C}$  with a 0.7% drop in photovoltaic efficiency and the temperature of the PV module goes down to  $8^\circ\text{C}$  in the PV-T evaporator with an increase of 1.5% in photovoltaic efficiency. It was evaluated by Alobaid et al. (2017) that using solar absorption cooling systems saved 50% of primary energy as compared to vapor-compression air conditioning systems and 10 to 35% maximum electrical efficiency of PV-T was acquired.

Sukamongkol et al. (2010) proposed a simulation model governed by five key mathematical models in order to predict the performance of a condenser heat recovery with a hybrid PV-T air heater to regenerate desiccant for decreasing the energy use of an air conditioning room. Experimental tests were also carried out under outdoor and indoor conditions for three consecutive days for validating the simulation model. A consensus was found between the simulation results and experimental measurements. A hybrid PV-T air heater in cooperation with the condenser saved almost 18% of the total energy used by the air conditioning system. The average daily PV-T photovoltaic efficiencies of the experimental and simulated were 6.45% and 6.05% respectively and the thermal efficiency was almost 60%. Cremers et al. (2015) conducted an experimental study using two differently designed hybrid PV-T collectors where the performance of the PV-T collectors is evaluated using backside shielding and without using backside shielding to know which building integration design is more suitable for cooling applications. Using backside shielding leads to a higher zero-loss collector efficiency factor and the heat loss coefficient goes up which is better for cooling.

### Comparison of grid power, PV and PV-Ts for cooling purpose

Heat and electricity are produced by the PV-T collector at once. There is a need for cooling using the excess heat produced by the collector during the summer season. Due to the fact that heat produced by the collector can only be used during the winter season. The heat available during summer is used for cooling purposes using an absorption chiller. In the southern parts, the summer season lasts around 6 months with 3 peak months. These months require only 6 hours of cooling but the latter half requires 12 hours of cooling. Annually, cooling is required for 1620 hours approximately. If 3 months of partial usage and 3 months of full usage is assumed.

- Case I: Air-conditioning with direct grid power

On average, a central air-conditioner uses 1 kWh per ton per hour (Association, 2021). Take a two-ton air conditioner as an example that runs for 12 hours a day. The usage would be 24 kWh per day. Assuming that the cost of electricity €0.30 per kWh (this depends on the country and €0.30 per kWh is for Germany, highest in EU-27 (Eurostat, 2021)). If the air-conditioner runs completely (12 hours per day) for 3 months and runs partially (6 hours per day) then the total cost of using an air-conditioner for the whole year would be €972 (complete use: €648 and partial use: €324).

- Case II: Air-conditioning PV power only

The daily mean electrical yield is 3.21 kWh/kW<sub>p</sub>/day and the total energy output of a mono-crystalline silicon PV collector is 194.79 kWhm<sup>-2</sup> per year, respectively (Abdul-Ganiyu et al., 2020). To cover the annual cooling demand, three PV panels are required approximately (3 months of partial and 3 months of complete use). The annual total cost would be €555 if the average cost is assumed as €0.16. This is approximately 43% lower than the annual grid power used to run an air-conditioner.

- Case III: Air-conditioning with PV-T integrating absorption chiller

An absorption chiller takes surplus heat from the PV-T collector and provides cooling. Consider a lithium bromide absorption cooler with a COP of 0.73 and a PV-T collector with 73% thermal and 10.5% photovoltaic efficiency. Annually, 2096.5 kWh of heat and 298.5 kWh of electricity is produced by the PV-T collector with an area of 1.65 m<sup>2</sup>. The yearly daily average yield of the collector is 5.75 kWh of heat and 0.82 kWh electricity with a total efficiency of 83.5% (Ma, Li, and Kazemian, 2020). Using a single PV-T collector, the annual cooling yield is 1540 kWh and roughly 2 collectors are required to cover the annual cooling demand.

The payback time is 6.1 years using a PV system and it is 16.7 years using a PV-T system which is 2.7 times higher than the PV system (Herrando et al., 2019). PV-T based absorption cooling system saves 50% of primary energy in comparison with a vapor-compression air-conditioning system (Alobaid et al., 2017).

#### 1.6.4 Greenhouse drying

Drying is very popular in developing countries for the preservation of agricultural products and food by simply using solar dryers that have various typologies. A schematic diagram of solar air-based PV-T drying is illustrated in Figure 1.20. A study was conducted by Tiwari, Tiwari, and Al-Helal (2016) to evaluate the performance of PV-T mixed-mode greenhouse solar dryer. Experimentally, the overall energy was 2.03 kWh and theoretically, it was 1.92 kWh. A theoretical model for PV-T greenhouse solar dryer has been proposed by Tiwari and Tiwari (2016) under forced mode to evaluate different parameters for the climate of New Delhi. The numerical model developed was also validated by experimental measurements. It was found that more than 130 kWh thermal energy was gained from the PV-T greenhouse dryer in July and roughly 70 kWh was gained in the month of January. During the month of July, the total electrical energy gain is approximately 15 kWh whereas it was around 17 kWh for the month of January. The average overall thermal efficiency was between 65 and 72%. The study concludes that the proposed greenhouse dryers performed well in all conditions.

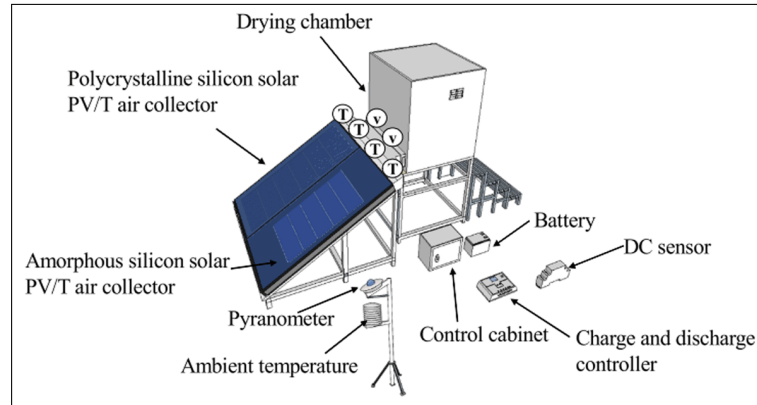


FIGURE 1.20: Schematic diagram of solar hot-air drying system (Kong et al., 2020a).

Koyuncu (2006) found that the overall performance of these greenhouse solar dryers can be enhanced by using a chimney and a black coated absorber. It was also found that the drying of products using a greenhouse dryer is 2-5 times more efficient than open sun dryers having better quality. Tiwari et al. (2016) has presented another thermal mathematical modeling along with the design and fabrication of a PV-T integrating greenhouse for biogas heating. The system includes 3 glazed PV-T collectors with greenhouse inclined at  $30^\circ$  from the horizontal plane and this PV-T system can be used for crop drying, improving the production of biogas and crop cultivation along with the generation of electricity. 12.76 kWh was found to be the overall thermal energy for a clear day without load with drying chamber temperature exceeding  $50^\circ\text{C}$  for the New Delhi climate in the month of May. It is also found that the regular dusting of PV-T greenhouse results in higher thermal performance. According to the study, the PV-T greenhouse is appropriate for the production of biogas during both clear and cloudy conditions. Additionally, a detailed thermal model of an air-based PV-T integrating greenhouse system was proposed by Tiwari, Agrawal, and Tiwari (2018). It is obvious that the maximum allowable temperature for every crop is different and it can be changed by varying the mass flow rate. It is found that overall thermal efficiency was 56.30% and 11.26% electrical efficiency at a mass flow rate of  $0.01 \text{ kgs}^{-1}$ . The developed drying setup is useful during the daytime while the PCM-based thermal storage is recommended to be useful at nighttime. These systems perform better under the forced mode option and are the most sustainable options for crop drying by integrating a DC fan and this fan is operated from the power produced by the PV module (Tiwari and Gaur, 2014).

### 1.6.5 Desalination

Solar desalination is a process in which mineral components are removed from saline water using solar radiation and it can be used for human consumption and irrigation. It is a fundamental requirement to have drinking water to stay alive and this need can be met by PV-T based solar distillation, co-generating electricity and fresh water. Thermal desalination is a good solution to get fresh drinking water. Usually, a high temperature is required for this and a high temperature can be attained by using concentrating PV-T collectors. The desalination process is divided into two categories:

- active solar still

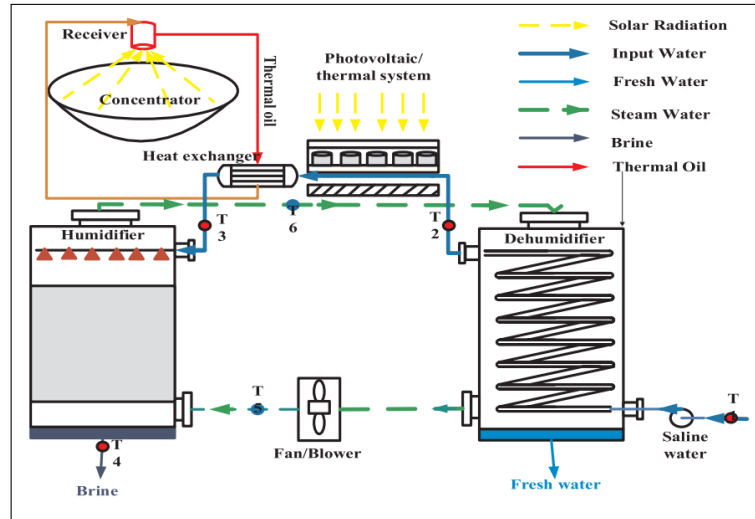


FIGURE 1.21: Schematic diagram of hybrid solar desalination (Rafiei et al., 2019).

- passive solar still.

Sathyamurthy et al. (2015) carried out a comparative study for different types of solar still models on the basis of performance. An experimental investigation of two PV-T solar stills (single slope passive and single slope active) was conducted by Kumar and Tiwari (2010) for the composite climate of New Delhi. The maximum monthly yield of 100 kg was obtained from the passive solar still and from the active solar still, the maximum production of 224 kg was obtained during the month of July. According to the results of the study, the production during December rapidly fell to almost 100 kg for active solar still and less than 25 kg for passive solar still. Kumar and Tiwari (2008) have designed and examined under New Delhi climate a self-sustainable PV-T integrated active solar still. This design can be used in far-flung areas and generates more than 3.5 times higher yield than the passive solar still. Moreover, it saves 43% of the power used to operate the pump. Ong et al. (2012) proposed a novel thermally driven multi-effect membrane distillation concept for isolated islands and coastal regions by developing a mathematical model under steady-state conditions to forecast the performance of the system with a prediction accuracy of 95.2%. For larger scale-up membrane distillation systems, the presented modeling approach can be used. Additionally, this approach is feasible, economical, and has a longer life owing to the use of polymeric materials.

Sotehi, Chaker, and Maalouf (2016) conducted a theoretical study in order to produce fresh water in the climate of Ouargla city. The numerical simulations were carried out for the whole year using TRANSYS 17 software in order to examine the performance of the system. Moreover, Gaur and Tiwari (2010) have carried out a study on PV-T hybrid solar still to optimize the number of PV-T collectors. An overall picture of hybrid solar desalination is presented in Figure 1.21. The results show, that the daily yield is almost 7.9 kg and the maximum yield was produced by four PV-T collectors. Additionally, it is found that by increasing the number of collectors, daily yield increases and daily solar still efficiency decreases 40% with the numbers of collectors increasing from 2 to 10 (with  $0.055 \text{ kgs}^{-1}$  mass flow rate and 50 kg mass of water). It is found that solar still efficiency and the daily yield reduces by enhancing the mass of water from 50 kg to 200 kg with a mass flow rate of  $0.055 \text{ kgs}^{-1}$  for the same number of PV-T collectors.

### 1.6.6 District heating/cooling

District heating/cooling as presented in Figure 1.22 is another interesting application of a hybrid PV-T system. Usually, a large collector area can have a high cooling capacity and a larger collector area is linked with the storage that needs empty space. The parabolic trough collectors occupy more heat and have high thermal efficiency due to this they are recommended for district cooling. District heating/cooling can be very useful for regions like Gulf, Mediterranean, and South Asia. The benefits of this technology are reduced energy and operation costs, community energy management, safer operation, reduced CFC utilization via district cooling and increased reliability.

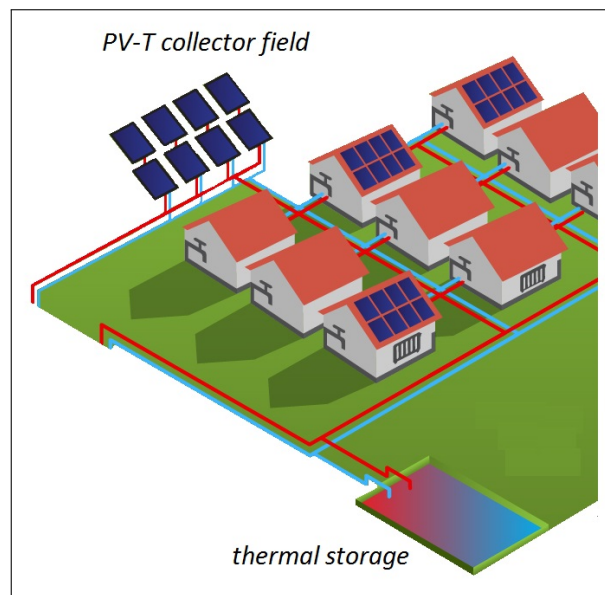


FIGURE 1.22: Schematic diagram of PV-T district heating.

In the North European climate, Pakere, Lauka, and Blumberga (2018) analyzed optimal integration of hybrid PV-T in district heating systems. The assumed area is between 1000 to 3000 m<sup>2</sup> for 8 different scenarios in this study. It is found by the hourly analyses that the produced solar power ranges from 109 to 307 MWh annually and a higher solar fraction can be obtained with maximum PV-T installation but at a higher cost. Golla, Staudt, and Weinhardt (2019) have conducted a comparative case study. A conventional cooling system was compared with the presented absorption-based air conditioner. An absorption chiller that functions using the excessive heat generated by the PV-T plant provides cooled fluid to buildings within the district cooling network. In this study, it was supposed that the PV-T plant has 70% thermal efficiency with a photovoltaic efficiency of 12%, and a COP of 0.8 for the absorption chiller. Most of the time heating is required during the night and early morning hours and cooling is required from 1PM to 4 PM which goes with the peak production time from the PV-T plant. The time when cooling is provided using only a PV plant is 988 hours and the time when cooling is provided using a PV-T plant is 1617 hours which is 62.9% more than the cooling provided by a PV plant alone.

Participation and ownership of a community in a renewable project with a focus on supplying and sharing energy within the community by reducing the peak demand is called community energy. Depending on the energy usage, a thermal user can be an electric consumer and a thermal consumer can also be an electric producer. Luo et al. (2019) presented a linear programming model for optimization of

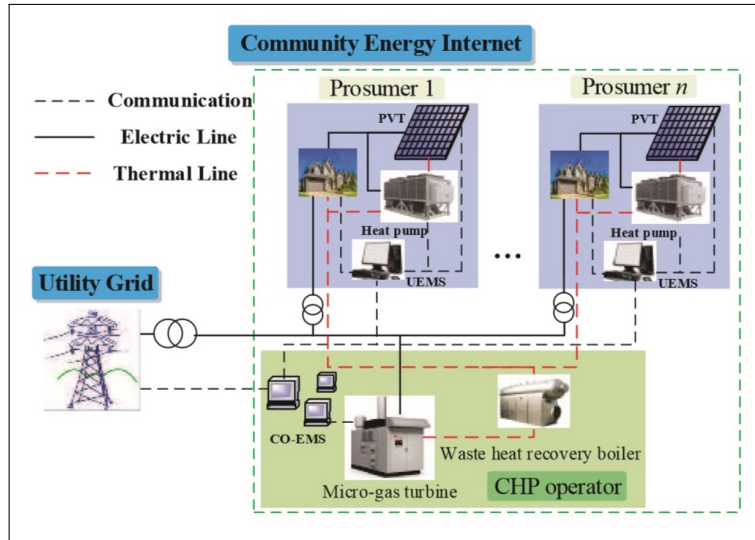


FIGURE 1.23: Structure of Community Energy Internet (CEI) with PV-T and heat pump (PVT-HP) prosumers (Liu et al., 2018).

the structure and operation of a distributed resource system with district energy networks on a virtual island with four buildings in the South China Sea. It was found that the cooling consumption of building 4 is much lower than that of the other sites in spite of the fact that the PV-T collectors, water tank, and absorption chillers space are the same for all the buildings. When energy networks are applied, the cost at building 4 is lowered by 16.11%. To balance the energy system via the energy networks, surplus energy is supplied to the other sites. It was found that this energy network decreased the cost of the entire system. Additionally, the distance and imbalance between the energy supply and demand can greatly affect the network layout. Liu et al. (2018) used a consensus approach for distributed energy sharing in community energy internet (CEI). The structure is presented in Figure 1.23. A social welfare maximization model was built and a consensus-based completely distributed algorithm was designed to address the problem. Moreover, the proposed model is validated by selecting six residential buildings.

### 1.6.7 Trigeneration

Nowadays, trigeneration application is thoroughly researched. Zhou et al. (2019) conducted a study in which a roll-bond PV-T heat pump system was used to examine tri-generation performance theoretically and experimentally during summer. The system is in a co-generation mode in winter and has heating and electrical power generation. The numerical model is validated and the experimental results are in accordance with the simulation results. It was found that the proposed model has the potential to obtain tri-generation (i.e., hot water, space cooling, and electricity) for buildings with high efficiency and long-term stable conditions. The cumulative electrical power generation was approximately 2 kWh with the thermal energy of 6.13 kWh, and cooling power of 18.5 kWh during the whole refrigeration process. Calise, d'Accadia, and Vanoli (2012) proposed a novel polygeneration case study producing electricity, space heating, cooling, and domestic hot water. The system has PV-T collectors, an absorption chiller, storage tanks, auxiliary heaters, heat exchangers, pumps, controllers, and a cooling tower. The thermal energy which is obtained from the panels is used to run the absorption chiller whereas the electrical

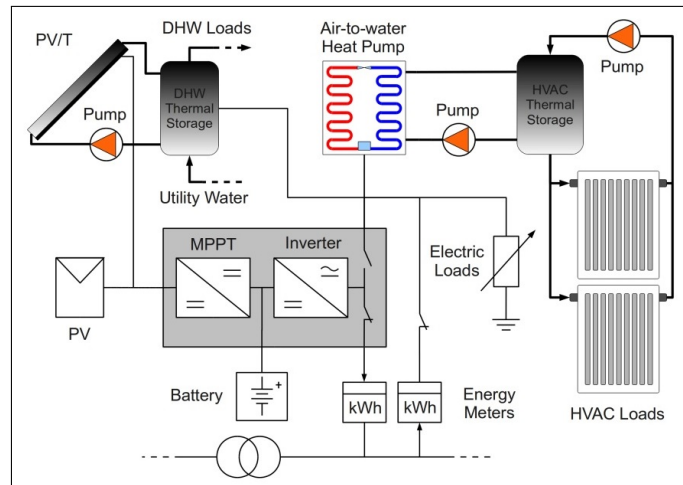


FIGURE 1.24: Schematic diagram of PV-T tri-generation system setup (Joyce et al., 2011).

energy generated from the collectors is used for system loads and building lights. The supplementary electricity is shifted to the grid. According to the simulation results, it is technically feasible to produce electricity, space heating, space cooling, and domestic hot water throughout the year.

Joyce et al. (2011) modeled another heat pump-based trigeneration PV-T system in order to meet the demand of an urban single-family. This system produces electricity, heating, domestic hot water, ventilation, and air conditioning (HVAC) as well. This model is presented in Figure 1.24 with the simplest and most reliable configuration. The simulations were performed for the Lisbon climatic conditions and approximately 6188 kWh of annual energy is required to meet the comfort levels of the building (i.e heating, cooling, domestic hot water, and home applications). According to the results, the system can generate electrical energy of 6795 kWh (PV: 5493 kWh and PV-T: 1302 kWh) at an average efficiency of 13.45% and 1618 kWh of thermal energy through PV-T collectors.

### 1.6.8 Refrigeration

Refrigeration is an application of PV-T systems that can be used in marts, medical laboratories, and slaughterhouses, especially for isolated islands and coastal regions. Liang et al. (2020) investigated experimentally the refrigeration performance of a PV-T heat pump system using four roll-bond PV-T modules in northern China on a summer night. In Figure 1.25, a schematic of the proposed PV-T heat pump system in the refrigeration mode is presented. The COP during the chilled water process under cloudy conditions varies between 2.4 and 3.4 with an average value of 2.66 and under clear conditions, it fluctuates between 2.6 and 3.4 with an average value of 2.99. There is an increase of 12.4% more under clear conditions than the latter ones. The results indicate that the proposed system can achieve refrigeration with high performance and is practically feasible. A novel hybrid dissipation PV-T heat pump for refrigeration was developed by Lu et al. (2020). The steady-state simulation model of the system has been made and then validated through experimental results. The PV-T module can utilize night sky radiation and convection with the surrounding air with an average heat dissipation flux of almost 420 W per m<sup>2</sup>. The

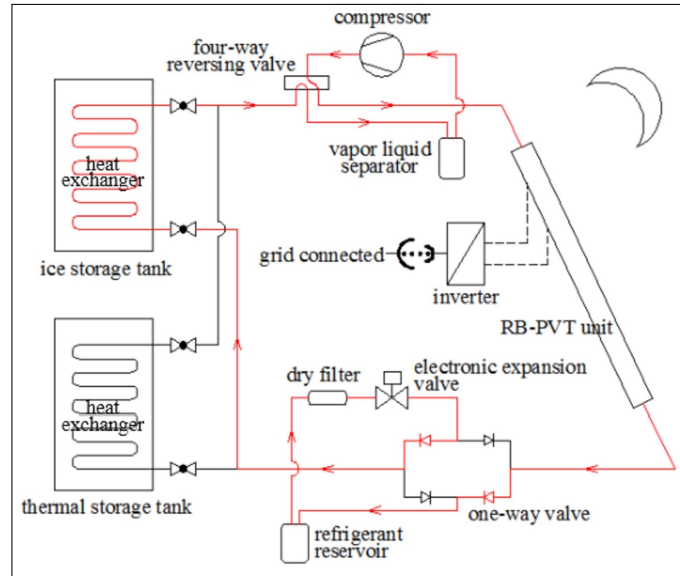


FIGURE 1.25: Schematic diagram of the proposed PV-T heat pump system on refrigeration mode (Liang et al., 2020).

variation in wind speed and temperature can enormously influence the refrigeration performance and PV-T module heat dissipation performance. It was shown by the experimental results that the average  $COP_{ref}$  varies between 1.8 and 2.1 under different ambient conditions but is not much affected by the relative humidity.

### 1.6.9 Heat Pump integrated with a PV-T collector

It is a priority to save energy, decreased the cost of heating and cooling. The heat pump combined with a PV-T collector performs better than a standard PV-T heating/ cooling system. The devices get heat and transfer this heat to a high-temperature medium from a low-temperature medium. They are effective in places like Ottawa, Canada where the temperature is extra chilly. The heat pump combined with the PV-T is less effective due to the fact that enough heat is not produced when the ambient temperature falls. The advantage of using a PV-T system is the combined generation of both heat and electricity. The electricity generated by the collector can be used to raise the temperature in an attempt to obtain the desired temperature. As reported by natural resources Canada (Energy star, 2018) almost 3.3 kWh of heat is gained for every 1 kWh of electricity used to power the heat pump at 10°C. A PV collector supported by a heat pump can be used for cooling the PV module.

Koşan et al. (2020) analyzed the performance of the PV-T assisted heat pump drying system. It was found that thermal efficiency varies between 38.51 and 70.56% with an average efficiency of 56.37% depending on ambient conditions. The average electrical efficiency obtained was 12.25% with a maximum efficiency of 14.02%. Using 8 PV-T collectors for a two-stage Italian house with a volume of 374 m<sup>3</sup>, Noro and Lazzarin (2018) determined the economic performance of the hybrid PV-T heat pump system. With the intention of getting domestic hot water, the inlet temperature is set around 12°C and the water supplied to the user is 45°C. A control system is suggested to drive the system for space heating. A three-way valve is assumed to bypass the storage if the temperature of the storage tank is lower than the temperature of water from the radiant floor plant. If the solar radiation is higher than 300 Wm<sup>-2</sup> and the temperature from the PV-T collector is greater than 7°C than the

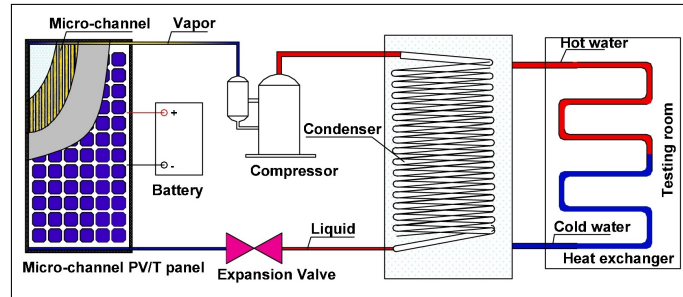


FIGURE 1.26: Solar driven direct-expansion heat pump system employing the novel PV/minichannels-evaporator modules (Zhou et al., 2020).

storage temperature, the pump turns on. Lastly, if the temperature from the PV-T collector is lower than  $3^{\circ}\text{C}$ , not considering solar radiation into account, the pump turns off. The average thermal and electrical energy produced by the PV-T collectors was 3315 and 2636 kWh per year for three different cities (Venice, Rome, and Crotona). Additionally, the results indicate that the primary energy saved is between 35% and 65%, and discounted payback of the investment can be around 10 years in mild climates. Kong et al. (2020b) has conducted a study where the payback period of the unit was 7.87 years with an annual grid energy saving of 23.76 MWh using PVT-cascade heat pump design. A numerical and experimental study done by Zhou et al. (2020) to explore the performance of a solar-driven heat pump system employing micro-channel PV-T modules for the room of  $150\text{ m}^2$  with room temperature remaining at  $18.5^{\circ}\text{C}$ . A schematic diagram of a solar-driven direct-expansion heat pump system is presented in Figure 1.26. The average thermal efficiency was 55.0% and the photovoltaic efficiency of the PV-T system was 13.7%. The simulation results are consistent with the experimental ones, with a maximum error of 7.2%. It was also determined that the use of a microchannel tube can enrich efficiency.

## 1.7 Software tools

The feasibility study of a solar installation needs design and simulation tools to optimize the energy production taking into account different characteristics such as solar radiation in the considered location, panels technology, orientation, inclination, shadow, storage, etc. To this end, various software have been developed. Engineers and researchers use these tools for the sizing of the power plant, pre-feasibility analysis and optimization, technical and economic analysis in order to avoid system over-size, poor reliability, and high installation and maintenance costs.

A review of 19 software tools for hybrid energy systems is presented in (Sinha and Chandel, 2014): HOMER, Hybrid2, RETScreen, iHOGA, INSEL, TRNSYS, Dymola, iGrhyso, HYBRIDS, RAPSIM, SOMES, SOLSTOR, HySim, HybSim, IPSYS, HySys, ARES, SOLSIM and HYBRID DESIGNER. It should be mentioned that these software are general platform for an entire system (building, process, etc) analysis, design and management and not only for solar. In addition to this list, there are many other specific solar software applications to be mentioned such as HelioScope, Aurora, BlueSol, Solarius, PVWatts Calculator, SolarEdge, Polysun, PVGIS, Candela3D, PVCASE, KACO, SMA Sunny Design, FRONIUS, PV Designer, PV-DesignPro, PV F-Chart, PV\*SOL, PVsyst, PVWatts, RetScreen, Solar Advisor Model (SAM), PV Planner, SOLARGIS, Solar Pro.

A number of these software tools are suitable for solar thermal plants to simulate hot water needs, the definition of the hydraulic circuit of the installation, tank storage and collectors. Besides, many PV inverters and ST components manufacturers provide their one free software in order to size and design a solar system generally with their products (for instance inverters from MASTERVOLT Syscalc, INGECON SUN PLANNER, ABB Solar PVSize...). As far as solar energy is concerned, solar radiation and meteorological data are necessary. Related data is often embedded in the software tool or can be found using available databases such as Solcast, OpenSolarDB, World Radiation Data Centre (WRDC), SoDa HelioClim3, NASA SSE, Global Solar Atlas, Global solar Atlas, Worldclimate, etc. Note that in the software tools SOLARGIS, PVGIS, one can already find TMY data (typical meteorological year data). Despite a wide choice of software tools for designing solar installations, they all have limitations. In (Wijeratne et al., 2019), 23 solar PV design and management software tools are analyzed and their disadvantages are highlighted.

## 1.8 Hybrid PV-T products and market

The solar-thermal technology market is expanding rapidly due to its benefits but at present, the market is comparatively small. In 2015, the energy provided by renewable energy sources was 13.8% of the global energy supply and less than 2% came from solar (International Energy Agency, 2016). Solar energy has a lot of capability to become a leading energy source in the future and since 2000, the average annual growth rate of PV-T technology and photovoltaic technology is 11.7% and 44.1%. In the future, these PV-T systems coupled to heat pumps can cover more than 60% of heating and 50% cooling demand for urban residential buildings (Ramos et al., 2017). Solar technology installation's growth rate is high in Europe, even though the initial cost is high and the available solar radiation is less as compared to other regions. The investment in solar-thermal technology depends on the availability of solar radiation, higher availability makes it cheaper than natural gas and electricity. Figure 1.27 below shows the solar-thermal energy yield and total installed capacity across the world from the year 2000 to 2015.

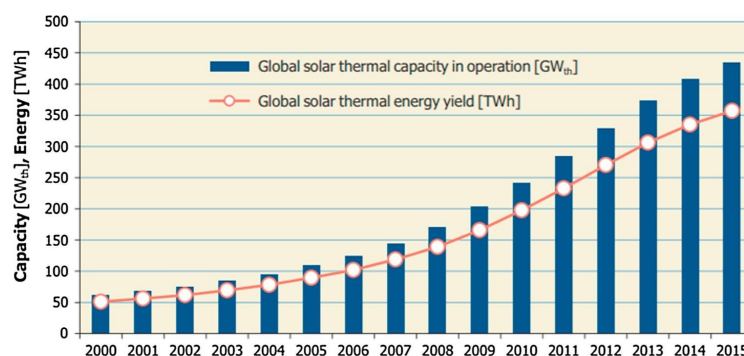


FIGURE 1.27: Global solar thermal installed capacity and energy yield (Mauthner, Weiss, and Spork-Dur, 2014).

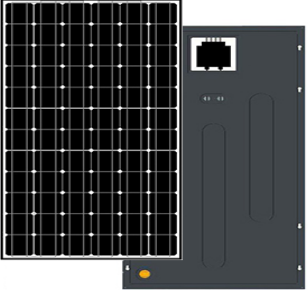
Most of the PV-T modules available in the market are given in Table 1.1 below with their specifications such as working medium, weight, solar cell type, covered/uncovered, area, electric and thermal yield per panel.

TABLE 1.1: PV-T products available in the market and their specifications.

Name of product	Specifications	Example
Solar one hybrid collector (3F Solar)	<ul style="list-style-type: none"> <li>• Uncovered flat plate with thermal insulation</li> <li>• Water-based</li> <li>• Solar cells: mono cSi</li> <li>• Collector Area: 1.60 m<sup>2</sup></li> <li>• Weight: 42 kg</li> <li>• Electricity yield: 290 Wp</li> <li>• Thermal yield: 825 Wp</li> </ul>	
Volthera PVT (Alius)	<ul style="list-style-type: none"> <li>• Uncovered flat plate without thermal insulation</li> <li>• Separate heat exchanger</li> <li>• Water/glycol-based</li> <li>• Solar cells: mono/poly cSi</li> <li>• Collector Area: 1.60 m<sup>2</sup></li> <li>• Electricity yield: 275 Wp</li> </ul>	

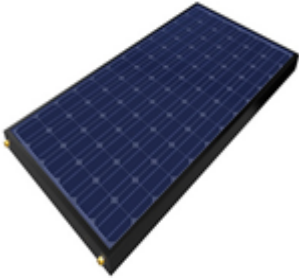
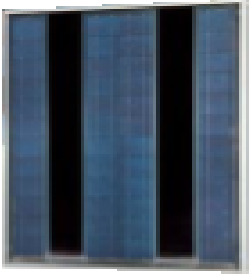
Continued on next page

Table 1.1 – Continued from previous page

Name of product	Specifications	Example
CHN210-72M-PVT (China Land)	<ul style="list-style-type: none"> <li>• Uncovered flat plate without thermal insulation</li> <li>• Water-based</li> <li>• Solar cells: mono cSi</li> <li>• Collector Area: 1.60 m<sup>2</sup></li> <li>• Weight: 25 kg</li> <li>• Heat efficiency: 45%</li> <li>• Electricity yield: 210 Wp</li> </ul>	
Multi Energy Panel (Energiedak-Solartech)	<ul style="list-style-type: none"> <li>• Uncovered flat plate with thermal insulation</li> <li>• Separate thermal absorber unit</li> <li>• Water-based (3 l per min)</li> <li>• Solar cells: mono/poly cSi</li> <li>• Collector Area: 1.60 m<sup>2</sup></li> <li>• Light weight</li> <li>• Electricity yield: 275 Wp</li> </ul>	

Continued on next page

Table 1.1 – Continued from previous page

Name of product	Specifications	Example
Volther Powertherm (Solimpeks Solar Energy Corporation)	<ul style="list-style-type: none"> <li>• Covered flat plate</li> <li>• Water-based</li> <li>• Solar cells: mono cSi</li> <li>• Collector Area: 1.47 m<sup>2</sup></li> <li>• Weight: 34.40 kg</li> <li>• Heat efficiency: 45%</li> <li>• Thermal yield: 680 Wp</li> <li>• Electrical efficiency: 12.9%</li> </ul>	
PT-U-250/193 (NO-VO by H'ORMANN)	<ul style="list-style-type: none"> <li>• Covered flat plate</li> <li>• Water-based</li> <li>• Solar cells: mono cSi</li> <li>• Collector Area: 1.1 m<sup>2</sup></li> <li>• Electric yield: 193 Wp</li> </ul>	

Continued on next page

Table 1.1 – Continued from previous page

Name of product	Specifications	Example
Twin Solar (Grammer Solar)	<ul style="list-style-type: none"> <li>• Air-based with collector area 2 m<sup>2</sup></li> <li>• Solar cells: mono/poly cSi</li> <li>• Weight: 47 kg</li> <li>• Temperature controlled</li> <li>• Electrical yield: 18 Wp</li> <li>• Up to 125 m<sup>3</sup> per hour warm fresh air into building</li> </ul>	
Z10 Solar CHP (Suncore)	<ul style="list-style-type: none"> <li>• Concentrated collector and coolant based (9 l per min)</li> <li>• Solar cells: multi-junction concentrator</li> <li>• Weight: 540 kg</li> <li>• Collector Area: 12 m<sup>2</sup></li> <li>• Azimuth range: 0-360°</li> <li>• Electrical yield: 1.5 kWp</li> <li>• Thermal yield: 6.5 kW</li> </ul>	

*Continued on next page*

Table 1.1 – Continued from previous page

Name of product	Specifications	Example
Twin Solar (SYSTOVI)	<ul style="list-style-type: none"> <li>• Air-based</li> <li>• Solar cells: mono cSi</li> <li>• Collector Area: 1.5 m<sup>2</sup></li> <li>• Weight: 20.7 kg</li> <li>• Ventilated PV module</li> <li>• Heat recovery system</li> <li>• Heat during the winter, cool air over the summer</li> <li>• Temperature controlled</li> <li>• Electrical yield: 250 Wp</li> <li>• Thermal yield: 450 W</li> </ul>	

## 1.9 Future developments

The easy availability of solar energy makes solar technology's future bright. Solar-thermal technology is growing rapidly and despite a lot of theoretical and experimental research, there is still a lot of scope for further improvements in future product development. New technological advancements in the past few years make this technology, cheaper, reliable, and more effective. The focus of the current research is to, improve PV efficiency by reducing the solar cell temperature, minimizing heat losses, and improving thermal efficiency by changing components of the panel and introducing new working fluids. Solar cell plays a vital role in PV efficiency, currently, silicon-based solar cells are the most popular and widely used with a record efficiency of 22% (Schindler et al., 2017a). The rise in temperature affects the performance of silicon-based solar cells, efficiency drops approximately 1%, with the rise of 2°C cell temperature. Another drawback of using silicon-based solar cells is most of the photon energy is wasted as heat and there is a lot of scope for a solar cell in concentrated type PV-T systems (Joshi and Dhoble, 2018).

Another material of solar cells is introduced by combining inorganic and organic materials to reduce the cost and ensure the high efficiency of solar cells. This hybrid technology also referred to as fourth-generation technology is in the development stage and these cells are less affected by the increase in temperature as compared to silicon-based cells. To dominate silicon-based technology, the new material needs to occupy more sunlight and convert energy into electricity more efficiently. Air and water are the most widely used working fluids in PV-T systems because of their availability but these fluids have a few drawbacks such as there is low heat transfer in air-based systems and corrosion and freezing issues in water-based systems. There is a need to explore more about phase change materials and nano-fluids because of their high thermal conductivity and heat capacity properties and also these materials have the ability to operate in different temperature conditions. A comprehensive overview is given by Mofijur et al. (2019) about PCM benefits, usage, and storage. Insulation heat loss to surroundings and space are the biggest problems in PV-T thermal storage and advancement in it will help in the growth of PV-T systems.

One of the most affordable and efficient ways of transferring heat without temperature drop is through heat pipes, which use principles of both phase transition and thermal conductivity, and have a very high thermal conductivity (Gang et al., 2011). A heat pipe is a very high heat transfer element and transfers heat via the working fluid phase change within a tube. This can be placed at the backside of the PV panel to extract heat from the PV module, which plays an essential role to enhance the efficiency of the collector (Cui et al., 2022). Further, there are fewer freezing issues and corrosion is eliminated in heat pipe-based PV-T systems. Most of the experimental work presented is for a short duration of time and there is a need to conduct experiments for a period of 365 days.

Glass filters and liquid filters are other promising solutions to enhance performance. An absorber is a vital component in designing a PV-T system and oils especially recycled used engine oil can be used as an absorber material because of its thermo-physical properties. This will not only enhance the performance of the PV-Ts but reduce environmental pollution as well. Most PV-T designs are with a cooling fluid flowing in an open-loop or a closed-loop, but using a hybrid cooling system of air and water will improve the overall efficiency of the collector. The software tools are needed but expertise is needed to enable the designer to achieve a good design and it is true for PV-T systems where electrical and thermal skills are required.



## Chapter 2

# Modeling of a PV-T collector

The first work on PV-T systems was presented by Florschuetz (1979) where the main concept of the PV-T collector was presented by assuming a linear correlation between PV cell temperature and its efficiency. Since then, various theoretical and experimental investigations have been presented. Slimani et al. (2017) presented thermal-electrical models in detail where the performance of air-based PV-T collectors is evaluated for the Algiers climatic conditions. Four different configurations were studied including a simple PV module. The other three configurations include; a basic PV-T collector, a glazed PV-T collector and a dual-channel PV-T collector. The thermal and electrical performance of an air-based PV-T collector was examined theoretically by Hegazy (2000) based on the energy balance concept. A comparative study was done by Malvi, Dixon-Hardy, and Crook (2011), where a 1-D energy balance model is presented incorporating PCM. Using the 1-D energy balance model, the performance of the panel is evaluated. The model is divided into five layers; glass cover, PV cell layer, copper plate, PCM layer and, insulated frame. The thermal performance of solar installations has been studied by Cristofari et al. (2002) where technical characteristics are optimized, and the influence of various parameters is presented theoretically. A number of different configurations and multiple thermal models have been reported with the influence of various parameters on the performance of the PV-T systems.

Chaabane, Mhiri, and Bournot (2014) proposed two different numerical models and study the effect of PCM on thermal performance by integrating PCM directly in the collector. Based on the control volume finite difference approach, a dynamic model with water as a working fluid is developed by Chow (2003) and the energy balance matrix is obtained. The collector is divided into various sections and each section consists of a single water tube. The PV cell layer is in direct contact with the water tube. There is direct heat transfer from the PV plate to the tube. Zondag et al. (2002) presented four different numerical models with three steady-state models and one dynamical model. The model was built on a single pipe winding (serpentine shape) to measure the performance of the system. The model is full time-dependent quasi 3D and includes second-order differentiations. The absorber plate and the PV laminate are split up in two directions; parallel to the flow and perpendicular to the flow whereas the top layer is separated; parallel to the flow.

In this chapter, the modeling of a PV-T collector is presented using air and water as working fluids. Further, for air as a working fluid, two separate models are presented. In an air-based model-I, air flows below the PV module whereas air runs above the PV module in air-based model-II. The fundamental equations are determined for the thermal part using a bond graph approach which is a generic and general tool to represent thermal transfers. It is a graphical sketch of a physical system, represented by symbols and lines. It consists of elements of resistance, compliance, and inertance which are interconnected by junctions, bonds, and flow of energy or

power. Effort  $e$  and flow  $f$  are two power conjugated variables in the bond graph and in physical domains the way of selection of these two variables is different. There can be multiple domains and this system contains two subsystems that are;

- thermal subsystem
- hydraulic subsystem.

In a thermal subsystem, the effort variable is represented by temperature  $T$  whereas the flow variable as heat flow  $\dot{Q}$ , solar flow  $G$  and enthalpy  $\dot{H}$ . In a hydraulic subsystem, the pressure  $P$  is an effort variable and mass flow  $\dot{m}$  is the flow variable. Resistance  $R$ , compliance  $C$ , and inertance  $I$  are classified as a single port and contain no source of power, convert the supplied energy into stored or dissipated energy, and are classified as passive elements. Sources are the active elements that provide power to the system, they are single port and can be either flow source  $S_f$  or effort source  $S_e$ . Junctions are multi-port elements, that differ on the basis of how effort and flow are carried across. There exists two types of junctions, the 1-junction, and the 0-junction.

- In 0-Junction, all connected bonds constrained to have the same efforts whereas flows sum up to zero.
- 1-junction has equality of flows and the algebraic sum of efforts is zero.

A bond graph can include multiple domains, when a fluid is flowing and heat transfer is involved, thermal and hydraulic energies are combined and are represented by a circle around a bond as shown in a bond graph presented in Figure 2.6.

For 0-Junction, effort equation (Borutzky, 2009) is given as:

$$e_{i1} = \dots = e_{im} = e_{o1} = \dots = e_{on} \quad (2.1)$$

and has flow equation

$$\sum_{k=1}^m f_{ik} = \sum_{k=1}^n f_{ok} \quad (2.2)$$

For 1-Junction, flow equation is given as:

$$f_{i1} = \dots = f_{im} = f_{o1} = \dots = f_{on} \quad (2.3)$$

and has effort equation

$$\sum_{k=1}^m e_{ik} = \sum_{k=1}^n e_{ok} \quad (2.4)$$

Each layer is broken up into two parts: one is dissipated by conduction and the other is stored by the layer. 0-junction relates to the compliance element whereas 1-junction relates to the resistance element.

The relationship between generalized effort and generalized flow corresponding to resistance and compliance elements are written as (2.5) and (2.6):

$$f(t) = \frac{1}{R} e(t), \quad (2.5)$$

where

$$e(t) = \frac{1}{C} \int f(t) dt \quad (2.6)$$

When two objects with two different temperatures are in contact with each other, heat energy pass between them. In hot materials, molecules move faster and hit the cold object molecules which are in contact with the hot object. Heat transfer coefficient  $h$  is the inverse of thermal heat flow and using (2.5) thermal heat flow for the resistance element between two layers a and b is given by:

$$\dot{Q} = \frac{1}{R}(T_a - T_b)A \quad (2.7)$$

Using (2.6), temperature  $T$  of each layer with thermal heat capacity  $C$  and thermal heat flow  $\dot{Q}$  accumulated by each layer can be written as:

$$T = \frac{1}{C} \int \dot{Q} dt \quad (2.8)$$

Thermal heat capacity with density  $\rho$ , volume  $V$  and specific heat capacity  $C_l$  for each layer is given by:

$$C = \rho V C_l \quad (2.9)$$

When the solar radiation hits the collector, fraction of it is reflected by the surface, part of it is transmitted and the remaining part is absorbed by the surface. At a rate of  $I_{sun}$  in Watts, solar radiation energy absorbed by the glass cover is:

$$G_g = A_{mod} \alpha_g I_{sun} \quad (2.10)$$

and the energy absorbed by the PV cell layer and is:

$$G_c = A_{mod} \tau_g \alpha_c I_{sun} \beta, \quad (2.11)$$

where  $\alpha_g$  and  $\alpha_c$  are absorptance of glass cover and PV cell whereas  $\tau_g$  is the transmittance of the glass cover.

To take the atmosphere into account, sky temperature  $T_s$  (Chaabane, Mhiri, and Bournot, 2014) is given by Swinbank (1963) associates sky temperature with local air temperature and requires no knowledge of the dew point temperature.

$$T_s = 0.0552 T_{am}^{1.5} \quad (2.12)$$

For an overcast day, sky temperature is equivalent to ambient temperature. The heat convection takes place at the top and bottom surfaces of the collector. Convective heat coefficient strongly depends on the wind speed  $V_w$  and is defined by the following equations (Carvajal and Araya, 2012).

$$h_{v,am} = \begin{cases} 5.7 + 3.8V_w, & \text{for } V_w < 5 \text{ ms}^{-1} \\ 6.47 + V_w^{0.78}, & \text{for } V_w > 5 \text{ ms}^{-1} \end{cases} \quad (2.13)$$

$R_{r,gs}$  is the radiation heat flow between sky and glass cover. Where  $\sigma$  is Stefan Boltzmann constant and radiation heat transfer coefficient (Amori and Al-Najjar, 2012) between two surfaces (glass – sky) is;

$$h_{r,gs} = \sigma \epsilon_g \frac{(T_g + T_s)(T_g^2 + T_s^2)(T_g - T_s)}{T_g - T_{am}} \quad (2.14)$$

TABLE 2.1: Thermal parameters of the air-based and water-based collectors.

Parameter	Value
Solar radiation coefficient ( $\delta$ )	0.052
Transmissivity of glass ( $\tau_g$ )	0.84
Absorbtivity of glass ( $\alpha_g$ )	0.10
Absorbtivity of cell ( $\alpha_c$ )	0.90
Thermal expansion coefficient ( $\beta_p$ )	0.0045
Absorbtivity of tedlar ( $\alpha_t$ )	0.80
Packing factor ( $\beta$ )	0.88
Thermal conductivity of air ( $\lambda_f$ )	0.026 Wm <sup>-1</sup> K <sup>-1</sup>
Thermal conductivity of water ( $\lambda_w$ )	0.60 Wm <sup>-1</sup> K <sup>-1</sup>
Thermal conductivity of glass ( $\lambda_g$ )	1.1 Wm <sup>-1</sup> K <sup>-1</sup>
Thermal conductivity of cell ( $\lambda_c$ )	148 Wm <sup>-1</sup> K <sup>-1</sup>
Thermal conductivity of tedlar ( $\lambda_t$ )	0.2 Wm <sup>-1</sup> K <sup>-1</sup>
Thermal conductivity of absorber ( $\lambda_r$ )	240 Wm <sup>-1</sup> K <sup>-1</sup>
Thermal conductivity of insulator ( $\lambda_i$ )	0.034 Wm <sup>-1</sup> K <sup>-1</sup>
Module area - for air ( $A_{mod}$ )	1.28*0.32 m <sup>2</sup>
Air channel area ( $A_{hz}$ )	1.28*0.30 m <sup>2</sup>
Module area - for water ( $A_{mod}$ )	1.65*1 m <sup>2</sup>
Width of air channel ( $W$ )	0.30 m

Radiative heat transfer between two parallel elements  $a$  and  $b$  is;

$$h_{r,ab} = \sigma \left[ \frac{(T_a + T_b)(T_a^2 + T_b^2)}{\frac{1}{\epsilon_a} + \frac{1}{\epsilon_b} - 1} \right] \quad (2.15)$$

$R_{c,ab}$  is the conduction heat flow and conductive heat transfer coefficient between two parallel layers  $a$  and  $b$  (Slimani et al., 2017) is given as;

$$h_{c,ab} = \frac{1}{\frac{l_a}{\lambda_a} + \frac{l_b}{\lambda_b}} \quad (2.16)$$

Electric power  $E_p$  generated by photovoltaic module (Florschuetz, 1979) can be written as:

$$E_p = I_{sun} A_{mod} \eta_c = I_{sun} A_{mod} \eta_{ref} \left[ 1 - \beta_p (T_c - T_{c,ref}) + \delta \ln \left( \frac{I_{sun}}{I_{sun,ref}} \right) \right] \quad (2.17)$$

A bond graph approach is used to model the thermal part of air-based and water-based PV-T collectors. The performance of a PV-T collector is characterized by its fluid temperature rise, thermal and electrical efficiencies, and the net available energy. The focus is to present a nonlinear dynamic models which give a realistic and reasonable performance of the system. Glass cover is the top layer of the PV-T collector and the purpose of adding the glass cover is to protect the PV cell layer and reduce the heat loss to ambient. This will eventually improve the thermal efficiency of the system.

Few assumptions have been considered for the air-based and water-based thermal models such as:

- heat transfer between the ground and the panel is over sighted.
- pressure losses are neglected.
- temperature is assumed to be homogeneous for each layer.
- radiation heat exchange at the bottom and edge losses are neglected due to the fact that the temperature difference at the bottom is small.

## 2.1 Air-based PV-T model-I

Air-based PV-T collectors are very common and are mostly used for space heating and drying purposes. In these type of collectors, cold air is injected from one side and heat or warm air is collected along with the electrical gain on the other end of the panel as illustrated in Figure 1.2. In this model, the fluid flows below the PV module, and Figure 2.1 shows the division of panel in various layers;

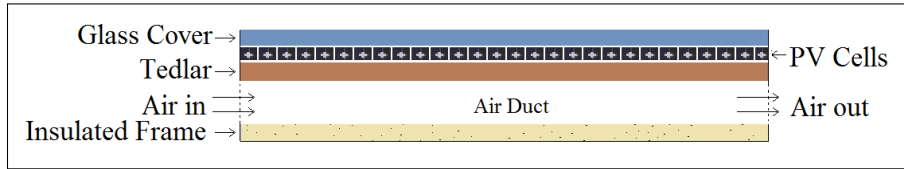


FIGURE 2.1: Cross-sectional view of an air-based PV-T collector with fluid flowing below PV module.

- a glass cover
- a PV solar cells layer
- tedlar layer (thermoplastic floor)
- an air channel
- thermally insulated frame.

### 2.1.1 Bond graph modeling

Each of the layers can be interpreted in the following five equations using the bond graph model presented in Figure 2.2.

for glass cover ( $g$ ):

$$M_g C_g \frac{dT_g}{dt} = A_{mod} [\alpha_g I_{sun} - h_{r,gs}(T_g - T_s) - h_{v,am}(T_g - T_{am}) - h_{c,gc}(T_g - T_c)], \quad (2.18)$$

where module area is written as;

$$A_{mod} = xy \quad (2.19)$$

for PV cell layer ( $c$ ):

$$M_c C_c \frac{dT_c}{dt} = A_{mod} [\tau_g \alpha_c I_{sun} \beta + h_{c,gc}(T_g - T_c) - h_{c,ct}(T_c - T_t)] - E_p \quad (2.20)$$

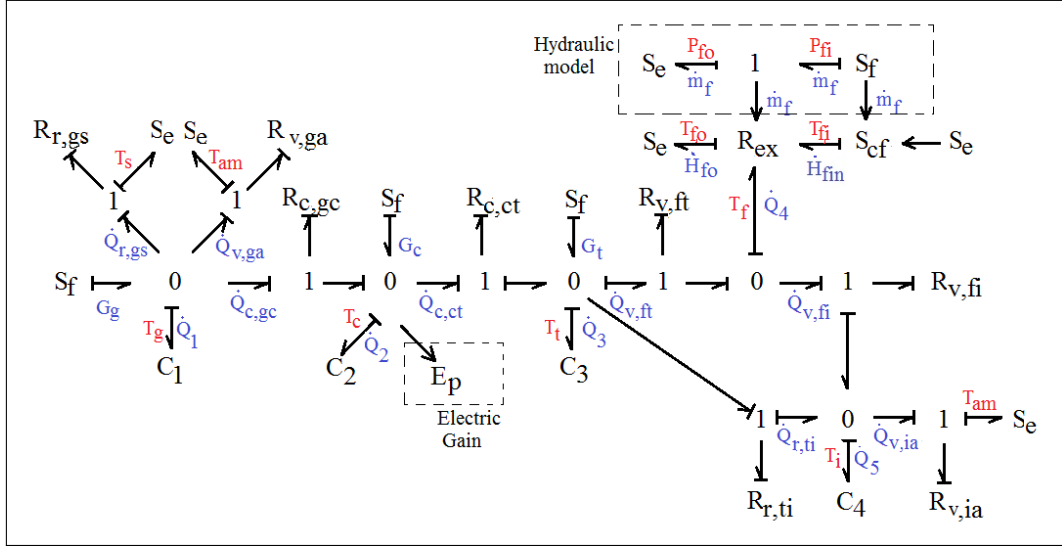


FIGURE 2.2: Bond graph model-I of air-based PV-T collector.

for tedlar layer ( $t$ ):

$$M_t C_t \frac{dT_t}{dt} = A_{mod} [\tau_g \alpha_t I_{sun} (1 - \beta) + h_{c,ct} (T_c - T_t) + h_{v,ft} \zeta (T_f - T_t) - h_{r,ti} \zeta (T_t - T_i)], \quad (2.21)$$

where

$$\zeta = \frac{A_{hz}}{A_{mod}}$$

$R_{ex}$  is the heat exchange between tedlar, fluid and thermal insulator. The useful energy gain is (Oueslati, Mabrouk, and Mami, 2011);

$$\dot{H}_{fo} - \dot{H}_{fi} = \dot{m}_f C_f (T_{f,o} - T_{f,i}) \quad (2.22)$$

for air flowing in air channel ( $f$ ):

$$\dot{m}_f C_f (T_{f,o} - T_{f,i}) = W dx [h_{v,tf} (T_t - T_f) + h_{v,fi} (T_i - T_f)] \quad (2.23)$$

with

$$T_f = \frac{T_{f,i} + T_{f,o}}{2}, \quad (2.24)$$

where  $W$  is width of air channel and using  $x = 0$ ,  $T_{f,o} = T_{f,i}$ .

$R_{v,tf}$  and  $R_{v,fi}$  are the convection heat flows and convective heat transfer coefficients between two elements (air – tedlar and air – insulator) (Duffie and Beckman, 2013) are;

$$h_{v,tf} = h_{v,fi} = N_u \frac{\lambda_f}{d_{hy}} \quad (2.25)$$

where  $N_u$  is the Nusselt number and is given as;

$$N_u = 0.023 R_e^{0.8} P_r^{0.4} \quad (2.26)$$

The Reynold number  $R_e$  and Prandtl number  $P_r$  are given as;

$$R_e = \frac{\dot{m}_f d_{hy}}{A_f \mu_f} = \frac{\rho_f d_{hy}}{\mu_f} V_f \quad (2.27)$$

and

$$P_r = \frac{\mu_f}{\lambda_f} C_f \quad (2.28)$$

for insulator ( $i$ ):

$$M_i C_i \frac{dT_i}{dt} = A_{hz} [h_{r,ti}(T_t - T_i) + h_{v,fi}(T_f - T_i) - h_{v,am}(T_i - T_{am})], \quad (2.29)$$

where  $A_{hz}$  is air channel area.

The above five equations for each layer of the PV-T collector are obtained using the bond graph approach and are compatible with the equations obtained by (Slimani et al., 2017). However, here, a bond graph technique is used to model the PV-T instead of the energy conservation principle used in (Slimani et al., 2017). Hopefully, both approaches are consistent.

**Remark 1:** Additionally, an extra glass cover with an enclosed air space can be added over the PV module to add the glazing. The glazed PV-T model will have an extra equation for the top glass cover. The heat transfer occurs by convection in the closed air space whereas heat transfer occurs by radiation between the top and bottom glass components. This extra glass cover increases the temperature of all the layers of the PV-T collector which will result in low PV efficiency but enhanced thermal efficiency.

for top glass cover ( $tg$ ):

$$M_{tg} C_{tg} \frac{dT_{tg}}{dt} = A_{mod} [\alpha_g I_{sun} - h_{r,tgs}(T_{tg} - T_s) - h_{v,am}(T_{tg} - T_{am}) - h_{r,gtg}(T_{tg} - T_g)], \quad (2.30)$$

where the solar radiation absorbed by the bottom glass cover becomes  $A_{mod} \alpha_g^2 I_{sun}$  and the energy absorbed by the cell layer becomes  $A_{mod} \tau_g^2 \alpha_c I_{sun} \beta$ .

**Remark 2:** Moreover, an absorber can be included just above the thermal insulation and below an air channel to see how it affects the performance of the collector. In this scenario, air flows between tedlar layer and absorber sheet. Here, the convective heat transfer occurs between the elements (air-tedlar and air-absorber) and conduction occurs between the absorber sheet and insulation.

for absorber ( $r$ ):

$$M_r C_r \frac{dT_r}{dt} = A_{mod} [-h_{r,tr}(T_r - T_t) - h_{c,ri}(T_r - T_i) - h_{v,fr}(T_r - T_f)] \quad (2.31)$$

It would be a good choice to add PCM type absorber instead of aluminium or copper. In this way, the heat will be stored for long time.

## 2.1.2 Identification

This part concerns system identification which refers to the problem of estimating an unknown system and the main purpose is to construct a model that approximates the behavior of a system using input and output data. In automated control, the dynamic system model is a mathematical description of the relationship between inputs and outputs of the system. In this section, identification of the thermal part of the PV-T system is performed, with a mass flow rate  $\dot{m}_f$  considered as the input and outlet temperature of the duct  $T_{f,o}$  taken as output. To this end, input-output data is required from real measurements or from simulation. The solar radiation input is an uncontrollable variable because it depends on the meteorological conditions and might vary during the day. Herein, we consider the latter to generate data for

two different values of mass flow rate, each with different solar radiation: 250, 500, and 750  $\text{Wm}^{-2}$ . Using a system identification toolbox, different order of transfer functions were tested in order to find the one which fits the best. It was found that a simple order 1 gives the closest response to our system. Using six sets of input-output data corresponding to 6 operating points, we obtained six different first-order transfer functions with time constants (resp. gain) ranging 229, 236, 250, 334, 336, 339 seconds (resp. -2.29, -7.78, -11.75, -10.68, -21.52, -32.2) with an average of  $T_{avg} = 278$  s (resp.  $k_{avg} = -13.06$ ). Therefore, the average transfer function denoted  $G_{avg}$  can be written as;

$$G_{avg} = \frac{T_{f,o}}{\dot{m}_f} = \frac{k_{avg}}{1 + sT_{avg}} = -\frac{0.047}{s + 0.0036} \quad (2.32)$$

This simple model gives a satisfactory approximation of the behavior of the non-linear system considering the numerical values of the parameters. However, the model is just valid on a few operating points. It is good enough for the purpose of control.

## 2.2 Air-based PV-T model-II

In this section, a new PV-T thermal model with air flowing above the PV module is presented as shown in Figure 2.3. The cold air is injected from one end and warm air is collected other end of the panel as illustrated in Figure 1.2. A PV-T collector consists of;

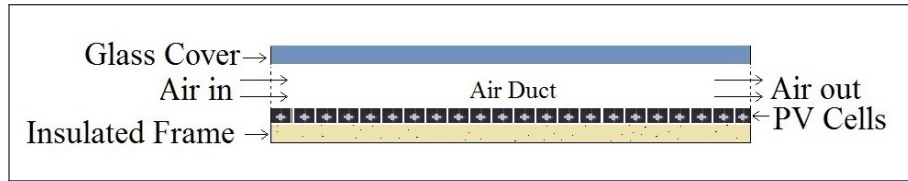


FIGURE 2.3: Cross-sectional view of an air-based PV-T collector with fluid flowing above PV module.

- a glass cover that protects the cell layer and reduce heat losses to the ambient
- an air channel through which the fluid runs
- a layer of PV cells
- an insulator to prevent heat loss.

### 2.2.1 Bond graph modeling

The governing equations using Figure 2.4 for each of the components e.g. glass cover, cell layer, insulation and for air channel using (2.7) and (2.8) can be written as: for glass cover (g):

$$M_g C_g \frac{dT_g}{dt} = A_{mod} [\alpha_g I_{sun} + h_{r,gs}(T_s - T_g) + h_{v,am}(T_{am} - T_g) - h_{v,gf}(T_g - T_f) - h_{r,gc}(T_g - T_c)] \quad (2.33)$$

The heat exchange between components glass, air channel, and cell layer is  $R_{ex}$  and usable energy gain that warms an air channel is given by (2.22).

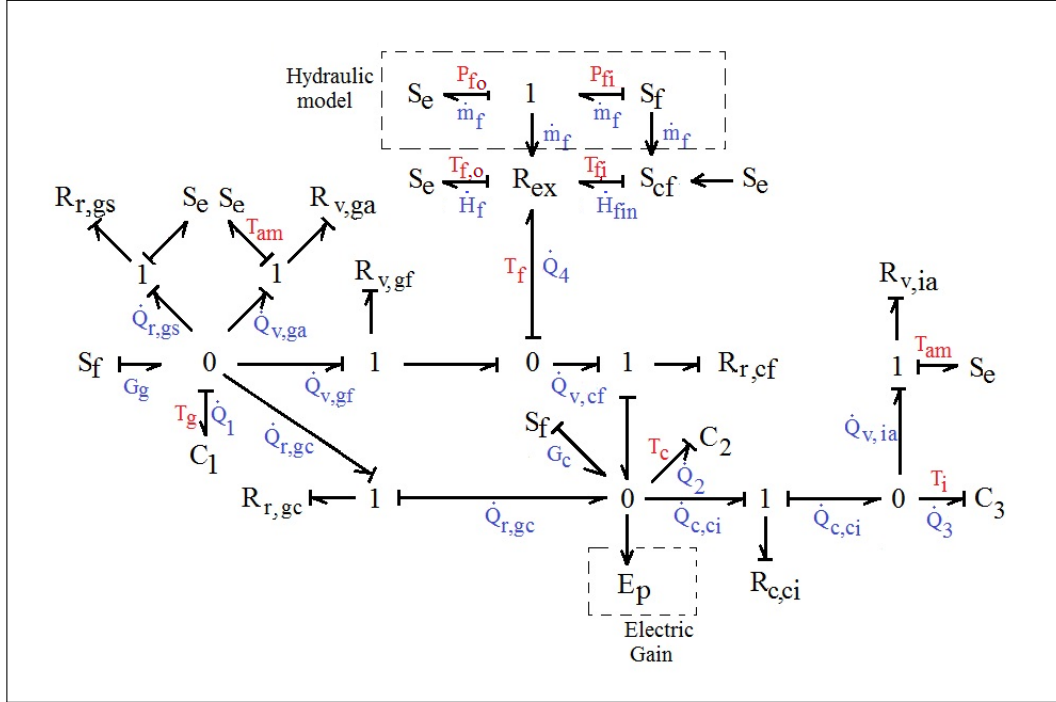


FIGURE 2.4: Bond graph model-II of air-based PV-T collector.

for air-flowing in air channel ( $f$ ):

$$\dot{m}_f C_f (T_{f,o} - T_{f,i}) = W dx [h_{v,gf} (T_g - T_f) + h_{v,fc} (T_c - T_f)], \quad (2.34)$$

where  $W$  is width of air channel and using  $x = 0$ ,  $T_{f,o} = T_{f,i}$ .  $T_{f,i}$  is the inlet temperature of the air channel whereas  $T_{f,o}$  is the output temperature and the mean temperature  $T_f$  is calculated using (2.24).

$R_{v,gf}$  and  $R_{v,fc}$  are the convection heat flows and convective heat transfer coefficient is calculated using following relation (Duffie and Beckman, 2013);

$$h_{v,gf} = h_{v,fc} = \frac{N_u \lambda_f}{d_{hy}}, \quad (2.35)$$

where  $N_u$  is the Nusselt number and can be found using (2.26).

for PV cell layer ( $c$ ):

$$M_c C_c \frac{dT_c}{dt} = A_{mod} [\tau_g \alpha_c I_{sun} \beta - h_{v,cf} (T_c - T_f) - h_{r,gc} (T_c - T_g) - h_{c,ci} (T_c - T_i)] - E_p \quad (2.36)$$

for insulator ( $i$ ):

$$M_i C_i \frac{dT_i}{dt} = A_{hz} [h_{c,ci} (T_c - T_i) - h_{v,am} (T_i - T_{am})] \quad (2.37)$$

The radiation heat exchange at the base is disregarded, considering the minimal temperature difference at the base and the surrounding. The flow channel parameters are significant design parameters affecting the performance of the PV-T collector.

Thermal efficiency is defined as the ratio of useful energy gain to the incident solar energy over the same period of time. Applying useful energy gain (2.22), the

thermal performance of the PV-T collector is;

$$\eta_{th,f} = \frac{\dot{m}_f C_f (T_{f,o} - T_{f,i})}{A_{mod} I_{sun}} \quad (2.38)$$

PV efficiency of the PV-T panel is defined as ratio of electrical gain to the total incident energy and written as;

$$\eta_{ele} = \frac{E_p}{A_{mod} I_{sun}} \quad (2.39)$$

The overall efficiency  $\eta_{ov,f}$  is the sum of thermal efficiency (2.38) and electrical efficiency (2.39) of a PV-T collector and can be calculated as follows:

$$\eta_{ov,f} = \eta_{ele} + \eta_{th,f}. \quad (2.40)$$

## 2.2.2 Linearization and state-space representation

The state space description is useful for simulation of the system dynamic behavior. An approximation of a multi-dimensional nonlinear function by a multidimensional tangent in a point (operating point) is linearization. The linearization procedure requires the computation of the Jacobian matrices and the dynamic model is described by

$$\dot{x} = Ax + Bu + Ev \quad (2.41)$$

where matrices  $A$ ,  $B$  and  $E$  are obtained from the computation of the Jacobians

$$A = \begin{bmatrix} \frac{\partial f_1}{\partial x_1} & \frac{\partial f_1}{\partial x_2} & \frac{\partial f_1}{\partial x_3} \\ \frac{\partial f_2}{\partial x_1} & \frac{\partial f_2}{\partial x_2} & \frac{\partial f_2}{\partial x_3} \\ \frac{\partial f_3}{\partial x_1} & \frac{\partial f_3}{\partial x_2} & \frac{\partial f_3}{\partial x_3} \end{bmatrix} \Big|_{(x^*, u^*)},$$

$$B = \begin{bmatrix} \frac{\partial f_1}{\partial u} & \frac{\partial f_2}{\partial u} & \frac{\partial f_3}{\partial u} \end{bmatrix}^T \Big|_{(x^*, u^*)},$$

similarly,

$$E = \begin{bmatrix} \frac{\partial f_1}{\partial v_1} & \frac{\partial f_1}{\partial v_2} & \frac{\partial f_1}{\partial v_3} \\ \frac{\partial f_2}{\partial v_1} & \frac{\partial f_2}{\partial v_2} & \frac{\partial f_2}{\partial v_3} \\ \frac{\partial f_3}{\partial v_1} & \frac{\partial f_3}{\partial v_2} & \frac{\partial f_3}{\partial v_3} \end{bmatrix} \Big|_{(x^*, u^*)}.$$

If the aim is to find a linearized model that approximates the nonlinear model at the neighborhood of the operating point. The nonlinear model can be written as;

$$\begin{cases} \dot{X} = f(X, U, v) \\ Y = g(X, U) \end{cases}, \quad (2.42)$$

where the state  $X$  contains the temperatures of each layer as state variables;

$$X = [x_1 \ x_2 \ x_3]^T = [T_g \ T_c \ T_i]^T, \quad (2.43)$$

whereas controlled input  $U$  is mass flow rate  $\dot{m}_f$  and  $v$  are the perturbations (e.g.  $T_{am}$ ,  $I_{sun}$  and  $V_w$ ). Lets suppose, consider an operating point defined by the subscript 'eq', then if we denote by  $(X_{eq}$  and  $U_{eq})$  the equilibrium point for the state and the input, then for small variations (i.e  $x = X - X_{eq}$ ,  $u = U - U_{eq}$ , and  $y = Y - Y_{eq}$ ), we obtain

the following linearized state-space representation described as:

$$\begin{cases} \dot{x} = Ax + Bu \\ y = Cx + Du \end{cases} \quad (2.44)$$

where

$$A = \left. \frac{\partial f}{\partial X} \right|_{X_{eq}, U_{eq}}, \quad B = \left. \frac{\partial f}{\partial U} \right|_{X_{eq}, U_{eq}}, \quad C = \left. \frac{\partial g}{\partial X} \right|_{X_{eq}, U_{eq}} \quad \text{and} \quad D = \left. \frac{\partial g}{\partial U} \right|_{X_{eq}, U_{eq}}$$

The perturbations are not included here and are taken as constants. The output of the system is the outlet temperature of the fluid  $T_{f,o}$  from the air channel of the PV-T collector.

## 2.3 Water-based PV-T model

In this section, a bond graph approach is used to model the thermal part of a water-based PV-T collector by incorporating a tedlar layer and parallel tubes. The performance of a PV-T collector is characterized by its water temperature rise, thermal and electrical efficiencies, and the net available energy. The focus is to present a non-linear dynamic model of a water-based PV-T collector which gives a realistic and reasonable performance of the system. In a PV-T panel configuration, cold water is supplied from one end of the panel, and warm water is collected along with the electrical gain from the other end of the panel as shown in Figure 1.2. Figure 1.5 shows the thermal model of the panel, composed of several layers;

- a glass layer
- solar cells layer
- a tedlar layer under PV cells
- an absorber
- a metallic tube with bond (see Figure 2.5a)
- a water channel
- a thermally insulated frame to reduce heat losses.

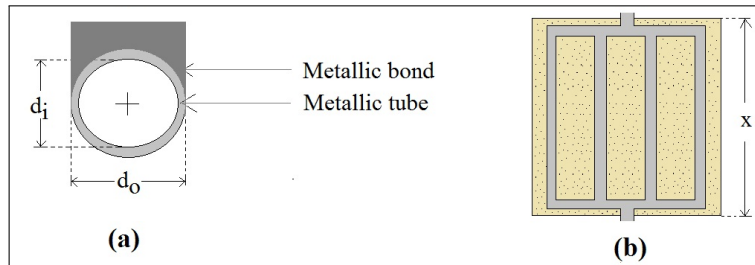


FIGURE 2.5: (a) Metallic tube and bond. (b) PV-T collector flow dynamics.

There are four parallel water tubes available through which fluid flows and these tubes are fitted and pressed with the bond to the insulator layer as shown in Figure 1.5. Water is inserted from a single point, then it is distributed equally to all the tubes and warm water is collected from the other end of the panel as shown in Figure 2.5b.

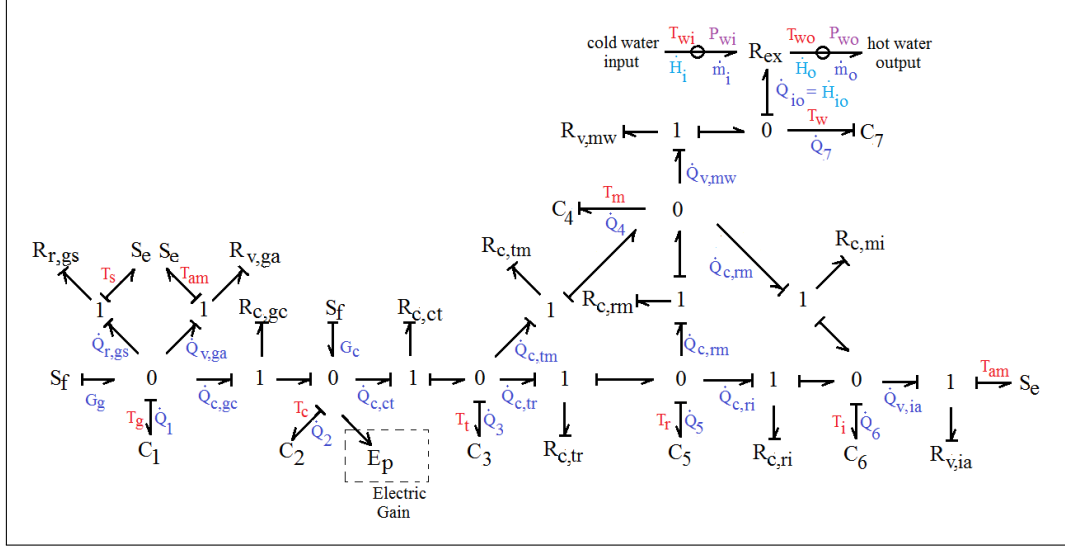


FIGURE 2.6: Bond graph model of water-based PV-T collector.

### 2.3.1 Bond graph modeling

The governing equations of the thermal model were determined using a bond graph technique. The equations for each layers using (2.7) and (2.8) are respectively given by:

for glass cover (g):

$$M_g C_g \frac{dT_g}{dt} = A_{mod} [\alpha_g I_{sun} - h_{r,gs}(T_g - T_s) - h_{v,am}(T_g - T_{am}) - h_{c,gc}(T_g - T_c)] \quad (2.45)$$

for PV cell layer (c):

$$M_c C_c \frac{dT_c}{dt} = A_{mod} [\tau_g \alpha_c I_{sun} \beta + h_{c,gc}(T_g - T_c) - h_{c,ct}(T_c - T_t)] - E_p \quad (2.46)$$

for tedlar layer (t):

$$M_t C_t \frac{dT_t}{dt} = A_{mod} h_{c,ct}(T_c - T_t) - A_{tm} h_{c,tm}(T_t - T_m) - A_{tr} h_{c,tr}(T_t - T_r) \quad (2.47)$$

for absorber layer (r):

$$M_r C_r \frac{dT_r}{dt} = A_{tr} h_{c,tr}(T_t - T_r) - A_{rm} h_{c,rm}(T_r - T_m) - A_{ri} h_{c,ri}(T_r - T_i) \quad (2.48)$$

for metallic tubes (m):

$$M_m C_m \frac{dT_m}{dt} = A_{tm} h_{c,tm}(T_t - T_m) + A_{rm} h_{c,rm}(T_r - T_m) - A_{mi} h_{c,mi}(T_m - T_i) - A_{mw} h_{v,mw}(T_m - T_w) \quad (2.49)$$

The inside area of the tube  $A_w$  can be written as:

$$A_w = \pi d_i x \quad (2.50)$$

and the area of the bond  $A_{mo}$  with width of bond  $w_{mo}$  is found using;

$$A_{mo} = w_{mo}x \quad (2.51)$$

In the heat transfer processes, convective heat coefficients add inversely in series and the overall heat transfer coefficient with contact area, and with a bond thickness  $l_{mo}$  and thermal conductivity  $\lambda_{mo}$  is:

$$\frac{1}{h_{v,wm}A_{wm}} = \frac{1}{h_w A_w} + \frac{l_{mo}}{\lambda_{mo} A_{mo}}, \quad (2.52)$$

where heat transfer coefficient for fully developed laminar flow can be written as  $h_w$  (Chow, 2003).

$$h_w = \frac{4.364\lambda_w}{d_i} \quad (2.53)$$

There is a change in temperature and in enthalpy in the water tube during heat exchange and the energy gain (Bergene and Løvvik, 1995) can be written as:

$$\dot{H}_{oi} = \dot{H}_o - \dot{H}_i = \dot{m}_w C_w (T_{wo} - T_{wi}) \quad (2.54)$$

for water flowing in the tubes ( $w$ ):

$$M_w C_w \frac{dT_w}{dt} = A_{mw} h_{v,mw} (T_m - T_w) + \dot{m}_w C_w (T_{wi} - T_{wo}) \quad (2.55)$$

$T_{wi}$  is the inlet temperature to the channel whereas  $T_{wo}$  is the output temperature of the water channel and the mean temperature  $T_w$  is given as:

$$T_w = \frac{T_{wi} + T_{wo}}{2} \quad (2.56)$$

for insulator ( $i$ ):

$$M_i C_i \frac{dT_i}{dt} = A_{mi} h_{c,mi} (T_m - T_i) + A_{ri} h_{c,ri} (T_r - T_i) - A_{mod} h_{v,iam} (T_i - T_{am}) \quad (2.57)$$

$R_{v,iam}$  is the convective heat flow and convective heat transfer coefficient between insulator and surrounding is given as;

$$\frac{1}{h_{v,iam}} = \frac{1}{h_{v,am}} + \frac{l_i}{2\lambda_i} \quad (2.58)$$

Applying useful energy gain (2.54), the thermal performance of PV-T collector (M'Sirdi et al., 2018) is;

$$\eta_{th,w} = \frac{\dot{m}_w C_w (T_{wo} - T_{wi})}{A_{mod} I_{sun}} \quad (2.59)$$

Using (2.39), the overall efficiency is calculated as follows:

$$\eta_{ov,w} = \eta_{ele} + \eta_{th,w} \quad (2.60)$$

In water-based PV-T systems, most of the heat is extracted from the PV module as compared to air-based PV-T systems. This is because, the air has low heat transfer and as a result, water-based systems have better thermal and electrical efficiency.

### 2.3.2 State-space representation

The radiation heat transfer coefficient between the glass layer and sky  $h_{r,gs}$  (2.14) contains the states and since the term does not vary much so we consider it as a constant by taking the mean of all the values. The water-based thermal model then can be expressed in the state-space form:

$$\begin{cases} \dot{x} = Ax + B(x)u + Gv \\ y = Cx + Dv \end{cases}, \quad (2.61)$$

where the state  $x$  contains state variables and are defined as;

$$x = [T_g \ T_c \ T_t \ T_r \ T_m \ T_w \ T_i]^T$$

The output  $y$  is the outlet water temperature  $T_{wo}$ , mass-flow rate  $\dot{m}_w$  is defined as controlled input  $u$ ,  $v$  contains disturbances and can be written as:

$$v = [T_{am} \ I_{sun} \ T_{wi}]^T$$

It is assumed that the components of  $v$  are known.

The state matrix  $A$  is defined as follows:

$$A = \begin{bmatrix} a_{11} & a_3 & 0 & 0 & 0 & 0 & 0 \\ b_1 & a_{22} & b_4 & 0 & 0 & 0 & 0 \\ 0 & c_1 & a_{33} & c_2 & c_3 & 0 & 0 \\ 0 & 0 & d_1 & a_{44} & d_2 & 0 & d_3 \\ 0 & 0 & e_1 & e_2 & a_{55} & e_3 & e_4 \\ 0 & 0 & 0 & 0 & f_1 & -f_1 & 0 \\ 0 & 0 & 0 & g_1 & g_2 & 0 & a_{77} \end{bmatrix},$$

$$B(x) = [0 \ 0 \ 0 \ 0 \ 0 \ -f_2(T_w - T_{wi}) \ 0]^T$$

$$G = \begin{bmatrix} k_{11} & a_5 & 0 \\ 0 & b_5 & 0 \\ 0 & 0 & 0 \\ 0 & 0 & 0 \\ 0 & 0 & 0 \\ 0 & 0 & 0 \\ g_3 & 0 & 0 \end{bmatrix}$$

$$C = [0 \ 0 \ 0 \ 0 \ 0 \ 2 \ 0]$$

$$D = [0 \ 0 \ -1]$$

The parameters are defined in the appendix A.

### 2.3.3 Multiple model construction

There are several methods that can be used to procure multiple model which includes identification, linearization, and mathematical transformation. The proposed multiple model method is based on a convex polytopic transformation of nonlinear functions that use the boundedness of nonlinear terms.

In order to simplify  $B(x(t))$  for the thermal model (2.61), we make a change of variable which will allow us later to design the observer. A new sixth state  $\theta_w(t)$  is

introduced as:

$$\theta_w(t) = T_w(t) - T_{wi} \quad (2.62)$$

The thermal model with this change of variables becomes:

$$\begin{cases} \dot{\bar{x}}(t) = A\bar{x}(t) + \bar{B}(\bar{x}(t))u(t) + \bar{G}v(t) - P\dot{T}_{wi} \\ y(t) = C\bar{x}(t) + \bar{D}v(t) \end{cases}, \quad (2.63)$$

where the state  $\bar{x}$  contains state variables and is defined as;

$$\bar{x} = [T_g \ T_c \ T_t \ T_r \ T_m \ \theta_w \ T_i]^T$$

The new matrices  $\bar{B}(\bar{x}(t))$ ,  $\bar{G}$ , and  $\bar{D}$  can be written as:

$$\bar{B}(\bar{x}(t)) = [0 \ 0 \ 0 \ 0 \ 0 \ -f_2\theta_w(t) \ 0]^T$$

$$\bar{G} = \begin{bmatrix} k_{11} & a_5 & 0 \\ 0 & b_5 & 0 \\ 0 & 0 & 0 \\ 0 & 0 & 0 \\ 0 & 0 & e_3 \\ 0 & 0 & -f_1 \\ g_3 & 0 & 0 \end{bmatrix}$$

$$P = [0 \ 0 \ 0 \ 0 \ 0 \ 1 \ 0]^T$$

$$\bar{D} = -D = [0 \ 0 \ 1]$$

In the model (2.63), the only varying term is  $a_{22}$ :

$$a_{22} = h(I_{sun}) = b_2 + b_3 I_{sun}, \quad (2.64)$$

where  $h(I_{sun})$  is bounded:  $b_2 + \underline{I_{sun}}b_3 \leq h(I_{sun}) \leq b_2 + \overline{I_{sun}}b_3$ .

Thus, the nonlinear term can be transformed such that:

$$h(I_{sun}) = \mu_1(I_{sun}) \cdot [b_2 + \underline{I_{sun}}b_3] + \mu_2(I_{sun}) \cdot [b_2 + \overline{I_{sun}}b_3],$$

where  $\underline{I_{sun}} = \min\{I_{sun}\}$ ,  $\overline{I_{sun}} = \max\{I_{sun}\}$  and

$$\mu_1 + \mu_2 = 1 \quad (2.65)$$

which enables us to obtain:

$$\mu_1 = \frac{I_{sun} - \underline{I_{sun}}}{\overline{I_{sun}} - \underline{I_{sun}}} \quad (2.66)$$

$$\mu_2 = \frac{\overline{I_{sun}} - I_{sun}}{\overline{I_{sun}} - \underline{I_{sun}}} \quad (2.67)$$

The corresponding multiple model is given by:

$$\begin{cases} \dot{\bar{x}} = \sum_{i=1}^2 \mu_i A_i \bar{x} + \bar{B}(\bar{x})u + \bar{G}v - P\dot{T}_{wi} \\ y = C\bar{x} + \bar{D}v \end{cases} \quad (2.68)$$

The number of models depends on the number of nonlinear terms. If there exist  $j$  nonlinear terms, then the multiple model constitutes no more than  $2^j$  local models.

Thus, there are 2 possible local models available described by  $A_1$  and  $A_2$  as follows

$$A_1 = \begin{bmatrix} a_{11} & a_3 & 0 & 0 & 0 & 0 & 0 \\ b_1 & b_2 + \overline{I_{sun}}b_3 & b_4 & 0 & 0 & 0 & 0 \\ 0 & c_1 & a_{33} & c_2 & c_3 & 0 & 0 \\ 0 & 0 & d_1 & a_{44} & d_2 & 0 & d_3 \\ 0 & 0 & e_1 & e_2 & a_{55} & e_3 & e_4 \\ 0 & 0 & 0 & 0 & f_1 & -f_1 & 0 \\ 0 & 0 & 0 & g_1 & g_2 & 0 & a_{77} \end{bmatrix}$$

$$A_2 = \begin{bmatrix} a_{11} & a_3 & 0 & 0 & 0 & 0 & 0 \\ b_1 & b_2 + \overline{I_{sun}}b_3 & b_4 & 0 & 0 & 0 & 0 \\ 0 & c_1 & a_{33} & c_2 & c_3 & 0 & 0 \\ 0 & 0 & d_1 & a_{44} & d_2 & 0 & d_3 \\ 0 & 0 & e_1 & e_2 & a_{55} & e_3 & e_4 \\ 0 & 0 & 0 & 0 & f_1 & -f_1 & 0 \\ 0 & 0 & 0 & g_1 & g_2 & 0 & a_{77} \end{bmatrix}.$$

## 2.4 Drying using air-based PV-T collector

The drying of agricultural products is very popular in developing countries. It is a critical process and must ensure that the dried material satisfies the recommended specifications. A lot of work is already been done by the researchers in this field as discussed in Chapter 1 but there is room for improvement and is always ongoing to:

- Define the features and characteristics of good dried material, not only in terms of moisture content but also in terms of composition, mechanical and biological properties.
- Recommend a drying scenario in terms of drying temperature, residence time as well as other physical variables.
- Design a drying process.
- Consider different energy sources specially to incorporate renewable ones.
- Minimize energy consumption.
- Control the dehydration process.

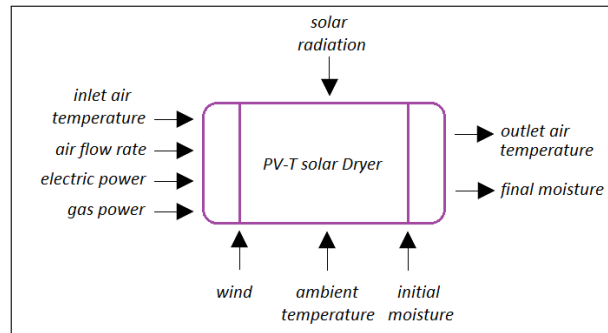


FIGURE 2.7: Bloc-diagram of the solar dryer.

The dehydration process might change the quality of the products otherwise dried products are a good source of nutrients. The control of the drying process is vital to ensure the quality of dried products in terms of visual aspects, flavor, color, retention of nutrients and contaminants content. This section analyses the use of PV-Ts and their performance for drying. A block diagram of a PV-T drying system is presented in Figure 2.7. The recirculation of air coming from the outlet end of the air channel is also considered to enhance the solar dryer efficiency by heat recovery.

The main factors in this study that influence the drying process are drying temperature, ambient and inlet temperatures, solar radiation, wind speed and mass flow rate. Other factors that can affect the performance of the drying process are relative humidity, initial moisture and thermal and electrical sources. A high temperature may damage the product to dry and the germination capacity while a low temperature may extend drying time and microbial contamination. Mass flow rate is a very important parameter and is the main control action that must be designed to ensure the temperature requirement in the drying chamber. Solar energy is the main source but other sources may be added to overcome the solar intermittence that are gas, electric and geothermal.

### Proposed scheme

The waste heat at the outlet end of the drying chamber can be recovered and used to enhance the efficiency of the system. The electricity generated by the PV-T collector can be stored in batteries and used when needed through electrical resistance as given in Figure 2.8. The above equation (2.23) using the mean air temperature (2.24)

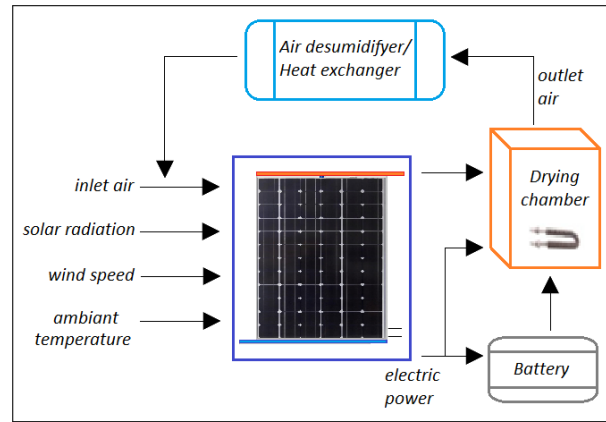


FIGURE 2.8: The solar dryer with air recirculation.

can be written as;

$$T_{f,o} = \frac{h_v A_c (T_t + T_i) - h_v A_c T_{f,i} + \dot{m}_f C_f T_{f,i}}{\dot{m}_f C_f + h_v A_c} \quad (2.69)$$

Given a reference temperature  $T_{f,o}^{ref}$  for drying to be maintained during a given time period, then the mass flow rate  $\dot{m}_f$  has to be set to the following value:

$$\dot{m}_f = \frac{h_v A_c [T_t + T_i - (T_{f,o}^{ref} + T_{f,i})]}{C_f (T_{f,o}^{ref} - T_{f,i})} \quad (2.70)$$

**Recycling scenario:**

Here, it is considered that the outlet air is recycled from the drying chamber to the input of the PV-T collector as illustrated in Figure 2.8, obviously by using a process or a treatment that avoids recycling the moisture. Moreover, it is assumed that the input temperature  $T_{f,i}$  that is injected to the collector is proportional to the output air temperature  $T_{f,o}$ , given by

$$T_{f,i} = \eta_{ra} T_{f,o}, \quad (2.71)$$

where  $\eta_{ra}$  is the efficiency of the temperature air recycling. Then, there exists a control in terms of air flow if (2.70) is positive, which translates to the condition

$$T_{f,o} < \frac{T_t + T_i}{1 + \eta_{ra}} \quad (2.72)$$

Under recycling scenario, the expression (2.69) becomes

$$T_{f,o} = \frac{h_v A_c (T_t + T_i)}{\dot{m}_f C_f (1 - \eta_{ra}) + h_v A_c (1 + \eta_{ra})} \quad (2.73)$$

While equation (2.70) becomes:

$$\dot{m}_f = \frac{h_v A_c [T_t + T_i - T_{f,o}^{ref} (1 + \eta_{ra})]}{C_f T_{f,o}^{ref} (1 - \eta_{ra})} \quad (2.74)$$

It can be seen from (2.73) that the output air temperature can be close to its maximum depicted in (2.72) if the recycling efficiency is high and the mass flow rate is low which means that it is only required to set the mass flow rate to a low value that allows:

- Collection of the heat from solar energy
- Moisture removal
- Heat recovery from the outlet air exiting drying chamber.

## 2.5 Modeling using artificial intelligence

Artificial intelligence (AI) or machine intelligence is one of the emerging technologies and is expected to grow rapidly in the near future. It is the development of smart machines that have the ability to perform tasks that require human intelligence e.g., self-driving cars, face detection, etc, and is divided into two types:

- Strong artificial intelligence
- Weak artificial intelligence

In strong AI, the machine thinks exactly like humans do whereas weak AI is limited to a specific area. Machine learning is an application or subfield of artificial intelligence that allows the machine to perform specific tasks accurately by learning from past experiences or past data. Deep learning is a subset or type of machine learning based on artificial neural networks (ANN) and uses multiple layers between the input and output layers as illustrated in Figure 2.9. The learning is further divided into two categories:

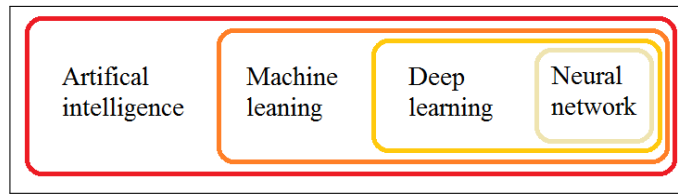


FIGURE 2.9: Applications and subsets of artificial intelligence.

- Supervised learning
- Unsupervised learning
- Error correction learning

AI has been applied for modeling, control, prediction, optimization, forecasting, and identification of complex systems. Several machine learning models have been used for various applications. In this section, regression model is used and multi-output decision tree algorithm is implemented for water-based collector by considering four inputs (i.e.,  $I_{sun}$ ,  $T_{am}$ ,  $V_w$  and  $\dot{m}_w$ ) and two outputs (i.e.,  $T_{wo}$  and  $\eta_{ele}$ ). Simulations are performed for the water-based model and actual values of the two outputs are obtained by considering the inputs data.

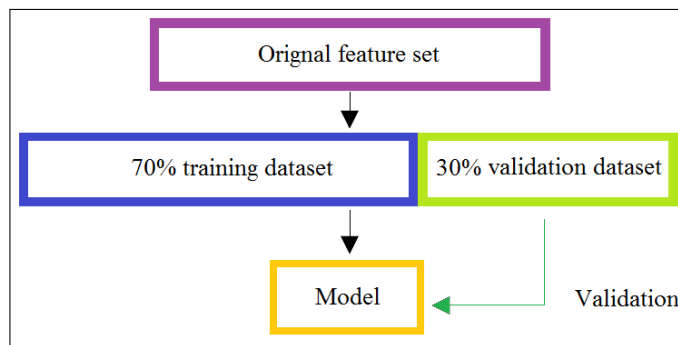


FIGURE 2.10: Schematic representation.

### 2.5.1 Decision tree algorithm

A decision tree is a supervised machine learning approach that makes use of input-output data sets to train models. It is an advanced algorithm that determines the importance and contribution value of input parameters (Rakhra et al., 2021). It builds a regression model in the form of a tree structure and the aim is to develop a model that predicts the target variable based on several input variables. The data is split using a binary tree and starts at the root node until left with leaf nodes or terminal nodes. One major advantage of a decision tree is that it is simple and easy to understand. The model can be developed using the following steps:

- import data set
- separate the target variable
- data is split into a train set and a test set (see Figure 2.10)
- scaling is done using a min-max function

- model creation and implementation (decision tree multi-output regressor is used)
- mean squared error (MSE) and accuracy are calculated
- lastly, validation is done using the test data.

The data can be expressed in the form:

$$(\iota, Y) = (\iota_1, \iota_2, \iota_3, \iota_4, Y_1, Y_2) \quad (2.75)$$

$Y$  is the target and dependent variable whereas  $\iota$  consists of features that are used for the task. Mean squared error is the average squared difference between actual value and the estimated value and is written as:

$$\text{MSE} = \frac{1}{n} \sum_{i=1}^n (Y_i - \hat{Y}_i)^2, \quad (2.76)$$

where  $n$  is the sample size,  $Y_i$  is the actual value of  $i^{\text{th}}$  case and  $\hat{Y}_i$  represents the predicted value of  $i^{\text{th}}$  case. Similarly, root-mean square error (RMSE) is calculated using (Abdurohman, Putrada, and Deris, 2022):

$$\text{RMSE} = \sqrt{\text{MSE}}. \quad (2.77)$$

## 2.5.2 Artificial neural network

Artificial neural networks (ANNs) have high learning ability and capability of identifying complex nonlinear systems. Hence, the ANN modeling technique is used, as a powerful tool, to predict and determine the thermal output and photovoltaic efficiency. In a multilayer neural network, one or more hidden layers are utilized in order to obtain accurate results. The network consists of an input layer, an output layer and at least one hidden layer sandwiched between the input and output layers as illustrated in Figure 2.11. Here, there are four input nodes and the output of the linear combiner is the sum of the product of all the inputs with their respective weights and can be expressed as

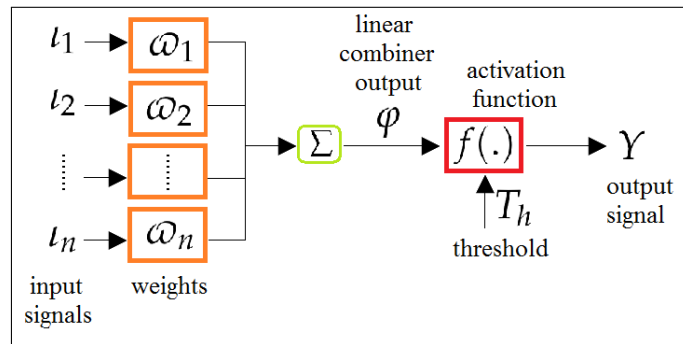


FIGURE 2.11: Basic model of the neural network.

$$\phi = \sum_{i=1}^n w_i l_i, \quad (2.78)$$

whereas the output signal becomes

$$Y = f(\varphi - T_h) \quad (2.79)$$

The output of the neural network is compared with the target output and the difference between the two is computed which is the error. The process is continued until the error is zero or the difference is within the target threshold and when it is achieved the neural network is trained. For training, it only requires input-output data and based on it the neural network understands and learns the relation between input and output.

## 2.6 Results and Discussion

The performance of the collector depends on several parameters: ambient temperature, solar radiation, mass flow rate, wind speed, fluid flowing (e.g. water or air), and thickness of various components. The values of the parameters i.e. absorptivity, transmissivity, emissivity and thermal conductivity for the PV-T components are provided in Table 2.1. The Matlab program is used for the proposed numerical designs and climatic parameters. Simulations are a good way to analyze the thermal performances of the PV-T collectors and allow the ability to conduct detailed investigations of the temperature distribution of all the components of the collector.

### 2.6.1 Air-based model-I

The typical distribution of solar radiation and ambient temperature during daytime is given in Figure 2.12 under a sample of southern France climatic conditions. The

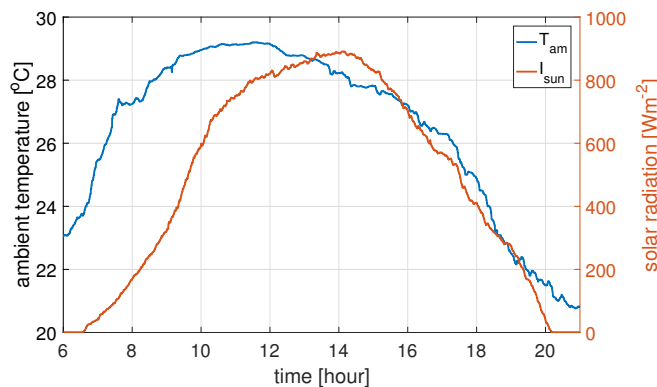


FIGURE 2.12: Hourly variation of solar radiation and ambient temperature.

sample is taken during the daytime because of high solar radiation and ambient temperature. Both parameters vary, depending on the weather conditions. During the summer season, the intensity of the sun is high and so does the values of solar radiation and the maximum value for it is  $880 \text{ Wm}^{-2}$ . The inlet air temperature is considered the same as the ambient temperature for air-based models. The temperature evolution of glass, PV cell, tedlar, air, and insulation with the mass flow rate of  $0.02 \text{ kgs}^{-1}$  are presented for model-I without an absorber component in Figure 2.13.

The outcomes convey that the maximum ambient temperature is around  $29^\circ\text{C}$  and the outlet air temperature from the duct goes to  $34^\circ\text{C}$ . The heat transfer is small

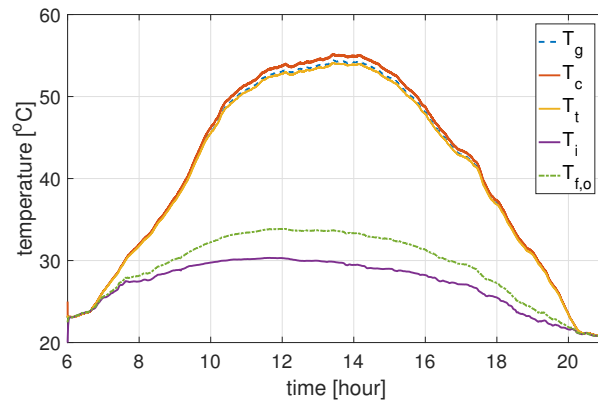


FIGURE 2.13: Temperature evolution of PV-T components for air-based model-I without an absorber component.

because of low heat capacity and low thermal conductivity. It is obvious that the temperature of the PV module component is higher than the other components. The temperature of the insulation remains close to the ambient temperature because of ambient conditions and no major rise in fluid temperature.

The electrical efficiency of the PV module highly depends on the PV cell temperature whereas the thermal efficiency of the collector depends on the temperature of the air at the outlet end. It can be seen in Figure 2.14, that the average electrical efficiency of the PV module is approximately 15% whereas the thermal efficiency of the collector is between 25 to 30% during the day hours.

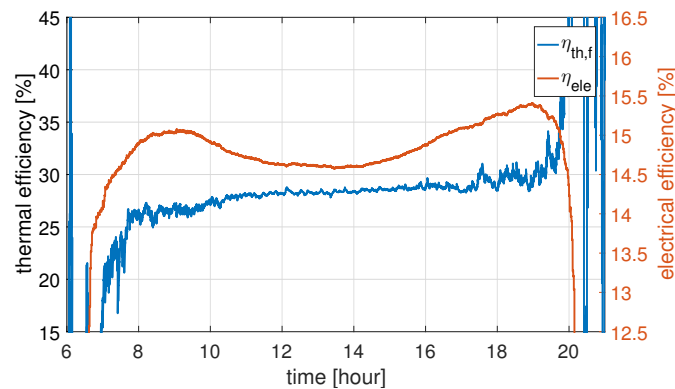


FIGURE 2.14: Daily hourly variation of electrical and thermal efficiencies for air-based model-I without glazing.

The outlet air temperature highly depends on the mass flow rate. Here, the results in Figure 2.15 show that with an increase in mass flow, the outlet temperature starts decreasing. This means that higher output can be obtained by taking low values for the mass flow rate.

The results in Figure 2.16 indicate that the addition of glazing increases the thermal efficiency but at the cost of PV efficiency. The daily thermal efficiency obtained is between 30% to 40% and the daily average PV efficiency is around 14.5%. Similar daily temperature evolution of PV-T components for glazed collector are found where the PV cell and outlet air temperatures are higher than the non-glazed case as shown in Figure B.1 in appendix B.

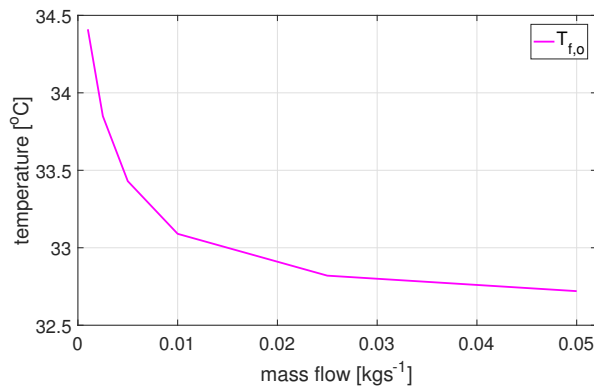


FIGURE 2.15: Variation of outlet air temperature with the increase in mass flow rate at  $T_{am} = T_{f,i} = 30\text{ }^{\circ}\text{C}$  and  $I_{sun} = 500\text{ Wm}^{-2}$ .

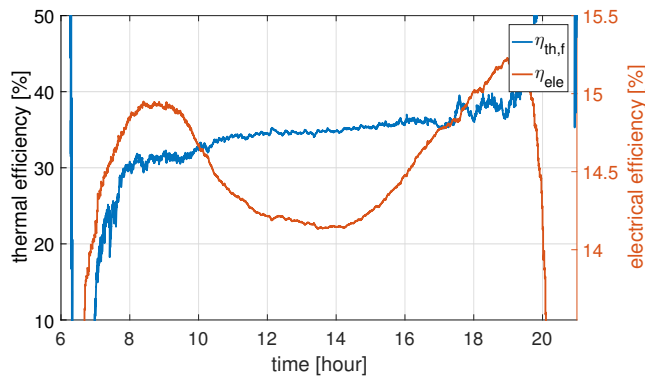


FIGURE 2.16: Daily hourly variation of electrical and thermal efficiencies for air-based model-I with glazing.

Further, the performance of air-based model-I by adding an absorber component just above insulation is analyzed to know its influence on the thermal output. The obtained results indicates that the inclusion of an absorber component increases the temperature of the air at the outlet end but no significant rise in temperature as shown in Figure 2.17.

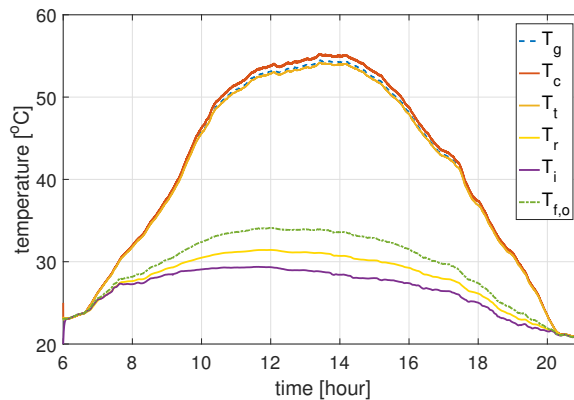


FIGURE 2.17: Temperature evolution of PV-T components for air-based model-I with an absorber component.

### 2.6.2 Air-based model-II

Similar ambient temperature and solar radiation profile, presented in Figure 2.12 is considered for this model. Both solar radiation and ambient temperature increase with time and reach a maximum value around noon. The ambient temperature reaches a maximum value of  $29^{\circ}\text{C}$  and solar radiation goes to  $880\text{ Wm}^{-2}$ , at the solar noon. The temperature evolution of air-based model-II is presented in Figure

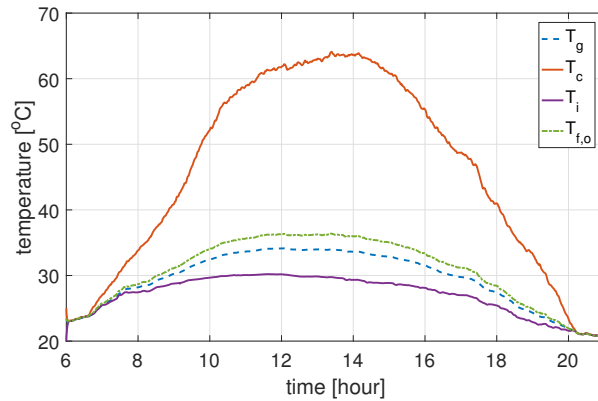


FIGURE 2.18: Temperature evolution of a PV-T components for air-based model-II.

2.18. The output temperature of the air channel goes to approximately  $37^{\circ}\text{C}$  with the mass flow rate of  $0.02\text{ kgs}^{-1}$ , despite the fluid (air) having low heat transfer. The temperature of the PV module component is higher than the other components.

A rise in the PV cell temperature directly affects the PV efficiency. Hourly variation of electrical efficiency and thermal efficiency for the solar device is shown in Figure 2.19. It can be observed that as the cell temperature rises above the reference value that is  $25^{\circ}\text{C}$ , the PV efficiency starts to fall. The average daily PV efficiency for model-II is approximately 14.5% whereas it is higher in the previous proposed model. This is mainly due to the fact that the cell temperature here is high but the average thermal efficiency is around 44% which is much higher than in the previous case.

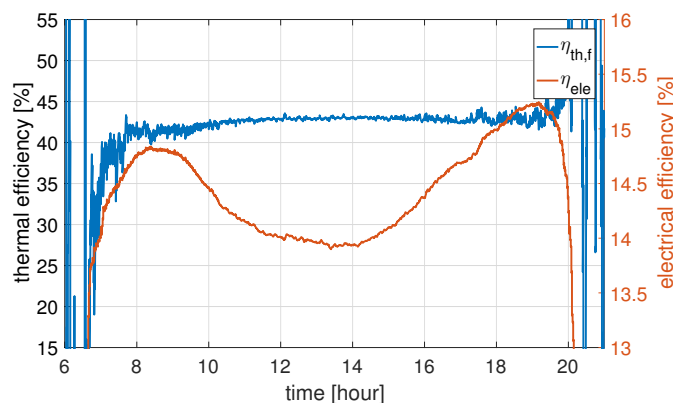


FIGURE 2.19: Daily hourly variation of electrical and thermal efficiencies for air-based model-II.

### 2.6.3 Validation of Air-based model-II

The results obtained from the proposed physical model are then compared with the CFD results. It can be observed that the obtained CFD results, presented in Figure 2.20 are compatible with the physical results illustrated in Figure 2.18. Despite mesh structure and convergence criteria in the CFD study, the results are in good agreement with the physical results and validate the viability of the proposed model.

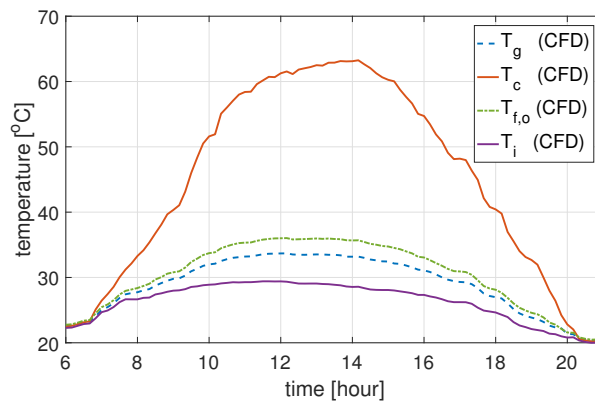


FIGURE 2.20: Temperature evolution of a PV-T components for air-based model-II (CFD study).

Temperature distribution of the four components of the collector is shown in Figure 2.21 and as one unit in Figure B.3 (see appendix B) at 13:00 (solar noon) when the ambient temperature and solar radiation are maximum. It can be observed that on the left side of the PV cell component the color is lighter which means lower temperature and on the right end of the collector it is the opposite.

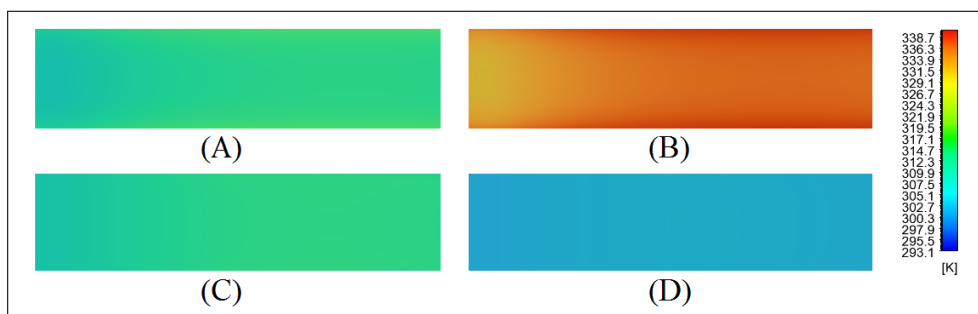


FIGURE 2.21: Temperature distributions of the air-based PV-T collector components; (a) Glass cover. (b) PV cell layer. (c) Fluid (air channel). (d) Insulator.

In CFD, the mesh independency study is proceeded in order to obtain an appropriate mesh structure. The average temperature is increased by up to 356 thousand cells to get significant change and due to this, the mesh structure has 356 thousand mesh elements and is presented in appendix B (see Figure B.2). Skewness is defined as the difference between the shape of the cell and the shape of an equilateral cell of equivalent volume. Highly skewed cells can decrease accuracy and destabilize the solution. In the final mesh structure, the maximum skewness value measured is  $2.17 \times 10^{-10}$  and the average skewness value is  $1.32 \times 10^{-10}$ . All the CFD details are mentioned in Chapter 3.

### 2.6.4 Drying

Simulations have been performed and the results are presented to illustrate the usefulness of recycling. The influence and importance of mass flow rate is not very well documented in previous studies on solar drying. The influence of mass flow rate on the PV-T components is studied under different conditions for ambient temperature (30 and 34°C) and solar radiation (400 and 700 Wm<sup>-2</sup>). The obtained results with the mass flow (0.0025, 0.0075 and 0.02 kgs<sup>-1</sup>, respectively.) are as follows: Figure 2.22 is obtained using ambient conditions (30°C and 400 Wm<sup>-2</sup>) whereas Figure 2.23 is obtained using conditions (34°C and 700 Wm<sup>-2</sup>). It can be observed that low values of  $\dot{m}_f$  implies higher temperatures for all the components.

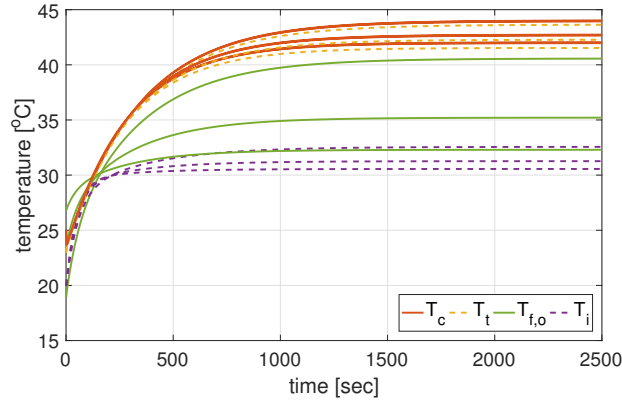


FIGURE 2.22: Temperature evolution of cell layer, tedlar layer, fluid and insulator at  $T_{amb} = 30^\circ\text{C}$  and  $I_{sun} = 400 \text{ Wm}^{-2}$  (for mass flow = 0.0025, 0.0075 and 0.02 kgs<sup>-1</sup>).

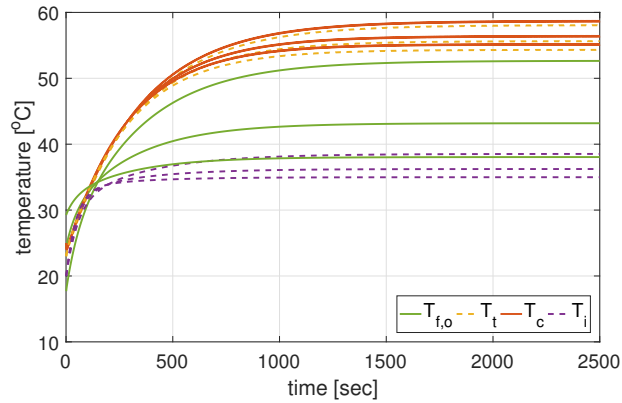


FIGURE 2.23: Temperature evolution of cell layer, tedlar layer, fluid and insulator at  $T_{amb} = 34^\circ\text{C}$  and  $I_{sun} = 700 \text{ Wm}^{-2}$  (for mass flow = 0.0025, 0.0075 and 0.02 kgs<sup>-1</sup>).

Now, let us consider a reference value for the outlet air temperature, for instance  $T_{f,o}^{ref} = 47.50, 52.50$  and  $57.50^\circ\text{C}$  with a solar radiation of  $800 \text{ Wm}^{-2}$  and ambient temperature of  $35^\circ\text{C}$ . Then one can use equation (2.70) to compute the mass airflow as a control action to ensure the given  $T_{f,o}^{ref}$ . In fact, the above equation (2.70) (resp. (2.74)) can be considered for an open-loop control without air recirculation (resp. with air recirculation). This control is very useful for simulation analysis and also

in a process with a relatively stable environment. However, it may be sensitive to changes in external variables and to parameter variations that are better attenuated with closed-loop control.

The results indicate that to achieve (47.50, 52.50 and 57.50°C) outlet temperature from the duct and with ambient and inlet temperatures to the duct kept as 35°C and solar radiation as 800 Wm<sup>-2</sup>, then one has to reduce the mass flow rate to (0.0059, 0.0036 and 0.0023 kgs<sup>-1</sup>) in order to get the desired temperature. This means a lower mass flow is required to get a higher output temperature as presented in Figure 2.24. If the ambient temperature and inlet temperature injected to the duct is 35°C with solar radiation set to 900 Wm<sup>-2</sup>, then the outlet temperature of the duct goes to 44.46°C with a mass flow rate of 0.01 kgs<sup>-1</sup> (see Figure 2.25).

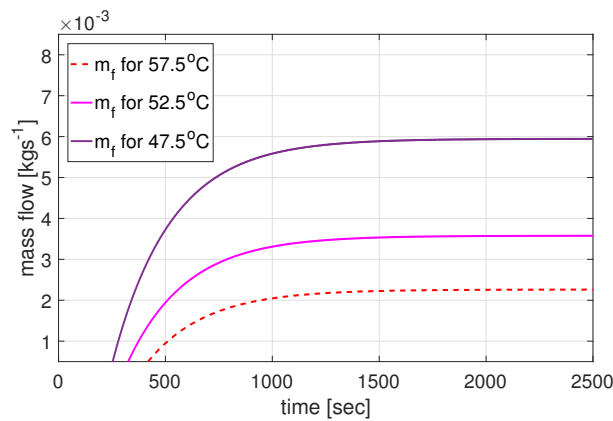


FIGURE 2.24: Mass flow required to achieve a desire output temperature (47.50, 52.50 and 57.50°C).

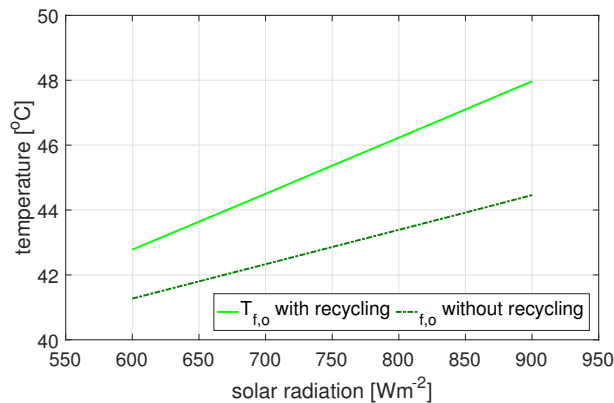


FIGURE 2.25: With and without recycling profile for air outlet temperature and solar radiation.

### Recycling scenario:

It is assumed that the input temperature  $T_{f,i}$  of the airflow is proportional to the output air temperature  $T_{f,o}$  given in (2.71) and under the recycling scenario, the air output temperature and airflow rate expression become (2.73) and (2.74). Using (2.73), the air output temperature rises to 42.78°C from 41.27°C with solar radiation set to 600 Wm<sup>-2</sup>. Similarly, with the solar radiation of 900 Wm<sup>-2</sup> and the inlet temperature

injected to the duct is  $35^{\circ}\text{C}$ , the temperature rises from  $44.46^{\circ}\text{C}$  to  $47.97^{\circ}\text{C}$  under the recycling scenario. Figure 2.25 shows the increase of the outlet temperature when solar radiation increases, including the recycling case. An interesting observation is that at lower solar radiation, the outlet temperature difference is small whereas it gets bigger with an increase in solar radiation.

### 2.6.5 Water-based model

The temperature evolution for glass cover, PV cell, tedlar, absorber, insulator, metallic tube, and fluid is shown in Figure 2.26 for a water-based model. The solar radiation and ambient temperature profiles are presented in Figure 2.12. Temperatures rise with the increase in ambient conditions and fall with the drop. Ambient temperature and solar radiation vary, depending on the weather conditions. During the daytime, the maximum solar radiation available is  $880\text{ Wm}^{-2}$  which occurs at 13:00 (local time) when the ambient temperature is maximum too.

The temperature of PV module components is highest around this point with the PV cell temperature going to approximately  $49^{\circ}\text{C}$ . It is obvious that the PV cell temperature is higher than the other components temperature whatever the value of solar radiation and ambient temperature. The inclusion of a glass cover on top not only protects the PV module but causes an increase in PV cell temperature due to which the fluid temperature rises. However, the PV efficiency drops with a rise in cell temperature. Further, the fluid temperature rises to  $43^{\circ}\text{C}$  with the inlet water temperature of  $20^{\circ}\text{C}$ , the mass flow rate is kept constant at  $0.005\text{ kgs}^{-1}$ , and the insulator thickness of  $0.08\text{ m}$ . It can be seen that each component in the PV-T collector has a higher temperature than the ambient temperature.

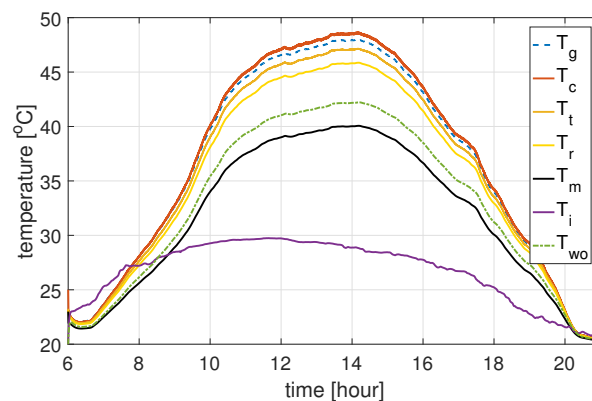


FIGURE 2.26: Daily temperature evolution of water-based PV-T components.

The percentage of incident solar energy that is transformed into electricity is photovoltaic conversion efficiency. The photovoltaic and thermal efficiencies of the collector are presented in Figure 2.27. Here, the results showed that with an increase in solar radiation and cell temperature (see Figure 2.26) the PV efficiency decreases, and by the end of the day, it increases with the decrease in solar radiation and cell temperature under the same mass flow rate. The average PV efficiency during the daytime is 11.28% with values ranging between a minimum of 10.74% and a maximum of 12%. The thermal efficiency directly depends on mass flow rate, outlet water temperature and solar radiation, as these parameters vary, the thermal efficiency varies. The daily efficiency of the collector is between 30% to 45%.

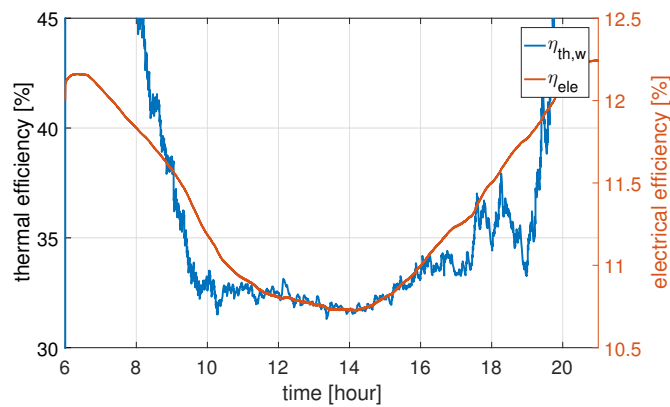


FIGURE 2.27: Hourly variation of PV efficiency and thermal efficiency.

A step-change in solar radiation is used in order to know the dynamic response and is presented in Figure 2.28. The solar radiation is reduced from  $150 \text{ Wm}^{-2}$  to  $50 \text{ Wm}^{-2}$  and results indicate that the response is not sudden; it takes time to reach the destination point. Moreover, it can be seen that the temperature rise is faster than the temperature drop.

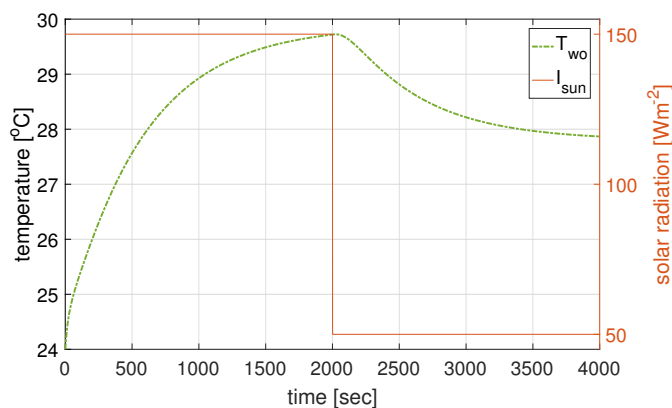


FIGURE 2.28: Fluid temperature with a step change in solar radiation.

Insulation stops accumulated heat thermal losses through sides and rare parts of the collector and enhances the efficiency of the collector. An analysis of Figure 2.29 illustrates that an increase in an insulator thickness leads to an increase in fluid temperature but there is a sudden change in outlet temperature if the thickness is less than 0.05 m. Additionally, for economical reasons, thicknesses of more than 0.08 m is not required as the energy losses become constant.

Wind speed has a major influence on the performance of the PV-T collector, especially during the summer season. This is mainly due to the fact that convective exchange is higher. The results in Figure 2.30 show that an increase in wind speed leads to the degradation of thermal efficiency (2.59). The thermal efficiency drops with the increase in wind speed from  $1 \text{ ms}^{-1}$  to  $5 \text{ ms}^{-1}$  and with the solar radiation of 500 and  $750 \text{ Wm}^{-2}$ , the thermal efficiency varies between 32% and 46%.

For the cost-effectiveness of a PV-T collector, the selection of mass flow rate is an important factor for the pump capacity. Figure 2.31 illustrates the effect of mass

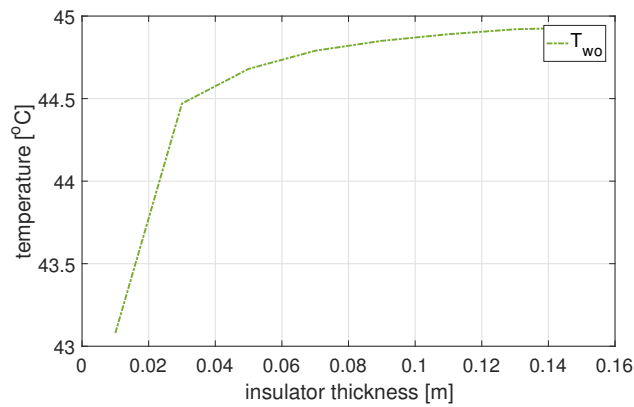


FIGURE 2.29: Influence of insulator thickness on the output temperature.

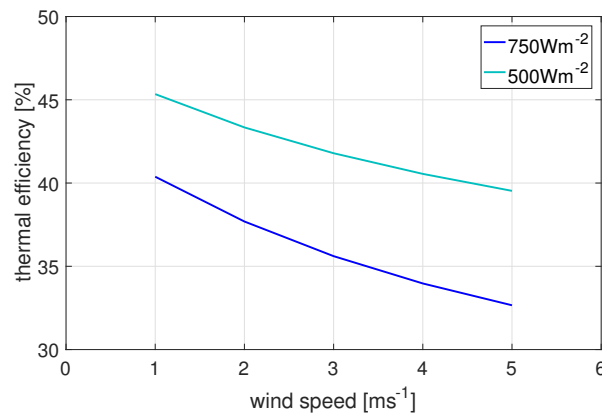


FIGURE 2.30: Influence of wind speed on thermal efficiency.

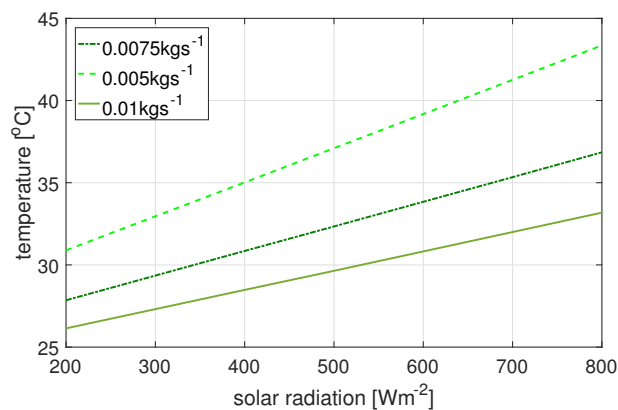


FIGURE 2.31: Influence of mass flow rate on the output temperature.

flow rate on the outlet temperature by varying solar radiation. The results indicate that with an increase in mass flow rate, the fluid temperature drops. An interesting observation is that at a lower mass flow rate the temperature rise/drop is small compared to a higher mass flow rate. Further, with an increase in solar radiation, the temperature difference between two different mass flow rates increases.

In Section 2.3, a multiple model for a water-based PV-T collector is presented.

Initially, the simulations are performed to see the response of the nonlinear model (2.63) and its corresponding multiple model (2.68). The obtained results indicate a good representation of the nonlinear system.

### 2.6.6 Validation of Water-based PV-T model

The results obtained from the proposed model are then compared with previous studies found in the literature (Dubey and Tiwari, 2008; Tiwari and Sodha, 2006; Chow, 2003; Zondag et al., 2002) and are summarized in Table 2.2 and Figure 2.32. It can be observed in both Table 2.2 and Figure 2.32 that there is good compatibility between the experimental results and the simulated results obtained using the proposed water-based model.

TABLE 2.2: Summary of results for the current work and other studies in literature.

Reference	$T_{wo}$	$\dot{m}_w$	$I_{sun}$	$T_{am}$	$T_c$	$l_i$	$\eta_{ele}$
Current study	44.50	0.005	870	34	51.50	0.08	10.49
$R_1$	43	0.090	Spring		$\simeq 51$	0.10	10.50 - 11
$R_2$	$\simeq 44$	0.005	812	35	$\simeq 50$	0.05	-
$R_3$	46.40	0.005	800	-	51.72	-	$\simeq 9$
$R_4$	40	0.005	800	20	-	0.02	9.70

It should be noted that units in the table for temperature is  $^{\circ}\text{C}$ , mass flow in  $\text{kgs}^{-1}$ , solar radiation in  $\text{Wm}^{-2}$ , thickness in m, electrical efficiency in % whereas R represents the references and are;

$R_1$ : Dubey and Tiwari (2008)       $R_2$ : Tiwari and Sodha (2006)  
 $R_3$ : Chow (2003)       $R_4$ : Zondag et al. (2002)

The hybrid PV-T collector has been experimentally studied by Dubey and Tiwari (2008), equipped with a glass cover encased in an aluminium metallic box with 0.1 m glass wool insulation below the absorber to reduce bottom losses. The experimental value of cell temperature goes to  $52^{\circ}\text{C}$  whereas outlet temperature was found at  $43^{\circ}\text{C}$  with the same insulation and weather conditions. However, the mass flow rate in the current model is kept lower to a value of  $0.005 \text{ kgs}^{-1}$ , thus there is a difference in outlet water temperature. Moreover, the PV efficiency and cell temperature are found similar.

The numerical results obtained in the present study were also compared with other numerical and experimental results found in (Tiwari and Sodha, 2006). The reduction in insulator thickness and solar radiation drops the outlet water temperature so with insulator thickness of 0.05 m and solar radiation of  $812 \text{ Wm}^{-2}$ , the obtained results are in good agreement. Furthermore, the values computed by the developed model with the same mass flow rate were compared with the values reported in (Chow, 2003). The results of the current study are close to the ones obtained by Chow (2003).

Our data is also compatible with the experimental results in (Zondag et al., 2002). The two parameters due to which the outlet temperature difference is high are insulation thickness which is 0.08 m (resp. an ambient temperature of  $34^{\circ}\text{C}$ ) in this study compared to 0.02 m (resp.  $20^{\circ}\text{C}$  in (Zondag et al., 2002)). On the other hand, their results are in good agreement with ours when the solar radiation is taken as  $800 \text{ Wm}^{-2}$  with an ambient temperature of  $20^{\circ}\text{C}$  and insulator thickness of 0.02 m. It is worth it

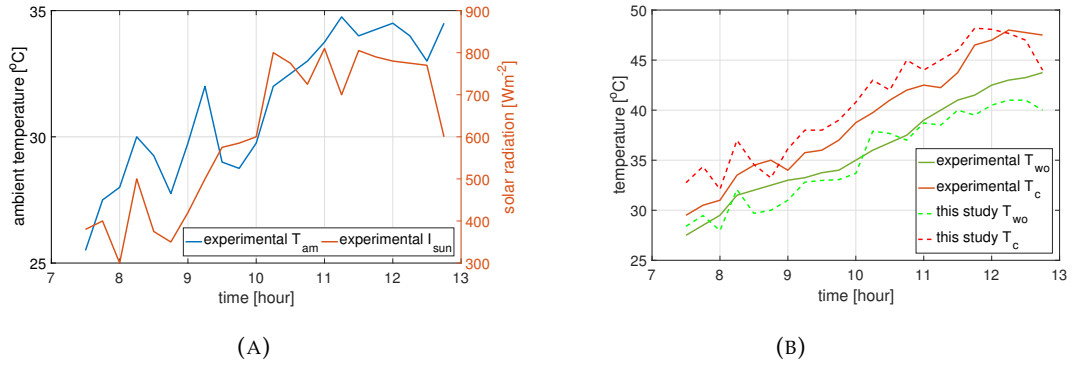


FIGURE 2.32: (a) Hourly evolution of solar radiation and ambient temperature experimentally. (b) Hourly evolution of temperatures ( $T_c$  and  $T_{wo}$ ) both experimentally (experimental studies) and theoretically (this study).

to mention that the highest PV efficiency achieved in the current work is close to the maximum value obtained experimentally in other studies in the literature referred in Table 2.2.

The hybrid PV-T system has also been experimentally studied by Huang et al. (2001) to understand the performance of an integrated photovoltaic and thermal solar system (IPVTS) and the experimental variations of solar radiation and ambient temperature along with PV cell temperature and fluid temperature obtained is shown in Figure 2.32. The experimental climatic data for a sunny day in May is shown in Figure 2.32a and is used in our proposed model to know the hourly variation of PV cell temperature and fluid temperature as illustrated in Figure 2.32b. It should be noted that in numerical simulation, the wind speed was taken with a value of  $2 \text{ ms}^{-1}$ , insulator thickness is 0.08 m, and water mass flow rate is taken as  $0.006 \text{ kgs}^{-1}$ . The results show that the numerical simulations are fairly close to the experimental data with a small difference. This difference is mainly due to the fact that all the parametric values (e.g. thickness of the layers and material used for absorber and insulator, etc), geometry, and design used in this study might be different from experimental setup built-in experimental studies. As a general conclusion, the simulation results founded by the numerical model developed in this study and the experimental studies (Huang et al., 2001) validate the viability of the proposed model.

### 2.6.7 Decision tree algorithm and neural network

In this section, comparative results of the decision tree algorithm and neural network are presented. The upper and lower bounds of the inputs are presented in Table 2.3 and the aim is to develop a model which must work within these limits.

TABLE 2.3: Lower and upper bounds of input variables.

Input variable	$I_{sun}$ ( $\text{Wm}^{-2}$ )	$T_{am}$ ( $^{\circ}\text{C}$ )	$V_w$ ( $\text{ms}^{-1}$ )	$\dot{m}_w$ ( $\text{kgs}^{-1}$ )
upper bound	700	31	5	0.05
lower bound	100	21	1	0.005

In the decision tree algorithm, 70% of the data is used for learning whereas 30% of the dataset is employed as test data and is later used for validation purpose. An accuracy score of 75% is achieved with a mean squared error of  $1.14 \times 10^{-2}$  and the root mean square error calculated is 0.107. The obtained results in Figure 2.33 are satisfactory and indicate that there is under-fitting and the actual results are not accurately predicted especially for the output water temperature  $T_{wo}$ . Therefore, in order to predict the outputs accurately, ANN is a good solution to proceed.

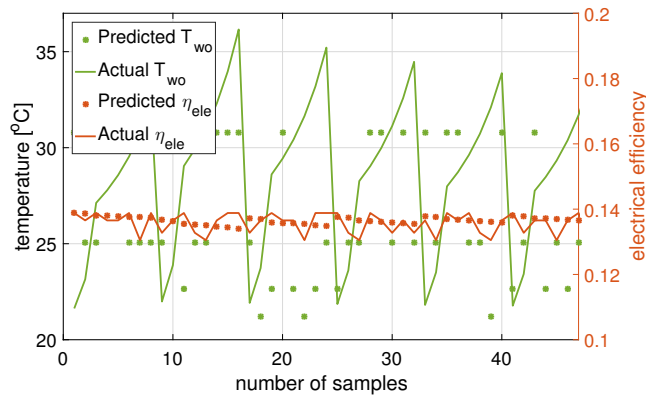


FIGURE 2.33: Comparison of actual and predicted outputs using decision tree algorithm.

In a neural network, there are three layers with the visible input layer having four neurons, two neurons for the output layer and sixteen neurons for the hidden layer that is sandwiched between input and output layers. For the training purpose, the Levenberg-Marquardt Backpropagation algorithm is used. It is widely used for network training purpose because of its fast and accurate results. The threshold limit or the convergence limit, in this case, is  $1 \times 10^{-7}$ . The performance is checked using mean squared error and the best performance is successfully reached as shown in Figure 2.34.

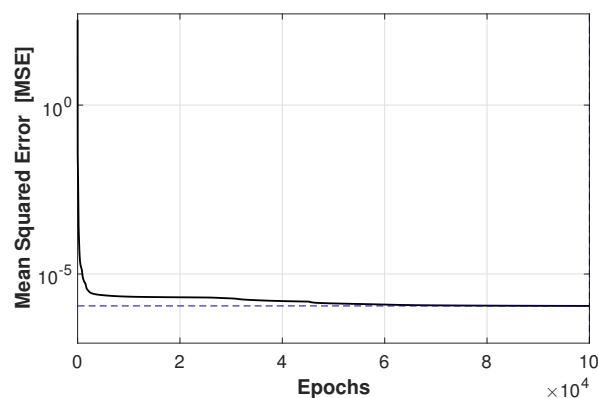


FIGURE 2.34: Mean squared error using neural network.

The found results in Figure 2.35 show that the actual outputs are accurately predicted using a neural network. There are small differences in the electrical efficiency output but the output water temperature is accurately predicted for all the samples.

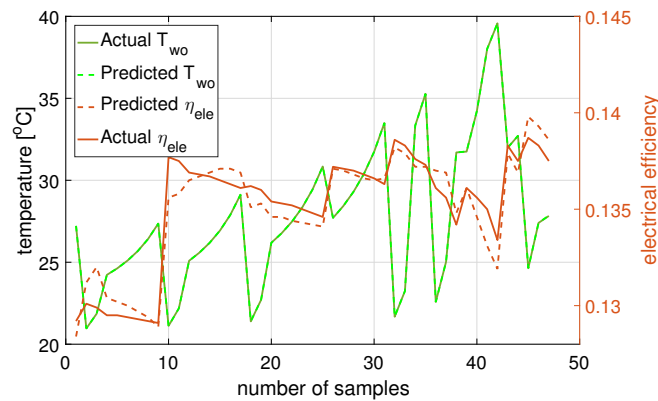


FIGURE 2.35: Comparison of actual and predicted outputs using neural network.

## 2.7 Conclusion

The modeling has been performed using a bond graph technique which can be adapted to other PV-T designs and configurations. The obtained results for the air-based PV-T model-I confirm that the heat transfer using air as a working material is small because of low heat capacity and low thermal conductivity. It confirms that the increase in the mass flow rate reduces the outlet temperature for both air-based and water-based collectors. It is obvious that the temperature of the PV module is higher than other components and goes to a maximum value at the solar noon for all the models. The inclusion of glazing enhances the thermal efficiency but at the cost of PV efficiency. The outlet water temperature rise is faster than the temperature drop with a step-change in solar radiation

A sensitivity analysis of the physical and external variables has been performed for the water-based model and the following conclusions can be drawn:

- The insulator thickness is an important design parameter, influencing the performance of a collector. The higher outlet water temperature is achieved with the insulator thickness of more than 0.08 m but for economical reasons, thicknesses of more than this is not required as the energy losses become constant.
- The PV-T collector shows higher thermal efficiency if the wind speed is low and the thermal efficiency can be enhanced with the increase of fluid mass flow rate. The thermal efficiency drops from 46% to 32% with an increase in wind speed from  $1 \text{ ms}^{-1}$  to  $5 \text{ ms}^{-1}$ .
- At a lower mass flow rate, the temperature rise/drop is small compared to high mass flow rates.

The thermal energy obtained from the PV-T collector can also be used for various heating applications and for cooling purposes by utilizing the electricity generated by the PV module to run a heat pump. Under the recycling scenario in solar drying, the air output temperature rises. There is a significant rise (between air output and recycled air output) as the solar radiation increases compared to lower solar radiation. It can be concluded that ANN which is a deep learning technique has a better accuracy in predicting the outputs compared with decision tree algorithm which is a machine learning approach. Consequently, developed models are user-friendly and artificial intelligence approach could be used as an alternative in order to reduce the cost.

## Chapter 3

# Design and Optimization

In the past, various types of PV-T collectors had been proposed with theoretical and experimental analysis where the storage tank is placed separately from the PV-T collector. The tank is either placed on top of the collector or on the side of the collector as shown in Figure 3.1.



FIGURE 3.1: (a) Storage tank placed separately from the collector. (b) Storage tank placed on-top of the collector.

Various theoretical and experimental investigations had been presented. Sun et al. (2022) analyzed the experimental and numerical performance of four unglazed mono-crystalline PV-T modules in a series connection integrated with PCM water storage. The performance of a flat-plate water-based PV-T system with a separate insulated water reservoir was evaluated using an analytical technique in Kumasi, Ghana (Abdul-Ganiyu et al., 2021). Experimental thermal performance of a PV-T installation with a storage tank has been studied by Huang, Sung, and Yen (2013) whereas thermal model was developed by Herrando, Markides, and Hellgardt (2014) to estimate the performance of a PV-T system with a separate water storage unit. Additionally, an auxiliary heater was used in order to meet the temperature requirements of the end-user on cloudy days. Guarracino et al. (2016) presented a dynamic model of a PV-T with a sheet and tube thermal absorber where the storage tank is placed separately. The tank has been modeled as a fully mixed tank and the influence of various parameters such as the effect of the emissivity and absorptivity on the system performance were studied at steady-state and at varying operating and atmospheric conditions. Many storage tank configurations have been reported such as cylindrical, rectangular, triangular and trapezoidal (Kumar and Rosen, 2011).

In this investigation, a new design is proposed where the storage tank is placed just beneath the PV-T collector and is directly in contact with an absorber component

of the PV-T module. The objective of this study is not only to interpret the variation of temperatures of each component of the collector and outlet temperature from the storage tank but also to study electrical and thermal efficiencies.

### 3.1 System description

The overall PV-T arrangement comprises of several layers as shown in Figure 3.2:

- a glass layer is a top covering and the inclusion of it is to protect the PV cell layer and reduce the heat loss to the ambient. This will eventually improve the thermal efficiency of the system.
- a cell layer that is separated from the top glass cover by an air-gap.
- a protective tedlar layer below the PV cells.
- an absorber plate.
- a closed-loop serpentine tube that is fixed at the back of the absorber.
- fluid which flows within the serpentine tube.
- water storage tank.
- thermal insulation to reduce heat losses while improving structural strength.

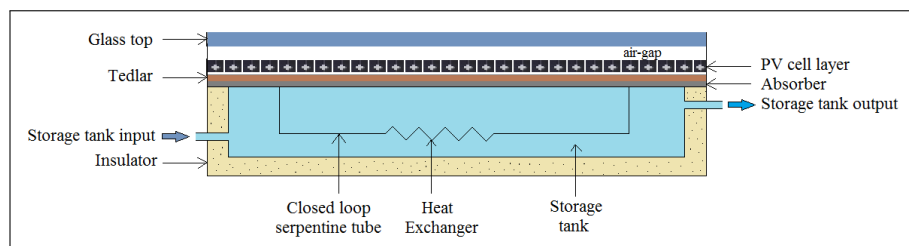


FIGURE 3.2: Cross-sectional view of hybrid photovoltaic-thermal system integrating a storage tank.

The serpentine tube extracts the heat from the top of the collector and transfers it to the tank fluid. The tube is fitted and pressed at the back side of the absorber plate with a bond. The outlet fluid coming from the top enters the heat exchanger located inside the storage tank, heats the water in the tank, exits the tank and returns to the inlet point of the collector. The storage unit lies just beneath the absorber plate and is thermally insulated from all the sides to minimize heat losses and improve structural strength.

Few assumptions have been made for the thermal part:

- The losses at the edges of a collector are negligible because of full insulation.
- The effect of friction in the pipe is over-sighted.
- At the surface, solar radiation, wind speed, and ambient temperature are uniform boundary conditions.
- Partial shading and dust at the top of the collector are neglected.
- Pressure losses are overlooked

- Radiation heat exchange at the bottom is neglected.

Moreover, a resistance heater is included as a complementary source in order to get the required outlet temperature from the storage tank during the winter season or on cloudy days. The pump used for the serpentine fluid increases efficiency but it can be removed as it is an additional element and consumes electrical power generated by the PV module.

## 3.2 Electrical model

The PV module is an assembly of polycrystalline silicon solar cells that produce photocurrent when exposed to sunlight and act like diodes in the absence of light radiation. The mathematical representation of a PV cell is modeled with a single diode. The electrical model of the collector is based on the single diode model of a photovoltaic module in which five electrical parameters light current  $I_{ph}$ , diode reverse  $I_o$ , series resistance  $R_s$ , shunt resistance  $R_{sh}$  and diode ideality factor  $\gamma$  derive the electrical behavior of the solar device. These five parameters directly depend on the cell temperature and solar radiation. This type of modeling provides a proper trade-off between simplicity and precision (Zhao et al., 2021).

The current-voltage (I-V) characteristic of a PV module with a single diode is governed by:

$$I = I_{ph} - I_o \left[ \exp \left( \frac{V + IR_s}{N_s \gamma V_t} \right) - 1 \right] - \frac{V + IR_s}{R_{sh}}, \quad (3.1)$$

where thermal voltage  $V_t$  (Monjezi et al., 2020) is as follows:

$$V_t = \frac{K_B T_c}{q} \quad (3.2)$$

The five parameters are calculated at particular solar radiation and temperature from limiting conditions of open-circuit voltage  $V_{oc}$ , short-circuit current  $I_{sc}$ , current and voltage at maximum power point ( $I_{mp}$  and  $V_{mp}$ ) using the reciprocals of the slopes at the short and open-circuit point, given by:

$$R_{s0} = - \left( \frac{dV}{dI} \right)_{V=V_{oc}} \quad (3.3)$$

$$R_{sh0} = - \left( \frac{dV}{dI} \right)_{I=I_{sc}} \quad (3.4)$$

The light-generated or photogenerated current  $I_{ph}$  is given by

$$I_{ph} = I_{sc} \left( 1 + \frac{R_s}{R_{sh}} \right) + I_o \left[ \exp \left( \frac{I_{sc} R_s}{a} \right) - 1 \right], \quad (3.5)$$

where modified ideality factor  $a$  is as follows:

$$a = \gamma N_s V_t$$

and series resistance  $R_s$  can be expressed as

$$R_s = R_{s0} - \left[ \left( \frac{a}{I_o} \right) \exp \left( \frac{-V_{oc}}{a} \right) \right] \quad (3.6)$$

TABLE 3.1: Electrical parameters of the PV module at standard test conditions.

Parameter	Value
Cell type	Polycrystalline silicon
Short circuit current ( $I_{sc,ref}$ )	8.68 A
open-circuit voltage ( $V_{oc,ref}$ )	38.28 V
Maximum power current ( $I_{mp,ref}$ )	8.11 A
Maximum power voltage ( $V_{mp,ref}$ )	31.24 V
Maximum power ( $P_{mp,ref}$ )	250 W
Temperature coefficient of short-circuit current ( $T_{I,sc}$ )	$0.005 \text{ A}^\circ\text{C}^{-1}$
Temperature coefficient of open-circuit voltage ( $T_{V,oc}$ )	$-0.118 \text{ V}^\circ\text{C}^{-1}$
Series resistance ( $R_s$ )	$0.8 \Omega$
Number of cells ( $N_s$ )	60
The electrical conversion efficiency ( $\eta_{ref}$ )	15.5%

with leakage current represented by shunt resistance is

$$R_{sh} = R_{sh0} \quad (3.7)$$

$$a = \frac{V_{mp} + I_{mp}R_{s0} - V_{oc}}{\left[ \ln \left( I_{sc} - \frac{V_{mp}}{R_{sh}} - I_{mp} \right) - \ln \left( I_{sc} - \frac{V_{oc}}{R_{sh}} \right) + \left( \frac{I_{mp}R_{sh}}{I_{sc}R_{sh} - V_{oc}} \right) \right]} \quad (3.8)$$

The diode reverse current  $I_o$  is given by

$$I_o = \left( I_{sc} - \frac{V_{oc}}{R_{sh}} \right) \exp \left( \frac{-V_{oc}}{a} \right) \quad (3.9)$$

and the short circuit current  $I = I_{sc}$  at  $V = 0$  is

$$I_{sc} = I_{ph} \left( \frac{R_{sh}}{R_s + R_{sh}} \right) - I_o \left( \frac{R_{sh}}{R_s + R_{sh}} \right) \left[ \exp \left( \frac{I_{sc}R_s}{a} \right) - 1 \right] \quad (3.10)$$

with  $R_{sh} \gg R_s$ , the above expression can be written as

$$I_{sc} = I_{ph} - I_o \left[ \exp \left( \frac{I_{sc}R_s}{a} \right) - 1 \right] \quad (3.11)$$

Similarly, open-circuit voltage  $V = V_{oc}$  at  $I = 0$  is

$$V_{oc} = R_{sh}I_{ph} - I_oR_{sh} \left[ \exp \left( \frac{V_{oc}}{a} \right) - 1 \right] \quad (3.12)$$

The electrical parameters of the PV module at standard test conditions are provided in Table 3.1. Using the reference conditions, parameters light current  $I_{ph}$ , short-circuit current  $I_{sc}$ , open-circuit voltage  $V_{oc}$  and modified idility factor  $a$  can be calculated as follows:

$$I_{ph} = \left( \frac{I_{sun}}{I_{sun,ref}} \right) [I_{ph,ref} + T_{I,sc}(T_c - T_{c,ref})], \quad (3.13)$$

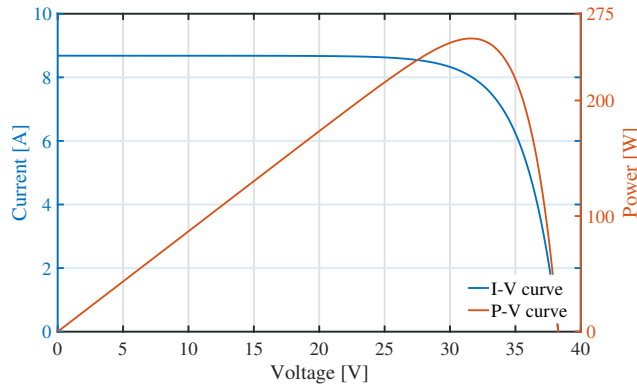


FIGURE 3.3: Current–voltage (I-V) and power-voltage (P-V) characteristics curve- STC conditions.

$$I_{sc} = \left( \frac{I_{sun}}{I_{sun,ref}} \right) [I_{sc,ref} + T_{I,sc}(T_c - T_{c,ref})], \quad (3.14)$$

$$V_{oc} = V_{oc,ref} + a \ln \left( \frac{I_{sun}}{I_{sun,ref}} \right) + T_{V,oc}(T_c - T_{c,ref}), \quad (3.15)$$

and

$$a = a_{ref} \left( \frac{T_c}{T_{c,ref}} \right) \quad (3.16)$$

where  $T_{I,sc}$  and  $T_{V,oc}$  are temperature coefficient of short-circuit current and open-circuit voltage. The parameters solar radiation  $I_{sun,ref}$ , cell temperature  $T_{c,ref}$ , photo-generated current  $I_{ph,ref}$ , short-circuit current  $I_{sc,ref}$ , open-circuit voltage  $V_{oc,ref}$  and modified ideality factor  $a_{ref}$  are at the reference conditions.

First, (3.14) and (3.15) are used to find  $I_{sc}$  and  $V_{oc}$ . Next, the five parameters are calculated using the relations (3.5), (3.6), (3.7), (3.8) and (3.9). Finally, using the measured voltage values, the cell current (3.1) is calculated.

The current-voltage and power-voltage characteristics for polycrystalline module at Standard Test Conditions;  $I_{sun} = 1000 \text{ Wm}^{-2}$  and  $T_c = 25^\circ\text{C}$  are illustrated in Figure 3.3. The amount of output power in PV systems is significantly relevant to the level of solar radiation and ambient temperature. The maximum generated photovoltaic power by the module is as follows:

$$P_{mp} = I_{mp}V_{mp} \quad (3.17)$$

where  $I_{mp}$  is the current at the maximum power point and  $V_{mp}$  is the voltage at the maximum power point.

Thus, the electrical efficiency is the ratio between the maximum power  $P_{mp}$  generated by the PV module and the total solar energy incident on the surface of the collector  $A_c$  and is determined by

$$\eta_{ele} = \left( \frac{P_{mp}}{A_c I_{sun}} \right) \quad (3.18)$$

whereas in terms of parameters and reference conditions, the PV efficiency (Slimani

et al., 2017) is calculated by

$$\eta_{ele} = \eta_{ref} \left[ 1 - \beta_p(T_c - T_{c,ref}) + \delta \ln \left( \frac{I_{sun}}{I_{sun,ref}} \right) \right], \quad (3.19)$$

where  $\delta$  is solar radiation coefficient and  $\beta_p$  is temperature coefficient.

### 3.3 Thermal model

The thermal part of the PV-T embedded with the tank model is based on the energy conservation principle and for each layer of the collector, an energy balance considering radiative, convective and conductive thermal exchanges between the layers.

Change in internal energy = Energy received - Energy lost

$$M_j C_j \frac{dT_j}{dt} = \sum_{er} Q_j - \sum_{el} Q_j, \quad (3.20)$$

where *er* represents energy received and *el* represents energy lost.

The convective heat transfer coefficient in an enclosed space (Li et al., 2022) is:

$$h_{v,gc} = \frac{N_{ua} k_a}{l_a}, \quad (3.21)$$

where

$$N_{ua} = \left[ 1 + 1.44 \left( 1 - \frac{1708}{R_a \cos \theta} \right)^* \left( 1 - \frac{1708(\sin 1.8\theta)^{1.6}}{R_a \cos \theta} \right) + \left( \left( \frac{R_a \cos \theta}{5830} \right)^{1/3} - 1 \right)^* \right]$$

with

$$R_a = \frac{g \cos \left( \frac{\pi}{2} - \theta \right) \beta_p \Delta T L_a^3 \rho_a^2 C_a}{k_a \mu_a}$$

The brackets signified by the superscript \* go to zero when they are negative.

The dynamic energy balance includes the masses and the heat capacities of each layer forming the module. The energy balance equations for the collector and storage tank are given by

Glass (*g*):

$$M_g C_g \frac{dT_g}{dt} = A_{mod} [\alpha_g I_{sun} - h_{r,gs}(T_g - T_s) - h_{v,am}(T_g - T_{am}) - h_{gc}(T_g - T_c)], \quad (3.22)$$

where combined heat transfer coefficient  $h_{gc}$  between glass and PV cell layer is the sum of radiative heat transfer coefficient (2.15) and convective heat transfer coefficient (3.21) and is given by

$$h_{gc} = h_{r,gc} + h_{v,gc}$$

PV cell layer (*c*):

$$M_c C_c \frac{dT_c}{dt} = A_{mod} [\tau_g \alpha_c I_{sun} \beta - h_{gc}(T_c - T_g) - h_{c,ct}(T_c - T_t)] - E_p \quad (3.23)$$

where electric power  $E_p$  generated by the photovoltaic module can be calculated using (2.17).

TABLE 3.2: Thermal parameters of the collector.

Parameter	Value
Transmissivity of glass ( $\tau_g$ )	0.93
Absorbivity of glass ( $\alpha_g$ )	0.06
Absorbivity of cell ( $\alpha_c$ )	0.90
Thermal expansion coefficient ( $\beta_p$ )	0.0045
Absorbivity of tedlar ( $\alpha_t$ )	0.80
Packing factor ( $\beta$ )	0.88
Thermal conductivity of air ( $\lambda_a$ )	0.026 Wm <sup>-1</sup> K <sup>-1</sup>
Air gap ( $l_a$ )	0.02 m
Thermal conductivity of glass ( $\lambda_g$ )	1.1 Wm <sup>-1</sup> K <sup>-1</sup>
Thickness of glass ( $l_g$ )	0.0032 m
Thermal conductivity of cell ( $\lambda_c$ )	148 Wm <sup>-1</sup> K <sup>-1</sup>
Thickness of cell ( $l_c$ )	0.0002 m
Thermal conductivity of tedlar ( $\lambda_t$ )	0.2 Wm <sup>-1</sup> K <sup>-1</sup>
Thickness of tedlar ( $l_t$ )	0.001 m
Thermal conductivity of absorber ( $\lambda_r$ )	240 Wm <sup>-1</sup> K <sup>-1</sup>
Thickness of absorber ( $l_r$ )	0.001 m
Thermal conductivity of insulator ( $\lambda_i$ )	0.034 Wm <sup>-1</sup> K <sup>-1</sup>
Module area ( $A_{mod}$ )	1.65*1 m <sup>2</sup>
Tank dimension	1.49*0.84*0.12 m <sup>3</sup>
Heat exchange effectiveness ( $\epsilon_H$ )	0.40

Tedlar layer ( $t$ ):

$$M_t C_t \frac{dT_t}{dt} = A_{mod} [\tau_g \alpha_t I_{sun} (1 - \beta) - h_{c,ct} (T_t - T_c)] - A_{tr} h_{c,tr} (T_t - T_r), \quad (3.24)$$

Absorber ( $r$ ):

$$M_r C_r \frac{dT_r}{dt} = A_{tr} h_{c,tr} (T_t - T_r) - A_{rm} h_{c,rm} (T_r - T_m) - A_{rta} h_{v,rta} (T_r - T_{ta}) - A_{ri} h_{c,ri} (T_r - T_i), \quad (3.25)$$

Serpentine tube ( $m$ ):

$$M_m C_m \frac{dT_m}{dt} = A_{rm} h_{c,rm} (T_r - T_m) - A_{mw} h_{v,mw} (T_m - T_w) - A_{mta} h_{v,mta} (T_m - T_{ta}), \quad (3.26)$$

where

$$\frac{1}{A_{mw} h_{v,mw}} = \frac{1}{h_w \pi d_i L} + \frac{1}{c_b L}$$

The heat transfer coefficient in the pipe depends on the flow regime (turbulent, or laminar) and is given by

$$h_w = \begin{cases} 0.23 R_e^{0.8} P_r^{0.4} \frac{\lambda_w}{d_{hy}}, & \text{for } R_e \geq 2300 \\ 4.364 \frac{\lambda_w}{d_{hy}}, & \text{for } R_e < 2300 \\ 2 \frac{\lambda_w}{d_{hy}}, & \text{for } \dot{m}_w = 0 \text{ kgs}^{-1} \end{cases} \quad (3.27)$$

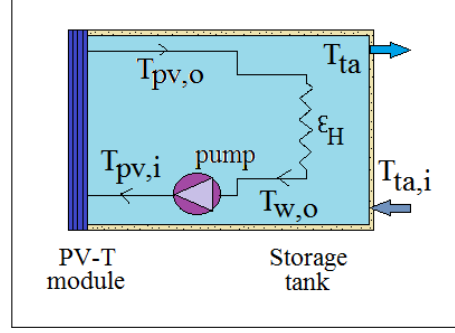


FIGURE 3.4: Schematic diagram of a closed-loop system.

In general, the conduction of the bond is very large and can be therefore neglected  $1/c_b \approx 0$  (Touafek, Khelifa, and Adouane, 2014). There is a change in temperature and enthalpy in the water tube during heat exchange and the energy gain can be expressed as (Bergene and Løvvik, 1995):

$$\dot{H} = \dot{H}_o - \dot{H}_i = \dot{m}_w C_w (T_{pv,o} - T_{pv,i}) \quad (3.28)$$

Serpentine fluid ( $w$ ):

$$M_w C_w \frac{dT_w}{dt} = \dot{m}_w C_w (T_{pv,i} - T_{pv,o}) - A_{mw} h_{v,mw} (T_w - T_m) \quad (3.29)$$

where  $T_w$  is the arithmetic mean of inlet temperature  $T_{pv,i}$  and outlet temperature  $T_{pv,o}$  and can be expressed as

$$T_w = \frac{T_{pv,i} + T_{pv,o}}{2}$$

The temperature at the outlet of the heat exchanger immersed in the tank, that is  $T_{w,o}$  can be written as

$$T_{w,o} = T_{pv,o} - \epsilon_H (T_{pv,o} - T_{ta})$$

The serpentine tube is a closed-loop system as illustrated in Figure 3.4. If it is assumed that there is no heat loss/heat gain for fluid flowing in the tube from exiting the heat exchanger and entering the collector, then this can be expressed as follows:

$$T_{w,o} = T_{pv,i}$$

Storage tank ( $ta$ ):

$$M_{ta} C_{ta} \frac{dT_{ta}}{dt} = \dot{q}_a + \dot{q}_b - A_{rta} h_{v,rta} (T_{ta} - T_r) - A_{mta} h_{v,mta} (T_{ta} - T_m) - A_{tai} h_{v,tai} (T_{ta} - T_i) \quad (3.30)$$

where  $\dot{q}_a$  is the energy for hot water and can be written as

$$\dot{q}_a = \dot{m}_{ta} C_{ta} (T_{ta,i} - T_{ta}),$$

and if  $T_{ta,i} > T_{ta}$  then  $\dot{q}_a = 0$ .

Similarly,  $\dot{q}_b$  is the rate of energy added from the collector to the tank and can be expressed as

$$\dot{q}_b = \dot{m}_w C_w \epsilon_H (T_{pv,o} - T_{ta})$$

if  $T_{ta} > T_{pv,o}$  then there is no heat addition to the storage tank and  $\dot{q}_b = 0$ .

One important heat transfer process is between the absorber plate and the water in the storage tank and natural convection is taken into account as a mode of heat transfer and the average heat transfer coefficient (Fujii and Imura, 1972) is written as

$$h_v = \frac{N_{ue}k}{L_c} \quad (3.31)$$

For an inclined heating surface, average Nusselt number  $N_{ue}$  estimation can be calculated using the following relation (Kumar and Rosen, 2011):

$$N_{ue} = 0.56(G_{re}P_{re} \cos \theta)^{1/4}, \quad (3.32)$$

where where  $\theta$  is the angle of the absorber surface relative to the vertical. Grashof number  $G_{re}$  and Prandtl number  $P_{re}$  can be calculated using following relations:

$$G_{re} = \frac{\rho^2 g \alpha (T_r - T_{ta}) L_c^3}{\mu^2}, \quad (3.33)$$

where  $\rho$  is density,  $g$  is gravitational acceleration,  $\alpha$  is coefficient of volume expansion and  $L_c$  is the characteristic length.

$$P_{re} = \frac{v}{\kappa} = \frac{\mu C_p}{k}, \quad (3.34)$$

where  $v$  is kinematic viscosity,  $\kappa$  is thermal diffusivity,  $\mu$  is dynamic viscosity,  $C_p$  is heat capacity and  $k$  is thermal conductivity of fluid.

Insulator ( $i$ ):

$$M_i C_i \frac{dT_i}{dt} = A_{mod} h_{v,iam} (T_{am} - T_i) - A_{tai} h_{v,tai} (T_i - T_{ta}) - A_{ri} h_{c,ri} (T_i - T_r) \quad (3.35)$$

By applying useful energy gain (3.28), the thermal performance of the PV-T collector is;

$$\eta_{th} = \frac{\dot{m}_w C_w (T_{pv,o} - T_{pv,i})}{A_{mod} I_{sol}} \quad (3.36)$$

Similarly, the photovoltaic efficiency of the collector can be calculated using (2.39). Therefore, the overall efficiency  $\eta_{ov}$  is the sum of thermal efficiency  $\eta_{th}$  and electrical efficiency  $\eta_{ele}$  of a PV-T system and can be found using the expression:

$$\eta_{ov} = \eta_{el} + \eta_{th}. \quad (3.37)$$

### 3.3.1 Addition of electrical resistance

During the winter season, or on a cloudy day, in order to meet hot-water requirements, an extra resistance heater is integrated with the system as illustrated in Figure 3.5. This electrical resistance will take power generated from the PV module directly or through a battery. It ensures that the temperature of the delivered hot water to the user reaches the required value. The heating element is chemically etched stainless steel and is equipped with electrical resistance wires inside. In this case, the it is assumed as a short cylinder whose diameter  $d_{he}$  is 0.02 m and length  $L_{he}$  of 0.4 m. The surface area  $A_{s,he}$  of the bottom of the heater is

$$A_{s,he} = \pi d_{he} L_{he} \quad (3.38)$$

The heat flux depends on the temperature difference between the surface tempera-

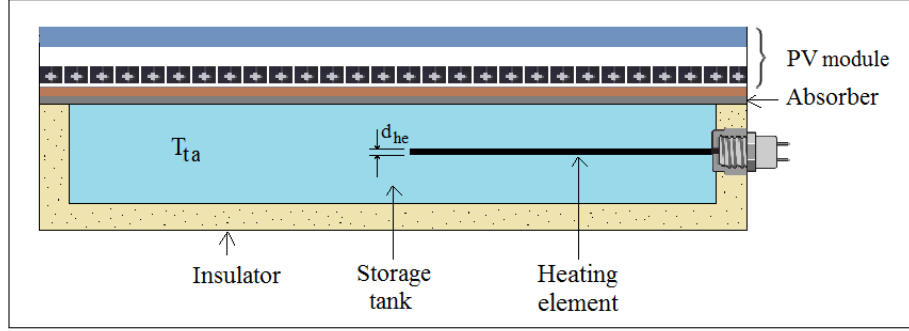


FIGURE 3.5: Cross-sectional view of hybrid photovoltaic-thermal system equipped with heating element.

ture of the heater  $T_{sth}$  and the temperature of the fluid  $T_{ta}$ , that is  $\Delta T_{he}$  (Cengel, Klein, and Beckman, 1998).

- if  $\Delta T_{he} < 30^\circ\text{C}$ , the heat flux in this case can be determined from Rohsenow relation, that is

$$\dot{q}_{nu} = \mu_L h_{fg} \left( \frac{g(\rho_l - \rho_v)}{\vartheta} \right)^{1/2} \left( \frac{C_{pl}(T_{sth} - T_{ta})}{C_{sf} h_{fg} P_{rl}^n} \right)^3, \quad (3.39)$$

where  $\mu_L$  is viscosity of the liquid,  $h_{fg}$  is enthalpy of vaporization,  $g$  is the gravitational acceleration,  $\rho_l$  is density of liquid,  $\rho_v$  is density of vapors,  $\vartheta$  is surface tension of liquid-vapor interface,  $C_{pl}$  is specific heat of the liquid,  $C_{sf}$  is experimental constant that depends on surface-fluid combination,  $P_{rl}$  is prandtl number and  $n$  is experimental constant that depends on the fluid.

- if  $\Delta T_{he} > 30^\circ\text{C}$ , the heat flux, in this case, is given by

$$\dot{q}_{fl} = C_{fi} \left( \frac{g k_v^3 \rho_v (\rho_l - \rho_v) [h_{fg} + 0.4 C_{pv} (T_{sth} - T_{ta})]}{\mu_v d_{he} (T_{sth} - T_{ta})} \right)^{1/4} (T_{sth} - T_{ta}), \quad (3.40)$$

where  $k_v$  is the thermal conductivity of vapor,  $C_{pv}$  is the specific heat of vapor,  $\mu_v$  is the viscosity of vapor and since, the storage tank is a horizontal cylinder, so  $C_{fi}$  is taken as 0.62.

The vapor properties are to be evaluated at the film temperature  $T_{fl}$ , given as

$$T_{fl} = \frac{T_{sth} + T_{ta}}{2} \quad (3.41)$$

which is average temperature of the film. The rate of heat transfer  $\dot{Q}_{he}$  becomes

$$\dot{Q}_{he} = A_{s,he} \dot{q}_{he} \quad (3.42)$$

with convection heat transfer  $h_{v,he}$  expressed as

$$h_{v,he} = \frac{\dot{q}_{he}}{T_{sth} - T_{ta}} \quad (3.43)$$

and the electric power consumed by the electrical resistance is equal to the rate of heat transfer to the water and is respectively, given as

$$\dot{W}_{he} = \dot{Q}_{he} \quad (3.44)$$

The rate of heat transfer to the water stored in the storage tank is to be found using (3.42). This will then be added in (3.30), in order to know the rise in storage tank temperature using the resistance heater. For a high surface temperature of the resistance heater, radiation heat transfer also occurs across the vapor film and should be taken into account.

### 3.3.2 Influence of internal geometrical parameters

This section provides valuable information regarding the influence of various parameters such as material, heat extraction fluid and thickness of various components on the outlet fluid temperature and storage tank temperature.

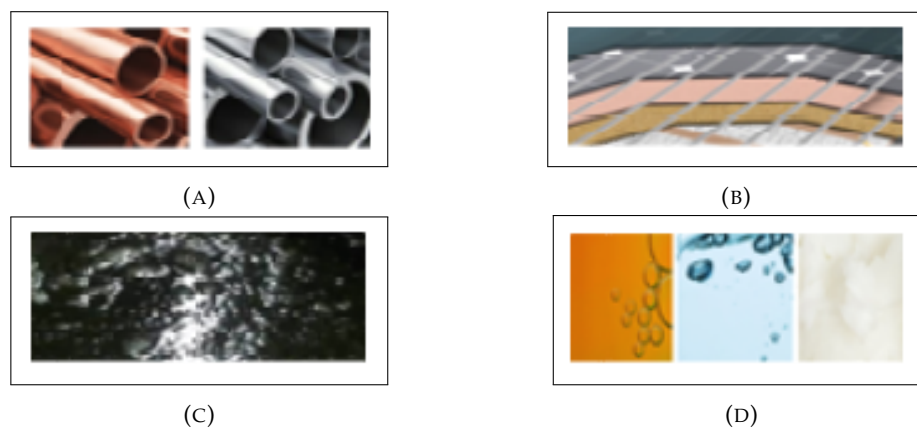


FIGURE 3.6: (a) Copper and aluminium as materials. (b) Thickness of the materials. (c) Used engine oil as an absorber material. (d) Glycol, Water and Paraffin wax as serpentine fluids.

#### Material

In PV-T system design, the material of the components plays a crucial role in acquiring high energy conversion efficiency and cost-effectiveness. The selection of suitable material for the absorber and tube is the basic step in the design and development of such systems. A PV-T system comes either with or without a thermal absorber. Generally, the absorber is placed between a PV module and the heat extraction medium. Similarly, for liquid-based PV-T collectors, single or multiple tubes are used through which the heat extraction medium runs. These components directly affect both the electrical and thermal performance of the collector by extracting the heat from the PV module and transferring it to the working fluid. Mostly, aluminium and copper are used as thermal absorbers and tube materials in a PV-T system.

Additionally, used engine oil is proposed as a replacement for absorber material. Waste engine oil pollution is very common in many countries, in particular third world countries. This can be recycled in a useful way, due to its thermo-physical properties to reduce environmental pollution.

### Thickness of the component

For cost-effectiveness and PV-T performance, the thickness of a component is an important parameter. Generally, the thickness of glass cover, PV cells and tedlar do not vary much. Therefore, in this study, the influence of insulator thickness and absorber thickness is analyzed to see how it affects the heat extraction fluid and tank fluid temperatures. Let's consider insulator thickness as an example, insulation not only reduces heat losses but also improves structural strength. This means a higher thickness value is required but at the same time price is also another factor and extra insulation takes extra space.

### Heat extraction fluid

A heat transfer fluid plays a vital role by extracting the unused heat from the PV module through circulation within the installation or else the temperature can go very high as discussed in Chapter 1. A suitable fluid selection is also very important to improve the performance of the system. Air or water are commonly used as heat extraction fluids as they are easily available. Air has low heat transfer whereas water has high thermal conductivity and heat capacity but comes with freezing issues. This design considers various fluids e.g. water, water mixed with glycol 50wt%, pure glycol and phase change material to see their influence. Glycol used in PV-T collectors is different from typical propylene glycol. A stable and efficient glycol must be used in order to avoid exposure to high temperatures which will result in the deterioration of glycol, making the fluid acidic. This acidic fluid will make the metallic tubes rusty and create corrosion problems. Figure 3.6d illustrates various heat transfer fluids which may be selected for different applications.

## 3.4 Computational fluid dynamics study

In this section, the CFD model of the hybrid PV-T system has been set up with boundary conditions specified in Figure 3.7. These conditions are applied on top of the glass surface.

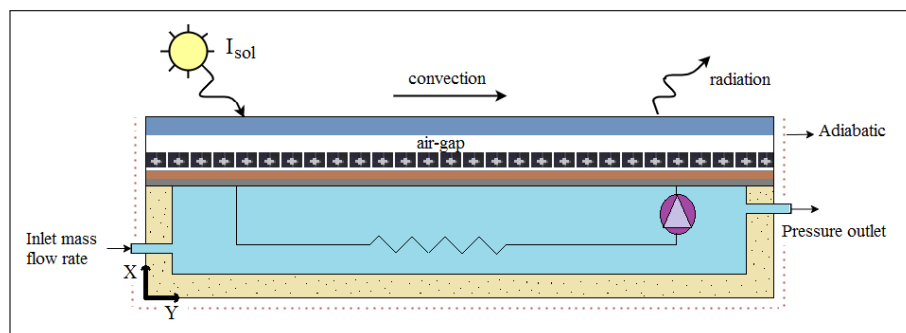


FIGURE 3.7: A schematic diagram of the boundary conditions.

The following assumptions are taken into account when formulating the three-dimensional and steady-state mathematical models;

- Air is incompressible.
- Reynolds-averaged Navier-Stokes (RANS) equations are applicable, and the realizable  $K_t-\epsilon_d$  turbulence model is used at high air fluid flow rates.

- Thermophysical properties of PV-T materials constant in time, uniform in space, and temperature independent.
- Lateral and bottom surfaces of the PV-T system assumed as adiabatic.
- Surface-to-surface radiation inside the PV-T system is negligible.

Governing equations of fluid dynamics can be simplified into three main equations that are for continuity, momentum and energy.

- for continuity

$$\frac{\partial}{\partial x}(u) + \frac{\partial}{\partial y}(v) + \frac{\partial}{\partial z}(w) = 0, \quad (3.45)$$

where  $u$ ,  $v$  and  $w$  represent the directional velocity of the components.

The equation for the conservation of linear momentum is obtained by applying Newton's second law. The net force which acts on the fluid particle is equal to the time rate of change of the linear momentum of the fluid particle. Here, the left-hand side represents the net rate at which momentum leaves the control volume due to fluid motion across its boundaries whereas the right-hand side represents the sum of net pressure force and net force due to viscous shear stress.

- for x-momentum

$$\frac{\partial}{\partial x}(uu) + \frac{\partial}{\partial y}(uv) + \frac{\partial}{\partial z}(uw) = -\frac{dp}{\rho dx} + \frac{(\mu + \mu_t)}{\rho} \left[ \frac{\partial^2 u}{\partial x^2} + \frac{\partial^2 u}{\partial y^2} + \frac{\partial^2 u}{\partial z^2} \right] \quad (3.46)$$

- for y-momentum

$$\frac{\partial}{\partial x}(uv) + \frac{\partial}{\partial y}(vv) + \frac{\partial}{\partial z}(vw) = -\frac{dp}{\rho dy} + \frac{(\mu + \mu_t)}{\rho} \left[ \frac{\partial^2 v}{\partial x^2} + \frac{\partial^2 v}{\partial y^2} + \frac{\partial^2 v}{\partial z^2} \right] \quad (3.47)$$

- for z-momentum

$$\frac{\partial}{\partial x}(uw) + \frac{\partial}{\partial y}(vw) + \frac{\partial}{\partial z}(ww) = -\frac{dp}{\rho dz} + \frac{(\mu + \mu_t)}{\rho} \left[ \frac{\partial^2 w}{\partial x^2} + \frac{\partial^2 w}{\partial y^2} + \frac{\partial^2 w}{\partial z^2} \right], \quad (3.48)$$

where  $\mu$  is the dynamic viscosity and  $\mu_t$  represents the turbulent viscosity.

- for energy

$$\frac{\partial}{\partial x}(\rho u_j CT) = \frac{\partial}{\partial x_j} \left[ K_t \frac{\partial T}{\partial x_j} \right] - \frac{\partial}{\partial x_j} \left[ \left( \frac{C\mu_t}{\sigma_k} \right) \frac{\partial T}{\partial x_j} \right], \quad (3.49)$$

where  $\mu_t$  is the turbulent viscosity and is defined as:

$$\mu_t = \rho C_\mu \frac{K_t^2}{\epsilon_d}, \quad (3.50)$$

where  $C_\mu$  and  $\sigma_k$  are constants and can be found in the theory guide of ANSYS-FLUENT (Manual, 2009). The realizable  $K_t$ - $\epsilon_d$  model is used for modeling the turbulent flow in the serpentine channel as it has certain advantages on adverse pressure gradients, separation, and recirculation (Khoshvaght-Aliabadi and Alizadeh, 2015; Iaccarino, Kalitzin, and Elkins, 2003). The modelled transport equations for  $K_t$  and  $\epsilon_d$  are

$$\frac{\partial}{\partial t}(\rho K_t) + \frac{\partial}{\partial x_j}(\rho K_t u_j) = \frac{\partial}{\partial x_j} \left[ \left( \mu + \frac{\mu_t}{\sigma_k} \right) \frac{\partial K_t}{\partial x_j} \right] + G_k + G_b - \rho \epsilon_d - Y_m + S_k \quad (3.51)$$

and

$$\frac{\partial}{\partial t}(\rho\epsilon_d) + \frac{\partial}{\partial x_j}(\rho\epsilon_d u_j) = \frac{\partial}{\partial x_j} \left[ \left( \mu + \frac{\mu_t}{\sigma_\epsilon} \right) \frac{\partial \epsilon_d}{\partial x_j} \right] + \rho C_1 S \epsilon_d - \rho C_2 \frac{\epsilon_d^2}{K_t + \sqrt{\nu \epsilon_d}} + C_{1\epsilon} \frac{\epsilon_d}{K_t} C_{3\epsilon} G_b + S_\epsilon, \quad (3.52)$$

where

$$C_1 = \max \left[ 0.43, \frac{\eta}{\eta + 5} \right], \quad (3.53)$$

$$\eta = S \frac{K_t}{\epsilon_d}, \quad (3.54)$$

$$S = \sqrt{2S_{ij}^2}, \quad (3.55)$$

where  $G_k$  represents the generation of turbulence kinetic energy due to the mean velocity gradients,  $G_b$  is the generation of turbulence kinetic energy due to buoyancy.  $Y_M$  represents the contribution of the fluctuating dilatation in compressible turbulence to the overall dissipation rate.  $C_2$  and  $C_{1\epsilon}$  are constants whereas  $\sigma_k$  and  $\sigma_\epsilon$  are the turbulent Prandtl numbers for  $K_t$  and  $\epsilon_d$ .  $S_k$  and  $S_\epsilon$  are user-defined source terms and these calculation methods and constants can be found in the theory guide of ANSYS-FLUENT (Manual, 2009) in more detail. In mathematics, convergence describes limiting behavior, particularly of an infinite sequence or series toward some limit. Convergence is also often measured by the level of residuals, the amount by which discretized equations are not satisfied, and not by the error in the solution. The CFD user should therefore be aware of this, in deciding what convergence criterion should be used to assess a solution. The convergence criteria for mass and momentum equations are defined as  $10^{-6}$ , and as  $10^{-8}$  for the energy equation. In computational fluid dynamics, the SIMPLE algorithm is a frequently used numerical method for solving Navier-Stokes equations and the SIMPLE algorithm uses a relationship between velocity and pressure corrections to enforce mass conservation and obtain the pressure field.

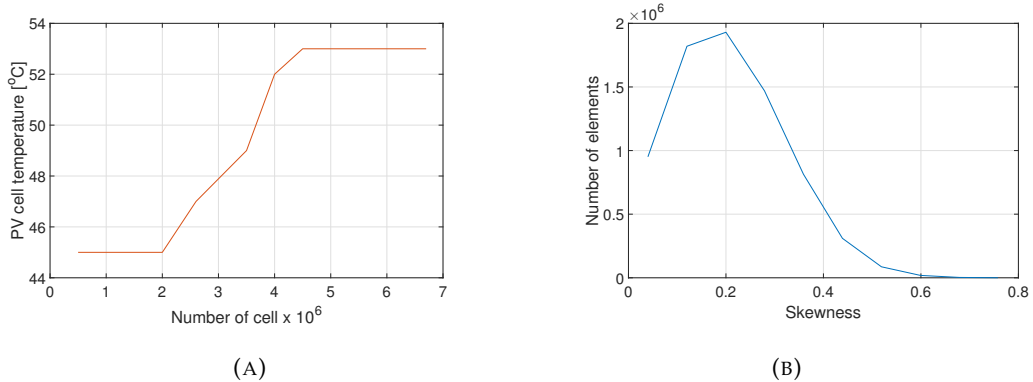


FIGURE 3.8: (a) Mesh independency. (b) Mesh quality distribution of the hybrid PV-T system.

The change in the average temperature of the PV cell with a different number of mesh elements is illustrated in Figure 3.8a. The average temperature is increased by up to 4.5 million cells to get significant change. For this reason, the mesh structure has 4.5 million mesh elements and is preferred for the other case studies. The skewness distribution of the mesh structure is presented in Figure 3.8b. The maximum

skewness value measured is 0.758 and the average skewness value is 0.207. The obtained mesh structure is assumed appropriate for the remaining cases in the current study as well.

### 3.5 Optimization

In this section, optimization is performed for a water-based model without a storage tank to see its effect on the output and how the thickness of the component and mass flow rate influences the output. The output of the system is the temperature of the water exiting the tube. The PV-T collector is composed of several layers;

- a glass cover
- PV solar cell layer
- tedlar
- an absorber
- tube
- water
- thermal insulation

#### 3.5.1 Genetic algorithm

The Genetic algorithm (GA) is used to optimize the design parameters of the water-based hybrid PV-T collector. The design parameters that are taken into account in the first part are;

- thickness of a glass cover ( $l_g$ )
- thickness of the tedlar ( $l_t$ )
- thickness of an absorber ( $l_r$ )
- insulator thickness ( $l_i$ )

The upper and lower bounds of each design parameter are set, as listed in Table 3.3. The genetic algorithm is an optimization method that mimics the behavior of natural selection and is commonly used to generate high-quality solutions to optimization by relying on biologically inspired operators.

TABLE 3.3: Lower and upper bounds of the design parameters.

Design parameters	$l_g$ (mm)	$l_t$ (mm)	$l_r$ (mm)	$l_i$ (mm)
upper bound	5	1.5	2	80
lower bound	2	0.5	0.5	10

The first thing is a selection of the best individuals with the best fitness, next is crossover in which two individuals are chosen and their genes are combined to produce a new one and lastly, mutation introduces a random change to create a new one and this is performed until the best solution is achieved. The method tries to

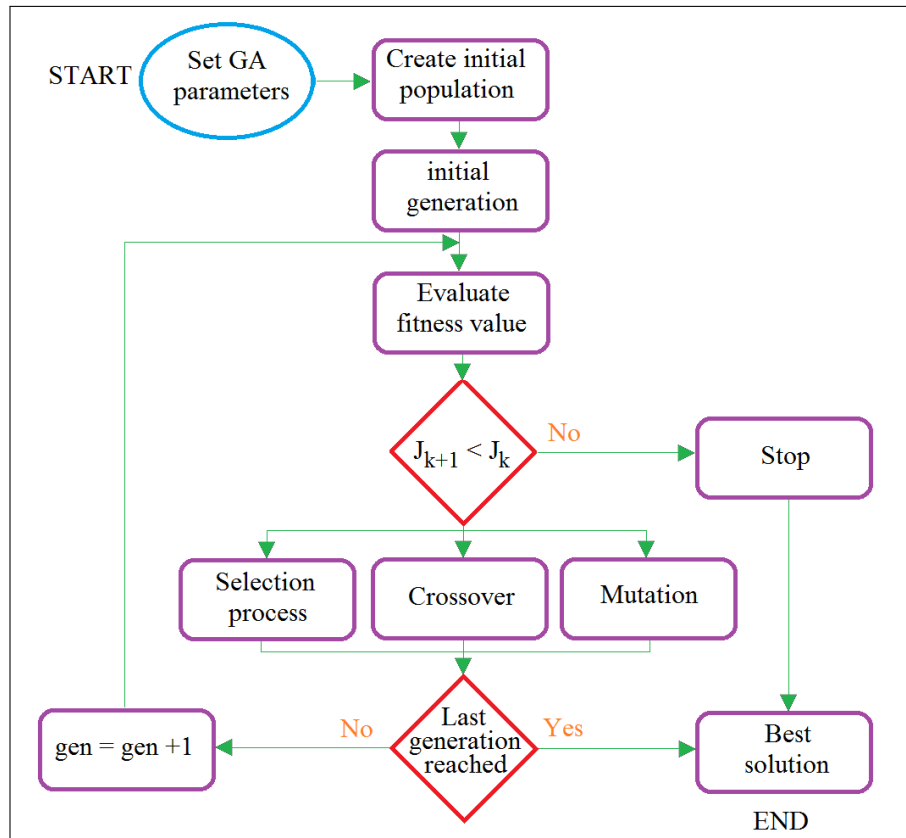


FIGURE 3.9: Genetic algorithm flowchart.

find the minimum of function  $f(p)$  by selecting  $p$  using the rules of natural selection and these rules can be implemented in various ways. To minimize the function, the following steps can be followed. The first step is to generate an initial population of design parameters randomly where each individual is defined by a different  $p$  and the individuals respect the defined boundaries of  $p$  where optimal solutions are likely to be found. The next step is to evaluate  $f(p)$  and calculate the fitness of each individual. The third step is to select a portion of the existing population to breed a new generation. The flow chart of the genetic algorithm with all the steps is presented in Figure 3.9.

The diversity is maintained which enhances the capacity of finding a global minimum. The top 10% individuals are chosen that are fairly different using the fitness-based process. It is quite difficult or even impossible to define a fitness expression and in some cases, a simulation may be used to determine the fitness function value. Lastly, the remaining 90% of the population is generated using the rules that resemble the behavior of a child's genes to its parents or in other words share many of the characteristics of its parents. For the simulation part, the MATLAB takes the binary string, represents  $p$  of each parent and merges them in a similar way, how genes behave in reproduction with crossover and random selection of genes of both parents. The new individual genes are bound to observe the defined boundaries of  $p$  and must resemble the parents, inheriting the best traits from each parent. After having a new generation, this generational process is repeated until a termination condition has been reached that can be a solution is found that satisfies minimum criteria, a fixed number of generations reached, a solution has reached a point such that successive iterations no longer produce better results or a combination of the mentioned

criteria. Here, it stops when a given number of a period is achieved when the function stops to make a difference between the two different functions. To achieve a good balance between optimum results and optimization time, the GA parameters should be selected with suitable values that are provided in Table 3.4.

TABLE 3.4: Genetic algorithm optimization parameters.

Parameters	Value
population size	500
crossover rate	0.8
mutation rate	0.05
maximum number of generations	1000

The dynamical system can be expressed as:

$$\dot{x} = f(x, p) \quad (3.56)$$

where  $p$  are the parameters that can change to minimize the function and the state vector  $x$  is given by

$$[T_g \ T_c \ T_t \ T_r \ T_m \ T_w \ T_i]^T \quad (3.57)$$

The aim is to maximize the outlet temperature of the water  $T_{wo}$  which is a complex task since the output is a function of the states and the time, respectively. It would be much better to use the calculus of variations and the theory of optimal control approach to perform such a task where  $p$  could be selected as a control variable and maximize the cost function  $J$  which is described as

$$J = \int_0^T T_{wo}(x(t), p) dt \quad (3.58)$$

This generates a Two-Point Boundary Value Problem that minimizes (3.58), locally but this is a complex task to solve numerically. Therefore, it is better to try to optimize the mean of the output function. The cost function is given by

$$J = -\overline{T_{wo}} = -\frac{\int_0^T T_{wo}(x(t)) dt}{T} \quad (3.59)$$

Since the genetic algorithm only minimizes function and minimizing the negative of a cost function is effectively maximizing it. It should be noted that in (3.59), once the initial conditions for  $x$  are defined and the decision vector that is control vector  $p = [l_g \ l_t \ l_r \ l_i]^T$  in the optimal control problem, the above system can be solved. The state vector is in fact just a function of time or in the context of optimization, defining the initial conditions for the given system, its solution is a function of the thickness of the layers ( $l_g$ ,  $l_t$ ,  $l_r$  and  $l_i$ ). Since the solution of the above mentioned system is found through a numerical algorithm, (3.59) is not an effective approach in getting the  $\overline{T_{wo}}$ . Numerically, it is more efficient to just compute in all-time steps that there is a solution for the states and use the discrete formula for the mean, which can be described by the following expression

$$J = -\overline{T_{wo}} = -\frac{\sum_{i=1}^N T_{wo}(t_i)}{N} \quad (3.60)$$

Therefore, now there is a need to minimize (3.60) with the proposed algorithm and  $N$  represents the number of time steps. However, this would generate an obvious solution because an increase or decrease in parameter thickness either will increase the outlet temperature of an air-channel to the maximum possible value or decrease it to the lowest value. To counter this, the inclusion of price limitations for each component is a good way to solve the problem. It is assumed that the price of the variables is a linear function of the variable itself and can be expressed as:

$$P = P_g l_g + P_t l_t + P_r l_r + P_i l_i, \quad (3.61)$$

where  $P_g$ ,  $P_t$ ,  $P_r$  and  $P_i$  are the price per thickness of the variables  $l_g$ ,  $l_t$ ,  $l_r$  and  $l_i$ . The price per thickness is measured as a proportion of average price per thickness. The proportions considered for this problem are ( $P_g = 0.433P_{avg}$ ,  $P_t = 0.067P_{avg}$ ,  $P_r = 0.333P_{avg}$  and  $P_i = 0.167P_{avg}$ ). Where  $P_{avg}$  is the average price per thickness. Using (3.61), the new objective function becomes:

$$J_{obj} = -\overline{T_{wo}} + \zeta(P - P_{des})^2, \quad (3.62)$$

where  $\zeta$  is the enforcing desired price, the higher the value of  $\zeta$ , the closer the actual price will be to the desired price and  $P_{des}$  represents the desired price.

With an increase in mass flow rate, the fan power consumption increases which leads to a reduction in photovoltaic efficiency. The upper and lower bounds of mass flow are set as  $0.05 \text{ kgs}^{-1}$  and  $0.005 \text{ kgs}^{-1}$ . As mentioned previously that if the mass flow is optimized by maximizing the output, this would generate an obvious solution. In this case, the inclusion of maximizing PV efficiency is a good way to solve the problem. Therefore, the objective function for this case can be expressed as;

$$J_{obj2} = -Y\overline{T_{wo}} - (1 - Y) \frac{\sum_{i=1}^N \eta_{ele}(t_i)}{N}, \quad (3.63)$$

where the constant  $Y$  is in the range  $[0,1]$ . This way by choosing  $Y$  as one, just the output is maximized and choosing  $Y$  equal to zero, maximizes the PV efficiency only. A value between zero and one will be a combination of both depending on which parameter matters the most. It should be noted that similar GA parameters provided in Table 3.4 are chosen for the mass flow rate case as well.

## 3.6 Results and discussion

### 3.6.1 PV-T collector with embedded tank

The performance of the collector highly depends on parameters such as surrounding temperature, wind speed, solar radiation, mass flow rate, type of fluid, materials used and thickness of various layers that are provided in Tables 3.2 and 3.5. The inclusion of a glass cover on top not only protects the PV module but increases the PV cell temperature due to which the temperature of the fluid, flowing within the serpentine tube increases. Ambient temperature and solar radiation vary, depending on the weather conditions. Three different cases are considered for this study with different solar radiation, ambient temperature and inlet temperature of the tank that are presented in Table 3.5.

The values considered in these cases are for the summer season with

- Case-I represents daytime when the solar radiation is maximum ( $850 \text{ Wm}^{-2}$ ) which occurs at noon when the ambient temperature is maximum too ( $35^\circ\text{C}$ ).

TABLE 3.5: Ambient conditions considered for three different cases

Cases	$T_{am}$ ( $^{\circ}\text{C}$ )	$I_{sun}$ ( $\text{Wm}^{-2}$ )	$T_{ta,i}$ ( $^{\circ}\text{C}$ )
Case-I	35	850	20
Case-II	30	600	15
Case-III	28	250	15

- Case-II represents the morning time of the peak summer or it could also represent the time between winter and peak summer seasons.
- In Case-III, the ambient conditions are for a cloudy season when limited solar radiation is available that is  $250 \text{ Wm}^{-2}$ .

The mass flow rate and wind speed in these cases are fixed to  $V_w = 2 \text{ ms}^{-1}$  and  $\dot{m}_w = 0.02 \text{ kg}^{-1}$ . An air gap with a depth of 0.02 m is included between glass and PV components for case-I which makes a rise in PV cell temperature and due to this, the fluid temperature in the serpentine tube rises and as a consequence of this, the tank temperature also rises as shown in Figure 3.10. However, the PV efficiency drops with every rise of  $1^{\circ}\text{C}$  in cell temperature. The temperature of PV module components is highest in all of the cases with the PV cell temperature going to approximately  $56^{\circ}\text{C}$  for case-I using a gap between the glass and PV cell components. It is obvious that the PV cell temperature is higher than the other component's temperature whatever the value of solar radiation and ambient temperature. The additional temperature of PV-T components for physical analysis for the three cases with  $0.01 \text{ kgs}^{-1}$  mass flow are provided in Table B.1 in appendix B. In Figure 3.11, average temperature

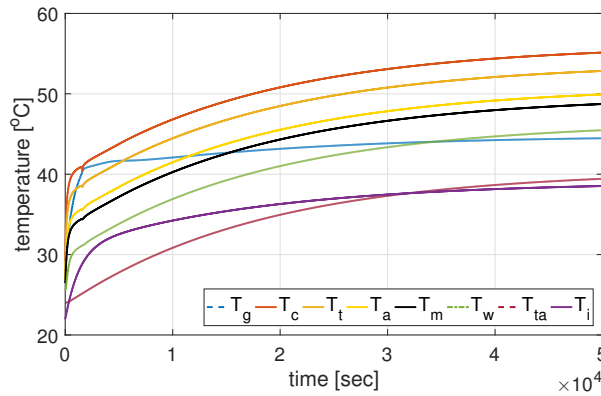


FIGURE 3.10: Average temperature evolution of each component of the collector for case-I with an air-gap between the glass cover and PV cell layer.

evolution for a similar case is presented and it can be observed that with no air gap, the temperatures of all the components of the collector excluding the glass cover fall and this temperature drop increase the PV efficiency but the thermal efficiency of the system deteriorates. Figure 3.12 presents the average temperature evolution for the second case and here the results indicate that with the decrease in ambient conditions and by decreasing the inlet temperature of the storage unit, the temperature of all the PV-T components falls. The cell temperature changes from  $52^{\circ}\text{C}$  to  $39^{\circ}\text{C}$

whereas the storage tank temperature comes to approximately  $29^{\circ}\text{C}$  from  $38^{\circ}\text{C}$ . Similar temperature evolution curves are obtained for the third case and the final temperature for each component is provided in Table 3.6. Since the storage tank is just beneath the absorber layer, the temperature for the top components initially rises faster and then the temperature rise is slow due to the high volume of water in the tank.

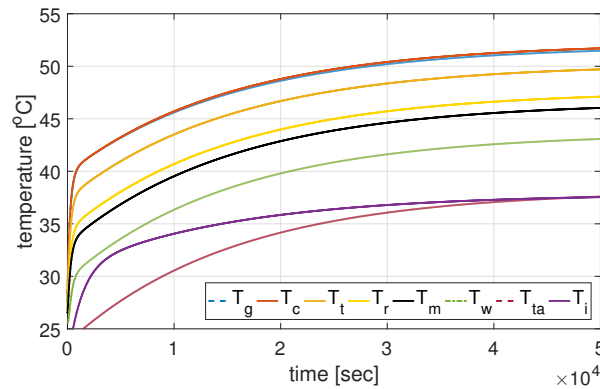


FIGURE 3.11: Average temperature evolution of each component of the collector for case-I without an air-gap between the glass cover and PV cell layer.

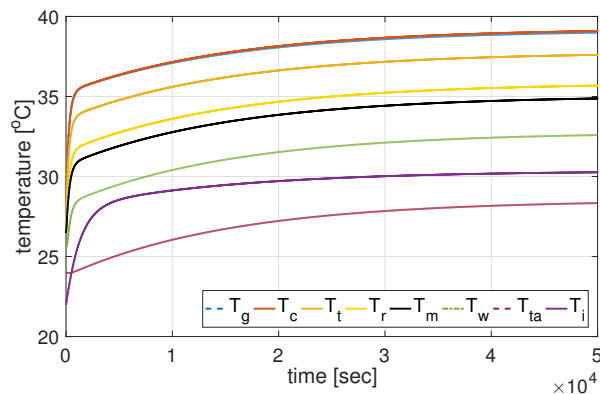


FIGURE 3.12: Average temperature evolution of each component of the collector for case-II without an air-gap between the glass cover and PV cell layer.

The PV efficiency of a collector is presented in Figure 3.13 and the results indicate that with an increase in solar radiation, the PV efficiency decreases. It is 14.93% for case-I whereas it is 16.50% at low solar radiation and ambient temperature when the PV cell temperature is close to normal operating temperature. The thermal efficiency for the first case is 47.47% whereas it drops to 40% for case-II. The drop is not only because of the ambient conditions but also due to the low inlet temperature injected to the tank.

In computational fluid dynamic studies, the same three cases are simulated using ANSYS. Three temperatures are very important, PV cell layer, serpentine fluid and tank temperature. The PV cell and serpentine fluid temperatures directly affect the PV efficiency whereas serpentine fluid and tank temperatures directly affect

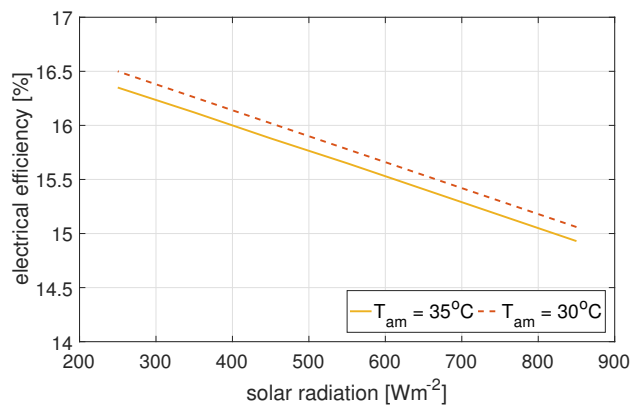


FIGURE 3.13: Variation of PV efficiency and solar radiation.

the thermal efficiency of the system. The temperature distribution of the PV cell is illustrated in Figure 3.14a. The average temperature of the component calculated is 53.80°C for case-I, 40.94°C for the second case and 28.76°C for the third weather conditions. It can be noticed that the edges of the PV component have higher temperatures compared to the center. This is because the storage unit and serpentine tube lie in the center and extract the heat from the PV module. The serpentine tube consists of two main parts, the first is the serpentine tube and another is the heat exchanger and its effectiveness is assumed as 0.40. The serpentine tube is fixed at the back of the absorber plate and absorbs the heat stored in the PV layer and transfers it to the tank fluid via a heat exchanger.

Figure 3.14b shows the temperature distribution of the fluid circulating within the serpentine tube. The average temperature of the fluid found is 43.63°C for the first case, 33.16°C for the second case and 26.31°C for the last case. It can also be seen that the temperature of the heat exchanger and serpentine tube region is different from one another. The temperature distribution of the storage tank with different inlet storage tank temperature is presented in Figure 3.14c where the temperatures are 37.10°C, 26.78°C, 20.74°C, respectively for the three cases. The temperatures on the top side of the tank fluid are high in all cases because the absorber also transfers some heat to the tank fluid and decreases in the direction of the ground. For case-I, the remaining components (i.e. glass, tedlar and absorber) temperature distribution is presented in Figure B.4 in appendix B having almost the same temperature.

The obtained physical results are compared with CFD results and are summarized in Table 3.6. It can be seen that the physical results are close to the ones obtained using the CFD study with the average error found in case-I is 3.40%, 4.10% for the second case and 2.87% for the third case. The error found for each component in all three cases is presented in Table B.2 in appendix B. The possible reasons that small differences occur are due to the heat exchanger effectiveness in the physical model which is assumed as a constant. In reality or in CFD analysis this value continuously changes depending on the flow rate and component temperature. Mesh structure and convergence criteria of the CFD model are other possible reasons. As a general conclusion, the simulation results are founded on the model developed in this study and the CFD studies validate the viability of the proposed model.

The thermal performance of a system is evaluated where the influence of various parameters is presented that are absorber and thermal insulation.

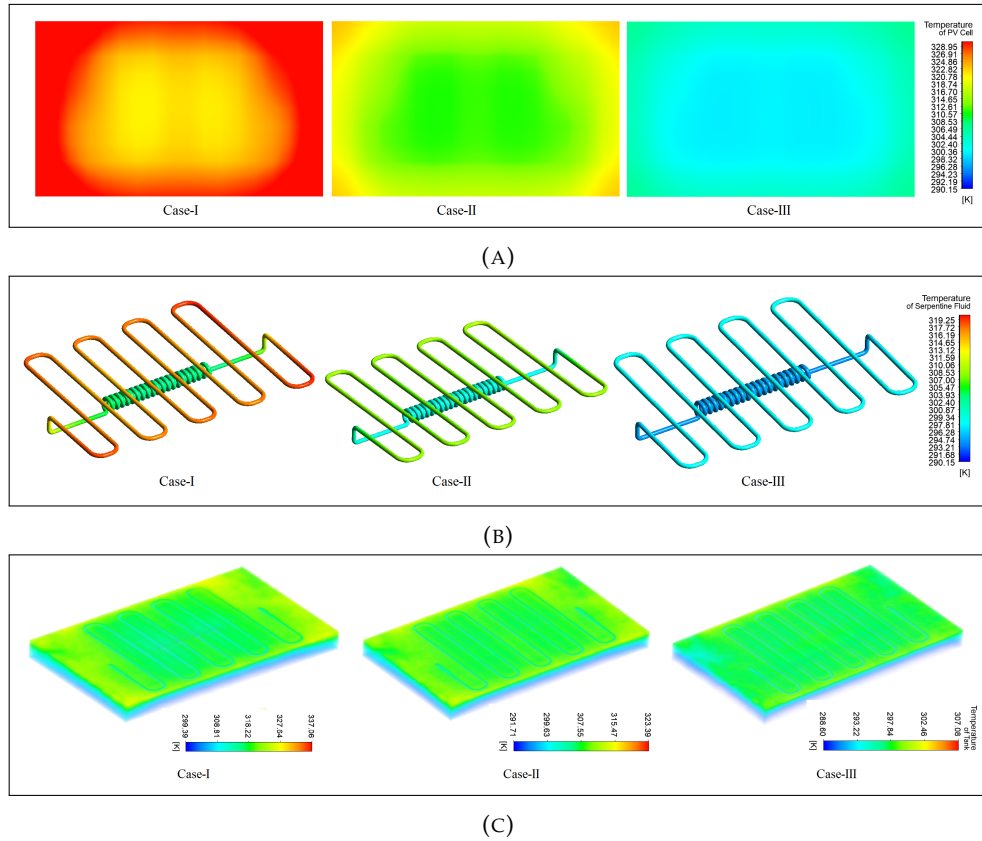


FIGURE 3.14: Temperature distributions for the three different cases (a) PV cell layer. (b) Serpentine tube fluid. (c) Storage tank fluid.

TABLE 3.6: Temperature of the PV-T collector components for physical and CFD analysis.

Component	Temperature ( $^{\circ}\text{C}$ )					
	Case I		Case II		Case III	
	Physical	CFD	Physical	CFD	Physical	CFD
Glass	51.83	53.59	39.10	40.81	29.20	28.75
PV cell	52.07	53.80	39.21	40.94	29.22	28.76
Tedlar	50.08	53.39	37.72	39.59	28.50	28.53
Absorber	47.49	51.20	35.81	38.01	27.61	28.14
Serpentine tube	46.43	46.55	35.00	34.33	27.22	26.04
Serpentine fluid	43.48	43.63	32.72	33.16	26.03	26.31
Storage tank	38.02	37.10	28.48	26.78	22.02	20.74
Insulator	37.75	36.12	30.33	28.91	26.35	24.59

### Influence of thickness

The insulator thickness directly affects the tank temperature and the results indicate that with a thickness of 0.025 m, tank temperature is approximately  $35^{\circ}\text{C}$ . The thickness is increased to 0.05 m and then to 0.08 m, the storage tank temperature rises to approximately  $36^{\circ}\text{C}$  and above  $37^{\circ}\text{C}$ . Higher storage tank temperature can be achieved with high insulator thickness but for economical reasons, a thickness of more than 0.10 m is not required as the energy losses become constant. Further,

the absorber thickness is decreased from 1 mm to 0.75 mm and then to 0.50 mm. The results show that by decreasing the thickness of an absorber, serpentine fluid temperature increases approximately  $1^{\circ}\text{C}$  which means there is some rise in storage tank temperature, as well. It is worth it to mention that when the serpentine tube temperature increases, the PV cell temperature drops and increases the PV efficiency of the collector.

### Influence of material

In PV-T system design, the material of the components plays a crucial role in acquiring high energy conversion efficiency and cost-effectiveness. For all the three mentioned above, aluminium is used as an absorber material whereas copper is used as a serpentine tube material. It is a good option to change the material of the two components to know how it affects the fluid temperature flowing within the serpentine tube. The average serpentine fluid temperature drops from  $43.63^{\circ}\text{C}$  to  $43^{\circ}\text{C}$  by changing tube material from copper to aluminium. This is because copper has high thermal conductivity but aluminium is lighter, has no corrosion issues and is a bit cheaper as compared to copper. Similarly, the results indicate that by changing the absorber material from aluminium to copper, the average temperature of the fluid rises from  $43.63^{\circ}\text{C}$  to  $44.39^{\circ}\text{C}$ . It is also noticed that the increase in outlet temperature of the tube is much higher than the average fluid temperature using copper as a material. Similar temperature differences are obtained by changing the material and thickness with the physical model.

Further, used engine oil is used as an absorber material to know its influence and because of its thermo-physical properties. The obtained results indicate that the tank temperature rises to  $40.37^{\circ}\text{C}$  from  $37.10^{\circ}\text{C}$ . Another interesting observation is that using engine oil extracts more heat from the PV module by reducing the cell temperature from  $53.80^{\circ}\text{C}$  to  $52.79^{\circ}\text{C}$ .

### Influence of heat extraction medium

Heat extraction medium is important and the influence of it is analyzed by taking various fluids for the serpentine tube that are water mixed with glycol, pure glycol and phase change material (i.e Paraffin wax). For the initial results, pure water is considered as it is easily available but using water has some drawbacks i.e freezing, low heat transfer as compared to other liquids. The results in Table 3.7 indicate that the temperature of the fluid goes to approximately  $47^{\circ}\text{C}$  from  $43.63^{\circ}\text{C}$  for pure glycol and PCM whereas the tank temperature rises to approximately  $45^{\circ}\text{C}$ . Water mixed with glycol is a good option as it is cheaper and has better heat transfer compared to pure water.

TABLE 3.7: Influence of heat extraction fluid running within the serpentine tube.

Fluid	$T_w (^{\circ}\text{C})$	$T_{ta} (^{\circ}\text{C})$
pure water	43.63	37.10
pure glycol	46.86	45.10
water/glycol 50wt%	45.45	43.71
paraffin wax (PCM)	46.63	44.73

The results are mentioned for serpentine fluid and tank temperatures, additional results for all the remaining components temperature for glycol, water mixed with

glycol, PCM and used engine oil as an absorber are mentioned in Tables B.3 and B.4 in the Appendix B.

### Electrical resistance

Lastly, an electrical resistance is added when there is limited solar radiation available. It can be observed in Figure 3.15 that the temperature around the electrical resistance element area is very high as compared to the other part of the storage unit. The average temperature of the storage tank using a 250 W heater rises to 32.16°C with very limited solar radiation available. The location of a resistance heater is important, if it is close to the outlet point of the storage unit then the user will receive a high temperature compared to other locations. Usually, for the vertical storage tank, two resistance heaters are used, one on the top side and one on the bottom side. If two resistance heaters are used in this case, it will meet the user requirement considering that the required temperature by the user is 40°C. Approximately, 33°C temperature is calculated using the physical model with the same specifications.

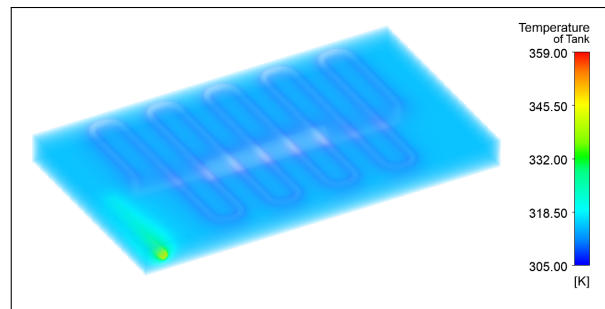


FIGURE 3.15: Temperature distributions of the storage tank fluid incorporating an electric heater.

### 3.6.2 Optimization

The Matlab program is used for the proposed genetic algorithm that offers the user a lot of flexibility and the ability to perform the optimization in parallel. The aim is to select the best vector  $p$  that minimizes the scalar function  $f(p)$ , also called the objective function. The function tolerance of  $1 \times 10^{-12}$  is used to calculate the stall generation, i.e., if the objective function during the optimization process does not vary more than this value, it has stalled or in other words, there is no room for improvement even if a smaller value is chosen. If the maximum number of generations that is 1000 is reached, the algorithm stops. The bounds of each design parameter are set, listed in Table 3.3 and the GA parameters are chosen with suitable values (see Table 3.4). Using upper and lower bounds, the obtained cell temperature, water outlet temperature and PV efficiency are listed in Table 3.8 by considering the ambient temperature of 35°C and solar radiation of  $850 \text{ Wm}^{-2}$ . It can be observed that there is a small difference in temperatures if the thickness is changed for a single collector but for big solar plants these small variations will make a big difference.

The optimized values obtained for glass thickness is 3.8 mm, tedlar thickness is 1.4 mm, absorber thickness is 0.9 mm and insulator thickness is 18 mm as shown in Figure 3.16a. Mass flow is very important as it directly affects cell temperature, PV efficiency and especially the water outlet temperature and the daily evolution is presented in Figure 3.17. Here  $Y$  (see (3.63)) is important which lies in the range

TABLE 3.8: Summary of temperatures and efficiency considering upper and lower bounds.

Component	$l$ (m)	$T_c$ ( $^{\circ}\text{C}$ )	$T_{wo}$ ( $^{\circ}\text{C}$ )	$\eta_{ele}$ (%)
glass ( $g$ )	0.002	49.70	43.16	14.97
	0.005	49.92	43.28	14.95
tedlar ( $t$ )	0.0005	48.69	44.26	15.04
	0.0015	50.60	42.44	14.90
absorber ( $r$ )	0.0005	49.85	43.23	14.95
	0.002	49.70	43.08	14.97
insulator ( $i$ )	0.01	48.84	42.21	15.03
	0.08	49.87	43.22	14.95

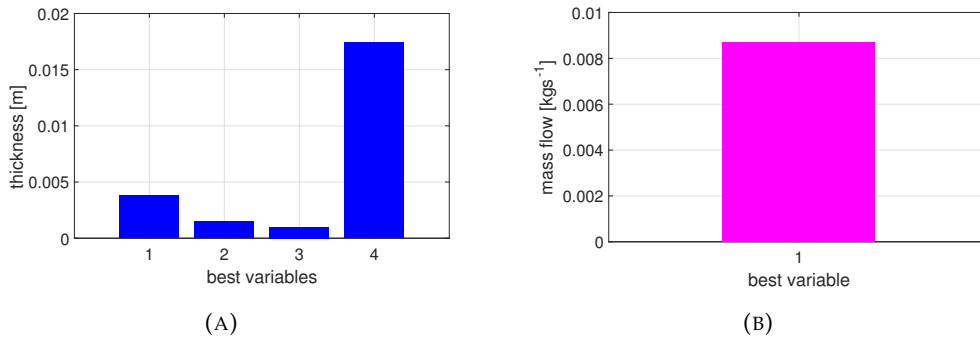


FIGURE 3.16: (a) Best thickness variables. (b) Best mass flow.

[0,1] so if it is chosen close to one, this means outlet water temperature is important whereas by taking it close to zero implies PV efficiency is important. Thus, the value of the outlet water temperature and PV efficiency lies between the two curves illustrated in Figure 3.17. The optimized value for the mass flow is  $0.008 \text{ kgs}^{-1}$  as

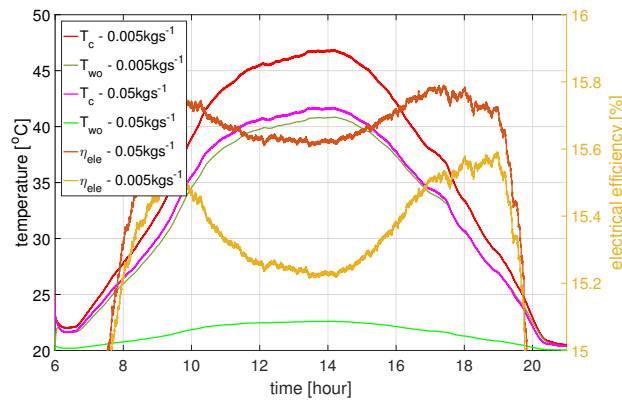


FIGURE 3.17: PV cell, outlet water temperature and PV efficiency evolution with high mass flow and low mass flow.

presented in Figure 3.16b by taking a suitable  $Y$  considering maximum output and PV efficiency. Using these values, the optimized value of outlet water temperature, cell temperature and PV efficiency are illustrated in Figure 3.18 that are  $37^{\circ}\text{C}$ ,  $48^{\circ}\text{C}$  and 15%.

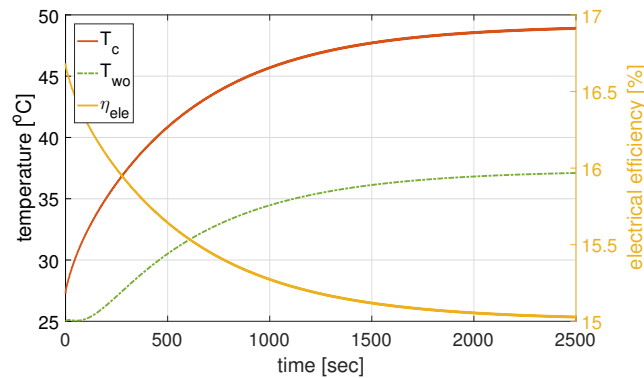


FIGURE 3.18: PV cell, outlet water temperature and PV efficiency with optimized thickness and mass flow.

### 3.7 Conclusion

In this Chapter, a new design of a PV-T collector integrating a storage tank and its complete thermal model is proposed. The consistency of the physical model has been validated by comparing the results with the CFD results. The occurring differences are small enough to be considered due to the assumptions considered in the physical model and mesh structure and convergence criteria in the CFD study. The following conclusions can be drawn;

- The inclusion of an air gap increases the temperature of all the components enhancing the thermal efficiency but at the cost of PV efficiency.
- A thickness of more than 0.08 m is not required because of economical reasons and the energy losses become constant.
- Using copper as an absorber and serpentine tube material, the fluid temperature rises whereas it drops with an increase in absorber plate thickness.
- Heat extraction medium is an important design parameter, and the obtained results indicate that water mixed with glycol is a good choice as it is easily available and cheaper whereas pure glycol and PCM have a high heat transfer rate.
- The abundance of used or waste engine oils can be recycled, making the system less expensive and ensuring environmental sustainability.
- Storage tank is integrated with a resistance heater as a backup to ensure continuous use during the winter season, or on a cloudy day to compensate the temperature reduction.

Further, a genetic algorithm is used to perform the optimization. It is observed that there occur small differences in the temperature when the component thickness is changed but for big plants, these small variations will make a big difference. The obtained results showed the control parameter (mass flow rate) is an important parameter directly affecting the outlet water temperature and lower values of it reduce the cost and PV efficiency.

## Chapter 4

# Observation and Control

The content of this chapter is control and observation of hybrid PV-T systems. To design a controller for a process, it is necessary for one to know the mathematical model of the process. The proposed mathematical models describe the real system but there is always uncertainty because of disturbances and unpredictable dynamics. The controllers are designed so that certain designated signals, such as tracking errors are minimized but doing it is not an easy task because there are uncertainties, errors in measuring signals and trade-offs in design, such as stability. In general, the aim is to make the output behave in the desired way by manipulating the control input.

In the first half of the chapter, numerous controllers are designed to track the desired output temperature of the collector even with the presence of disturbances. The control strategies employed in the past such as MPPT, model predictive and fuzzy logic control are for PV systems only to ensure a good extraction of the maximal electrical power (Rezk et al., 2019; Metry et al., 2016). Different types of controllers can be utilized to control the collector temperature and (Kalogirou, 2003) covers relative temperature ranges required for various solar industrial processes. Simple control loops were utilized by Allouhi et al. (2017) for a milk processing industry that compared the temperature in the hot side of the heat exchanger with the bottom of the solar tank, to activate/deactivate the pump of the secondary circuit. A PID type controller was designed by Hassine et al. (2014) for a solar thermal plant to regulate the supply temperature. In (Álvarez et al., 2016), a model predictive control (MPC) algorithm for a low-temperature thermosolar plant was proposed to optimally manage the changes between the different operating modes of the facility. However, this strategy needs an accurate prediction model of the process. A robust controller for a heat exchanger is designed by Vasičkaninová et al. (2018) using six different robust control approaches for a real-time laboratory platform and the  $H_\infty$  and  $H_2$  controllers are recommended on the basis of robustness, performance, and controller structure. A new nonlinear H-infinity control approach for optimizing olive-oil extraction and a nonlinear H-infinity control approach to the problem of control of closed-chain robotic mechanisms is presented in (Rigatos et al., 2018; Rigatos, Siano, and Pomares, 2017) where the stability properties of the control scheme are proven through Lyapunov analysis.

In the second half of the chapter, two different observers are designed for the water-based PV-T collector. Designing observers for nonlinear systems is a challenging problem due to its importance in automatic control design such as control, monitoring and fault diagnosis. Observers are the dynamic systems that provide an estimate of the internal state of a plant using its input-output measurements (Kalsi et al., 2010). In the context of observer's design, several works have been proposed for state estimation (Akhenak, 2004; Ichalal, Mammar, and Ragot, 2016). A general observer theory is developed with an emphasis on a single output system and a

new procedure, based on a special canonical form for multiple-output systems has been developed by Luenberger (1966). A new air-based mathematical model and its fractional-order observer in the time domain was established by Ouhsaine et al. (2017). The temperatures of all nodes are estimated and the asymptotic stability of the estimation error is analyzed. Further, linear matrix inequality (LMI) is used to compute the observer gains. A real-time Luenberger type state observer is designed by Kicsiny and Varga (2012) for solar thermal heating system and the algorithm for the practical use is presented. Wang, Rosas, and Qian (2015) designed a non-linear observer for solar heater system considering only four components to estimate the missing state variables. A comparative study has been performed both numerically and experimentally by Wang and Gao (2003) to analyze the performances and characteristics of high-gain, sliding-mode, and extended state observers.

A simple method to design a full-order observer for linear systems with unknown inputs is presented by Darouach, Zasadzinski, and Xu (1994) along with two examples and necessary conditions for the existence of the observer were provided. A full-order state observer for bounded inputs bilinear systems subjected to unknown disturbances is designed and investigated by Rafaralahy et al. (1996) based on gain optimization of both the linear and the bilinear parts of the observation error dynamics. It was concluded that the proposed observers are applicable to a large class of bilinear systems subjected to unknown disturbances. An unknown input fuzzy bilinear fault diagnosis observer is designed by Saoudi, Chadli, and Braiek (2013) for dynamic systems that can be described by Takagi-Sugeno fuzzy bilinear models subject to unknown disturbance. A design procedure for full-order and reduced-order observers with unknown inputs is presented using two different approaches (Hui and Žak, 2005). The state of the observed system is decomposed into known and unknown components in the first approach whereas the second approach combines sliding modes.

## 4.1 Air-based model

### 4.1.1 PI-controller design

A proportional, integral and derivative (PID) controller is a feedback controller that is widely used in the HVAC industry and industrial control systems. The controller assists to track the desired set point despite the presence of disturbances. The output temperature of the collector representing the main factor and should be controlled. The airflow rate is used as a control variable to adjust the desired temperature. Thus, the controlled variable is measured and compared to the reference one. The error is used as the input of the controller that, calculates the new control signal which is sent to the plant as shown in Figure 4.1. The advantage of using a PI controller is that the steady-state error is eliminated which is important when using an average transfer function but with a narrower range of stability. The controller is more suitable for practical implementation, therefore, a PI controller is designed for air-based model-I, based on the transfer function obtained in (2.32).

$$G_{avg}(s) = \frac{b}{s + a} \quad (4.1)$$

The continuous transfer function of PI controller is obtained through Laplace transform as:

$$C(s) = K_p + \frac{K_i}{s} \quad (4.2)$$

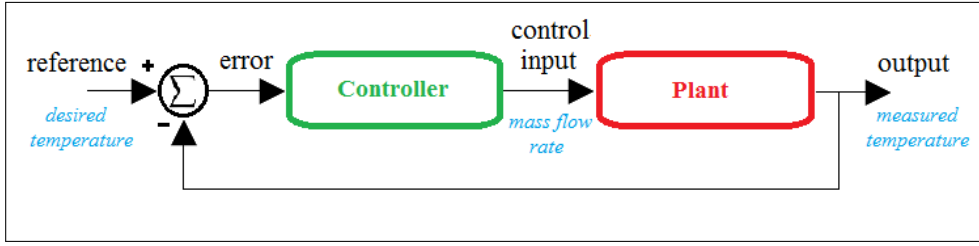


FIGURE 4.1: Simple feedback control loop.

The transfer function of the closed loop system from reference to output is  $F(s)$ .

$$F(s) = \frac{b(K_p s + K_i)}{s^2 + (a + bK_p)s + bK_i} \quad (4.3)$$

This transfer function  $F(s)$  denominator which is closed loop characteristic polynomial is compared with the second order general equation (4.4), assuming that desired characteristic polynomial is;

$$s^2 + 2\zeta\omega_0 s + \omega_0^2 \quad (4.4)$$

The controller parameters are then given by

$$K_p = \frac{2\zeta\omega_0 - a}{b} \quad (4.5)$$

$$K_i = \frac{\omega_0^2}{b} \quad (4.6)$$

The parameter  $\omega_0$  determines the response speed while  $\zeta$  relates to the damping.

#### 4.1.2 H-infinity using feedback control approach

H-infinity control methods are designed to achieve stabilization with guaranteed performance. The section proposes a control method for feedback control of the thermal model of an air-based PV-T model-II. The linearization is based on the computation of the system's Jacobian matrices round its current operating point. Next, for the linearized equivalent model of the collector, an H-infinity feedback controller is designed. This requires the solution of an algebraic Riccati equation at each time-step of the control algorithm. The efficiency of the control scheme is displayed analytically.

The initial nonlinear thermal model of the collector is described in the form

$$\dot{x} = f(x, u, v) \quad x \in \mathbb{R}^m, u \in \mathbb{R}^n, v \in \mathbb{R}^q \quad (4.7)$$

where  $u$  is the control input that is the mass flow rate  $\dot{m}_f$ ,  $v$  are the external disturbances that include solar radiation  $I_{sun}$ , ambient temperature  $T_{am}$  and the wind speed  $V_w$  with bounded values and these disturbances are assumed to be known. The state vector  $x$  contains the temperatures of each layer as state variables and is written as;

$$x = [x_1 \ x_2 \ x_3]^T = [T_g \ T_c \ T_i]^T \quad (4.8)$$

The output of the system is the outlet temperature of the fluid  $T_{f,o}$  from the air channel of the PV-T collector.

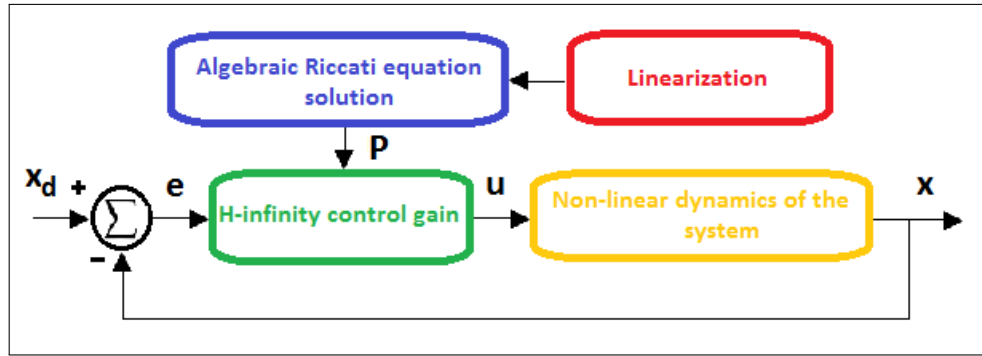


FIGURE 4.2: Control scheme for hybrid PV-T thermal model.

### Linearization of the thermal model

Here, the linearization of the thermal model is performed at each iteration of the control method round its current operating point  $(x^*, u^*)$ .  $x^*$  is the present value of the system's state vector and  $u^*$  is the last sampled value of the control input that was exerted on the PV-T system. The linearized form of the thermal model of the PV-T collector in Chapter 2 can be efficiently controlled after applying an H-infinity control method.

### H-infinity feedback control

The H-infinity controller stands for the solution of the optimal control problem under external perturbations. The solution of a min-max is represented in which perturbation tries to maximize the cost function whereas the control input tries to minimize a cost function that comprises a quadratic term of the state vector's tracking error. Since it is a feedback control problem so the output is translated to the states in order to design a controller. The states are found that are compatible with the output and the controller will aim to track these desired states which makes output track the desired output. The control scheme for the proposed thermal model is presented in Figure 4.2.

The reference setpoints for the state vector is described as  $x_d = [T_{gd} \ T_{cd} \ T_{id}]^T$ . The tracking of the setpoints is achieved by applying the control input. It is assumed that the control input  $u$  differs from the control input  $u_d$  at every time instant. The quadratic cost function incorporates the disturbance effects. The problem of disturbance rejection for the thermal model that is linearized in the above section and is described as (2.41) needs to be managed efficiently. Because of the perturbation term  $v$  that exists in the system, a classical LQR control approach cannot be considered for such a problem. Unlike PID control, the stability of the control loop is assured in the case of changes of operating points.

In this H-infinity control scheme, a feedback control method is designed to track the system state vector and simultaneously consider the worst possible disturbances that affect the collector performance. The disturbance maximizes the cost function and a control signal is computed to minimize the worst possible disturbance imposed externally onto the PV-T system. The controller design is based on min-max optimization where there could exist the worst possible disturbance. Although, the optimization problem solution is directly connected to parameter  $\rho$ . The parameter  $\rho$  determines the reward of the disturbances effects whereas parameter  $r$  finds out the penalization of the control input and the parameters  $r, \rho > 0$ . The optimal feedback

law is written in the form

$$u(t) = -Kx(t), \quad (4.9)$$

with the feedback control gain  $K$  given by

$$K = \frac{1}{r} B^T P, \quad (4.10)$$

where  $P$  is a positive semi-definite symmetric matrix that can be found from the Riccati equation solution

$$A^T P + PA + Q - P \left( \frac{2}{r} BB^T - \frac{1}{\rho^2} EE^T \right) P = 0, \quad (4.11)$$

In such a case to find the stabilizing feedback control an algebraic Riccati equation has to be repetitively solved at each iteration of the control algorithm. The riccati equation is based on the H-infinity controller and minimizes the cost function. The matrix  $Q$  is a positive definite symmetric matrix. The outcome of the Riccati equation is a positive definite symmetric matrix  $P$  and the values of the matrix depend on the values of parameters  $\rho$  and  $r$ . The parameter  $\rho$  must be greater than the lower bound  $\rho_{min}$  for which the H-infinity control problem has a solution. In other words, the satisfactory value of  $\rho$  lies in the interval  $[\rho_{min}, \infty]$ .

The above mentioned control algorithm is based on state feedback and regulates the state variables. The aim of this study is to track the desired output that is outlet temperature of the fluid  $T_{f,od}$  coming from the air channel. The structure of the controller becomes

$$u(t) = -K(x(t) - x_d(t)) + u_d \quad (4.12)$$

where  $x_d$  and  $u_d$  are the desired states and desired control input. The desired output must be converted to the desired states and for that purpose, states and control input needs to be found, making  $\dot{T}_g, \dot{T}_c, \dot{T}_i$  and  $T_{f,o} - T_{f,od} = 0$  and the solution of this system is the desired state vector  $x_d$  and control input signal  $u_d$ . For each step, described as

$$x_d = [x_{1d} \ x_{2d} \ x_{3d}]^T = [T_{gd} \ T_{cd} \ T_{id}]^T \quad (4.13)$$

This completes the structure of the controller in order to track the desired output.

### 4.1.3 H-infinity control using mixed sensitivity approach

The need is to design a controller that is robust against all types of disturbances. Consider a general control configuration as presented in Figure 4.3, where  $K(s)$  is the controller to be designed,  $P(s)$  is the generalized plant that contains plant, weights, and uncertainties. The generalized plant has exogenous inputs  $w$  with disturbance  $v$  and reference  $r$ , a control input  $u$ , a controlled output  $z$  and a measured output  $y$ . The closed-loop transfer matrix from  $w$  to  $z$  is given by:

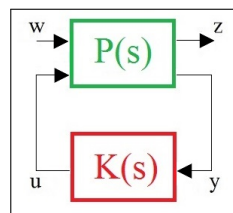


FIGURE 4.3: Generalized feedback system.

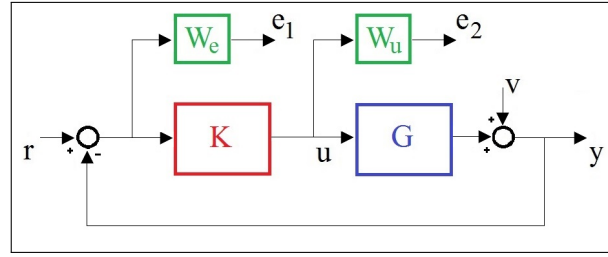


FIGURE 4.4: Complete control scheme.

$$T_{zw} = F_l(P, K) = P_{11} + P_{12}K(I - P_{22}K)^{-1}P_{21}, \quad (4.14)$$

where  $F_l(P, K)$  is referred to as lower linear fractional transformation of  $P$  and  $K$ . Thus, the designed controller should meet the internal stability of the closed-loop system and minimize the  $H_\infty$  norm of  $F_l(P, K)$  (You, Chen, and He, 2010). For the design of a controller, two templates  $W_e(s)$  and  $W_u(s)$  are considered for the sensitivity functions  $S$  and  $KS$  respectively. The structure of the templates is given by:

$$\frac{1}{W_e(s)} = \frac{s + \omega_b \epsilon_b}{s/M_s + \omega_b} \quad (4.15)$$

$$\frac{1}{W_u(s)} = \frac{\epsilon_1 s + \omega_{bc}}{s + \omega_{bc}/M_u} \quad (4.16)$$

Figure 4.4 shows the representation of the generalized control configuration of the system with all the inputs and outputs associated. The generalized plant  $P$  can be defined for the structure in Figure 4.4 as follows

$$P(s) = \begin{pmatrix} W_e & -W_e & -W_e G \\ 0 & 0 & W_u \\ 1 & -1 & -G \end{pmatrix} \quad (4.17)$$

The model is linearized around  $X_{1,eq} = 30$ ,  $X_{2,eq} = 41$  and  $X_{3,eq} = 25$  with  $U_{eq} = 0.05 \text{ kgs}^{-1}$  and a controller is designed. The transfer function obtained using linearized state space model is

$$G(s) = \frac{48s^3 + 1.80s^2 + 0.02s + 6e^{-5}}{s^3 + 0.04s^2 + 4.27e^{-4}s + 1.34e^{-6}} \quad (4.18)$$

The obtained transfer function is adequate for the purpose of control. For the templates, to define parameter  $W_e$ ,  $M_s = 2$  is opted to guarantee a reasonable module margin and parameter  $\epsilon_b$  is chosen 0.001 to make sure a steady-state approximately equal to zero. The choice of  $\omega_b$  impacts the closed-loop bandwidth of  $S$  and in order to acquire a tradeoff between a fast response of the system and robustness, we select  $\omega_b = 3$ . A higher value of  $\omega_b$  is chosen to make the system respond faster but there is a repercussion and will lose a little robustness. For specification of  $W_u$ ,  $\omega_{bc}$  is considered 4 related to the bandwidth of the sensitivity function  $KS$  and must be greater than  $\omega_b$  so that the controller can act over the plant. The parameter  $\epsilon_1$  is selected to be smaller (i.e., 0.0001) in order to get a good robust controller that rejects the disturbances.

The controller is calculated in the MATLAB with the function *hinfsyn* and  $\gamma = 0.505$  is obtained, that is satisfactory. In Figure 4.5, the templates used for the design

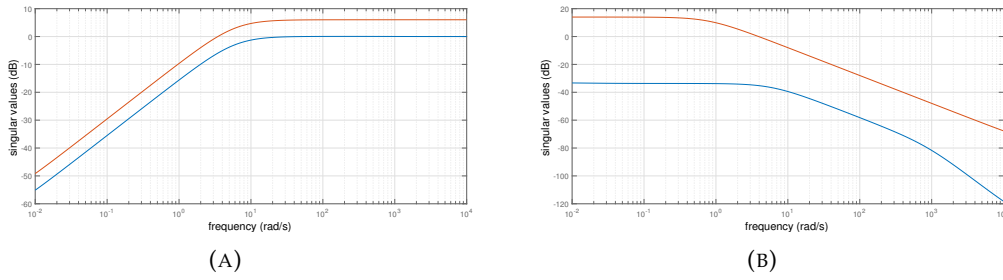


FIGURE 4.5: Sensitivity functions of the robust control system: (a) Sensitivity function. (b) Controller\*Sensitivity.

of the H-infinity controller (in red) and sensitivity functions are appreciated. Since the sensitivity functions are below the templates, the controller satisfies the design specifications. The controller can be written as;

$$K(s) = \frac{1.21e^{-7}s^5 + 7.55e^{-3}s^4 + 109s^3 + 4.16s^2 + 0.05s + 1.46e^{-4}}{s^5 + 886s^4 + 35s^3 + 0.46s^2 + 2.18e^{-3}s + 3.31e^{-6}}$$

It should be noted that the order 5 of the controller  $K(s)$  is quite high compared to the order 3 of the linear model. For the sake of simplicity, we considered model reduction such as *balred* in MATLAB that uses implicit balancing techniques to compute the reduced-order approximation. After several trials and assessments of model reduction, we selected the controller reduced model of order 2 which gives the best compromise between simplicity and performance:

$$K_{red}(s) = \frac{1.21e^{-7}s^2 + 0.12s + 1.80e^{-3}}{s^2 + 1.56e^{-2}s + 4.09e^{-5}}. \quad (4.19)$$

## 4.2 Water-based model

### 4.2.1 Sliding mode control

Sliding mode control (SMC) is a nonlinear control method that alters the dynamics of a nonlinear system by applying a discontinuous control signal. It has several practical applications, particularly in robotics i.e. motion control for jet-propelled marine vehicles. It features properties of accuracy, implementation, simplicity and robustness against parameter variations and disturbances. One major advantage of using SMC is the closed-loop response becomes totally insensitive to some particular uncertainties once in the sliding mode. In this study, the aim is to control the fluid output temperature  $T_{wo}$  to the desired value using mass flow rate  $\dot{m}_w$  as a control variable.

The approach is to design a control law that imposes all system trajectories to converge on a surface in the state space, also known as the sliding surface that is described as;

$$S = y - y_{ref} = 0 \quad (4.20)$$

such that the system trajectory exhibits desirable behavior. Thus, the time derivative of (4.20) is given by:

$$\dot{S} = \dot{y} - \dot{y}_{ref} = C\dot{x} + \bar{D}\dot{v} - \dot{y}_{ref} \quad (4.21)$$

using (2.63) in (4.21), one gets

$$\dot{S} = C(A\bar{x} + \bar{B}(\bar{x})u + \bar{G}v - P\dot{T}_{wi}) + \bar{D}\dot{v} - \dot{y}_{ref} \quad (4.22)$$

or equivalently

$$\dot{S} = CA\bar{x} + C\bar{B}(\bar{x})u + C\bar{G}v - CP\dot{T}_{wi} + \bar{D}\dot{v} - \dot{y}_{ref} \quad (4.23)$$

If  $\dot{S} = 0$  is taken into account, (4.23) yields equivalent control which allow us to cancel known terms on right hand side.

$$u_{eq} = -[C\bar{B}(\bar{x})]^{-1}[CA\bar{x} + C\bar{G}v - P\dot{T}_{wi} + \bar{D}\dot{v} - \dot{y}_{ref}] \quad (4.24)$$

If reachability condition  $S\dot{S} < 0$  is fulfilled, the switching surface is known to be attractive.

$$(y - y_{ref})(C\bar{B}(\bar{x})u_c) < 0 \quad (4.25)$$

The model was simulated using the following control law

$$u = u_c + u_{eq}, \quad (4.26)$$

where  $u_c$  ensures convergence to chosen surface and can be written as:

$$u_c = \lambda \text{sign}(y - y_{ref}) \quad (4.27)$$

Since,  $C\bar{B}(\bar{x})$  is negative,  $\lambda$  is taken as positive to satisfy (4.25).

## 4.2.2 Neural network control

A neural network is an effective tool for highly nonlinear systems and from the control point of view, it can be taken into consideration as a nonlinear dynamic block. Its performance is better than conventional control methods. In this section, numerous controllers based on the neural network are discussed in order to control the water output temperature. The neural network-based controllers are capable of controlling the PV-T system's outlet temperature by varying the mass flow rate. The presented techniques are practical and simple to construct and implement the controller.

### Basic neural network control

In this part, a simple neural network based control system is proposed and the approach is to train the controller by collecting data through simulations. Since the aim is to control mass flow and track the desired water temperature, so for training, the outputs are mass flow and electrical efficiency whereas water temperature, wind speed, ambient temperature and solar radiation are chosen as inputs. The hidden layers are located between the input and output layer where the data processing is done. The artificial neural network (ANN) goes into the training process for its learning and understanding the relationship between the inputs and outputs as discussed in detail in Chapter 2. Once the network is trained, the reference value for the output water temperature is set and the obtained mass flow can be directly injected to the nonlinear model. Basically, the controller is trained as an inverse model of the system and connected to it as shown in Figure 4.6.

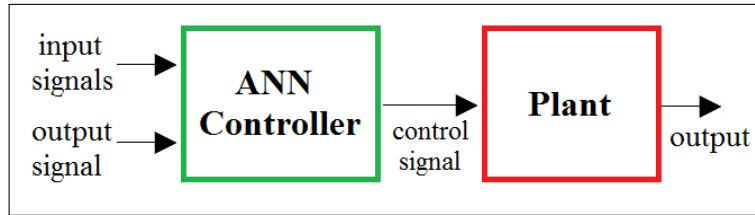


FIGURE 4.6: Scheme for a simple controller implementation.

### Neural network predictive control

In this part, a neural network model predictive controller for the system described in Chapter 2 is presented. It is basically a type of model-based predictive control, where the model for predictions is a neural network. It is based on solving an optimization problem for the control actions. The optimizer computes future control actions that minimize the difference between a model of the system and desired performance. Two steps are involved in the control procedure; the first step is system identification of the plant model, which is a multilayer network where the network is trained by making use of previous inputs and outputs to predict future system performance. The second step is control design where the control input is calculated by the controller that will optimize the system's performance over a specified time. The predictions are used by optimization algorithm to determine the control signal. For the reason that optimization algorithm is used, the controller requires a substantial amount of on-line computation. The control evaluation consists of the minimization problem of the following performance criterion:

$$J_n = \sum_{i=n_1}^{n_2} (y_d(t+i) - y_r(t+i))^2 + \zeta \sum_{i=1}^{n_u} (\bar{u}(t+i-1) - \bar{u}(t+i-2))^2, \quad (4.28)$$

where  $\bar{u}$  is the tentative control signal determined by the optimization block and minimizes the performance index  $J_n$ ,  $n$  is the prediction horizon for output (e.g.  $n_2$ : cost horizon &  $n_u$ : control horizon),  $y_d$  is the desired signal and  $y_r$  is the neural network model signal. The optimal control signal  $u$  is injected into the plant and  $\zeta$  determines the contribution on the performance index. The block scheme of the model predictive control process is illustrated in Figure 4.7.

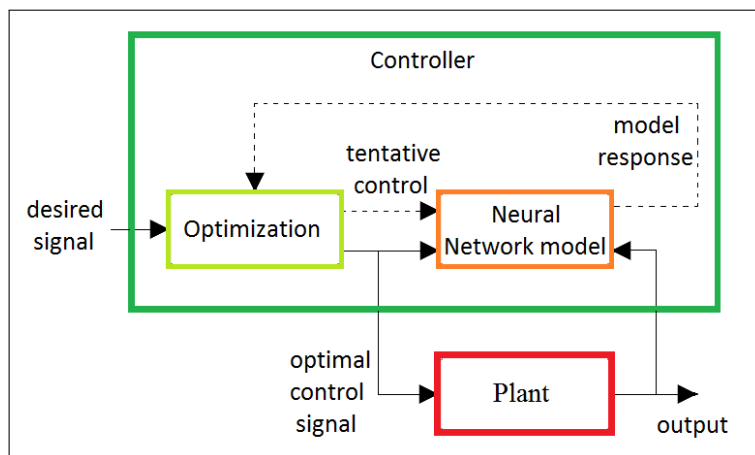


FIGURE 4.7: Structure of model predictive control process.

### NARMA-L2 control

In this part, NARMA-L2 control also referred to as feedback linearization control is presented for the described system. It transforms nonlinear system dynamics into linear dynamics by cancelling the non-linearities. Similar to neural network predictive control, the first step is system identification of the plant model. NARMA is a standard model and mimics the behavior of a discrete-time non-linear system. The control input  $u(k)$  must be determined based on output  $y(k)$  at the same time and the model of the given form is used.

$$y(k+a) = f[Y, U] + g[Y, U]u(k+1), \quad (4.29)$$

where  $a \geq 2$  and the two sub-functions,  $f$  and  $g$  are the two functions of previous inputs and outputs. This model representation is used in the form of past, current, and the future system parameters.

The relation between the control input and the output is linear and the control input is determined easily. Using the NARMA-L2 model, the controller can be expressed as:

$$u(k+1) = \frac{y_d(k+a) - f[Y, U]}{g[Y, U]}, \quad (4.30)$$

which is realizable for  $a \geq 2$ .

$$Y = [y(k), y(k-1), \dots, y(k-n+1)] \quad (4.31)$$

and

$$U = [u(k), u(k-1), \dots, u(k-n+1)], \quad (4.32)$$

where  $y_d(k+a)$  is the reference signal for output at  $a$  time steps ahead.

If the plant is a minimum phase system and the relative degree is well defined, the closed loop system is stable. The structure of the controller is given in Figure 4.8 where tapped delay line (TDL) supplies the signal at each specified time delay.

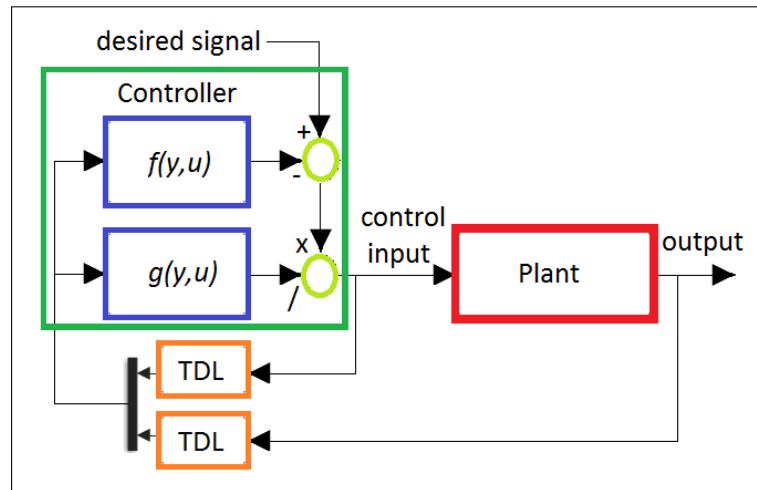


FIGURE 4.8: Structure of NARMA-L2 controller.

### 4.2.3 Observer design with known input

In this section, an observer is designed for estimating the states of the water-based multiple model (2.68). Linear matrix inequality (LMI) is used to compute the observer gain. First, let us notice  $\bar{B}(\bar{x})$  can be written as:

$$\bar{B}(\bar{x}) = \frac{-f_2 C^T C}{4} \bar{x} \quad (4.33)$$

Then (2.68) becomes

$$\dot{\bar{x}} = \sum_{i=1}^2 \mu_i A_i \bar{x} - \frac{f_2 C^T C}{4} \bar{x} u + \bar{G} v - P \dot{T}_{wi} \quad (4.34)$$

By adding and subtracting  $\frac{f_2 C^T \bar{D}}{4} v u$  in (4.34), we get:

$$\dot{\bar{x}} = \sum_{i=1}^2 \mu_i A_i \bar{x} - \frac{f_2 C^T C}{4} \bar{x} u - \frac{f_2 C^T \bar{D}}{4} v u + \frac{f_2 C^T \bar{D}}{4} v u + \delta,$$

where  $\delta = \bar{G} v - P \dot{T}_{wi}$  and since,  $y = C \bar{x} + \bar{D} v$ , the above equation becomes:

$$\dot{\bar{x}} = \sum_{i=1}^2 \mu_i A_i \bar{x} - \frac{f_2 C^T y}{4} u + \frac{f_2 C^T \bar{D}}{4} v u + \delta \quad (4.35)$$

#### Proposition:

An observer of system (2.68) is given by

$$\begin{cases} \dot{\hat{x}} = \sum_{i=1}^2 \mu_i A_i \hat{x} - \frac{f_2 C^T}{4} \hat{y} u + \frac{f_2 C^T \bar{D}}{4} v u + g(\hat{y}) + \delta, \\ \hat{y} = C \hat{x} + \bar{D} v \end{cases}, \quad (4.36)$$

where  $g(\hat{y})$  is chosen as:

$$g(\hat{y}) = \frac{f_2 C^T}{4} \hat{y} + L_i C \hat{x} \quad (4.37)$$

which can also be written as:

$$g(\hat{y}) = (L_i + \frac{f_2 C^T}{4}) \hat{y} \quad (4.38)$$

and  $L_i = L = (1/2) X^{-1} C^T$ ,  $i = 1, 2$ ;  $X$  is the positive definite matrix satisfying the LMI's.

$$\begin{cases} A_i^T X + X A_i - C^T C < -2\gamma X, & i = 1, 2, \\ X > 0 \end{cases}, \quad (4.39)$$

where  $\gamma > |f| > 0$ ,  $(-f)$  being the lowest the fastest pole of (2.68).

**Proof:**

The observer error  $\tilde{x} = \bar{x} - \hat{x}$  satisfies the equation

$$\dot{\tilde{x}} = \sum_{i=1}^2 \mu_i (F_i) \tilde{x}, \quad (4.40)$$

where  $F_i = A_i - LC$

$$\dot{\tilde{x}} = \sum_{i=1}^2 \mu_i (A_i - LC) \tilde{x} \quad (4.41)$$

with  $L = (1/2)X^{-1}C^T$

$$\sum_{i=1}^2 \mu_i A_i - LC = \sum_{i=1}^2 \mu_i A_i - \frac{1}{2}X^{-1}C^T C \quad (4.42)$$

premultiplying (4.42) by  $X$ , we get:

$$X\left(\sum_{i=1}^2 \mu_i A_i - LC\right) = X\left(\sum_{i=1}^2 \mu_i A_i - \frac{1}{2}X^{-1}C^T C\right)$$

or equivalently

$$X\left(\sum_{i=1}^2 \mu_i A_i - LC\right) = X\sum_{i=1}^2 \mu_i A_i - \frac{1}{2}C^T C \quad (4.43)$$

by transposing (4.43):

$$\left(\sum_{i=1}^2 \mu_i A_i - LC\right)^T X = \sum_{i=1}^2 \mu_i A_i^T X - \frac{1}{2}C^T C \quad (4.44)$$

by adding (4.43) and (4.44):

$$X\left(\sum_{i=1}^2 \mu_i A_i - LC\right) + \left(\sum_{i=1}^2 \mu_i A_i - LC\right)^T X = \sum_{i=1}^2 \mu_i A_i^T X + \sum_{i=1}^2 \mu_i X A_i - C^T C \quad (4.45)$$

$$= \sum_{i=1}^2 \mu_i (A_i^T X + X A_i - C^T C) < -2 \sum_{i=1}^2 \mu_i \gamma X \quad (4.46)$$

Since,  $\sum_{i=1}^2 \mu_i = 1$ , (4.46) can be written as:

$$= \sum_{i=1}^2 \mu_i (A_i^T X + X A_i) - C^T C < -2\gamma X \quad (4.47)$$

Next, let  $\sigma$  be an eigen value of  $X$  and  $z$  an associated eigen vector that is  $Fz = \sigma z$ .

The last inequality yields:

$$F^T X + X F < -2\gamma X \quad (4.48)$$

Premultiplying by  $z^*$  and postmultiplying by  $z$ , (4.48) gives:

$$z^* F^T X z + z^* X F z < -2\gamma z^* X z \quad (4.49)$$

with  $z^* F^T = \bar{\sigma} z^*$ , (4.49) becomes:

$$\bar{\sigma} z^* X z + z^* X \sigma z < -2\gamma z^* X z \quad (4.50)$$

since,  $X > 0$ ,  $\rightarrow \Re(\sigma) < -\gamma$ .

#### 4.2.4 Observer design with unknown input

The objective is to construct an observer subjected to an unknown input. It proposes an improvement in the design compared to our previous observer design where  $\hat{x}$  is estimated by knowing  $\dot{T}_{wi}$ . A Lyapunov approach is used to ensure stability and a Linear Matrix Inequality (LMI) is solved simultaneously in order to find a positive definite symmetric matrix subject to linear equality constraint. Necessary and sufficient conditions for the existence of such approach are given. A new sixth state  $\theta_w$  is introduced and is given by:

$$\theta_w = T_w - T_{wi}, \quad (4.51)$$

As a result, an equivalent system with change of variable can be constructed as follows:

$$\begin{cases} \dot{\bar{x}}(t) = \sum_{i=1}^2 \mu_i A_i \bar{x}(t) + \bar{B} \bar{x}(t) u(t) + \bar{G} v(t) - P \dot{T}_{wi} \\ y(t) = C \bar{x}(t) + T_{wi} \end{cases} \quad (4.52)$$

where  $\dot{T}_{wi}$  is unknown input,  $\bar{x}$  contains state variables and is defined as;

$$\bar{x} = [T_g \ T_c \ T_t \ T_r \ T_m \ \theta_w \ T_i]^T$$

The variation of  $T_{wi}$  is unknown and the noise is highly amplified when make a derivative. High frequency gives high values and taking a derivative of it will give much higher values and considering it as unknown input could avoid the trouble. It should be noted that the only dissimilar term in  $x$  and  $\bar{x}$  is the sixth state and the actual state  $x_6$  can be calculated using the relation:

$$x_6 = \bar{x}_6 + T_{wi}$$

The new measured output  $Y(t)$  can be written as:

$$Y(t) = y(t) - T_{wi} \quad (4.53)$$

For the corresponding model,  $Y(t)$  is given by:

$$Y(t) = C \bar{x}(t) \quad (4.54)$$

In this section, an observer is designed for estimating the states of the multiple model.

#### Theorem 1:

If there exist  $D_i$ ,  $E$ ,  $L_i$ ,  $J$ , and  $H$  matrices with appropriate dimensions satisfying the constraints, the observer error is exponentially stable such that  $D_i$  is Hurwitz. If one can make the following constraints hold:

$$E^T X + X E = O \quad (4.55)$$

$$D_i^T X + XD_i < 0 \text{ for } i = 1, 2 \quad (4.56)$$

$$D_i S - SA_i + L_i C = 0 \quad (4.57)$$

$$J - SG = 0 \quad (4.58)$$

$$SP = 0 \quad (4.59)$$

$$ES - SB + HC = 0 \quad (4.60)$$

$$S = I_7 - MC \quad (4.61)$$

then  $\hat{x}$  converges to  $\bar{x}$ .

The existing conditions for the observer were given by Mechmeche, Hamdi, and Yahoui (2008), Darouach, Zasadzinski, and Xu (1994), and Rafaralahy et al. (1996). A constant gain unknown input observer for the system (4.52) is described with the following structure

$$\begin{cases} \dot{z}(t) = \sum_{i=1}^2 \mu_i D_i z(t) + Ez(t)u(t) + \sum_{i=1}^2 \mu_i L_i Y(t) \\ \quad + Jv(t) + Hu(t)Y(t) \\ \hat{x}(t) = z(t) + MY(t) \end{cases}, \quad (4.62)$$

where  $z$  is the state vector of dynamic system (4.62) and  $\hat{x}$  represents the estimation of states. The system is unknown input state observer if and only if

$$\lim_{t \rightarrow \infty} \|\hat{x}(t) - x(t)\| = 0$$

holds irrespective of the initialisations, the measured input and the unknown input.

**Proof:**

Let estimation error  $e$  be the difference between estimated and the actual states, and using the output equation in (4.62), one has

$$e(t) = \hat{x}(t) - \bar{x}(t) = z(t) + MY(t) - \bar{x}(t) \quad (4.63)$$

the dynamics of the state estimation error is as follows:

$$\begin{aligned} \dot{e} = \sum_{i=1}^2 \mu_i D_i e + \sum_{i=1}^2 \mu_i (D_i S - SA_i + L_i C) \bar{x} + (J - SG)v \\ - SP\dot{T}_{wi} + Eue + u(ES - SB + HC) \end{aligned} \quad (4.64)$$

If constraints (4.57)-(4.60) hold, state estimation error dynamics (4.64) reduces to

$$\dot{e}(t) = \sum_{i=1}^2 \mu_i D_i e(t) + Eu(t)e(t) \quad (4.65)$$

To prove the stability, let a function  $V = e^T X e$  be a Lyapunov candidate for error dynamic system (4.65) and  $X$  be a positive definite symmetric matrix. The time derivative of the lyapunov function, respectively gives

$$\dot{V} = e^T \left( \sum_{i=1}^2 \mu_i (D_i^T X + XD_i) + (E^T X + XE)u(t) \right) e(t), \quad (4.66)$$

or equivalently

$$\dot{V} = e^T T(u) e(t), \quad (4.67)$$

where

$$T(u) = \sum_{i=1}^2 \mu_i X_i + X_o u(t), \quad (4.68)$$

with  $X_i = D_i^T X + X D_i$  and  $X_o = E^T X + X E$ .

The asymptotic stability is ensured with constraints (4.55) and (4.56) if the derivative of the Lyapunov function is negative if and only if  $T(u)$  is negative definite for all admissible  $u(t)$ . The constraint (4.56) is satisfied if  $D_i$  is made Hurwitz, that is,  $\Re(\lambda(D_i)) < 0$  then there exists  $X$  which is a symmetric positive definite matrix. The proof is completed.

Now, let us find the unknown matrices of (4.62) using the constraints provided in Theorem 1. Taken into account the constraint (4.61), (4.59) yields:

$$P - MCP = 0 \quad (4.69)$$

the solution of this equation depends on the rank of matrix  $CP$ ,  $M$  exists if  $\text{rank}(CP) = \text{rank}(P)$ . The general solution of (4.69) exists and can be written as:

$$M = P(CP)^+ + \zeta(I - (CP)(CP)^+),$$

where  $\zeta$  is an arbitrary matrix with appropriate dimension and  $(CP)^+$  is the generalized inverse of  $(CP)$ . (Darouach, Zasadzinski, and Xu, 1994) shown that  $\zeta$  must be chosen such that  $M$  is of maximal rank and the obvious choice of matrix is  $\zeta = 0$  and this yields

$$M = P(CP)^+ \quad (4.70)$$

### Theorem 2:

The necessary conditions for the existence of structure (4.62) are

i)  $\text{rank}(CP) = \text{rank}(P)$

if it holds then, (4.69) is solvable otherwise observer cannot be constructed.

ii) The pair  $(C, SA_i)$  is detectable (observable) if and only if the rank condition holds

$$\text{rank} \begin{bmatrix} sI_7 - A & P \\ C & 0 \end{bmatrix} = 7 + \text{rank}(P)$$

for all  $s$  with  $\Re(s) \geq 0$ , but  $s \neq 0$ .

Suppose if these conditions are satisfied, then matrix  $D_i$  can be made stable and observer (4.62) exists. Using (4.61) in (4.57), the equation reduces to

$$D_i = SA_i - K_{oi}C, \quad (4.71)$$

where

$$K_{oi} = L_i - D_i M \text{ for } i = 1, 2 \quad (4.72)$$

and  $D_i$  should be Hurwitz, for that,  $(SA_i, C)$  should be detectable.  $K_{oi}$  can be computed by pole placement for the pair  $(SA_i, C)$  and (4.72) can be written as:

$$L_i = K_{oi} + D_i M \quad (4.73)$$

Substituting (4.71) in (4.56), LMI is solved for  $X$  and has a positive definite solution  $X$  if  $D_i$  is Hurwitz.

Substituting (4.61) in (4.55), the equation reduces to

$$E = SB - KC, \quad (4.74)$$

where

$$K = H - EM \quad (4.75)$$

Using (4.74) in (4.55), yields

$$(SB - KC)^T X + X(SB - KC) \quad (4.76)$$

or equivalently

$$(SB)^T X + X(SB) = (KC)^T X + X(KC) \quad (4.77)$$

if a new variable  $\zeta$  is introduced that is equal to (4.77) and particular solution of left hand side of (4.77) is  $XKC = (XKC)^T$  then  $\zeta$  can be written as:

$$\zeta = 2XKC, \quad (4.78)$$

where the solution of (4.78) exists only if  $\text{rank}(C^T) = \text{rank}[C^T \ (X^{-1}\zeta)^T]$  and  $K$  is then given by:

$$K = \frac{1}{2} X^{-1} \zeta C^+, \quad (4.79)$$

where  $(C^+)$  is the generalized inverse of  $C$ . If the above assumption does not holds, the solution can be obtained by minimizing  $\| KC - \frac{1}{2} X^{-1} \zeta \|_2$ , given by (4.79) with  $(C^+) = C^T (CC^T)^{-1}$ .

**Remark 1:**

The solar radiation  $I_{sun}$  and ambient temperature  $T_{am}$  are not chosen as unknown inputs because assumption (i) in theorem 2 is not satisfied. It is necessary condition to ensure the existence of such observer. Infact, the product of matrices  $C$  and  $P$  becomes zero.

**Remark 2:**

Fluid inlet temperature  $T_{wi}$  cannot be taken as unknown input because measured output  $Y(t)$  contains it and will make impossible for us to design such scheme for it.

**Remark 3:**

In order to simplify  $B$ , we made a change of variable  $\theta_w$  as given in (4.51) and this change results in an introduction of time derrivative of inlet water temperature. Since,  $\hat{T}_{wi}$  in (4.52) cannot be found directly so  $\hat{x}$  is estimated without knowing it.

The unknown input observer of the form (4.62) can be constructed by following the design procedure provided in section below.

**Algorithm:**

The design procedure can be summarised as follows:

1. Verify if assumption (i) is satisfied

2. Compute  $M$  using (4.70)
3. Compute  $S$  using (4.61)
4. Compute  $D_i$  in (4.71) by pole placement
5. Compute  $L$  using (4.73)
6. Using (4.56) and (4.71), compute  $X$  using LMI toolbox
7. Compute  $K$  using (4.79)
8. Compute  $E$  using (4.74)
9. Compute  $H$  using (4.75)

## 4.3 Results and Discussion

All the techniques presented are illustrated through simulation results.

### 4.3.1 Air-based Model

#### PI-controller

PI controller is widely used in industries and to make the solution simple a linear controller approach is used instead of a nonlinear approach. Based on the need to control the mass flow rate, the evolution of the temperature rise using PI-controller is shown in Figure 4.9 for air-based model-I. For PI-controller the parameters  $K_p$  and  $K_i$  are obtained using the average transfer function (2.32). For the plant, the whole nonlinear model is considered and different reference points are considered.

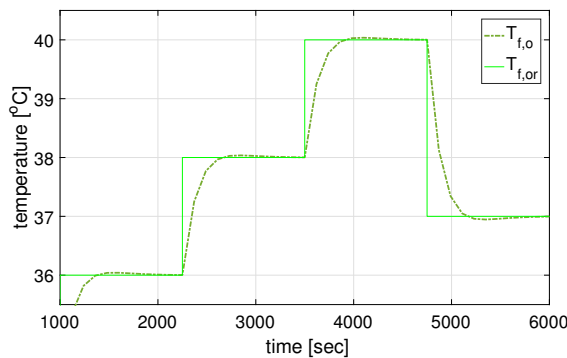


FIGURE 4.9: Response of PI-controller with constant solar radiation.

We have a complex model and it wasn't obvious to control it however in this approach, the obtained results are satisfactory. The controller tracks the reference point with a high settling time and a closed-loop time constant of 200 s. The desired temperature is  $T_{f,or}$  whereas the measured temperature  $T_{f,o}$  is in dotted line. Initially, constant solar radiation is applied to see the response of the controller and it can be observed that controller gets the temperature to the desired setting with the change in reference point. The controller parameters are  $K_p = -0.162$  and  $K_i = -0.00074$  with  $\zeta = 0.95$ . To avoid the overshoot a small value of  $\omega_o$  is chosen. The effect of solar radiation can be seen in Figure 4.10, even with the change in solar radiation the controller rejects the change and tracks the desired temperature.

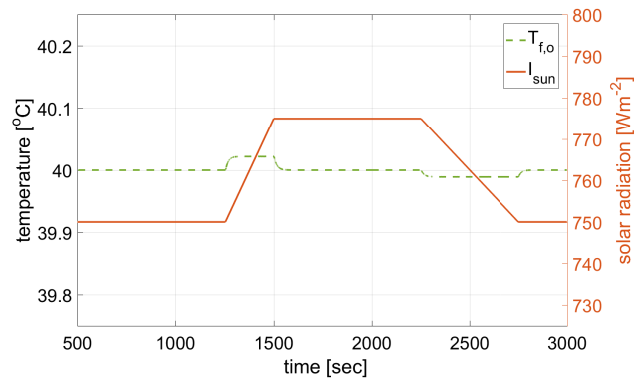


FIGURE 4.10: Tracking of desired temperature and disturbance rejection.

### H-infinity control

The performance of the designed nonlinear H-infinity control scheme is investigated through simulations. The proposed H-infinity feedback control requires the solution of a Riccati equation at each step of the control method. It can be observed in the presented results that the H-infinity control scheme achieves fast and accurate tracking of the reference setpoints. Figure 4.11 presents the external inputs that include solar radiation, ambient temperature and wind speed. Since these external inputs are considered as disturbances to the system and directly affect the state temperatures so it can be observed in Figure 4.12 that the desired value of the states is updated and tracked by rejecting the effects of the disturbances.

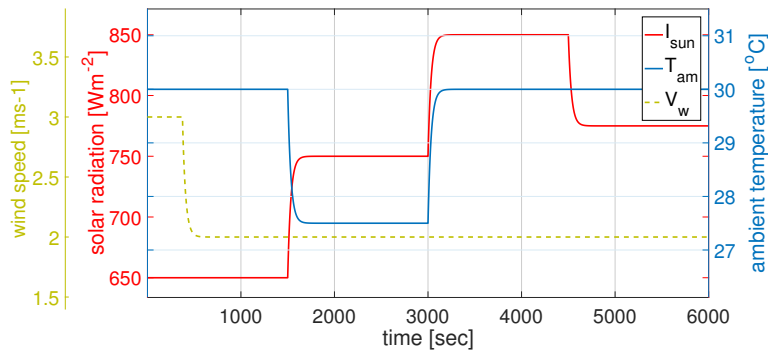


FIGURE 4.11: External inputs imposed on the system.

Figure 4.14 shows that the desired outlet temperature  $T_{f,od}$  is perfectly tracked even with the external inputs imposed on the system. Wind speed changes between the interval 0-500 s and at 1500 s, the ambient temperature goes from 30°C to 27.50°C and then comes back to 30°C at 3000 s. Similarly, solar radiation varies between the interval 1500 s to 4500 s. Moreover, the mass flow rate that is the control input, illustrated in Figure 4.13 cancels the effects of the external inputs at different intervals. Further, it can be seen that at 3000 s, both solar radiation and the ambient temperature rise. There is not a major change in mass flow despite desired output being changed from 37.50°C to 42.50°C.

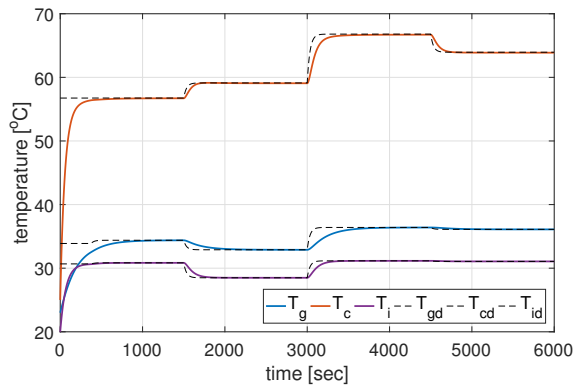


FIGURE 4.12: Tracking of reference setpoints by the state variables.

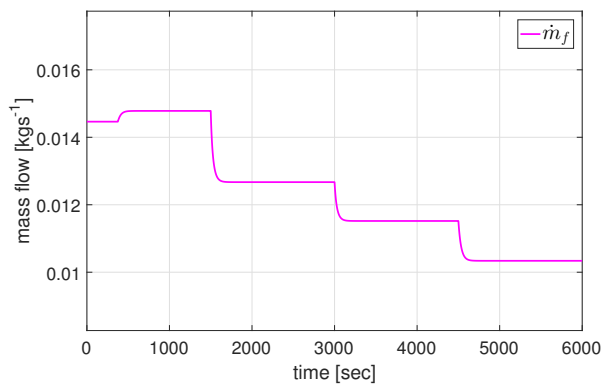


FIGURE 4.13: Evolution of the control input exerted on the system.

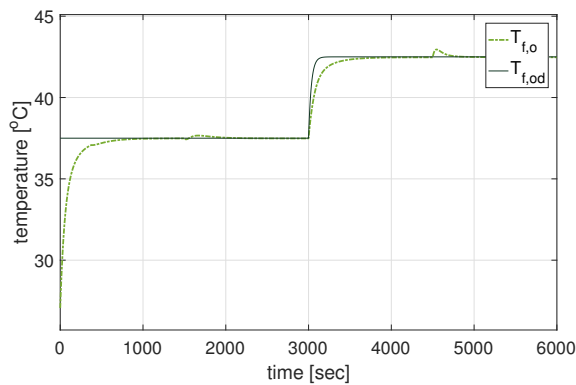


FIGURE 4.14: Evolution of the outlet temperature.

### 4.3.2 Water-based model

#### Sliding mode control

The control law is implemented in Section 4.2.1 and a series of simulations were performed with the proposed controller. Based on the need to control mass flow rate, the evolution of temperature rise using a sliding mode controller is presented. The controller tracks the reference point, illustrated in Figure 4.15.

It rejects the changes that occur in solar radiation and ambient temperature. It should be noted that the water inlet temperature  $T_{wi}$  is assumed as a constant. First,

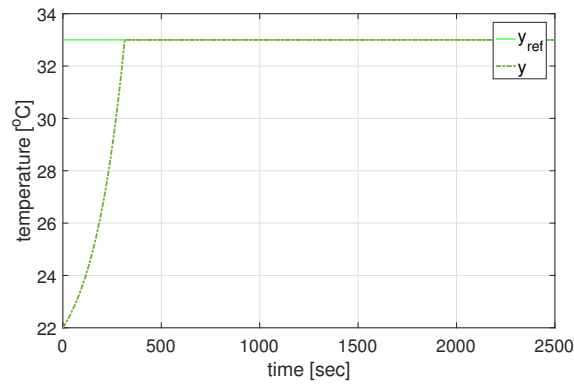


FIGURE 4.15: Convergence of output  $T_{w0}$  to the desired point  $y_{ref}$ .

ambient temperature is considered as constant and solar radiation is changed from  $750 \text{ Wm}^{-2}$  to  $650 \text{ Wm}^{-2}$  as illustrated in Figure 4.16. The control input  $\dot{m}_w$  changes according to the reference point which is set at  $33^\circ\text{C}$ .

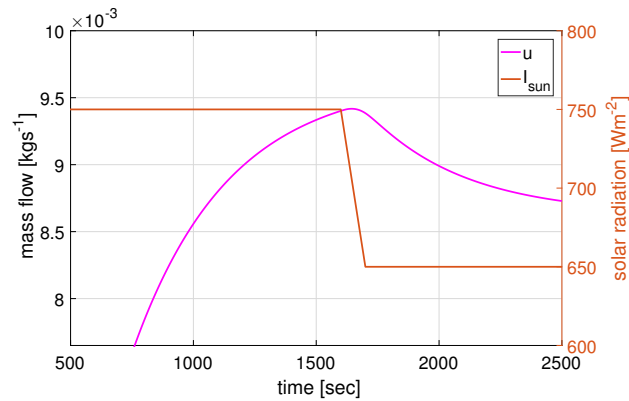


FIGURE 4.16: Control input with a change in solar radiation.

Next, solar radiation is assumed as a constant and ambient temperature varies from  $28^\circ\text{C}$  to  $24^\circ\text{C}$  as shown in Figure 4.17, with a similar value of reference point, it can be observed that the control input changes with a change in ambient temperature. In both cases, the mass flow drops in order to maintain the desired set point.

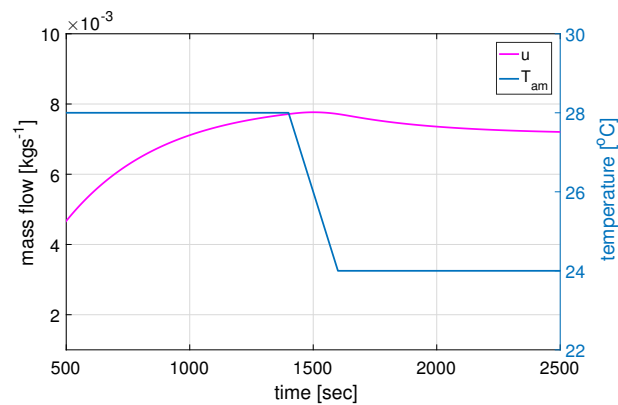


FIGURE 4.17: Control input with a change in ambient temperature.

### Artificial neural network control

Next, a simple neural network is used for the purpose of control and for training, the Levenberg–Marquardt Backpropagation algorithm is used. The best performance is successfully reached and is checked through MSE. The inputs and outputs are trained and the initial results showed that the outputs (i.e., mass flow and electrical efficiency) are accurately and efficiently predicted.

Random input values (i.e, for wind speed, ambient temperature and solar radiation) as shown in Figure 4.18 are chosen. The wind speed is changed from  $2 \text{ ms}^{-1}$  to  $4 \text{ ms}^{-1}$  between the interval 2000 s to 3000 s, ambient temperature is reduced from  $29^\circ\text{C}$  to  $27^\circ\text{C}$  around 5000 s and lastly solar radiation is raised from  $700 \text{ Wm}^2$  to  $750 \text{ Wm}^2$  just after 4000 s. The reference value of the water output temperature is set in order to obtain the control input which is the mass flow of the fluid and electrical efficiency (see Figure 4.19).

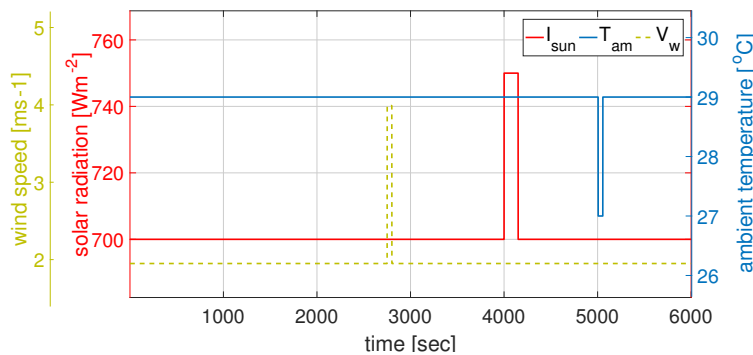


FIGURE 4.18: External inputs imposed on the system.

It can be observed that the control input which is the mass flow rate, cancels the effects of external inputs at different intervals mentioned above. The control input

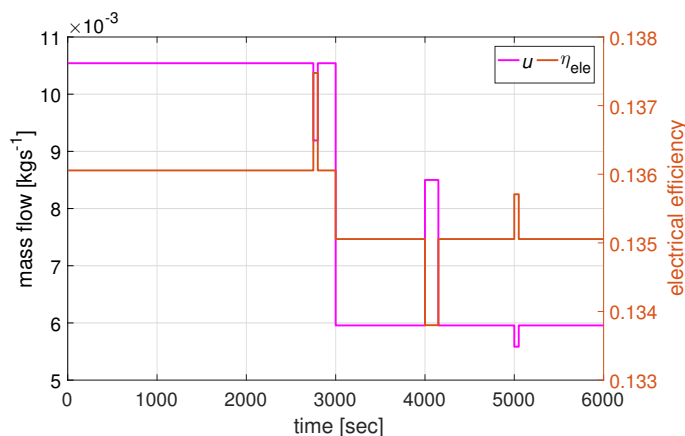


FIGURE 4.19: Evolution of the PV efficiency and control input.

is then injected to the real water-based model, and the results in Figure 4.20 show that the reference point is perfectly tracked even with the external inputs. Similarly, the corresponding states temperature evolution using the control input and external inputs is depicted in Figure 4.21.

In order to control the system using other neural network approaches, the first step is to get a NARMA model and predictive model of the system to be controlled.

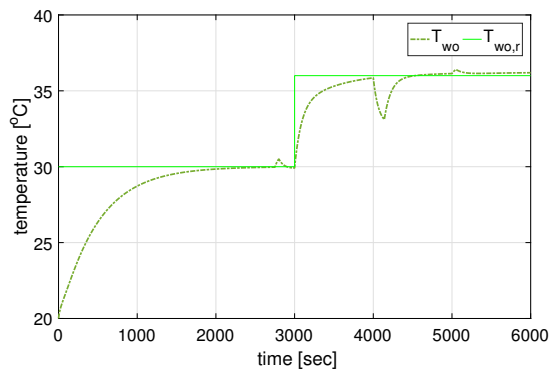


FIGURE 4.20: Evolution of the outlet temperature and disturbance rejection.

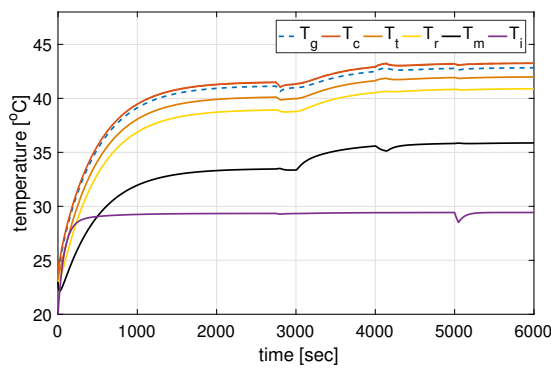


FIGURE 4.21: Evolution of state temperatures.

After accepting the generalization of the modeling of the presented structure, testing of the models can be done with the unseen data. Two delayed inputs, two delayed outputs and a total of 16 hidden layers are used as parameters for both predictive and NARMA-L2 controllers whereas  $\zeta$  for the predictive controller is chosen as 0.05.

The response of the predictive and NARMA-L2 controllers as well as basic neural network controller is compared in Figure 4.22. The obtained results indicate that the desired points are tracked by the controllers. It can be observed that the predictive controller is more accurate compared to the other two controllers. However, the performance of the controllers depend on the accuracy of the plant identification.

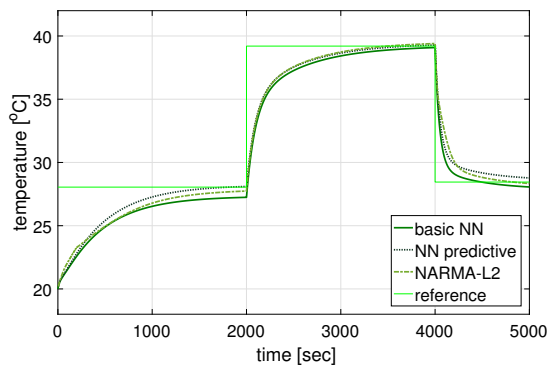


FIGURE 4.22: Response using basic controller, predictive controller and NARMA-L2 controller.

### Observer design

The performance of the proposed observer architecture presented in Section 4.2.3 is evaluated with simulations. Using MATLAB LMI toolbox *feasp* and by choosing  $\gamma = 1$ , (4.39) is solved for  $X$ . The system real states ( $\bar{x}$ ) presented in Figure 4.23 are tracked by the observer states ( $\hat{x}$ ) as illustrated in Figure 4.24. It can be observed that there is a reasonable agreement between the real and the estimated states of the system. The estimation error ( $\tilde{x}$ ) is plotted in Figure 4.25 and shows the evolution

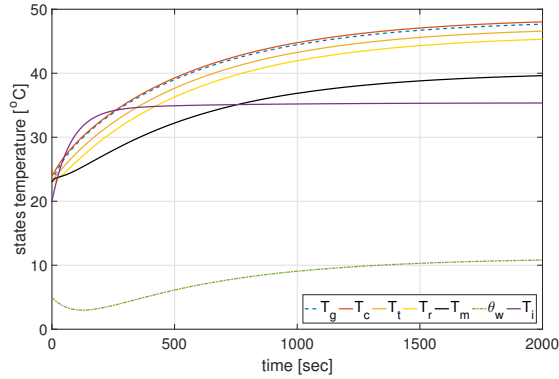


FIGURE 4.23: Real states of the system.

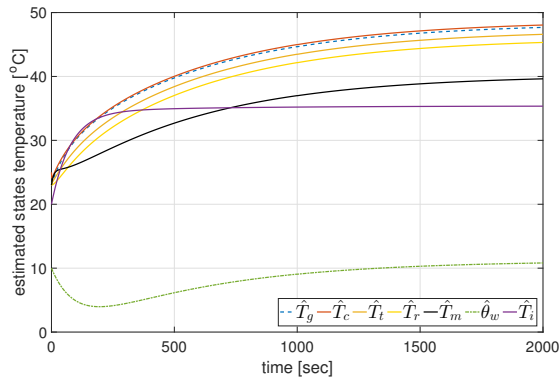


FIGURE 4.24: Estimation of states.

of the estimation error between the actual system variables and their corresponding observer ones. The estimation error converges to zero for all of the states, thus displaying the effectiveness of the proposed observer.

In Section 4.2.4, an observer with unknown input is presented and the multiple thermal model (4.52) is simulated using MATLAB/Simulink by randomly choosing systems initial condition  $\bar{x}_0 = [23 \ 25 \ 23 \ 23 \ 23 \ 3 \ 20]^T$  and observers initial condition  $z_0 = [23 \ 27 \ 23 \ 23 \ 24 \ 5 \ 20]^T$ . Even though, the unknown input is present, the state estimation error converges to zero for all of the states as presented in Figure 4.26.

To estimate the states of the system, the system was initially simulated without any unknown input. In Figure 4.27, it can be observed that there is a reasonable agreement between the true and estimated states of the system. The simulation results clearly agrees with the theory made on the observer exponential convergence.

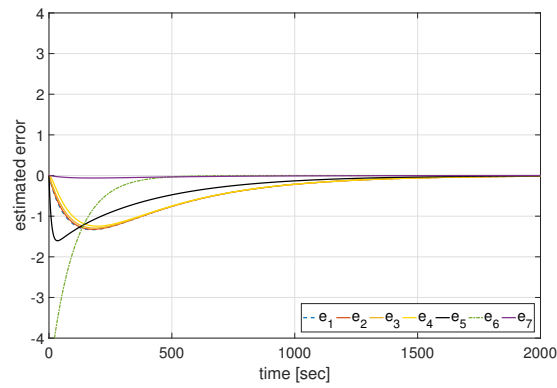
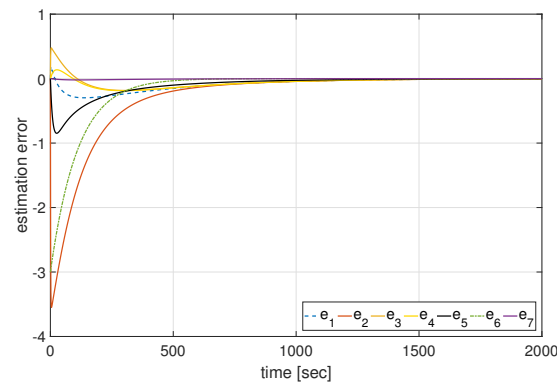


FIGURE 4.25: Estimation error.

FIGURE 4.26: State estimation errors:  $e_1$  through  $e_7$ .

The system's real states are tracked by the observer states. Further, a sinusoidal input  $T_{wi}$  is injected with similar conditions and Figure 4.28 illustrates that it affects the state  $\theta_w$  whereas there is a small effect on the state  $T_m$  since the fluid flows within the tube. However, the estimation of the state remained, which shows the robustness of the observer.

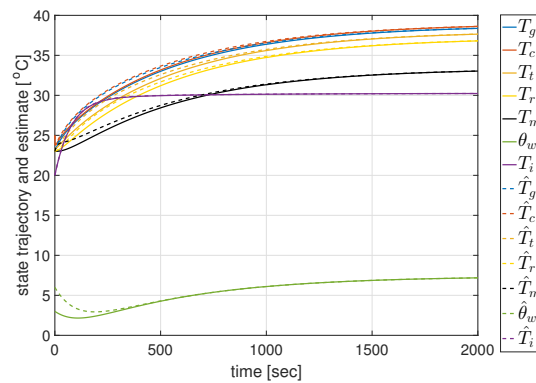


FIGURE 4.27: True states and their estimations without unknown input.

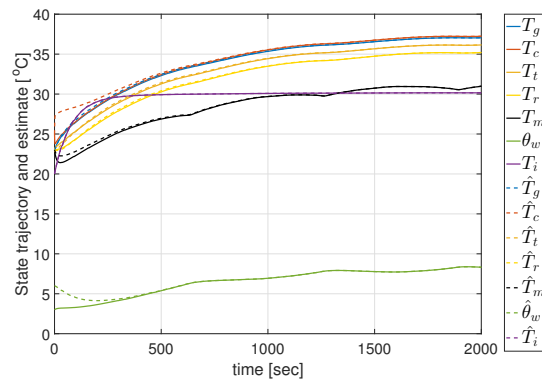


FIGURE 4.28: True states and their estimations with sinusoidal input  $T_{wi}$ .

## 4.4 Conclusion

In this chapter, we describe in detail the control scheme design of a PV-T system. A PI-controller and an H-infinity control method for air-based PV-T models is developed. H-infinity feedback control law is computed and unlike multiple local models-based control where the control method uses a single linearization point and requires the solution of only one Riccati equation to compute the feedback gain. However, in the proposed approach, the feedback control gain requires the solution of an algebraic Riccati equation at each iteration of the control method. The robustness features of H-infinity control enable to eliminate the effects of external perturbations. The stability properties of the control loop can be proved through Lyapunov analysis. It can be checked through Lyapunov analysis that the control scheme assures H-infinity tracking performance and in case of bounded disturbance terms, convergence to the reference setpoints.

Sliding mode control for a water-based model is designed and proven to guarantee good performance. The results indicate that the controller perfectly tracks the reference point. The controller rejects changes in solar radiation and ambient temperature and tracks the desired output temperature. The simplicity of the proposed controller makes it a good candidate for a practical application. Moreover, the ANN control approach is robust and its performance is better than conventional control methods. The models require a long time for the outlet temperature to reach a reference value but settle out to the exact target even with the change in external inputs. PI and neural network based controllers are more practical and simpler. The designed PI controller only works around a few operating points whereas H-infinity and sliding mode controllers work for all the operating points. Additionally, the H-infinity controller does not require an observer. The accuracy of the neural network based controllers highly depend on the plant identification.

Further, an observer is proposed that is efficient in estimating system states as shown by simulation results. Additionally, an observer is designed subjected to unknown input, an improvement in the design. The existence conditions are given using the Lyapunov stability approach. The estimation error converges to zero for all of the states, thus displaying the effectiveness of the proposed approach. The observer showed high robustness against unknown input and estimation of the states remained very accurate.



## Chapter 5

# Conclusion and Perspective

This thesis considers hybrid PV-T systems which have many potential advantages over conventional PV systems or conventional thermal collectors separately. They are beneficial in isolated places where there is no access to electricity. They provide more electricity and heat with limited roof space and reduce the installation cost compared to the two systems alone. The combined PV and thermal efficiency of the collector is higher than that of the PV module and solar thermal collector alone. These systems offer numerous benefits however the drawbacks cannot be ignored.

- The initial installation cost of these systems is higher and additional space is required for their applications.
- A possible drawback of these systems is that they highly depend on weather conditions and additional energy input is required to fulfill the supply of energy, especially during the winter season. In summer, there may be a waste of excess energy depending on the location but this can be solved through storage.

In the following, we address some concluding remarks for each chapter.

In Chapter 2, we introduce modeling that has been performed for PV-T systems using a bond graph approach. The obtained results confirm;

- Heat transfer using water-based collectors is higher than air-based collectors and there is a shift from air-based PV-T system to liquid-based PV-T systems.
- For the liquid-based PV-T collectors, it is recommended to optimize contact surfaces between the PV module and the tubes to enhance the overall efficiency of the system.
- The PV component has a higher temperature than other components using both air and water as heat extraction fluid.
- Addition of glazing increases the cost as well as the thermal output and is more suitable for hot water demand.
- In a water-based collector, because of economical reasons, more than 0.08 m of insulation is not required as the heat losses become constant.
- The wind speed affects the thermal performance, the thermal efficiency rises from 32% to 46% with the drop in wind speed from  $5 \text{ ms}^{-1}$  to  $1 \text{ ms}^{-1}$ .
- In solar drying, the temperature difference between air output and recycled air output is getting bigger at higher solar radiation.
- The predicted results obtained using the ANN model are more accurate than the ones obtained with the decision tree algorithm.

In Chapter 3, we present a new design of a PV-T collector integrating a storage tank and the following conclusions can be drawn:

- An inclusion of an air-gap increase the temperature of all the components.
- The temperature drops with an increase in absorber plate thickness whereas it rises using copper as a component material.
- The fluid temperature rises approximately 3°C using PCM and pure glycol whereas it rises 2°C using water mixed with glycol. Considering the cost and availability, water-mixed with glycol is a better option.
- Use of waste engine oil not only preserves the environment but also enhances the thermal output because of its thermo-physical properties.
- The electrical resistance is a mean to convert the electric power into thermal energy stored in the tank.
- Mass flow is a vital parameter that needs to be optimized with respect to the specific application depending on if electrical efficiency or fluid output is our priority.

Lastly, in Chapter 4, from the results;

- We can observe a stable regulation. Hence, despite any disturbance, the fluid output tends to the reference.
- Due to the nonlinear behavior of the system, special attention must be paid when tuning the controller.
- The robustness features of H-infinity control enable to eliminate the effects of disturbances.
- The performance using ANN control is better than a conventional controller.
- The designed observers are efficient in estimating the states of the system and the error converges to zero for all the states.

The market is still very small compared to conventional PV systems and the use of PV-T systems in industries is still marginal despite they can contribute to cover both electrical and thermal energy demand. A lot can be still done in this area of research. Some future work ideas are presented below:

- The thermal efficiency of a water-based PV-T collector can be improved by adding a PCM or nano-fluid whereas for air-based PV-T collectors the efficiency can be enhanced by adding fins in the air-channel.
- The components of PV-T such as glass and aluminium could be recycled at up to 90% for further production whereas up to 80% of silicon wafers are usually reusable after acid etching and enrichment.
- The use of new materials e.g PCM, nanofluids and accurate dynamic models that provides a pragmatic and practicable performance of the system are needed to improve PV-T technology.
- Most of the work presented is for a short duration of time and there is a need to conduct experiments for a period of 365 days.

- To enhance the performance of the controllers, new approaches must be introduced regarding the nonlinear behavior of the collector.
- Realistic disturbances can be included to examine the stability and accuracy of the observer.
- There is a need for physical experimentation to get a better knowledge of its feasibility and efficiency in real conditions.

Finally, in my personal opinion, I would like to say that the strongest feature of this thesis is its diversity. Throughout this document, one is introduced to the presentation, applications, mathematical modeling, design, CFD analysis, optimization, control design methodologies and observation of hybrid PV-T systems. I believe the improvements and the work done in this thesis will lead to sustainable development to a global energy perspective.



## Appendix A

# Additional Parameters

### A.1 Parameters used for multiple-model construction

$$a_1 = \frac{A_{mod}}{M_g C_g} \quad (A.1)$$

$$a_2 = \frac{A_{mod} h_{v,am}}{M_g C_g} \quad (A.2)$$

$$a_3 = \frac{A_{mod} h_{c,gc}}{M_g C_g} \quad (A.3)$$

$$a_4 = \frac{0.0552 A_{mod}}{M_g C_g} \quad (A.4)$$

$$a_5 = \frac{A_{mod} \alpha_g}{M_g C_g} \quad (A.5)$$

$$b_1 = \frac{A_{mod} h_{c,gc}}{M_c C_c} \quad (A.6)$$

$$b_2 = \frac{A_{mod} (-h_{c,gc} - h_{c,ct})}{M_c C_c} \quad (A.7)$$

$$b_3 = \frac{A_{mod} \eta_{ref} \beta_p}{M_c C_c} \quad (A.8)$$

$$b_4 = \frac{A_{mod} h_{c,ct}}{M_c C_c} \quad (A.9)$$

$$b_5 = \frac{A_{mod} \tau_g \alpha_c \beta - \eta_{ref} - \eta_{ref} \beta_p T_{c,ref}}{M_c C_c} \quad (A.10)$$

$$c_1 = \frac{A_{mod} h_{c,ct}}{M_t C_t} \quad (A.11)$$

$$c_2 = \frac{A_{tr} h_{c,tr}}{M_t C_t} \quad (A.12)$$

$$c_3 = \frac{A_{tm} h_{c,tm}}{M_t C_t} \quad (A.13)$$

$$d_1 = \frac{A_{tr} h_{c,tr}}{M_r C_r} \quad (A.14)$$

$$d_2 = \frac{A_{rm} h_{c,rm}}{M_r C_r} \quad (A.15)$$

$$d_3 = \frac{A_{ri}h_{c,ri}}{M_r C_r} \quad (\text{A.16})$$

$$e_1 = \frac{A_{tm}h_{c,tm}}{M_m C_m} \quad (\text{A.17})$$

$$e_2 = \frac{A_{rm}h_{c,rm}}{M_m C_m} \quad (\text{A.18})$$

$$e_3 = \frac{A_{mw}h_{v,mw}}{M_m C_m} \quad (\text{A.19})$$

$$e_4 = \frac{A_{mi}h_{c,mi}}{M_m C_m} \quad (\text{A.20})$$

$$f_1 = \frac{A_{mw}h_{v,mw}}{M_w C_w} \quad (\text{A.21})$$

$$f_2 = \frac{2C_w}{M_w C_w} \quad (\text{A.22})$$

$$g_1 = \frac{A_{ri}h_{c,ri}}{M_i C_i} \quad (\text{A.23})$$

$$g_2 = \frac{A_{mi}h_{c,mi}}{M_i C_i} \quad (\text{A.24})$$

$$g_3 = \frac{A_{mod}h_{v,iam}}{M_i C_i} \quad (\text{A.25})$$

$$a_{11} = -(a_1 h_{r,gs} + a_2 + a_3) \quad (\text{A.26})$$

$$a_{22} = b_2 + b_3 I_{sun} \quad (\text{A.27})$$

$$a_{33} = -(c_1 + c_2 + c_3) \quad (\text{A.28})$$

$$a_{44} = -(d_1 + d_2 + d_3) \quad (\text{A.29})$$

$$a_{55} = -(e_1 + e_2 + e_3 + e_4) \quad (\text{A.30})$$

$$a_{77} = -(g_1 + g_2 + g_3) \quad (\text{A.31})$$

## Appendix B

# Additional results

### B.1 Air-based PV-T model-I

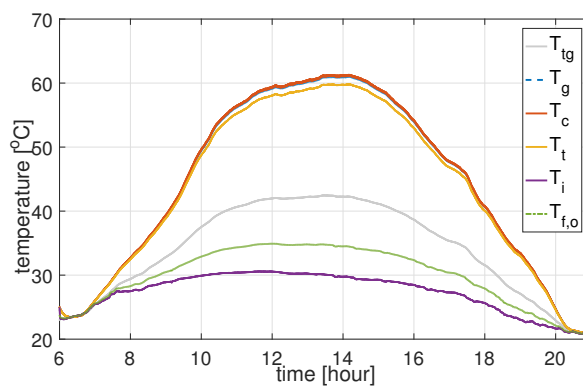


FIGURE B.1: Temperature evolution of a PV-T components for air-based model-I with glazing.

### B.2 Air-based PV-T model-II



FIGURE B.2: Mesh structure of air-based model-II.

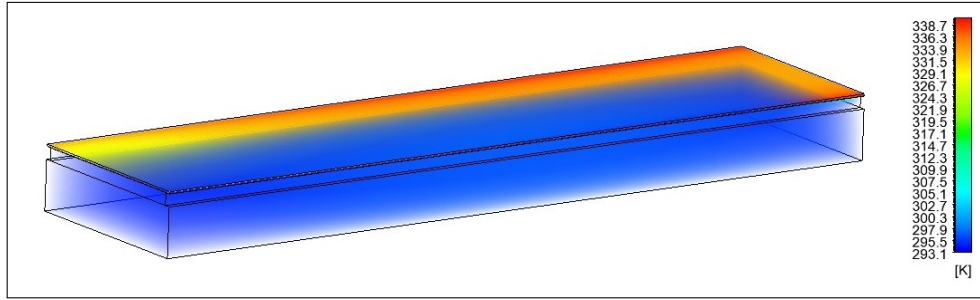


FIGURE B.3: Temperature distribution of PV-T collector (air-based model-II).

## B.3 PV-T collector with embedded tank

### B.3.1 Physical results

TABLE B.1: Temperature of the PV-T components for physical analysis (with  $0.01\text{kgs}^{-1}$  mass flow).

Component	Temperature ( $^{\circ}\text{C}$ )		
	Case-I	Case-II	Case-III
Glass ( $g$ )	52.45	39.60	29.54
PV cell ( $c$ )	52.70	39.72	29.56
Tedlar ( $t$ )	50.73	38.25	28.85
Absorber ( $r$ )	48.17	36.35	27.96
Serpentine tube ( $m$ )	47.23	35.65	27.62
Serpentine fluid ( $w$ )	45.24	34.10	26.80
Tank ( $ta$ )	37.84	28.33	21.78
Insulator ( $i$ )	37.79	30.36	26.40

TABLE B.2: Error for all the PV-T components.

Component	Error (%)		
	Case-I	Case-II	Case-III
Glass ( $g$ )	3.28	4.19	1.54
PV cell ( $c$ )	3.21	4.22	1.57
Tedlar ( $t$ )	6.19	4.72	0.10
Absorber ( $r$ )	7.24	5.78	1.88
Serpentine tube ( $m$ )	0.26	1.91	4.33
Serpentine fluid ( $w$ )	0.34	1.32	1.06
Tank ( $ta$ )	2.42	5.97	5.81
Insulator ( $i$ )	4.32	4.68	6.68
Average	3.40	4.10	2.87

### B.3.2 CFD results

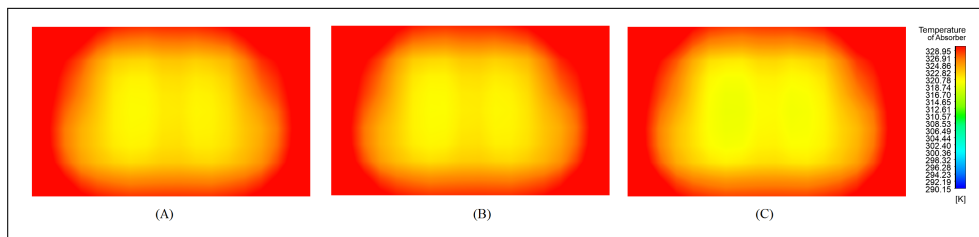


FIGURE B.4: Temperature distributions of Case-I; (a) Glass cover. (b) Tedlar layer. (c) Absorber plate.

### B.3.3 Influence of internal geometrical parameters

TABLE B.3: Pure glycol, water mixed with glycol and paraffin wax (PCM) as a serpentine fluid.

Component	Temperature ( $^{\circ}\text{C}$ )		
	Pure glycol	Water/Glycol	PCM
Glass ( $g$ )	57.65	54.03	57.36
PV cell ( $c$ )	57.91	54.25	57.61
Tedlar ( $t$ )	57.59	53.63	57.29
Absorber ( $r$ )	57.13	53.25	56.81
Serpentine tube ( $m$ )	49.96	47.13	48.83
Serpentine fluid ( $w$ )	46.86	45.45	46.63
Tank ( $ta$ )	45.10	43.71	44.73
Insulator ( $i$ )	35.38	34.91	34.85

TABLE B.4: Used engine oil as an absorber material.

Component	Temperature ( $^{\circ}\text{C}$ )
Glass ( $g$ )	52.59
PV cell ( $c$ )	52.79
Tedlar ( $t$ )	52.35
Absorber ( $r$ )	50.81
Serpentine tube ( $m$ )	43.78
Serpentine fluid ( $w$ )	41.60
Tank ( $ta$ )	40.37
Insulator ( $i$ )	35.51



# Bibliography

- Abbas, Zeshan et al. (2018). "Paraffin Wax As A Phase Change Material For Thermal Energy Storage: Tubes In Shell Type Heat Exchanger". In: *N. Am. Acad. Res* 1, pp. 39–52.
- Abdul-Ganiyu, Saeed et al. (2020). "Investigation of solar photovoltaic-thermal (PVT) and solar photovoltaic (PV) performance: A case study in Ghana". In: *Energies* 13.11, p. 2701.
- (2021). "Study effect of flow rate on flat-plate water-based photovoltaic-thermal (PVT) system performance by analytical technique". In: *Journal of Cleaner Production* 321, p. 128985.
- Abdurohman, Maman, Aji Gautama Putrada, and Mustafa Mat Deris (2022). "A Robust Internet of Things-based Aquarium Control System using Decision Tree Regression Algorithm". In: *IEEE Access*.
- Adnan, Ibrahim et al. (2009). "Hybrid Photovoltaic Thermal (PV/T) air and water based solar collectors suitable for building integrated applications." In: *American Journal of Environmental Sciences* 5.5, pp. 618–624.
- Akhenak, Abdelkader (2004). "Conception d'observateurs non linéaires par approche multimodèle: application au diagnostic". PhD thesis. éditeur inconnu.
- Alghoul, MA et al. (2005). "Review of materials for solar thermal collectors". In: *Anti-Corrosion methods and materials*.
- Allouhi, A et al. (2017). "Design optimization of a multi-temperature solar thermal heating system for an industrial process". In: *Applied Energy* 206, pp. 382–392.
- Alobaid, Mohammad et al. (2017). "A review of solar driven absorption cooling with photovoltaic thermal systems". In: *Renewable and sustainable energy reviews* 76, pp. 728–742.
- Álvarez, JD et al. (2016). "A practical hybrid predictive control algorithm for a low-temperature thermosolar plant". In: *Optimal Control Applications and Methods* 37.3, pp. 508–520.
- Amori, Karima E and Hussein M Taqi Al-Najjar (2012). "Analysis of thermal and electrical performance of a hybrid (PV/T) air based solar collector for Iraq". In: *Applied Energy* 98, pp. 384–395.
- Association, Yazoo Valley Electric Power (2021). *Average monthly appliance usage*. <http://www.yazoovalley.com/content/average-monthly-appliance-usage>. Accessed: 2021-02-11.
- Baljit, SSS, Hoy-Yen Chan, and Kamaruzzaman Sopian (2016). "Review of building integrated applications of photovoltaic and solar thermal systems". In: *Journal of Cleaner Production* 137, pp. 677–689.
- Bergene, Trond and Ole Martin Løvvik (1995). "Model calculations on a flat-plate solar heat collector with integrated solar cells". In: *Solar energy* 55.6, pp. 453–462.
- Bloem, JJ et al. (2012). "An outdoor test reference environment for double skin applications of building integrated photovoltaic systems". In: *Energy and Buildings* 50, pp. 63–73.

- Borutzky, Wolfgang (2009). "Bond graph modelling and simulation of multidisciplinary systems—An introduction". In: *Simulation Modelling Practice and Theory* 17.1, pp. 3–21.
- Brahim, Taoufik and Abdelmajid Jemni (2017). "Economic assessment and applications of photovoltaic/thermal hybrid solar technology: A review". In: *solar Energy* 153, pp. 540–561.
- Calise, Francesco, Massimo Dentice d'Accadia, and Laura Vanoli (2012). "Design and dynamic simulation of a novel solar trigeneration system based on hybrid photovoltaic/thermal collectors (PVT)". In: *Energy Conversion and Management* 60, pp. 214–225.
- Carvajal, Danilo and Dahyann Araya (2012). "Estimating the Energy Savings Potential in a Residential Area of Valparaiso (Chile) by Roof Integrated Unglazed Solar Collectors for Domestic Solar Water Heating". In: *CHEMICAL ENGINEERING* 29.
- Cengel, Yunus A, Sanford Klein, and William Beckman (1998). *Heat transfer: a practical approach*. Vol. 141. WBC McGraw-Hill Boston.
- Chaabane, Monia, Hatem Mhiri, and Philippe Bournot (2014). "Thermal performance of an integrated collector storage solar water heater (ICSSWH) with phase change materials (PCM)". In: *Energy conversion and management* 78, pp. 897–903.
- Chow, TT (2003). "Performance analysis of photovoltaic-thermal collector by explicit dynamic model". In: *Solar Energy* 75.2, pp. 143–152.
- Chow, TT, W He, and J Ji (2007). "An experimental study of facade-integrated photovoltaic water-heating system". In: *Applied thermal engineering* 27.1, pp. 37–45.
- Cremers, Jan et al. (2015). "Experimental analyses of different PVT collector designs for heating and cooling applications in buildings". In: *Energy Procedia* 78, pp. 1889–1894.
- Cristofari, Christian et al. (2002). "Modelling and performance of a copolymer solar water heating collector". In: *Solar Energy* 72.2, pp. 99–112.
- Cui, Yuanlong et al. (2022). "Current status and future development of hybrid PV/T system with PCM module: 4E (energy, exergy, economic and environmental) assessments". In: *Renewable and Sustainable Energy Reviews* 158, p. 112147.
- Darouach, Mohamed, Michel Zasadzinski, and Shi Jie Xu (1994). "Full-order observers for linear systems with unknown inputs". In: *IEEE transactions on automatic control* 39.3, pp. 606–609.
- DeJarnette, Drew et al. (2014). "Plasmonic nanoparticle based spectral fluid filters for concentrating PV/T collectors". In: *High and low concentrator systems for solar energy applications IX*. Vol. 9175. International Society for Optics and Photonics, p. 917509.
- Diwania, Sourav et al. (2020). "Photovoltaic–thermal (PV/T) technology: a comprehensive review on applications and its advancement". In: *International Journal of Energy and Environmental Engineering* 11.1, pp. 33–54.
- DUALSUN (2021). *Dual sun panels*. <https://dualsun.com/en/>. Accessed: 2021-02-11.
- Dubey, Swapnil and GN Tiwari (2008). "Thermal modeling of a combined system of photovoltaic thermal (PV/T) solar water heater". In: *Solar energy* 82.7, pp. 602–612.
- Duffie, John A and William A Beckman (2013). *Solar engineering of thermal processes*. John Wiley & Sons.
- Dupeyrat, Patrick et al. (2011). "Efficient single glazed flat plate photovoltaic–thermal hybrid collector for domestic hot water system". In: *Solar Energy* 85.7, pp. 1457–1468.

- Eicker, Ursula and Antoine Dalibard (2011). "Photovoltaic–thermal collectors for night radiative cooling of buildings". In: *Solar Energy* 85.7, pp. 1322–1335.
- Energy and Industrial Strategy (2016). *Evidence Gathering – Low Carbon Heating Technologies Hybrid Solar Photovoltaic Thermal Panels*. [https://assets.publishing.service.gov.uk/government/uploads/system/uploads/attachment\\_data/file/545246/Solar\\_PVT\\_FINAL\\_\\_1\\_.pdf](https://assets.publishing.service.gov.uk/government/uploads/system/uploads/attachment_data/file/545246/Solar_PVT_FINAL__1_.pdf). Accessed: 2022-03-06.
- Energy star (2018). *Natural resources Canada, Air-source heat pumps*. <https://www.nrcan.gc.ca/energy-efficiency/energy-star-canada/about-energy-star-canada/energy-star-announcements/publications/heating-cooling-heat-pump/air-source-heat-pumps/6831>. Accessed: 2021-01-15.
- Esmailzadeh, E et al. (2013). "Experimental investigation of hydrodynamics and heat transfer characteristics of  $\gamma$ -Al<sub>2</sub>O<sub>3</sub>/water under laminar flow inside a horizontal tube". In: *International Journal of Thermal Sciences* 63, pp. 31–37.
- Eurostat (2021). *Eurostat Statistics Explained, Electricity price statistics*. [https://ec.europa.eu/eurostat/statistics-explained/index.php/Electricity\\_price\\_statistics](https://ec.europa.eu/eurostat/statistics-explained/index.php/Electricity_price_statistics). Accessed: 2021-02-11.
- Fang, Guiyin, Hainan Hu, and Xu Liu (2010). "Experimental investigation on the photovoltaic–thermal solar heat pump air-conditioning system on water-heating mode". In: *Experimental Thermal and fluid science* 34.6, pp. 736–743.
- Florschuetz, LW (1979). "Extension of the Hottel-Whillier model to the analysis of combined photovoltaic/thermal flat plate collectors". In: *Solar energy* 22.4, pp. 361–366.
- Fong, KF et al. (2010). "Comparative study of different solar cooling systems for buildings in subtropical city". In: *Solar Energy* 84.2, pp. 227–244.
- Fujii, Tetsu and Hideaki Imura (1972). "Natural-convection heat transfer from a plate with arbitrary inclination". In: *International journal of heat and mass transfer* 15.4, pp. 755–767.
- Gang, Pei et al. (2011). "A numerical and experimental study on a heat pipe PV/T system". In: *Solar energy* 85.5, pp. 911–921.
- Gangadevi, R, BK Vinayagam, and S Senthilraja (2017). "Experimental investigations of hybrid PV/Spiral flow thermal collector system performance using Al<sub>2</sub>O<sub>3</sub> and water nanofluid". In: *IOP Conference Series: Materials Science and Engineering*. Vol. 197. 1. IOP Publishing, p. 012041.
- Garg, HP and RS Adhikari (1998). "Transient simulation of conventional hybrid photovoltaic/thermal (PV/T) air heating collectors". In: *International journal of energy research* 22.6, pp. 547–562.
- Gaur, MK and GN Tiwari (2010). "Optimization of number of collectors for integrated PV/T hybrid active solar still". In: *Applied Energy* 87.5, pp. 1763–1772.
- Golla, Armin, Philipp Staudt, and Christof Weinhardt (2019). "Combining PVT generation and air conditioning: A cost analysis of surplus heat utilization". In: *2019 International Conference on Smart Energy Systems and Technologies (SEST)*. IEEE, pp. 1–6.
- Good, Clara Stina et al. (2015). "Hybrid photovoltaic-thermal systems in buildings—a review". In: *Energy Procedia* 70, pp. 683–690.
- Guarracino, Ilaria et al. (2016). "Dynamic coupled thermal-and-electrical modelling of sheet-and-tube hybrid photovoltaic/thermal (PVT) collectors". In: *Applied Thermal Engineering* 101, pp. 778–795.
- Hasan, A and AA Sayigh (1994). "Some fatty acids as phase-change thermal energy storage materials". In: *Renewable energy* 4.1, pp. 69–76.
- Hasan, Afif (1994a). "Phase change material energy storage system employing palmitic acid". In: *Solar energy* 52.2, pp. 143–154.

- Hasan, Afif (1994b). "Thermal energy storage system with stearic acid as phase change material". In: *Energy Conversion and Management* 35.10, pp. 843–856.
- Hassine, I Ben et al. (2014). "Operational improvements of a large-scale solar thermal plant used for heat supply in the ham production". In: *Gleisdorf Solar* 154.
- He, Yurong et al. (2007). "Heat transfer and flow behaviour of aqueous suspensions of TiO<sub>2</sub> nanoparticles (nanofluids) flowing upward through a vertical pipe". In: *International journal of heat and mass transfer* 50.11-12, pp. 2272–2281.
- Hegazy, Adel A (2000). "Comparative study of the performances of four photovoltaic/thermal solar air collectors". In: *Energy Conversion and management* 41.8, pp. 861–881.
- Herrando, María, Christos N Markides, and Klaus Hellgardt (2014). "A UK-based assessment of hybrid PV and solar-thermal systems for domestic heating and power: system performance". In: *Applied Energy* 122, pp. 288–309.
- Herrando, María and Alba Ramos (2022). "Photovoltaic-Thermal (PV-T) Systems for Combined Cooling, Heating and Power in Buildings: A Review". In: *Energies* 15.9, p. 3021.
- Herrando, María et al. (2019). "Solar combined cooling, heating and power systems based on hybrid PVT, PV or solar-thermal collectors for building applications". In: *Renewable Energy* 143, pp. 637–647.
- Heyhat, MM et al. (2013). "Experimental investigation of laminar convective heat transfer and pressure drop of water-based Al<sub>2</sub>O<sub>3</sub> nanofluids in fully developed flow regime". In: *Experimental Thermal and Fluid Science* 44, pp. 483–489.
- Huang, BJ et al. (2001). "Performance evaluation of solar photovoltaic/thermal systems". In: *Solar energy* 70.5, pp. 443–448.
- Huang, Chao-Yang, Hsien-Chao Sung, and Kun-Lung Yen (2013). "Experimental study of photovoltaic/thermal (PV/T) hybrid system". In: *Int. J. Smart Grid Clean Energy* 2.2, pp. 147–151.
- Hui, Stefen and Stanisław Żak (2005). "Observer design for systems with unknown inputs". In: *International Journal of Applied Mathematics and Computer Science* 15, pp. 431–446.
- Iaccarino, Gianluca, Georgi Kalitzin, and Christopher J Elkins (2003). *Numerical and experimental investigation of the turbulent flow in a ribbed serpentine passage*. Tech. rep. STANFORD UNIV CA DEPT OF MECHANICAL ENGINEERING.
- Ichalal, Dalil, Said Mammar, and José Ragot (2016). "Auxiliary dynamics for observer design of nonlinear TS systems with unmeasurable premise variables". In: *IFAC-PapersOnLine* 49.5, pp. 1–6.
- International Energy Agency (2016). *KEY RENEWABLES TRENDS: DEVELOPMENT OF RENEWABLES AND WASTE IN THE WORLD - EU Agenda*. <https://euagenda.eu/upload/publications/untitled-69169-ea.pdf>. Accessed: 2022-03-06.
- Jadhao, Rohit R et al. (2017). "Differentiating the Performance of Solar Water Heater under Natural and Forced Circulation". In: *Intl. Research J. Engg. Tech.* 4.11.
- Ji, Jie, Tin-Tai Chow, and Wei He (2003). "Dynamic performance of hybrid photovoltaic/thermal collector wall in Hong Kong". In: *Building and Environment* 38.11, pp. 1327–1334.
- Ji, Jie et al. (2006). "Effect of fluid flow and packing factor on energy performance of a wall-mounted hybrid photovoltaic/water-heating collector system". In: *Energy and Buildings* 38.12, pp. 1380–1387.
- Jia, Yuting, Guruprasad Alva, and Guiyin Fang (2019). "Development and applications of photovoltaic-thermal systems: A review". In: *Renewable and Sustainable Energy Reviews* 102, pp. 249–265.

- Joshi, Sandeep S and Ashwinkumar S Dhoble (2018). "Photovoltaic-Thermal systems (PVT): Technology review and future trends". In: *Renewable and Sustainable Energy Reviews* 92, pp. 848–882.
- Joyce, António et al. (2011). "A PV/T and heat pump based trigeneration system model for residential applications". In: *ISES Solar World Congress*.
- Kalogirou, Soteris (2003). "The potential of solar industrial process heat applications". In: *Applied Energy* 76.4, pp. 337–361.
- Kalsi, Karanjit et al. (2010). "Sliding-mode observers for systems with unknown inputs: A high-gain approach". In: *Automatica* 46.2, pp. 347–353.
- Khalifa, Abdul-Jabbar N (1998). "Forced versus natural circulation solar water heaters: A comparative performance study". In: *Renewable energy* 14.1-4, pp. 77–82.
- Khoshvaght-Aliabadi, Morteza and Ahmad Alizadeh (2015). "An experimental study of Cu–water nanofluid flow inside serpentine tubes with variable straight-section lengths". In: *Experimental Thermal and Fluid Science* 61, pp. 1–11.
- Kicsiny, Richárd and Z Varga (2012). "Real-time state observer design for solar thermal heating systems". In: *Applied mathematics and computation* 218.23, pp. 11558–11569.
- Kim, Jin-Hee, Se-Hyeon Park, and Jun-Tae Kim (2014). "Experimental performance of a photovoltaic-thermal air collector". In: *Energy Procedia* 48, pp. 888–894.
- Kong, Decheng et al. (2020a). "Experimental study of solar photovoltaic thermal (PV/T) air collector drying performance". In: *Solar Energy* 208, pp. 978–989.
- Kong, Rithy et al. (2020b). "Performance and economic evaluation of a photovoltaic thermal (PV/T)-cascade heat pump for combined cooling, heat and power in tropical climate area". In: *Journal of Energy Storage* 30, p. 101507.
- Koşan, Meltem et al. (2020). "Performance analyses of sustainable PV/T assisted heat pump drying system". In: *Solar Energy* 199, pp. 657–672.
- Koyuncu, Turhan (2006). "An investigation on the performance improvement of greenhouse-type agricultural dryers". In: *Renewable energy* 31.7, pp. 1055–1071.
- Kumar, Rakesh and Marc A Rosen (2011). "Integrated collector-storage solar water heater with extended storage unit". In: *Applied Thermal Engineering* 31.2-3, pp. 348–354.
- Kumar, Shiv and Arvind Tiwari (2008). "An experimental study of hybrid photovoltaic thermal (PV/T)-active solar still". In: *International Journal of Energy Research* 32.9, pp. 847–858.
- (2010). "Design, fabrication and performance of a hybrid photovoltaic/thermal (PV/T) active solar still". In: *Energy Conversion and Management* 51.6, pp. 1219–1229.
- Lammle, Manuel, Maria Herrando, and Glen Ryan (2020). *Basic concepts of PVT collector technologies, applications and markets - International Energy Agency*. [https://task60.iea-shc.org/Data/Sites/1/publications/D5\\_Basic\\_concepts\\_of\\_PVT\\_technologies\\_200501.pdf](https://task60.iea-shc.org/Data/Sites/1/publications/D5_Basic_concepts_of_PVT_technologies_200501.pdf). Accessed: 2021-02-09.
- Li, Zhaomeng et al. (2022). "Parametric analysis on G-PV/T collector: Performance optimization and energy trade-off among two critical structures under various outside conditions". In: *Energy*, p. 124449.
- Liang, Ruobing et al. (2020). "Characteristics analysis of the photovoltaic thermal heat pump system on refrigeration mode: An experimental investigation". In: *Renewable Energy* 146, pp. 2450–2461.
- Lin, Wenye et al. (2014). "Development and evaluation of a ceiling ventilation system enhanced by solar photovoltaic thermal collectors and phase change materials". In: *Energy conversion and management* 88, pp. 218–230.

- Liu, Nian et al. (2018). "Distributed Energy Sharing for PVT-HP Prosumers in Community Energy Internet: A Consensus Approach". In: *Energies* 11.7, p. 1891.
- Lu, Shixiang et al. (2020). "Refrigeration characteristics of a hybrid heat dissipation photovoltaic-thermal heat pump under various ambient conditions on summer night". In: *Renewable Energy* 146, pp. 2524–2534.
- Luenberger, David (1966). "Observers for multivariable systems". In: *IEEE Transactions on Automatic Control* 11.2, pp. 190–197.
- Luo, Liang et al. (2020). "Optimal scheduling of a renewable based microgrid considering photovoltaic system and battery energy storage under uncertainty". In: *Journal of Energy Storage* 28, p. 101306.
- Luo, Xi et al. (2019). "Optimal design and cost allocation of a distributed energy resource (DER) system with district energy networks: A case study of an isolated island in the South China Sea". In: *Sustainable Cities and Society* 51, p. 101726.
- Ma, Tao, Meng Li, and Arash Kazemian (2020). "Photovoltaic thermal module and solar thermal collector connected in series to produce electricity and high-grade heat simultaneously". In: *Applied Energy* 261, p. 114380.
- Malvi, CS, DW Dixon-Hardy, and R Crook (2011). "Energy balance model of combined photovoltaic solar-thermal system incorporating phase change material". In: *Solar Energy* 85.7, pp. 1440–1446.
- Manual, UDF (2009). "ANSYS FLUENT 12.0". In: *Theory Guide*.
- Marcott, Shaun A et al. (2013). "A reconstruction of regional and global temperature for the past 11,300 years". In: *science* 339.6124, pp. 1198–1201.
- Mauthner, Franz, Werner Weiss, and Monika Spork-Dur (2014). *Solar Heat Worldwide Markets and Contribution to the Energy Supply 2014*. <http://www.iea-shc.org/data/sites/1/publications/Solar-Heat-Worldwide-2016.pdf>. Accessed: 2022-03-06.
- Mechmeche, C, H Hamdi, and H Yahoui (2008). "State observer for bilinear systems subjected to unknown inputs". In: *2008 5th International Multi-Conference on Systems, Signals and Devices*. IEEE, pp. 1–6.
- Metry, Morcos et al. (2016). "MPPT of photovoltaic systems using sensorless current-based model predictive control". In: *IEEE Transactions on Industry Applications* 53.2, pp. 1157–1167.
- Mofijur, Mahlia et al. (2019). "Phase change materials (PCM) for solar energy usages and storage: An overview". In: *Energies* 12.16, p. 3167.
- Monjezi, Alireza Abbassi et al. (2020). "Development of an off-grid solar energy powered reverse osmosis desalination system for continuous production of freshwater with integrated photovoltaic thermal (PVT) cooling". In: *Desalination* 495, p. 114679.
- Moradgholi, Meysam, Seyed Mostafa Nowee, and Ali Farzaneh (2018). "Experimental study of using Al<sub>2</sub>O<sub>3</sub>/methanol nanofluid in a two phase closed thermosyphon (TPCT) array as a novel photovoltaic/thermal system". In: *Solar Energy* 164, pp. 243–250.
- M'Sirdi, Nacer K et al. (2018). "Dynamic coupled electrical and thermal model for PV-T solar energy collectors". In: *2018 5th International Symposium on Environment-Friendly Energies and Applications (EFEA)*. IEEE, pp. 1–8.
- Murshed, SM Sohel and CA Nieto De Castro (2014). "Superior thermal features of carbon nanotubes-based nanofluids—A review". In: *Renewable and Sustainable Energy Reviews* 37, pp. 155–167.
- Noro, Marco and Renato M Lazzarin (2018). "Hybrid PhotoVoltaic–Thermal heat pump systems: energy and economic performance evaluations in different climates". In: *International Journal of Low-Carbon Technologies* 13.1, pp. 76–83.

- Nualboonrueng, Thipjak et al. (2012). "Field experiments of PV-thermal collectors for residential application in Bangkok". In: *Energies* 5.4, pp. 1229–1244.
- Ong, Chin Lee et al. (2012). "A novel concept of energy reuse from high concentration photovoltaic thermal (HCPVT) system for desalination". In: *Desalination* 295, pp. 70–81.
- Oueslati, H, S Ben Mabrouk, and A Mami (2011). "Evaluation of the performance of solar air collector by using Bond Graph approach". In: *International Review on Modelling and Simulations* 20.
- Ouhaine, Lahoucine et al. (2017). "A General fractional-order heat transfer model for Photovoltaic/Thermal hybrid systems and its observer design". In: *Energy Procedia* 139, pp. 49–54.
- Pakere, Ieva, Dace Lauka, and Dagnija Blumberga (2018). "Solar power and heat production via photovoltaic thermal panels for district heating and industrial plant". In: *Energy* 154, pp. 424–432.
- Pantic, S, L Candanedo, and AK Athienitis (2010). "Modeling of energy performance of a house with three configurations of building-integrated photovoltaic/thermal systems". In: *Energy and buildings* 42.10, pp. 1779–1789.
- Rafaralahy, Hugues et al. (1996). "Unknown input observer for bilinear systems with gain optimisation". In: *IFAC Proceedings Volumes* 29.1, pp. 4368–4373.
- Rafiei, Alireza et al. (2019). "Thermal analysis of a hybrid solar desalination system using various shapes of cavity receiver: Cubical, cylindrical, and hemispherical". In: *Energy Conversion and Management* 198, p. 111861.
- Rakhra, Manik et al. (2021). "Crop price prediction using random forest and decision tree regression:-a review". In: *Materials Today: Proceedings*.
- Ramos, Alba et al. (2017). "Hybrid photovoltaic-thermal solar systems for combined heating, cooling and power provision in the urban environment". In: *Energy conversion and management* 150, pp. 838–850.
- Rezk, Hegazy et al. (2019). "Design and hardware implementation of new adaptive fuzzy logic-based MPPT control method for photovoltaic applications". In: *Ieee Access* 7, pp. 106427–106438.
- Rigatos, G, Pierluigi Siano, and Jorge Pomares (2017). "A nonlinear H-infinity control approach for closed-chain robotic mechanisms". In: *2017 IEEE International Conference on Mechatronics (ICM)*. IEEE, pp. 31–36.
- Rigatos, Gerasimos et al. (2018). "Optimization of olive-oil extraction using nonlinear H-infinity control". In: *IFAC-PapersOnLine* 51.32, pp. 439–444.
- Royne, Anja, Christopher J Dey, and David R Mills (2005). "Cooling of photovoltaic cells under concentrated illumination: a critical review". In: *Solar energy materials and solar cells* 86.4, pp. 451–483.
- Rukman, Nurul Shahirah Binti et al. (2018). "Overview of Bifluid-based Photovoltaic Thermal (PVT) Systems". In: *International Journal of Power Electronics and Drive Systems* 9.4, p. 1912.
- Rukman, Nurul Shahirah Binti et al. (2019). "Electrical and thermal efficiency of air-based photovoltaic thermal (PVT) systems: An overview". In: *Indonesian Journal of Electrical Engineering and Computer Science* 14.3, pp. 1134–1140.
- Sachit, FA et al. (2018). "Nanofluids used in photovoltaic thermal (pv/t) systems". In: *International Journal of Engineering & Technology* 7.3.20, pp. 599–611.
- Santbergen, Rudi and RJ Ch van Zolingen (2008). "The absorption factor of crystalline silicon PV cells: A numerical and experimental study". In: *Solar energy materials and solar cells* 92.4, pp. 432–444.

- Saoudi, Dhikra, Mohammed Chadli, and Naceur Benhadj Braiek (2013). "State estimation of unknown input fuzzy bilinear systems: Application to fault diagnosis". In: *2013 European Control Conference (ECC)*. IEEE, pp. 2465–2470.
- Sardarabadi, Mohammad et al. (2017). "Experimental investigation of the effects of using metal-oxides/water nanofluids on a photovoltaic thermal system (PVT) from energy and exergy viewpoints". In: *Energy* 138, pp. 682–695.
- Sathe, Tushar M and AS Dhoble (2017). "A review on recent advancements in photovoltaic thermal techniques". In: *Renewable and Sustainable Energy Reviews* 76, pp. 645–672.
- Sathyamurthy, Ravishankar et al. (2015). "A review of different solar still for augmenting fresh water yield". In: *Journal of Environmental Science and Technology* 8.6, pp. 244–265.
- Schindler, Florian et al. (2017a). "How to achieve efficiencies exceeding 22% with multicrystalline n-type silicon solar cells". In: *Energy Procedia* 124, pp. 777–780.
- (2017b). "Optimized multicrystalline silicon for solar cells enabling conversion efficiencies of 22%". In: *Solar Energy Materials and Solar Cells* 171, pp. 180–186.
- Sinha, Sunanda and SS Chandel (2014). "Review of software tools for hybrid renewable energy systems". In: *Renewable and Sustainable Energy Reviews* 32, pp. 192–205.
- Slimani, Mohamed El Amine et al. (2017). "A detailed thermal-electrical model of three photovoltaic/thermal (PV/T) hybrid air collectors and photovoltaic (PV) module: Comparative study under Algiers climatic conditions". In: *Energy conversion and management* 133, pp. 458–476.
- SOLIMPEKS (2020). *Solimpeks, Solar energy corp.* <https://www.solimpeks.com/>. Accessed: 2021-02-11.
- Sotehi, O, A Chaker, and C Maalouf (2016). "Hybrid PV/T water solar collector for net zero energy building and fresh water production: a theoretical approach". In: *Desalination* 385, pp. 1–11.
- Sukamongkol, Yod et al. (2010). "Condenser heat recovery with a PV/T air heating collector to regenerate desiccant for reducing energy use of an air conditioning room". In: *Energy and buildings* 42.3, pp. 315–325.
- Sun, Vat et al. (2022). "Performance analysis on combined heat and power of photovoltaic thermal module integrated with phase change material-water storage". In: *Journal of Energy Storage* 47, p. 103614.
- Thong, Li Wah et al. (2016). "Analysis of photovoltaic panel temperature effects on its efficiency". In: *System* 18.19.
- Tiwari, Arvind and MS Sodha (2006). "Performance evaluation of solar PV/T system: an experimental validation". In: *Solar energy* 80.7, pp. 751–759.
- Tiwari, GN and Ankita Gaur (2014). "Photovoltaic thermal (PVT) systems and its applications". In: *2nd international conference on green energy and technology*. IEEE, pp. 132–138.
- Tiwari, Sumit, Sanjay Agrawal, and GN Tiwari (2018). "PVT air collector integrated greenhouse dryers". In: *Renewable and Sustainable Energy Reviews* 90, pp. 142–159.
- Tiwari, Sumit and GN Tiwari (2016). "Exergoeconomic analysis of photovoltaic-thermal (PVT) mixed mode greenhouse solar dryer". In: *Energy* 114, pp. 155–164.
- Tiwari, Sumit, GN Tiwari, and IM Al-Helal (2016). "Performance analysis of photovoltaic thermal (PVT) mixed mode greenhouse solar dryer". In: *Solar Energy* 133, pp. 421–428.
- Tiwari, Sumit et al. (2016). "Thermal modelling of photovoltaic thermal (PVT) integrated greenhouse system for biogas heating". In: *Solar Energy* 136, pp. 639–649.

- Tonui, JK and Y Tripanagnostopoulos (2008). "Performance improvement of PV/T solar collectors with natural air flow operation". In: *Solar energy* 82.1, pp. 1–12.
- Touafek, K, A Khelifa, and M Adouane (2014). "Theoretical and experimental study of sheet and tubes hybrid PVT collector". In: *Energy Conversion and Management* 80, pp. 71–77.
- Tripanagnostopoulos, Yiannis et al. (2002). "Hybrid photovoltaic/thermal solar systems". In: *Solar energy* 72.3, pp. 217–234.
- Vasičkaninová, Anna et al. (2018). "Robust controller design for a laboratory heat exchanger". In: *Applied Thermal Engineering* 128, pp. 1297–1309.
- Wang, Weiwen and Zhiqiang Gao (2003). "A comparison study of advanced state observer design techniques". In: *Proceedings of the 2003 American Control Conference, 2003*. Vol. 6. IEEE, pp. 4754–4759.
- Wang, Zhao, Roberto Rosas, and Chunjiang Qian (2015). "Nonlinear observer design for a solar thermal water heater system". In: *The 27th Chinese Control and Decision Conference (2015 CCDC)*. IEEE, pp. 4817–4822.
- Wijeratne, WM Pabasara U et al. (2019). "Design and development of distributed solar PV systems: Do the current tools work?" In: *Sustainable cities and society* 45, pp. 553–578.
- Xie, Huaqing, Wei Yu, and Wei Chen (2010). "MgO nanofluids: higher thermal conductivity and lower viscosity among ethylene glycol-based nanofluids containing oxide nanoparticles". In: *Journal of Experimental Nanoscience* 5.5, pp. 463–472.
- Yang, Tingting and Andreas K Athienitis (2012). "A study of design options for a building integrated photovoltaic/thermal (BIPV/T) system with glazed air collector and multiple inlets". In: *Energy Procedia* 30, pp. 177–186.
- You, Wei-qian, Huai-hai Chen, and Xu-dong He (2010). "Tracking control research of high-order flexible structures on the H-infinity control method". In: *2010 2nd International Conference on Advanced Computer Control*. Vol. 5. IEEE, pp. 111–115.
- Yousefi, Tooraj et al. (2012). "An experimental investigation on the effect of Al<sub>2</sub>O<sub>3</sub>-H<sub>2</sub>O nanofluid on the efficiency of flat-plate solar collectors". In: *Renewable Energy* 39.1, pp. 293–298.
- Zerrouki, A, A Boumedien, and K Bouhadeif (2002). "The natural circulation solar water heater model with linear temperature distribution". In: *Renewable energy* 26.4, pp. 549–559.
- Zhao, Lijun et al. (2021). "Grid-Tied PV-BES system based on modified bat algorithm-FLC MPPT technique under uniform conditions". In: *Neural Computing and Applications* 33.21, pp. 14929–14943.
- Zhou, Chao, Ruobing Liang, and Jili Zhang (2017). "Optimization design method and experimental validation of a solar pvt cogeneration system based on building energy demand". In: *Energies* 10.9, p. 1281.
- Zhou, Chao et al. (2019). "Experimental investigation on the tri-generation performance of roll-bond photovoltaic thermal heat pump system during summer". In: *Energy Conversion and Management* 184, pp. 91–106.
- Zhou, Jinzhi et al. (2020). "Numerical simulation and experimental validation of a micro-channel PV/T modules based direct-expansion solar heat pump system". In: *Renewable Energy* 145, pp. 1992–2004.
- Zondag, Herman A et al. (2002). "The thermal and electrical yield of a PV-thermal collector". In: *Solar energy* 72.2, pp. 113–128.

## Résumé long en Français

L'énergie joue un rôle vital dans la stabilité économique et la qualité de vie d'une nation. L'augmentation significative du niveau de vie par rapport à celui d'il y a un siècle, la demande énergétique mondiale a augmenté. La consommation élevée de sources d'énergie conventionnelles a provoqué une augmentation de la température mondiale. La température moyenne mondiale a augmenté au rythme de 1.7°C par siècle depuis 1970. Menacés par ce danger, et avertis par de nombreux scientifiques et chercheurs, presque tous les pays se tournent vers la technologie des énergies renouvelables. De nombreuses recherches sont en cours dans le domaine des énergies renouvelables, notamment l'énergie solaire, éolienne et thermique, et leur utilisation augmente rapidement de jour en jour. Ces sources d'énergie durables, à savoir l'énergie solaire, peuvent être trouvées en abondance tout au long de l'année. L'énergie solaire en tant que composant principal devient de plus en plus populaire et largement adoptée, en raison de nombreux facteurs; hausse des prix du carburant, technologie à faible émission de carbone, baisse des prix de l'énergie solaire photovoltaïque, réduction des factures d'énergie, respect de l'environnement, changement climatique et disponibilité mondiale de l'énergie solaire. Par conséquent, le développement des centrales solaires est plus rapide que celui des autres centrales électriques renouvelables dans le monde. On estime qu'il y aura 16% de la production d'énergie solaire photovoltaïque dans le monde d'ici 2050. Aujourd'hui, la capacité installée de l'énergie solaire photovoltaïque est d'environ 350 GW, le taux d'installation augmentera et d'ici 2040, la capacité installée atteindra la barre des 700 GW.

Un contexte général concernant les systèmes PV-T est fourni où il souligne la motivation derrière cela révélant explicitement la nécessité de développer de tels systèmes. Le contexte, les objectifs recherchés, les défis rencontrés, l'approche développée et les applications réalisées sont présentés. Environ 60 à 70% du rayonnement solaire absorbé par le module photovoltaïque est converti en chaleur et dans des conditions idéales, un maximum de 22% du rayonnement est converti en électricité par les technologies actuelles des panneaux PV. Le rayonnement infrarouge inutilisé est converti en chaleur, ce qui fait chuter l'efficacité électrique des cellules solaires d'environ 1% par 2°C. Les systèmes PV-T sont une bonne solution, ils offrent non seulement une électricité à faible émission de carbone, mais extraient également l'énergie thermique perdue simultanément via un moyen d'extraction de chaleur en combinant des modules photovoltaïques et solaires thermiques en une seule unité intégrée, en utilisant au mieux la surface surface des panneaux. Tout système PV-T hybride est composé de trois éléments principaux : les cellules solaires, un échangeur de chaleur à un ou plusieurs canaux de fluide et un fluide d'extraction de chaleur.

D'autres composants optionnels peuvent être ajoutés. Les cellules PV couramment utilisées dans les systèmes PV-T sont les cellules typiques en silicium monocristallin et polycristallin. Les deux peuvent être utilisés indifféremment en termes de performances thermiques. La priorité des systèmes PV-T est de générer de l'électricité tandis que la chaleur produite est gaspillée dans l'environnement par les pertes de chaleur radiative et convective si elle n'est pas utilisée à des fins de chauffage, c'est-à-dire le chauffage des locaux, l'eau chaude sanitaire, etc.

Le fluide caloporteur joue un rôle important en extrayant la chaleur inutilisée du module PV par circulation au sein de l'installation où la température peut atteindre jusqu'à 80°C. L'air et l'eau sont les deux fluides couramment utilisés pour extraire la chaleur des systèmes PV-T. Le PV-T à base d'air présente peu d'avantages par rapport aux capteurs à base de liquide ; pas de gel, pas d'ébullition et de fuite qui n'endommagera pas le panneau. Le seul inconvénient majeur des capteurs à air est le faible transfert de chaleur qui est dû à une faible capacité calorifique et à une faible conductivité thermique. Un capteur PV-T à base de liquide peut produire jusqu'à 40% d'énergie en plus que les capteurs photovoltaïques et solaires thermiques individuels installés sur la même surface. De plus, il existe un capteur PV-T bi-fluide qui utilise l'air et le liquide en même temps pour augmenter les performances thermiques. En dehors de cela, il existe des collecteurs PV-T à nano-fluide et à base de PCM. Les matériaux à changement de phase sont capables de stocker et de libérer de grandes quantités de chaleur latente lors d'un changement d'état (du solide au liquide et vice-versa). Afin d'améliorer les performances des panneaux PV-T, l'intégration d'une couche statique PCM solide-liquide peut être incorporée. Pendant la journée, le PCM fond en absorbant la chaleur du soleil. La nuit, le PCM gèle et libère sa chaleur latente, de sorte que la chaleur stockée dans le PCM peut être utilisée pour des applications thermiques. Dans les systèmes PV-T, les nanofluides ne sont pas seulement utilisés comme liquides de filtrage optique mais aussi comme fluide de refroidissement.

Deux types différents d'extraction de chaleur sont discutés, la circulation forcée et la circulation naturelle. Une pompe permet de faire circuler le fluide à l'intérieur d'un collecteur en circulation forcée et le fluide circule sous l'action de la force de flottabilité en circulation naturelle. La conception de systèmes de circulation naturelle n'est pas compliquée et coûte moins cher. En général, les systèmes basés sur la convection forcée ont un meilleur rendement thermique. Le rendement global du panneau est également meilleur du moment que le nombre de ventilateurs ou de pompe est optimisé afin de ne pas trop consommer d'énergie électrique. L'un des principaux inconvénients des capteurs solaires est qu'ils fonctionnent bien lorsque la lumière du soleil est directe, sinon une partie de la lumière du soleil est négligée si un système de suivi n'est pas mis en place. Le vitrage joue un rôle important dans la

conception d'un panneau PV-T. Il collecte plus d'énergie thermique, réduit les pertes de chaleur convective et radiative et, dans la plupart des cas, il agit comme une protection et protège le panneau PV sensible de plusieurs impacts environnementaux. Il en résulte une meilleure production d'énergie thermique du collecteur PV-T. Cependant, le vitrage réduit le rendement électrique dans une quantité dépendant de la transmissivité de la couche de vitrage. En ce qui concerne les coûts, les panneaux PV-T avec vitrage sont plus chers que les panneaux non vitrés, car ils utilisent un matériau supplémentaire.

Les PV-T hybrides sont comparés à l'utilisation séparée de panneaux photovoltaïques et solaires thermiques combinés dans une zone spatiale donnée. Dans les deux cas, on observe que les PV-T sont meilleurs que la combinaison solaire thermique et photovoltaïque du fait que le photovoltaïque couvre généralement des zones plus larges que le solaire thermique et que leur chaleur n'est pas récupérée. Le collecteur PV-T a plusieurs applications telles que le système thermique photovoltaïque intégré au bâtiment, la trigénération, le dessalement, la climatisation, le chauffage/refroidissement urbain, le séchage, le stockage de chaleur, la serre solaire, la réfrigération et les applications industrielles. Les applications du système PV-T sont divisées en fonction de leurs températures, comme indiqué dans le rapport du programme de chauffage et de refroidissement solaire de l'Agence internationale de l'énergie. Les applications à haute température nécessitent des températures élevées et sont utilisées pour certains procédés industriels. Les applications à moyenne température sont utilisées dans les bâtiments pour l'eau chaude sanitaire et le chauffage des locaux. Les applications à basse température concernent les systèmes de pompe à chaleur et le chauffage des piscines ou des spas. Pendant la saison hivernale, l'excès de chaleur produit par le collecteur est gaspillé et cette chaleur pourrait être utilisée à des fins de refroidissement. Une courte revue détaillée sur le refroidissement est présentée qui comprend; comment la technologie dessiccante, les refroidisseurs à absorption et à adsorption fonctionnent avec les PV-T. Il souligne également une comparaison de la puissance du réseau, du PV et des PV-T à des fins de refroidissement.

Le marché de la technologie solaire thermique se développe rapidement en raison de ses avantages, mais à l'heure actuelle, le marché est relativement petit. L'étude de faisabilité d'une installation solaire nécessite des outils de conception et de simulation pour optimiser la production d'énergie. À cette fin, divers logiciels développés ont été discutés. De plus, les modules PV-T disponibles sur le marché sont présentés avec leurs spécifications telles que le milieu de travail, le poids, le type de cellule solaire, couvert/non couvert, la surface, le rendement électrique et thermique par panneau. On peut conclure que la technologie solaire thermique se développe

rapidement et que la disponibilité facile de l'énergie solaire rend l'avenir de la technologie solaire brillant. Malgré de nombreuses recherches théoriques et expérimentales, il existe encore de nombreuses possibilités d'améliorations futures dans le développement de produits futurs qui sont discutés.

Ce projet de recherche concerne la modélisation, la conception, l'optimisation et le contrôle d'un système hybride photovoltaïque-thermique. Un certain nombre de configurations différentes et divers modèles thermiques ont été rapportés avec l'influence de divers paramètres sur les performances des systèmes PV-T. Une modélisation détaillée des systèmes PV-T est présentée et la modélisation nécessite une étude approfondie du transfert de chaleur entre les composants du collecteur. Trois modèles différents sont développés qui incluent; modèle à base d'air-I où l'air en tant que fluide caloporteur circule sous le module PV. Le collecteur est composé d'un couvercle en verre, de cellules photovoltaïques, d'un tedlar, d'un canal d'air et d'un isolateur. Dans le modèle II basé sur l'air, l'air circule au-dessus du module PV et est composé d'un couvercle en verre, d'un canal d'air, de cellules PV et d'un isolant. Enfin, dans le modèle à base d'eau, l'eau s'écoule dans les tubes parallèles. Le collecteur est constitué de différentes couches : une couverture en verre, des cellules photovoltaïques, un tedlar, un absorbeur, des tubes métalliques traversés par l'eau et un isolant. L'objectif est de développer des modèles dynamiques non linéaires qui donnent une performance réaliste et raisonnable du système. Les équations fondamentales pour la partie thermique sont déterminées à l'aide d'une approche de graphe de liaison qui est un outil générique et général pour représenter les transferts thermiques. Il se compose d'éléments de résistance, de conformité et d'inertie qui sont interconnectés par des jonctions, des liaisons et un flux d'énergie ou de puissance.

De plus, à l'aide d'une boîte à outils d'identification de système, différents ordres de fonctions de transfert ont été testés afin de trouver celle qui convient le mieux au modèle à base de l'air I. L'objectif est de construire un modèle qui se rapproche du comportement d'un système en utilisant des données d'entrée et de sortie. Ce modèle simple donne une approximation satisfaisante du comportement du système non linéaire. Cependant, le modèle n'est valable que sur quelques points de fonctionnement et est suffisamment bon pour le contrôle. Le modèle thermique est exprimé sous la forme d'espace d'état où l'état contient la température de chaque composant, le débit massique est défini comme l'entrée contrôlée, le rayonnement solaire, la température ambiante, la vitesse du vent et la température d'entrée du fluide comme perturbations. La description de l'espace d'état est utile pour la simulation du comportement dynamique du système. En outre, un modèle multiple est construit pour un modèle à base d'eau par transformation mathématique et le procédé est basé sur une transformation polytopique convexe de fonctions non linéaires qui utilisent la

délimitation de termes non linéaires. Le nombre de modèles dépend du nombre de termes non linéaires.

Le séchage des produits agricoles est très populaire dans les pays en développement et constitue un procédé critique. Cette étude porte sur l'application du système PV-T, un séchoir solaire basé sur des panneaux solaires hybrides et la récupération de la chaleur perdue ainsi que le recyclage de l'air. L'air de sortie est recyclé de la chambre de séchage vers l'entrée du collecteur PV-T, évidemment en utilisant un procédé ou un traitement qui évite le recyclage de l'humidité. On suppose que la température de l'air d'entrée qui est injecté dans le capteur est proportionnelle à la température de l'air de sortie. Enfin, le collecteur a été modélisé à l'aide d'un réseau de neurones artificiels et d'un algorithme d'arbre de décision. Un arbre de décision est une approche d'apprentissage automatique supervisé qui utilise des ensembles de données d'entrée-sortie pour former des modèles. Il construit un modèle de régression sous forme d'arborescence et le but est de développer un modèle qui prédit la variable cible à partir de plusieurs variables d'entrée. Les données sont divisées à l'aide d'un arbre binaire et commencent au nœud racine jusqu'à la gauche avec les nœuds feuilles ou les nœuds terminaux. De même, les réseaux de neurones artificiels ont une capacité d'apprentissage élevée et la capacité d'identifier des systèmes non linéaires complexes. Par conséquent, la technique de modélisation du réseau neuronal artificiel est utilisée, comme un outil puissant, pour prédire et déterminer la puissance thermique et l'efficacité photovoltaïque.

Les simulations sont un bon moyen d'analyser les performances thermiques des capteurs et permettent de mener des investigations détaillées sur la distribution de température de tous les composants du capteur. Les performances du capteur PV-T dépendent de plusieurs paramètres : la température ambiante, le rayonnement solaire, le débit massique, la vitesse du vent, le fluide qui s'écoule (par exemple l'eau ou l'air) et l'épaisseur des différents composants. Le programme Matlab est utilisé pour les conceptions numériques et les paramètres climatiques proposés. L'évolution de la température de toutes les composantes PV-T pour les trois modèles est présentée pour une distribution typique du rayonnement solaire et de la température ambiante sous un échantillon de conditions climatiques du sud de la France. L'échantillon est prélevé pendant la journée en raison du rayonnement solaire élevé et de la température ambiante. Les résultats indiquent que la température ambiante maximale est d'environ 29°C et que la température de l'air de sortie du conduit passe à 34°C pour le modèle à base d'air I, alors que pour le modèle à base d'air II, elle va à environ 37°C avec un débit massique de 0.02kgs<sup>-1</sup> et la température d'entrée est considérée comme identique à la température ambiante. De plus, la température de l'eau pour le capteur à base d'eau s'élève à 43°C avec une température d'entrée de l'eau de 20°C. Le transfert de chaleur utilisant l'air comme moyen de transfert de

chaleur est faible en raison de la faible capacité thermique et de la faible conductivité thermique. La température de l'isolant reste proche de la température ambiante du fait des conditions ambiantes et pas d'élévation importante de la température du fluide. Il est évident que la température du composant du module PV est supérieure à celle des autres composants pour tous les modèles. La performance du modèle à base d'air-I en ajoutant un composant absorbant juste au-dessus de l'isolant est analysée pour connaître son influence sur la puissance thermique mais aucune élévation significative de la température n'est constatée.

On observe que l'efficacité électrique moyenne du module PV est d'environ 15% alors que l'efficacité thermique du collecteur est comprise entre 25 et 30% pendant les heures de jour pour le modèle I à base d'air. L'ajout de vitrage améliore l'efficacité thermique quotidienne en évitant les pertes thermiques et en maximisant la puissance thermique. L'efficacité thermique constatée avec l'ajout de vitrage est comprise entre 30% et 40%. Cependant, le vitrage réduit l'efficacité électrique et l'efficacité PV quotidienne moyenne est d'environ 14.5%. L'efficacité quotidienne moyenne du PV pour le modèle aérien II est d'environ 14.5% alors qu'elle est plus élevée dans le modèle aérien I. Ceci est principalement dû au fait que la température de la cellule est ici élevée mais que l'efficacité thermique moyenne est d'environ 44%, ce qui est beaucoup plus élevé que dans le cas précédent. De même, le rendement thermique journalier moyen du capteur à eau est compris entre 30 et 45%. Une analyse de sensibilité des variables physiques et externes a été effectuée pour le modèle à base d'eau. L'épaisseur de l'isolant est un paramètre de conception important, influençant les performances d'un collecteur et pour des raisons économiques, des épaisseurs supérieures à 0.08 m ne sont pas nécessaires car les pertes d'énergie deviennent constantes. Le capteur PV-T présente une efficacité thermique plus élevée si la vitesse du vent est faible et passe de 46% à 32% avec une augmentation de la vitesse du vent de  $1\text{ms}^{-1}$  à  $5\text{ms}^{-1}$ . À un débit massique inférieur, l'augmentation/la chute de température est faible par rapport aux débits massiques élevés.

Les résultats obtenus à partir du modèle physique proposé (modèle à base de l'air II) sont ensuite comparés aux résultats CFD. On observe que les résultats CFD obtenus sont compatibles avec les résultats physiques malgré la structure du maillage et les critères de convergence dans l'étude CFD qui valident la viabilité du modèle proposé. De même, les résultats obtenus à partir du modèle à base d'eau proposé sont ensuite comparés aux études antérieures trouvées dans la littérature. On constate qu'il existe une bonne compatibilité entre les résultats expérimentaux et les résultats simulés. En conclusion générale, les résultats de simulation fondés par le modèle numérique développé dans cette étude et les études expérimentales trouvées dans la littérature valident la viabilité du modèle proposé.

Dans le scénario de recyclage en séchage solaire, la température de sortie d'air

augmente. Il y a une augmentation significative (entre le débit d'air et le débit d'air recyclé) à mesure que le rayonnement solaire augmente par rapport au rayonnement solaire inférieur. Un débit massique plus faible est nécessaire pour obtenir une température de sortie plus élevée. Un réseau de neurones artificiels qui est une technique d'apprentissage en profondeur a une meilleure précision dans la prédiction des sorties par rapport à un algorithme d'arbre de décision qui est une approche d'apprentissage automatique. Les modèles développés sont conviviaux et l'approche de l'intelligence artificielle pourrait être utilisée comme alternative afin de réduire les coûts.

Dans la section suivante, une nouvelle conception d'un capteur photovoltaïque-thermique qui intègre un réservoir de stockage à l'arrière du module thermique pour stocker la chaleur ainsi qu'une résistance électrique pour augmenter la production thermique si nécessaire est présentée. Le travail étudie la modélisation et la simulation CFD dans le but de fournir un modèle dynamique qui reflète un comportement réaliste du système. L'agencement PV-T global comprend un couvercle en verre, une couche de cellules PV, un tedlar, un absorbeur, un tube serpentin à travers lequel le fluide s'écoule, un réservoir de stockage et un isolateur. Le tube serpentin extrait la chaleur du haut du collecteur et la transfère au fluide du réservoir. L'unité de stockage se trouve juste en dessous de la plaque absorbante et est isolée thermiquement de tous les côtés pour minimiser les pertes de chaleur et améliorer la résistance structurelle. De plus, une résistance chauffante est incluse comme source complémentaire afin d'obtenir la température de sortie requise du réservoir de stockage pendant la saison hivernale ou par temps nuageux. Tout d'abord, le modèle électrique du collecteur est présenté, basé sur le modèle à une seule diode d'un module photovoltaïque dans lequel cinq paramètres électriques dérivent le comportement électrique du dispositif solaire. Ces cinq paramètres dépendent directement de la température de la cellule et du rayonnement solaire. La partie thermique du PV-T embarqué avec le modèle de réservoir est basée sur le principe de conservation d'énergie et pour chaque couche du collecteur, un bilan énergétique prenant en compte les échanges thermiques radiatifs, convectifs et conducteurs entre les couches. Quelques informations précieuses concernant l'influence de divers paramètres tels que le matériau (c'est-à-dire l'aluminium, le cuivre et l'huile moteur usée), le fluide d'extraction de chaleur (c'est-à-dire l'eau pure, l'eau mélangée avec du glycol, le glycol pur et le matériau à changement de phase) et l'épaisseur de divers composants sur la température du fluide de sortie et la température du réservoir de stockage sont également fournies.

Des simulations sont effectuées pour mettre en évidence l'utilité de la conception proposée. Trois cas différents sont considérés pour cette étude avec différents rayonnement solaire, température ambiante et température d'entrée du réservoir.

L'inclusion d'un espace d'air augmente la température de tous les composants améliorant l'efficacité thermique mais au détriment de l'efficacité PV. On constate qu'une épaisseur supérieure à 0.10 m n'est pas nécessaire pour des raisons économiques et les pertes d'énergie deviennent constantes. En utilisant du cuivre comme matériau absorbant et de tube serpentin, la température du fluide augmente alors qu'elle diminue avec une augmentation de l'épaisseur de la plaque absorbante. Le milieu d'extraction de chaleur est un paramètre de conception important, et les résultats obtenus indiquent que l'eau mélangée avec du glycol est un bon choix car elle est facilement disponible et moins chère alors que le glycol pur et le PCM ont un taux de transfert de chaleur élevé. L'abondance d'huiles moteur usagées ou usagées peut être recyclée, ce qui rend le système moins coûteux et garantit la durabilité environnementale. Enfin, le réservoir de stockage est intégré à une résistance chauffante en secours pour assurer une utilisation continue pendant la saison hivernale, ou par temps nuageux pour compenser la baisse de température. La modélisation s'avère utile pour analyser l'influence des paramètres géométriques internes, tels que l'épaisseur de l'isolant et de l'absorbeur, le type de fluide ainsi que les matériaux utilisés pour l'absorbeur et le serpentin. La cohérence du modèle physique a été validée en comparant les résultats avec les résultats CFD. Les différences qui se produisent sont suffisamment faibles pour être prises en compte en raison des hypothèses prises en compte dans le modèle physique et la structure du maillage et les critères de convergence dans l'étude CFD. L'erreur moyenne trouvée dans le cas-I est de 3.40%, 4.10% pour le deuxième cas et 2.87% pour le troisième cas.

L'optimisation de tels systèmes est très importante afin d'obtenir un rendement maximal qui est le plus d'énergie avec un coût moindre et cela nécessite d'analyser l'effet de divers paramètres. L'optimisation est effectuée pour un modèle à base d'eau et un algorithme génétique est utilisé pour optimiser les paramètres de conception en définissant les limites supérieure et inférieure de chaque paramètre de conception. Dans un premier temps, les paramètres de conception considérés sont l'épaisseur d'une couverture en verre, le tedlar, l'absorbeur et l'isolant. Le but est de maximiser la température de sortie de l'eau ce qui est une tâche complexe puisque le débit est fonction des états et du temps. L'inclusion de limitations de prix pour chaque composant est un bon moyen de résoudre le problème. Sinon, cela générerait une solution évidente car une augmentation ou une diminution de l'épaisseur du paramètre augmentera la température de sortie d'un canal d'air à la valeur maximale possible ou la diminuera à la valeur la plus basse. Ensuite, le débit massique est optimisé car une augmentation du débit massique augmente la consommation électrique du ventilateur, ce qui entraîne une efficacité PV inférieure. Encore une fois, la maximisation de la production générerait une solution évidente, de sorte que l'inclusion de la maximisation de l'efficacité PV est un bon moyen de résoudre le

problème. On observe qu'il se produit de petites différences de température lorsque l'épaisseur du composant est modifiée, mais pour les grandes plantes, ces petites variations feront une grande différence.

Les contrôleurs sont conçus pour suivre la température de sortie souhaitée même en présence de perturbations. Tout d'abord, un contrôleur de type PI est proposé pour le modèle I à base d'air et s'est avéré garantir de bonnes performances. L'objectif est de contrôler la température de sortie d'air à la valeur souhaitée en utilisant le débit d'entrée d'air comme variable de contrôle dans différentes conditions de fonctionnement. Ensuite, pour le modèle équivalent linéarisé du modèle II basé sur l'air, un contrôleur de rétroaction H-infini est conçu. Cela nécessite la résolution d'une équation algébrique de Riccati à chaque pas de temps de l'algorithme de commande. L'efficacité du schéma de contrôle est affichée de manière analytique. Les résultats indiquent que le contrôleur H-infini peut satisfaire les spécifications de suivi qui garantissent également une robustesse maximale aux perturbations externes. En outre, cette étude présente une conception de contrôleur en mode glissant et un contrôle basé sur un réseau neuronal artificiel pour un collecteur à base d'eau. L'objectif est de contrôler la température de sortie de l'eau à la valeur souhaitée. En commande par modes glissants, l'approche consiste à concevoir une loi de commande qui impose à toutes les trajectoires du système de converger sur une surface de l'espace d'état, également appelée surface de glissement. Enfin, pour le contrôle basé sur un réseau de neurones artificiels, l'approche consiste à former le contrôleur en collectant des données via des simulations. Les deux contrôleurs suivent le point de référence et rejettent les changements qui se produisent dans le rayonnement solaire, la température ambiante et la vitesse du vent.

La conception d'observateurs pour les systèmes non linéaires est un problème difficile en raison de son importance dans la conception de commandes automatiques telles que la commande, la surveillance et le diagnostic des défauts. Les observateurs sont les systèmes dynamiques qui fournissent une estimation de l'état interne d'une usine à l'aide de ses mesures d'entrée-sortie. Pour la première partie, une approche d'inégalité matricielle linéaire est utilisée pour concevoir un observateur permettant d'estimer les états du modèle thermique photovoltaïque-thermique bilinéaire. L'efficacité et la performance de l'observateur proposé dans l'estimation des états du système sont montrées par simulation. Dans la deuxième partie, l'objectif est de construire un observateur soumis à une entrée inconnue. Cette partie propose une amélioration de la conception par rapport à la partie précédente sur l'application d'un observateur d'état à entrée inconnue pour les systèmes photovoltaïques thermiques où  $\hat{x}$  est estimé en connaissant  $\dot{T}_{wi}$ . Une approche de Lyapunov est utilisée

pour assurer la stabilité et une inégalité de matrice linéaire est résolue simultanément afin de trouver une matrice symétrique définie positive soumise à une contrainte d'égalité linéaire. Les conditions nécessaires et suffisantes pour l'existence d'une telle approche sont données. Une procédure de conception est résumée et la technique proposée est enfin illustrée par des simulations. Les résultats indiquent que l'erreur d'estimation d'état converge vers zéro pour tous les états, montrant ainsi l'efficacité des schémas présentés.

**Abstract** — The standard of living has risen the global energy demand and fossil fuel energy usage is considered the main factor for the rise in global temperature. Renewable energy has been one of the main areas of interest by governments of nearly all countries. Solar energy is clean and the most abundant energy source available around the globe and a photovoltaic thermal (PV-T) system uses solar energy and provides heat and low carbon electricity at the same time. Different heat extraction mediums, hybrid design configurations and the main applications of PV-T collectors are addressed to highlight their feasibility and usefulness.

The focus of this thesis work is the modeling, design, optimization, and control of a hybrid PV-T collector. The modeling of the different configurations of hybrid PV-T collectors was conducted and studied in detail. It requires a thorough study of heat transfer between the collector's components and the proposed approach is based on a bond graph technique which is a generic and general tool to represent thermal transfers. A real engineering application, a solar dryer based on the PV-T collector and waste heat recovery along with air recirculation is also investigated.

The thesis presents a new design of a PV-T collector that incorporates a storage tank to store heat as well as an electrical resistance to increase thermal production when necessary. Computational fluid dynamics (CFD) simulation of a system and the subsequent validation of the proposed design are then presented. This study also focuses on assessing the influence of internal geometrical parameters. The achieved results permit to analyze the usefulness of the proposed design and validate the viability. Optimization of such systems is highly important in order to get maximum output that is the most energy with lower cost and this requires analyzing the effect of various parameters.

The temperature range of the collector must be controlled and the developed models are applied for the purpose of control and observation. The output temperature was controlled using a variety of controllers that are; a simple PI controller, H-infinity controller and sliding mode controller (SMC). Moreover, a multiple model is constructed and an observer is designed for estimating the states of the multiple model. A state observer with an unknown input is also developed, an improvement in the design. It was shown that the designed controllers track the desired set points and the proposed observers estimate the states of the collector, thus displaying the effectiveness. Finally, the hybrid PV-T collector was modeled by using artificial neural network (ANN) and also used for the purpose of control.

**Keywords:** Hybrid PV-T; Mathematical modeling; Design; Optimization; Control and Observation.

**Résumé** — Le niveau de vie a augmenté la demande mondiale d'énergie et la consommation d'énergie fossile est considérée comme le principal facteur de l'augmentation de la température mondiale. Les énergies renouvelables sont l'un des principaux domaines d'intérêt des gouvernements de presque tous les pays. L'énergie solaire est propre et la source d'énergie la plus abondante disponible dans le monde et un système photovoltaïque thermique (PV-T) utilise l'énergie solaire et fournit en même temps de la chaleur et de l'électricité à faible émission de carbone. Différents moyens d'extraction de chaleur, des configurations de conception hybrides et les principales applications des collecteurs PV-T hybrides sont abordés pour mettre en évidence leur faisabilité et leur utilité.

L'objectif de ce travail de thèse est la modélisation, la conception, l'optimisation et le contrôle d'un collecteur PV-T hybride. La modélisation des différentes configurations de collecteurs hybrides PV-T a été réalisée et étudiée en détail. Cela nécessite une étude approfondie des transferts de chaleur entre les composants du collecteur, l'approche proposée est basée sur une technique de graphe de liaison qui est un outil générique et général pour représenter les transferts thermiques. Une véritable application d'ingénierie, un séchoir solaire basé sur le collecteur PV-T et la récupération de la chaleur perdue ainsi que la recirculation de l'air est également étudiée.

La thèse présente une nouvelle conception d'un collecteur PV-T qui intègre un réservoir de stockage de la chaleur ainsi qu'une résistance électrique pour augmenter la production thermique lorsque cela est nécessaire. La simulation numérique de la dynamique des fluides d'un système et la validation ultérieure de la conception proposée sont ensuite présentées. Cette étude porte également sur l'évaluation de l'influence des paramètres géométriques internes. Les résultats obtenus permettent d'analyser l'utilité du design proposé et d'en valider la viabilité. L'optimisation de tels systèmes est importante afin d'obtenir un rendement maximal : le plus d'énergie possible à moindre coût et cela nécessite d'analyser l'effet de divers paramètres.

La plage de température du collecteur doit être contrôlée et les modèles développés sont appliqués à des fins de contrôle et d'observation. La température de sortie a été contrôlée à l'aide d'une variété de contrôleurs qui sont : un contrôleur PI simple, un contrôleur H-infinity et un contrôleur à mode glissant. De plus, un modèle multiple est construit et un observateur est conçu pour estimer les états du modèle multiple. Un observateur d'état avec une entrée inconnue est également développé, une amélioration de la conception. Il a été démontré que les contrôleurs conçus suivent les points de consigne souhaités et que les observateurs proposés estiment les états du collecteur, affichant ainsi l'efficacité. Enfin, le collecteur thermique PV-T a été modélisé en utilisant un réseau de neurones artificiels et utilisé à des fins de contrôle.

**Mots-clés:** Panneaux solaires hybrides; Modélisation mathématique; Conception; Optimisation; Contrôle et Observation